Development of a pH-responsive Implant for the Targeted Control of Feral Cats and the Protection of Native Mammals

Kyle Robert Charles Brewer
BSc (Hons)

A thesis submitted for the degree of
Doctor of Philosophy (PhD)

Applied Chemistry and Translational Biomaterials (ACTB) Group,
Centre for Pharmaceutical Innovation (CPI),
UniSA Clinical and Health Sciences (CHS)



University of
South Australia

2023

Contents

Chapter 1: Introduction 1

1.1 The Impacts of Invasive Mammalian Predators 1

1.1.1 Feral Cat Control Methods — An Overview 2

1.1.2 Toxicants 5

1.1.3 Problem Individuals 8

1.1.4 Population Protecting Implants 8

The Concept 8

Design Considerations 10

1.2 Subcutaneous Implants 12

1.2.1 Reservoir-type Implants for Drug Delivery 12

1.3 Polymer Synthesis 13

1.3.1 Polymer Synthesis — A Brief Overview 13

1.3.2 Conventional Free Radical Polymerisation 14

1.3.3 Plasticisers 17

1.3.4 Stimuli-responsive Polymers 20

1.4 Reverse Enteric Coatings 21

1.5 Polymer Membranes/Films as Barrier Coatings 26

1.6 Applicable Manufacturing Methods 28

1.6.1 Fluidised-bed Spray Coating 30

1.6.2 Hot-melt Extrusion 33

1.6.3 Implant Manufacture 36

1.7 Thesis Scope 37

1.7.1 Hypothesis 37

1.7.2 Research Objectives 37

1.7.3 Thesis Outline 38

1.8 References 42

Chapter 2: Scientec Research Pty Ltd and the Hard-Shell Delivery Vehicle — A State of the Art 55

2.1 Overview 55

2.2 Introduction 55
2.3 HSDV Samples Received for Testing 56
2.4 Results and Discussion 59
2.4.1 Critical Evaluation of HSDV Design and Manufacture 59
2.4.2 HSDV *In Vitro* Performance Evaluation 61
2.5 Conclusions 65
2.6 Experimental 67
2.6.1 Materials 67
2.6.2 Instrumentation 67
2.6.3 Procedures 67
In Vitro Stability Experiments *67*
In Vitro Release Experiments *68*
2.7 References 69
Chapter 3: Preliminary Implant Design and Manufacture 71
3.1 Overview 71
3.2 Results and Discussion 72
3.2.1 Implant Core Preparation 72
3.2.2 Synthesis and Characterisation of Poly[(2-vinylpyridine)$_x$-*co*-(butyl methacrylate)$_y$] (PVB) Copolymers 74
3.2.3 Thermal Characterisation of the PVB Copolymers 77
3.2.4 pH-dependent Solubility of the PVB copolymers 79
3.2.5 Water Absorption Properties of the PVB Copolymers 80
3.2.6 Manufacture and Evaluation of the PVB Implants 81
3.2.7 *In Vitro* Evaluation of PVB Implant Performance 83
3.2.8 *In Vivo* Evaluation of PVB Implant Performance 85
3.3 Conclusions 89
3.4 Experimental 90
3.4.1 Materials 90
3.4.2 Instrumentation 91
Gas Chromatography *91*
Proton Nuclear Magnetic Resonance Spectroscopy *91*

Gel Permeation Chromatography *92*

Modulated Differential Scanning Calorimetry *92*

Modulated Thermogravimetric Analysis *92*

Fluidised-bed Spray Coating *93*

Scanning Electron Microscopy *93*

Ultraviolet-visible Light Spectrophotometry *93*

3D Printing. *94*

3.4.3 Procedures 94

Synthesis of Poly[(2-vinylpyridine)$_x$-co-(butyl methacrylate)$_y$] *94*

Preparation of Implant Coating Formulations *95*

Copolymer Solubility *95*

Copolymer Water Absorption Testing *96*

Implant Manufacture *96*

Implant Embedment and Microtoming *97*

In Vitro Stability Experiments *97*

In Vitro Release Experiments *97*

In Vivo Stability Experiments *98*

Histological Analysis via Optical Microscopy *98*

Computed Tomography *99*

Statistical Analyses *99*

3.5 Appendix 100

3.5.1 Supplementary Figures 100

3.5.2 Copolymer Water Absorption: Effect of Excipients 103

3.5.3 Evaluation of the PVB Copolymers 60/40 and 40/60 as Reverse Enteric, Taste-masking Coatings 106

Methods *106*

Results and Discussion *107*

In Vitro Evaluation of the Taste-masking Performance of PVB 60/40 and 40/60 ..... *109*

3.6 References 113

Chapter 4: Synthesis and Characterisation of pH-responsive Copolymers for Reverse Enteric Coatings 115

4.1 Overview 115

4.2 Results and Discussion 115

4.2.1 Copolymers of 2-Vinylpyridine and Butyl Methacrylate, and Methyl Methacrylate or Isobornyl Methacrylate 115

4.2.2 Synthesis and Characterisation of Poly[(2-vinylpyridine)$_x$-*co*-(butyl methacrylate)$_y$-*co*-(methyl methacrylate)$_z$] (PVBM) Copolymers 116

4.2.3 Thermal Characterisation of the PVBM Copolymers 119

4.2.4 pH-dependent Solubility of the PVBM copolymers 121

4.2.5 Water Absorption Properties of the PVBM Copolymers 122

4.2.6 Poly[(2-vinylpyridine)$_x$-*co*-(butyl methacrylate)$_y$-*co*-(isobornyl methacrylate)$_z$] 122

4.2.7 Synthesis and Characterisation of Poly[(2-vinylpyridine)$_x$-*co*-(butyl methacrylate)$_y$-*co*-(isobornyl methacrylate)$_z$] (PVBI) Copolymers 123

4.2.8 Thermal Characterisation of the PVBI Copolymers 125

4.2.9 pH-dependent Solubility of the PVBI Copolymers 126

4.2.10 Water Absorption Properties of the PVBI Copolymers 127

4.2.11 Manufacture and Evaluation of the PVBI Implants 128

4.3 Conclusions 130

4.4 Experimental 131

4.4.1 Materials 131

4.4.2 Instrumentation 131

Nuclear Magnetic Resonance Spectroscopy 131

4.4.3 Procedures 131

Synthesis of Poly[(2-vinylpyridine)$_x$-co-(butyl methacrylate)$_y$-co-(methyl methacrylate)$_z$] 131

Synthesis of Poly[(2-vinyl pyridine)$_x$-co-(butyl methacrylate)$_y$-co-(isobornyl methacrylate)$_z$] 132

Preparation of Implant Coating Formulations 133

4.5 Appendix 134

4.5.1 Supplementary Figures 134

4.5.2 Evaluation of the PVBM Copolymers 30/50/20 and 40/50/10 as Reverse Enteric, Taste-masking Coatings 135

Fluidised-bed Spray Coating 135

In Vitro Evaluation of the Taste-masking Performance of PVBM 30/50/20 and 40/50/10 ..... *136*

4.6 References 139

Chapter 5: Manufacture and Evaluation of Implants with an Optimised Reverse Enteric Coating 140

5.1 Overview 140

5.2 Results and Discussion 141

5.2.1 Plasticisation of Poly[(2-vinylpyridine)$_x$-*co*-(butyl methacrylate)$_y$-*co*-(isobornyl methacrylate)$_z$] (PVBI 50/30/20) 141

5.2.2 Manufacture and Evaluation of the PVBI/EO$_{10}$ Implants 144

5.2.3 Investigation of the Mechanical Properties of the PVBI/EO$_{10}$ Implants 148

5.2.4 *In Vitro* Release Properties of the PVBI/EO$_{10}$ Implants 149

5.2.5 *In Vitro* Stability Properties of PVBI/EO$_{10}$ Implants 151

5.2.6 *In Vivo* Stability Properties of PVBI/EO$_{10}$ Implants 152

5.3 Conclusions 156

5.4 Experimental 157

5.4.1 Materials 157

5.4.2 Instrumentation 157

Mass Spectrometry *157*

Modulated Differential Scanning Calorimetry *157*

3D Printing *158*

5.4.3 Procedures 158

Synthesis of Ethyl Oleate *158*

Preparation of Coating Formulations *158*

Implant Manufacture *159*

Mechanical Testing *159*

In Vitro Release Experiments *159*

In Vivo Stability Experiments *160*

Computed Tomography *160*

Statistical Analyses *160*

5.5 Appendix 161

5.6 References 174

Chapter 6: Incorporation of Sodium Fluoroacetate and the Effects on Implant Performance 175

6.1 Overview 175

6.2 Results and Discussion 176

6.2.1 Manufacture and Evaluation of the 1080 Implants 176

6.2.2 Investigation of the Mechanical Properties of the 1080 Implants 181

6.2.3 *In Vitro* Release Properties of the 1080 Implants 182

6.2.4 *In Vitro* Stability Properties of the 1080 Implants 188

6.2.5 Assessment of 1080 Diffusion from 1080 Implants *In Vitro* 189

6.2.6 *In Vivo* Stability Properties of 1080 Implants 190

6.3 Conclusions 193

6.4 Experimental 195

6.4.1 Materials 195

6.4.2 Instrumentation 195

High-performance Liquid Chromatography 195

6.4.3 Procedures 195

Preparation of 1080 Core Coating Formulations 196

Implant Manufacture 196

In Vitro Release Experiments 196

In Vitro 1080 Diffusion Experiments 196

In Vivo Stability Experiments 197

1080 Residue Testing 197

Statistical Analyses 197

6.5 Appendix 198

6.5.1 Supplementary Figures 198

6.6 References 205

Chapter 7: Implant Cores Prepared *via* Hot-melt Extrusion and the Effects on Implant Performance 206

7.1 Overview 206

7.2 Results and Discussion 207

7.2.1 Hot-Melt Extrusion Optimisation of a Poly(ethylene glycol)-based Formulation 207
7.2.2 Critical Evaluation of the Loading Accuracy of PEG-B Extrudates 211
7.2.3 Manufacture and Evaluation of the HME Implants 213
7.3 Implant Performance 217
7.3.1 Investigation of the Mechanical Properties of the 1080 Implants 217
7.3.2 *In Vitro* Release Properties of the HME Implants 218
7.3.3 *In Vitro* Stability Properties of the HME Implants 221
7.4 Conclusions 222
7.5 Experimental 223
7.5.1 Materials 223
7.5.2 Instrumentation 224
Differential Scanning Calorimetry 224
Hot-melt Extrusion 224
Gel Permeation Chromatography 224
7.5.3 Procedures 225
Preparation of Hot-Melt Extrusion Formulations 225
Hot-melt Extrusion 225
Investigation of Hot-Melt Extrusion Formulation Homogeneity 226
In Vitro Release Experiments 226
Statistical Analyses 227
7.6 Appendix 227
7.6.1 Supplementary Figures 227
7.6.2 Hot-melt extrusion of poly(vinyl alcohol) 235
Preparation of Poly(vinyl alcohol) and Sorbitol/Glycerol Hot-melt Extrusion Formulations 235
Hot-melt Extrusion of Poly(vinyl alcohol) and Sorbitol/Glycerol 235
Results and Discussion 235
7.7 References 239
Chapter 8: Conclusions and Future Work 240
8.1 Conclusions 240
8.2 Future Work 245

8.2.1 Targeted Control of Problem Individuals 245
8.2.2 Next-generation Poison Baits 247
8.2.3 Reverse Enteric Pharmaceutical Formulations 249
8.3 Appendix 250
8.3.1 Implants Prepared *via* Additive Manufacturing 250
8.4 References 253
Chapter 9: Research Outputs 254
9.1 Publication Status of Thesis Research 254
9.2 Other Published Works During Candidature 255
9.3 Statement of Authorship 256

List of Figures

Figure 1.1: An illustrated overview of the population protecting implant concept. 9

Figure 1.2: General PPI design, featuring a poison 'core' and a reverse enteric coating. 12

Figure 1.3: A general scheme describing the three stages of CFRP: a) *initiation* of polymerisation *via* the homolytic cleavage of an initiator to generate primary radicals and addition of a radical initiator to a monomer; b) *propagation* of the polymer chain *via* the addition of a number of monomer units, and; c) *termination* of polymerisation by either dimerisation or disproportionation reactions. 16

Figure 1.4: A conceptual illustration of a) spray coating of a substrate and film formation from b) an organic solution, wherein i) the polymer chains begin to interpenetrate as the solvent evaporates, ii) an intermediate gel state is formed as evaporation continues, before iii) film formation occurs. In contrast spray coating from c) an aqueous dispersion, involves i) deposition of aqueous droplets containing polymer particles, ii) stratification of the particles during evaporation, iii) deformation and tight packing of the particles following continued evaporation, and finally iv) coalescence of the polymer particles to form a film. 31

Figure 1.5: Illustration of a) a fluidised-bed spray coating chamber and archetypal spray configurations for b) top-down spray coating, c) bottom-up spray coating, d) bottom-up spray coating with a Wurster column insert, and e) tangential spray coating. Note the fluidisation air flow (blue arrows), spray formulation (yellow), and trajectory of spray coating substrate (green arrows) 33

Figure 1.6: Simplified illustration of a hot-melt extruder, showing how the material for extrusion (a combination of thermoplastic carrier, API, and processing aids and/or excipients) is extruded through a die, *via* a heated barrel and rotating feeder screw. 34

Figure 1.7: Conceptual illustrations of the two approaches to PPI manufacture. a) The ABS filament substrate-based fluidised-bed spray coating approach and b) the hot-melt extrusion and fluidised-bed spray coating approach. 37

Figure 1.8: Graphical abstract illustrating the investigation of the copolymers synthesised in Chapters 3 and 4, as reverse enteric coatings for the taste-masking of pharmaceutical dosage forms.[214] 39

Figure 1.9: Graphical abstract illustrating the investigation of the non-toxic PPIs described in Chapter 5.[215] 40

Figure 1.10: Graphical abstract illustrating the development of the toxic PPIs described in Chapter 6.[213] 41

Figure 1.11: Graphical abstract illustrating the development of the non-toxic PPIs containing a HME core, and a fluidised-bed spray coated pH-responsive coating.[216] 41

Figure 2.1: Representative images of the HSDVs supplied by Scientec: a) HSDV-A, b) HSDV-B, c) HSDV-C, d) HSDV-D, and e) HSDV-E..... 58

Figure 2.2: Example images of RhB release for a) HSDV-A after 10 min, and b) HSDV-B after 4 h, in a pH 1.5 (37 °C) release solution. Note the implants were removed from the 37 °C sample oven prior to imaging. 62

Figure 2.3: Digital images showing the swelling and/or failure of representative a) HSDV-A, b) HSDV-B, c) HSDV-C, d) HSDV-D, and e) HSDV-E samples, during stability testing in Pluronics F127 hydrogels (25% $w.w^{-1}$ in PBS) at pH 7.4 and 37 °C (n = 3). 63

Figure 2.4: Images of a HSDV-A showing a) core material solubilised from the surface of HSDV-A immediately following immersion in Pluronics F127 (25% $w.w^{-1}$ PBS pH 7.4, 37 °C) as indicated by the presence of RhB (black arrows) and b) failure caused by swelling and leakage of the core material from the ends after 16 h in Pluronics F127. Images of a HSDV-B showing c) core material solubilised from the surface of HSDV-B immediately following immersion in Pluronics F127 (black arrow), and d) swelling and release of the core material at one end, after 35 min in a pH 1.5 solution (25 °C)..... 64

Figure 3.1: Representative digital images and scanning electron micrographs of a) an ABS filament substrate, b) a NaOAc core..... 74

Figure 3.2: a) Synthesis of poly[(2-vinylpyridine)$_x$-*co*-(butyl methacrylate)$_y$] (PVB x/y) copolymers *via* CFRP. b) Gel permeation chromatography (GPC) differential refractive index (DRI) chromatograms and c) proton nuclear magnetic resonance (^{1}H NMR) spectra (500 MHz, deuterated chloroform ($CDCl_3$), 21 °C) of the PVB series. 75

Figure 3.3: a) Reversing heat flow ($W.g^{-1}$) curves of the PVB copolymer series determined *via* MDSC. b) Weight (%) and derivative weight ($\%.°C^{-1}$) curve of PVB 50/50, representative of the PVB copolymer series. 78

Figure 3.4: The effect of PVB copolymer composition on solubility at pH 1.0, 1.5 and 2.0 (37 °C). Values are reported as the mean ± std. dev. (n = 3). 80

Figure 3.5: Water absorption (% $w.w^{-1}$) as a function of time from PBS (pH 7.4, 37 °C) for the PVB copolymer series..... 81

Figure 3.6: Representative digital images and scanning electron micrographs of a PVB implant..... 83

Figure 3.7: a) Release monitoring profile of MB ($\lambda_{max.}$ = 663 nm) from PVB implants, at 37 °C, in a pH 1.5 solution (3.5 mL). Traces are reported as the mean (solid line) ± std. dev.

(shaded area) (n = 5). b) Stability results of PVB implants in Pluronics F127 (25% w.w^{-1}, in PBS) at pH 7.4 and 37 °C (n = 10), over ~ 500 d. c) Representative images of a PVB implant during the stability experiment. Note the failure of the pictured implant following 345 d in Pluronics F127, as indicated by the presence of RhB and MB in the surrounding hydrogel. 84

Figure 3.8: a) PVB Implant (purple) and RFID microchip (black) implantation locations (top). FTC thickness (µm) as measured from tissue explants using point-to-point measurements with values reported as mean ± std. dev. of n = 5 (week 1), and n = 15 (weeks 2 and 4) measurements *p < 0.05 x t-test of difference = 0 (vs ≠) (middle). PVB implant diameter measurements obtained from CT scans of implants immediately after implantation and *in situ* during the study (bottom). b) Macroscopic images (post-mortem) of PVB implants *in situ*, captured prior to explantation — note the swelling of the implants and the containment of the core material. c) Haematoxylin and eosin (H&E)-stained samples of the explanted tissue, revealing the fibrous capsule surrounding the PVB implants. 87

Figure A3.1: GPC calibration curves prepared for the copolymer series, from aqueous solutions of each copolymer (10 mg.mL^{-1}, pH 1.0), injected at volumes between 10–100 µL.100

Figure A3.2: CT scans of intact PVB implants captured prior to euthanasia, with implants outlined with dashed white lines. 100

Figure A3.3: Graphs showing a) diameter measurements of the implanted control RFID microchips (n = 3), before (in air) and after (weeks 3 and 4) encapsulation in a FTC, obtained from CT scans during the *in vivo* stability study, b) histological analysis results of type I collagen content as measured from tissue explants using colour thresholding in ImageJ, with values reported as mean ± std. dev. from n = 6 (week 1), n = 2 (week 2) and n = 9 (week 4) measurements, and c) male Sprague-Dawley rat body masses (n = 3), recorded during the *in vivo* stability study (~ 30 d). 101

Figure A3.4: a) The silicon mould used for embedding implants in two-part epoxy. b) An embed affixed to a 3D-printed mounting block. c) The mounted embed fitted in a Thermo Scientific Microm HM 325 microtome..... 102

Figure A3.5: Example of an epoxy-embedded and microtomed PVB implant, and point-to-point measurements used to determine the thickness of the copolymer coating. 102

Figure A3.6: Images showing a) the locations of the PVB implants (purple) and the mini microchip (black) (superimposed over an image of a rat) for the *in vivo* stability study. b) A mini microchip and syringe implanter (1.4 × 8.5 mm) (top), and a PVB implant and syringe implanter (2.12 × 12 mm, bottom), both used during the *in vivo* stability study. 103

Figure A3.7: Water absorption exhibited by PVB 50/50 without and with the addition of the hydrophobic excipients a) octadecanol (12.7, 22.5, and 30.3% w.w^{-1}) and b) micronised talc (10% w.w^{-1}). All values are reported as mean ± std. dev. (n ≥ 4). 104

Figure A3.8: Representative digital images and scanning electron micrographs of a) a NaOAc core and PVB/octadecanol (22.5% w.w^{-1}) coated implant and b) a NaOAc core and PVB/talc (10% w.w−^{1}) coated implant..... 106

Figure A3.9: Suglets® coated with the model drug formulation containing PEG and RhB, coated at a mass gain of 6.2% w.w^{-1}..... 108

Figure A3.10: Suglets® coated with a) PVB 60/40 (5.2% w.w^{-1} mass gain), b) PVB 40/60 (5.4% w.w^{-1} mass gain). 109

Figure A3.11: Release profiles obtained of Suglets® coated with a PEG/RhB model drug formulation (6.2% w.w^{-1} mass gain), and a) PVB 60/40 (5.2% w.w^{-1} mass gain), or b) PVB 40/60 (5.4% w.w^{-1} mass gain), during dissolution in a pH 1.5 solution (37 °C), under stirring. Traces represent individual samples (n = 5), monitored *via* the absorbance maximum of RhB (λ_{max} = 556 nm). Note that in a) two samples show a > 100% release peak maximum, which was caused by a local increase in dye concentration, due to a lag in stirring during analysis.111

Figure 4.1: a) Synthesis of the poly[(2-vinylpyridine)$_x$-*co*-(butyl methacrylate)$_y$-*co*-(methyl methacrylate)$_z$] (PVBM) copolymers *via* CFRP. b) GPC differential refractive index (DRI) chromatograms and c) ^{1}H NMR spectra (500 MHz, deuterated chloroform ($CDCl_3$), 21 °C) of the PVBM copolymer series. 118

Figure 4.2: a) Reversing heat flow (W.g^{-1}) curves of the PVBM copolymer series obtained *via* MDSC. b) Weight (%) and derivative weight (%.°C^{-1}) curves of PVBM 30/40/30 — representative of the PVBM copolymer series — obtained *via* modulated thermogravimetric analysis (MTGA). 120

Figure 4.3: The pH-dependent solubility of the PVBM copolymers (37 °C), as determined by GPC. Values are reported as the mean ± std. dev. (n = 3). Note the absence of PVBM 30/40/30 and 30/50/30, due to their low solubility at pH 1.0. Standard curves used in the GPC analysis of copolymer solubility samples are provided in the Appendix **(Figure A4.1)**.121

Figure 4.4: Water absorption (% w.w^{-1}) determined at pH 7.4 and 37 °C for the PVBM copolymer series. All values are reported as mean ± std. dev. (n = 8)..... 122

Figure 4.5: a) Synthesis of poly[(2-vinylpyridine)$_x$-*co*-(butyl methacrylate)$_y$-*co*-(isobornyl methacrylate)$_z$] (PVBI) copolymers *via* CFRP. b) GPC DRI chromatograms and c) ^{1}H NMR spectra (500 MHz, $CDCl_3$, 21 °C) of the PVBI copolymer series. Carbon-13 nuclear magnetic resonance (^{13}C NMR) spectra are provided in the Appendix **(Figure A4.2)**. 124

Figure 4.6: a) Reversing heat flow (W.g^{-1}) curves of the PVBI copolymer series obtained *via* MDSC. b) Weight (%) and derivative weight (%.°C^{-1}) curves of PVBI 50/30/20 — representative of the PVBI copolymer series — obtained *via* MTGA. 126

Figure 4.7: The effect of PVBI copolymer composition on solubility at pH 1.0, 1.5, and 2.0 (37 °C). Values are reported as the mean ± std. dev (n = 3). Standard curves used in the GPC analysis of copolymer solubility samples are provided in the Appendix (**Figure A4.3**).127

Figure 4.8: Water absorption (% w.w^{-1}) determined at pH 7.4 and 37 °C for the neat PVBI copolymer series. 128

Figure 4.9: Representative a) OM images of PVBI implants, whole (top) and cross-sectioned (bottom). SEM micrographs of a whole PVBI implant showing b) the centre of the implant exhibiting dusting and large fractures in the coating, c) a magnified view of the dusted PVBI 50/30/20 particles, and d) the end of the implant, exhibiting large fractures and dusting. ... 129

Figure A4.1: GPC standard curves for the PVBM 40/50/10 and 40/40/20 copolymers. Standards were prepared from an aqueous solution of each copolymer (pH 1.0, ~ 10 mg.mL^{-1}) and analysed at injection volumes of 10–100 µL (equivalent to 10–100 ug of copolymer on column). 134

Figure A4.2: ^{13}C NMR spectrum (150 MHz, $CDCl_3$, 21 °C) of PVBI 50/30/20. 134

Figure A4.3: GPC standard curves for a) the PVBI 50/45/10 and 50/40/10 copolymers, and b) the PVBI 50/35/15 and 50/30/20 copolymers. Standards were prepared from an aqueous solution of each copolymer (pH 1.0, ~ 10 mg.mL^{-1}) and analysed at injection volumes of 10–100 µL (equivalent to 10–100 ug of copolymer on column). 135

Figure A4.4: Suglets® coated with a) PVBM 40/50/10 (6.5% w.w^{-1} mass gain), b) PVBM 30/50/20 (4.9% w.w^{-1} mass gain). 136

Figure A4.5: Release profiles obtained of Suglets® coated with a PEG/RhB model drug formulation (6.2% w.w^{-1} mass gain), and PVBM 40/50/10 (6.5% w.w^{-1} mass gain), during dissolution in a pH 1.5 solution (37 °C), under stirring. Traces represent individual samples (n = 5), monitored *via* the absorbance maximum of rhodamine b (λ_{max} = 556 nm). 137

Figure 5.1: a) Overlay of the reversing heat flow curves (in arbitrary units, a.u.) from modulated differential scanning calorimetry (MDSC) of PVBI, with 0, 5, 10, and 15% w.w^{-1} EO, showing their respective glass transitions and T_g values. b) Weight (%) and derivative weight (%.°C^{-1}) curves from the MTGA analysis of PVBI/EO_{10}. c) Effect of plasticisation with EO on the solubility of PVBI in pH 1.0, 1.5, and 2.0 solutions; values are reported as the mean ± std. dev. (n = 3), and the solubility results are also tabulated in the Appendix (**Figure A5.1**). d) Effect of plasticisation with 5, 10, and 15% w.w^{-1} EO on the water absorption of PVBI at pH 7.4 and 37 °C; values are reported as the mean ± std. dev. (PVBI n = 8, PVBI/EO_5 n = 5, PVBI/EO_{10} n = 5, and PVBI/EO_{15} n = 4), and the water absorption results are also tabulated in the Appendix (**Table A5.2**). 143

Figure 5.2: Representative digital images and scanning electron micrographs of a) an ABS filament substrate, b) a NaOAc core, c) a NaOAc core and PVBI/EO_{10} coated (300 µm)

implant, and d) an epoxy-embedded and microtomed NaOAc core and PVBI/EO_{10} coated (300 μm) implant, note the filled-in pit encircled in yellow..... 145

Figure 5.3: a) Flexural strength (σ_F) and flexural modulus (E_f) measurements of PVBI and PVBI/EO_{10} implants (n = 5), determined from force versus stroke curves generated through three-point flexural testing. All tests were conducted at ambient temperature (23 ± 1 °C), and all values were calculated for implants with fixed diameters (1.14 mm). σ_F and E_f values are reported as the mean ± std. dev. (n = 5), *p < 0.05 × 2-sample t-test of difference = 0 (vs ≠ 0). Force versus stroke curves from all tests are provided in the Appendix (**Figure A5.1**). b) Release monitoring profiles of MB from PVBI/EO_{10}-coated implants (100, 200, or 300 μm) at 37 ± 1 °C, in pH 1.0 or pH 1.5 (3.5 mL) release media. Traces are reported as the mean (solid line) ± std. dev. (shaded area) (n = 5). c) Stability results of PVBI/EO_{10} implants (100, 200, or 300 μm) in Pluronics F127 (25% $w.w^{-1}$,in PBS) at pH 7.4 and 37 °C (n = 6), over 350 days. Traces represent the number of stable implants (i.e., no failure of the PVBI/EO_{10} coating and release of the core material) for implants at each coating thickness. Images show the swelling and failure of a 100 μm PVBI/EO_{10} implant over 151 days and representative implants that were stable at 350 days..... 150

Figure 5.4: a) PVBI/EO_{10} implant (purple) and microchip (black) locations (top), implant diameter measurements obtained from CT images of implants *in situ* (middle), and fibrous tissue capsule (FTC) thickness (μm) as measured from tissue explants using point-to-point measurements in Olympus LabSens (bottom); values are reported as the mean ± std. dev. (week 0, n = 6; weeks 1–4, n = 3; weeks 6–12, n = 2), *p < 0.05 × t-test of difference = 0 (vs <). b) Macroscopic images (post-mortem) of implants *in situ*, captured prior to explantation, note the swelling of the implants and the containment of the core material. c) CT scans of intact implants captured prior to euthanasia, with implants encircled in white. d) Hematoxylin and eosin (H&E) and e) Masson's trichrome (MT) stained samples of the explanted tissue, revealing the FTC surrounding the implants; representative results for the 9-week implant are available in the Appendix (**Figure A5.3**). 154

Figure A5.1: Force versus stroke graphs obtained *via* three-point flexural testing of implants coated with a) 100, b) 200 and c) 300 μm PVBI, and d) 100, e) 200 and f) 300 μm PVBI/EO_{10} (n = 5 for all samples). 163

Figure A5.2: a) An implant coated with a 300 μm PVBI/EO_{10} coating submerged in a pH 1.5 release solution prior to release, b) during release, and c) an embedded time-lapse video footage of the release (×500 speed, 20 s duration)..... 164

Figure A5.3: Representative results of the PVBI/EO_{10} implant stability *in vivo.* a) Macroscopic images (post-mortem) of implants *in situ*, captured prior to explantation — note the loss of the core material for both 6-week samples (1) and (2). b) CT scans of intact implants captured immediately prior to euthanasia, with implants circled in white. c) H&E and d) MT-stained samples of the explanted tissue, for implants following 6 and 9 weeks *in situ*.165

Figure A5.4: Histological analysis results of type I collagen content as measured from tissue explants using colour thresholding in ImageJ, *p < 0.05 × t-test of difference = 0 (vs <). ... 166

Figure A5.5: a) ^{1}H NMR (500 MHz, $CDCl_3$, 21 °C) and b) ^{13}C NMR (150 MHz, $CDCl_3$, 21 °C) spectra of ethyl oleate. ... 167

Figure A5.6: ESI-MS spectrum of ethyl oleate. ... 168

Figure A5.7: Images of the a) stainless steel Shimadzu EZ-Test EZ-LX mechanical tester probe, b) mechanical tester probe fitted with the 3D-printed probe tip, c) 3D-printed flexural testing stage, d) 3D-printed probe tip and e) three-point flexural testing apparatus, prior to an implant being tested. ... 169

Figure A5.8: 3D-printed three-point flexural testing stage schematic drawings generated in Solidworks showing the a) top, b) bottom, c) left, d) demarcation of B-B cross-section, e) Left B-B cross-section and f) isometric views... 170

Figure A5.9: 3D-printed probe tip schematic drawings generated in Solidworks showing the a) demarcation of A-A cross-section, b) front A-A cross-section, c) front, d) bottom, e) hidden line visible and f) isometric views... 171

Figure 6.1: Representative digital images and scanning electron micrographs of a) a 1080 core, b) a 1080 core with a 300 µm PVBI/EO_{10} coating, and c) an epoxy-embedded and microtomed 1080 core with a 300 µm PVBI/EO_{10} coating; note the 'flared' ends of the core and copolymer coated 1080 implants. ... 179

Figure 6.2: a) Flexural strength (σ_F) and b) flexural modulus (E_f) measurements of the NaOAc and 1080 implants at different PVBI/EO_{10} coating thicknesses, determined *via* three-point flexural testing (Appendix, **Figure A6.1**). All tests were performed at 23 ± 1 °C, and all values are reported as the mean ± std. dev. (n = 5), p < 0.05 × 2-sample t-test of difference = 0 (vs ≠ 0) (Appendix, **Table A6.1)**... 182

Figure 6.3: a) Release profiles for 1080 implants with a 300 µm PVBI/EO_{10} coating, at pH 1.5, 37 °C (n = 4). b) Comparison of normalised absorbance spectra of NaOAc and 1080 implants, and MB solubilised in a pH 1.5 solution. ... 183

Figure 6.4: Release monitoring profiles of MB from 1080 implants with PVBI/EO_{10} coatings of 100, 200, or 300 µm thickness, at 37 °C, in a) pH 1.0 and b) pH 1.5 release media (3.5 mL). Traces are reported as the mean (solid line) ± std. dev. (shaded area) (n = 5). ... 185

Figure 6.5: a) Stability results of 1080 implants with 100, 200, or 300 µm PVBI/EO_{10} coatings in Pluronics F127 (25% w.w^{-1}, in 10 mM phosphate-buffered saline (PBS)) at pH 7.4 and 37 °C (n = 6), over 529 d. Images showing b) the swelling of a 1080 implant with a 300 µm PVBI/EO_{10} coating over 233 d, and c) representative implants that were stable at 529 d. ... 189

Figure 6.6: a) 1080 implant (purple) and microchip (black) locations (top), and number of surviving rats over time (bottom); the body masses of the rats were monitored throughout the study (Appendix, **Figure A6.8**). b) CT images captured immediately following implantation (i.e., day 0), with implants outlined in white. c) Representative macroscopic images (post-mortem) of implants *in situ* captured prior to explantation, after 56 d (failed) (top) and 230 d (stable) (bottom). d) Representative OM images of explants after 56 (failed) (top) and 230 d (stable) (bottom) taken on a 5 × 5 mm grid; note the protrusion of the ABS filament substrate through the polymer coating in both samples. Additional images of the remaining explants are available in the Appendix (**Figure A6.9c,d**). 192

Figure A6.1: Force versus stroke graphs obtained *via* three-point flexural testing of 1080 implants with a) 100, b) 200 and c) 300 µm PVBI/EO_{10} coatings (n = 5 for all samples). ... 198

Figure A6.2: Representative digital images and scanning electron micrographs of a) a 1080/tartrazine implant (i.e., containing tartrazine in the core instead of MB), b) a 1080/tartrazine implant with a 300 µm PVBI/EO_{10} coating, and c) an epoxy-embedded and microtomed 1080/tartrazine implant with a 300 µm PVBI/EO_{10} coating. 199

Figure A6.3: Release monitoring profiles of tartrazine from 1080/tartrazine implants at each PVBI/EO_{10} coating thickness (100, 200 or 300 µm) at 37 ± 1 °C, in pH 1.0 or pH 1.5 (3.5 mL) release media. Traces are reported as the mean (solid line) ± std. dev. (shaded area) (n = 5).200

Figure A6.4: Representative HPLC chromatograms of a) a 224 ppm 1080 standard solution prepared in PBS (pH 7.4) used in the generation of a standard curve, b) the presence and c) absence of 1080, determined in the receiving solution (PBS, pH 7.4) of respective 1080 implants (300 µm PVBI/EO_{10} coating) at 173 d. The peaks attributed to 1080 are indicated — where present — with arrows. 200

Figure A6.5: Digital images of the 1080 implants with a) 100 µm and b) 200 µm PVBI/EO_{10} coatings that failed under accelerated swelling conditions (PBS, PH 7.4, 37 °C). 201

Figure A6.6: Representative digital images of a 1080 implant (300 µm PVBI/EO_{10} coating) captured under accelerated swelling conditions (PBS, pH 7.4, 37 °C). 201

Figure A6.7: Cumulative release profile of 1080 from a failed 1080 implant (300 µm PVBI/EO_{10} coating) under accelerated swelling conditions (PBS, pH 7.4, 37 °C). The presence of 1080 was determined *via* HPLC (λ = 220 nm). Note the dashed line indicates the average calculated loading (3.12 mg) of 1080. 202

Figure A6.8: Rat body masses (n = 7), recorded during the *in vivo* stability experiment of the 1080 implants bearing a 300 µm PVBI/EO_{10} coating. 202

Figure A6.9: A summary of images captured during the *in vivo* stability study of the 1080 implants bearing a 300 µm PVBI/EO_{10} coating. a) CT images captured immediately following implantation (i.e., day 0), note the implants outlined in white. Photographs captured b) during

post-mortem examination *in* or *ex situ*, c) following explantation and the removal of most of the surrounding subcutaneous tissues, and d) following dissection of the fibrous tissue capsule and breakage of the explant. Note, the 5 × 5 mm grid used in the images of b) and c). 203

Figure A6.10: CT scans of 1080 implants (300 µm PVBI/EO_{10} coatings) recorded at the latest time point available prior to failure *in vivo*, with implants outlined in white. 204

Figure 7.1: Images of PEG-B extrudate samples after a) a single extrusion, b) a total of three extrusions, and c) images of PEG-B cores following rotary tumbling. Note the homogenous appearance of the samples following three extrusions in b), and the smooth edges afforded by rotary tumbling in c). 211

Figure 7.2: Representative digital images and scanning electron micrographs of a) a PEG-B core, b) a HME implant with a 300 µm PVBI/EO_{10} coating, and c) an epoxy-embedded and microtomed HME implant with a 300 µm PVBI/EO_{10} coating; note the slight defects caused by the microtoming process (white arrows). 216

Figure 7.3: a) Flexural strength (σ_F) and b) flexural modulus (E_f) measurements of ABS implants and HME implants (n = 5), determined from force *versus* stroke curves generated through three-point flexural testing (Appendix, **Figure A7.6**). All tests were conducted at ambient temperature (23 °C) and all values are reported as the mean ± std. dev. (n = 5), *p < 0.05 × 2-sample t-test of difference = 0 (vs ≠ 0) (**Table A7.1**). 218

Figure 7.4: Release monitoring profiles of tartrazine from HME implants with PVBI/EO_{10} coatings of 100, 200 or 300 µm, at 37 °C, in a) pH 1.0 or b) pH 1.5 release media (3.5 mL). Traces are reported as the mean (solid line) ± std. Dev. (shaded area) (n = 5)... 220

Figure 7.5: a) Stability results of HME implants with 100, 200, or 300 µm PVBI/EO_{10} coatings, in Pluronics F127 (25% $w.w^{-1}$, in phosphate-buffered saline (PBS)) at pH 7.4 and 37 °C (n = 6), over 280 d. b) Images showing the swelling of a HME implant (300 µm PVBI/EO_{10}) over 16 d, and c) representative implants that were stable at 114 d. 222

Figure A7.1: Image of a PEG-A extrudate sample, showing a heterogenous dispersion of NaOAc. 227

Figure A7.2: Heat flow ($W.g^{-1}$) curves (exo up) obtained *via* DSC analysis of neat a) PEG 6 kDa, b) PEG 600 kDa, c) NaOAc, and extruded d) PEG-A, and e) PEG-B formulations. ... 228

Figure A7.3: Digital images of the DCycle Extruder during extrusion, showing a small weight (i.e., paperclip, m = 3.75 g) affixed to the end of the extrudate, to achieve the target diameter (i.e., 1.2 mm). 229

Figure A7.4: Representative GPC DRI chromatograms of PEG a) 6 and b) 600 kDa standards, and c) a PEG-B core sample. d) GPC UV chromatogram a PEG-B core sample.

Standard curves prepared for e) PEG 6 and 600 kDa using the DRI detector, and f) tartrazine using the UV detector. 230

Figure A7.5: a) Images of the filament cutting apparatus, and schematic drawings of the filament cutting apparatus generated in Solidworks, showing the b) tamp used to secure filament during cutting, c) a double-edged razor blade holder used to cut the filament, and d) the cutting jig used to cut the PEG-B filament. Note the measurement labelled in red, which corresponds to the modelled distance between the cutting blade and the end stop for the filament. 231

Figure A7.6: Force *versus* stroke graphs obtained *via* three-point flexural testing of HME implants coated with a) 100, b) 200, and c) 300 µm PVBI/EO_{10} (n = 5 for all samples). 232

Figure A7.7: Images of the custom DCycle Extruder used to extrude the PEG-A and PEG-B hot-melt extrusion formulations. 232

Figure A7.8: Simplified schematic drawing of DCycle Extruder design, showing relevant dimensions of the internal components. 233

Figure A7.9: Images showing a) the abrasive paper (600 grit) lining b) the tumbling container, and c) the ceramic weights, all used to smooth the edges of the PEG-B cores. 233

Figure A7.10: Images of the *in vitro* release experimental apparatus, showing a) the stopper and polyester mesh and b) an implant suspended in the release solution during dissolution. 234

Figure A7.11: Overlay of the reversing heat flow curves ($W.g^{-1}$) from MDSC analyses of NaOAc, PVA 4-88, PVA/G3.5, PVA/$G_{7.1}$, and PVA/G_{11}, showing their respective glass transitions and T_g values, and melting point endotherms. 237

Figure A7.12: Example images of a failed extrusion, showing a) PVA/$S_{7.0}$ material prior to extrusion, and b) PVA/$S_{7.0}$ material following attempted extrusion. 238

Figure A8.1: Schematic drawings generated in Solidworks showing a) a 3D isometric view of the 3D printed capsule, b) a 3D cross-sectional view of the 3D printed capsule, and c) a schematic drawing of the 3D printed capsule with annotated measurements (in mm). Note the red arrow in b) indicating the location of the polymer seal. 251

Figure A8.2: Digital images of a) the end and b) side of a representative 3D printed implant containing a PEG core and a PVBI/EO_{10} polymer seal, and c) a series of 3D printed implant cross-sections, obtained following epoxy embedment and microtoming. 252

List of Tables

Table 1.1: Conventional methods for controlling invasive mammalian predator populations in Australia. 3

Table 1.2: Overview of selected examples of reverse enteric dosage forms, and the processing methods used in their preparation. 23

Table 2.1: Summary of HSDV designs and properties. 60

Table 3.1: Poly[(2-vinylpyridine)$_x$-*co*-(butyl methacrylate)$_y$] copolymer RU mol% ratios and molecular weight characteristics. 76

Table A3.1: Summary of two-tailed Student's t-test results. Tests were performed utilising a t-test of difference = 0 (vs. ≠). 103

Table A3.2: Summary of Suglet® batch properties before and after coating with model drug and copolymer formulations. 107

Table A3.3: Summary of *in vitro* release results of model drug and copolymer coated Suglets®. 110

Table 4.1: Summary of copolymer RU mol% ratios, molecular weight characteristics, and thermal properties. 117

Table 4.2: Summary of copolymer RU ratios, molecular weight characteristics, and thermal properties. 123

Table A4.1: Summary of Suglet® batch properties before and after coating with model drug and copolymer formulations. 136

Table A4.2: Summary of *in vitro* release results of model drug and copolymer coated Suglets®. 137

Table 5.1: Summary of implant dimensions following coating with the lead PVBI/EO$_{10}$ formulation. 147

Table 5.2: Summary of PVBI/EO$_{10}$ implant *in vitro* release results. 151

Table A5.1: Solubility (mg.mL^{-1}) of PVBI with and without plasticisation at pH 1.0, 1.5 and 2.0 (37 °C). 161

Table A5.2: Water absorption (% w.w^{-1}) determined for the copolymer series (pH 7.4, 37 °C). 162

Table A5.3: Summary of two-tailed Student's t-test results. 173

Table 6.1: Summary of implant dimensions at various stages during manufacture. 180

Table 6.2: Summary of 1080-implant *in vitro* release results when the core contained MB or tartrazine. 187

Table A6.1: Summary of two-tailed Student's t-test results (t-test of difference = 0 (vs. ≠). 204

Table 7.1: Summary of the feed ratios of the tested PEG-based HME formulations..... 209

Table 7.2: Feed and calculated mass ratios and loading accuracy of the components in the PEG-B extrudate..... 212

Table 7.3: Summary of HME implant dimensions at various stages during manufacture... 215

Table 7.4: Summary of HME implant *in vitro* release results..... 220

Table A7.1: Summary of two-tailed Student's t-test results (t-test of difference = 0 (vs. ≠). 234

Table A7.2: Summary of the feed ratios of the tested PVA-based HME formulations..... 236

Abbreviations

AIBN	2,2'-azobisisobutyronitrile
VP	2-vinylpyridine
ACN	Acetonitrile
ABS	Acrylonitrile butadiene styrene
API	Active pharmaceutical ingredient
ACTA	Animal Control Technologies Australia
Ar	Argon
APVMA	Australian Pesticides and Veterinary Medicines Authority
BMA	Butyl methacrylate
CPE	Canid pest ejector
CO_2	Carbon dioxide
^{13}C NMR	Carbon-13 nuclear magnetic resonance
$CHCl_3$	Chloroform
CPM	Chlorpheniramine maleate
CT	Computed tomography
CFRP	Conventional free radical polymerisation
$PVBI/EO_{10}$	Copolymer formulation of 10% $w.w^{-1}$ EO and PVBI 50/30/20
CRM	Crude reaction mixture
T_c	Crystallisation temperature
DF	Degrees of freedom
$CDCl_3$	Deuterated chloroform
DCM	Dichloromethane
DRI	Differential refractive index
DMF	Dimethylformamide
Đ	Dispersity
ESI-MS	Electrospray ionization-mass spectrometry
EtOH	Ethanol
FTC	Fibrous tissue capsule
FID	Flame-ionisation detector

E_f	Flexural modulus
σ_F	Flexural strength
FBR	Foreign body response
FFF	Fused-filament fabrication
GC	Gas chromatography
GET	Gastric half-emptying time
GPC	Gel permeation chromatography
T_g	Glass transition temperature
GPS	Global positioning satellite
HSDV	Hard-shell delivery vehicle
HPLC	High-performance liquid chromatography
HME	Hot-melt extrusion
HCl	Hydrochloric acid
IBMA	Isobornyl methacrylate
IPA	Isopropyl alcohol
LD_{90}	Lethal dose, 90%
LD_{99}	Lethal dose, 99%
LiCl	Lithium chloride
$MgSO_4$	Magnesium sulphate
MT	Masson's trichrome
LD_{50}	Median lethal dose
T_m	Melting point temperature
MeOH	Methanol
MMA	Methyl methacrylate
MB	Methylene blue
MFFT	Minimum film-forming temperature
MDSC	Modulated differential scanning calorimetry
MW	Molecular weight
N_2	Nitrogen
M_n	Number-average molecular weight
OA	Oleic acid

OM	Optical microscopy
H_3PO_4	Orthophosphoric acid
PAPP	*para*-aminopropiophenone
%RSD	Percentage relative standard deviation
PBS	Phosphate-buffered saline
PEG	Poly(ethylene glycol)
PIBMA	Poly(isobornyl methacrylate)
PLA	Poly(lactic acid)
PLLA	Poly(L-lactide)
PMMA	Poly(methyl methacrylate)
PVA	Poly(vinyl alcohol)
PVB	poly[(2-vinylpyridine)$_x$-*co*-(butyl methacrylate)$_y$]
PVBI	Poly[(2-vinylpyridine)$_x$-co-(butyl methacrylate)$_y$-*co*-(isobornyl methacrylate)$_z$]
PVBM	Poly[(2-vinylpyridine)$_x$-*co*-(butyl methacrylate)$_y$-*co*-(methyl methacrylate)$_z$]
PPI	Population protecting implant
KCl	Potassium chloride
t_0	Pre-polymerisation concentration (of monomer)
^{1}H NMR	Proton nuclear magnetic resonance
RFID	Radiofrequency identification
RU	Repeat unit
R_t	Retention time (min)
RhB	Rhodamine b
SEM	Scanning electron microscopy
NaOAc	Sodium acetate
NaCl	Sodium chloride
1080	Sodium fluoroacetate
$NaHCO_3$	Sodium hydrogen carbonate
Std. dev.	Standard deviation
SI	Subcutaneous implant
H_2SO_4	Sulphuric acid

THF	Tetrahydrofuran
T_d	Thermal degradation temperature
TGA	Thermogravimetric analysis
TFA	Trifluoroacetic acid
UV-vis	Ultraviolet-visible spectrophotometry
M_v	Volume-average molecular weight
M_w	Weight-average molecular weight

Navigation

Cross-references (also known as hyperlinks) are used throughout this thesis. Entries in the table of contents, list of figures, and list of tables (all in plain text or bold), or references to chapters and figures in the main text (all in bold) are cross-references. Accessing a cross-reference will navigate the reader to the location of the referenced item or section within the document. The use of the cross-references is recommended as throughout this thesis the reader will be referred to different items or sections within the document. Follow the brief instructions below to assist with using the cross-references while navigating the document.

If accessing this thesis as a Microsoft Word (.docx) document, while holding *ctrl*, *left-click* the cross-reference to access it. Press *alt+left arrow* to return to your previous position within the document.

If accessing this thesis as an Adobe Acrobat Reader (.pdf) document, *left-click* the cross-reference to access it, and either select the *previous view* button, or press *alt+left arrow* to return to your previous position within the document.

Note that the in-text citations presented in this document are not cross-references. A reference list of the in-text citations is provided at the end of each chapter.

Summary

Ongoing research into the effective control of invasive mammalian predators like the feral cat, and the conservation of species threatened by their activity, is crucial to ensure the preservation of global biodiversity. The need for this research is most dire in Australia, where feral cats have had a staggeringly disproportionate effect on endemic mammal species. Efforts to mitigate their effects using reintroduction programs, are often unsuccessful due to predation from single, control-resistant feral cats, termed “problem individuals”. This work reports the development of the population protecting implant (PPI), for the targeted control of problem individuals. PPIs are designed to be subcutaneously injected into native animals where they remain inert until they are preyed upon and ingested by a feral cat. A toxic payload is then released by the PPI once the gastric environment is reached, which eliminates the problem individual during its first predation event and safeguards the remaining reintroduced mammal population. Herein described is the prototypical development of the PPI. Its design, manufacture, and evaluation are reported within the context of their application towards mammal reintroduction programs in Australia.

Fundamental to the PPI concept and design is the spatiotemporal release of an encapsulated poison, which could be afforded by a poison ‘core’ and a pH-responsive coating. Current state-of-the-art pH-responsive coatings and technologies such as Eudragit® E 100 and the hard-shell delivery vehicle (respectively), were determined to be unsuitable for such an application. To address this knowledge gap, a series of copolymers containing the pH-responsive monomer 2-vinylpyridine, were synthesised. The copolymers were evaluated using a series of selection criteria thought to reflect the required physicochemical and thermal properties of a pH-responsive coating, and to ensure compatibility with the chosen manufacturing method, fluidised-bed spray coating.

A lead copolymer was identified, and fluidised-bed spray coating was used to manufacture non-toxic PPIs and evaluate their performance *in vitro*, and *in vivo* using a murine model. The PPIs exhibited excellent *in vitro* performance in terms of their stability and release within respective simulated subcutaneous and gastric environments. The *in vitro* results were supported by the favourable performance

of the PPIs *in vivo*. However, when toxic PPIs were manufactured by incorporating the poison sodium fluoroacetate (1080) in the core, the *in vivo* performance of the PPIs decreased significantly. The use of an insoluble coating substrate — a cylindrical acrylonitrile butadiene styrene (ABS) filament — which was required to prepare the core for each PPI, was determined to be the primary cause of failure, and an inherent flaw in the initial PPI design.

The removal of the ABS substrate, using a water-soluble core, was hypothesised to improve implant stability *in vivo*. To that end, hot-melt extrusion (HME) was then used to prepare a non-toxic, poly(ethylene glycol) (PEG)-based core. PPIs manufactured with the HME core and lead copolymer, exhibited favourable *in vitro* performance. However, the results suggested that an increase in the thickness of the lead copolymer coating would be required to mediate improved stability *in vivo*. Accordingly, future investigation should consider the *in vivo* evaluation of PPIs bearing a HME core, to determine whether a significant improvement in PPI stability can be achieved. Ultimately, the results described herein serve as an important foundation for the continued development of the PPI, and its potential to improve the likelihood of successful reintroduction programs in Australia, and the continued survival of Australia’s unique endemic mammal species.

Declaration

This thesis presents work carried out by myself and does not incorporate without acknowledgment any material previously submitted for a degree or diploma in any university; to the best of my knowledge, it does not contain any materials previously published or written by another person except where due reference is made in the text; and all substantive contributions by others to the work presented, including jointly authored publications, are clearly acknowledged.

Kyle Robert Charles Brewer



6th March 2023

Acknowledgements

When I started my PhD in 2018, I had no idea what my future would hold; years of experimental triumphs and tribulations, national and international conferences, countless posters and presentations, grants won and lost, teaching, supervision, a global pandemic, an internship, employment, new friends, mentors, and a few scientific publications. It has been an arduous and rewarding adventure, but none of it would have been possible without the people who supported, challenged, and guided me through it.

My principal supervisor, mentor, and friend, Associate Professor Anton Blencowe, thank you for taking a chance on an anxious undergraduate student. If you had not welcomed me into your lab eight years ago, I would not be the scholar I am today. Your support has never wavered, and I have always been deeply appreciative of your guidance. Your passion for science and your excitement for all things Chemistry (and 3D printing) are contagious and have spurred in me the same. I hope that being your student has been as rewarding and fun for you, as it has for me.

To my beautiful partner Christine, the person who this PhD has impacted the most. You have been my biggest source of support, inspiration, and motivation all these years. Without you by my side, I never would have made it this far. I cannot thank you enough, and I look forward to seeing what the future holds for us both. To my parents, Michelle and Jim, and my brothers, Aaron and Gage, your love and support have made me the person I am. I am so grateful to be a part of the Brewer family. I hope I have made you all proud.

To the ACTB group, my second family, and all its past and present members. We all began as colleagues, but I leave considering you all among my closest friends. I have lost track of the countless laughs we have shared, but they are without question the highlight of my PhD. You all helped share the burdens of my PhD, mostly while eating Korean fried chicken. I will miss the chicken, but I will miss your company more. Thank you for making me feel at home in the group, and for making the lab so much fun. I look forward to seeing all the great things you will achieve.

I want to thank all the people who have made my PhD experience an enjoyable one, with good humour, kindness, and camaraderie. There are far too many of you to name. From the amazing technical staff and PhD candidates at City East and West Campuses, to the administrative staff and senior academics within the Clinical and Health Sciences Unit. Thank you all.

I would like to express my gratitude to my collaborators Dr. Todd McWhorter, Dr. David Peacock, Dr. John Read, Dr. Katherine Moseby, and Ned Ryan-Schofield. Your commitment to this project both before and during my PhD has been greatly appreciated. Without your expertise, input, and field work, it would not have progressed as much as it did. I have thoroughly enjoyed our collaboration, and I am grateful to have had the opportunity to learn from you all. I wish you all the best for the future, and hope that one day we can safeguard our native animals with this technology.

I wish to acknowledge my receipt of project support and funding from the Australian Government Research Training Program. I also want to acknowledge the generous project funding offered through scholarships I was awarded from the Commonwealth Scholarships Program for South Australia, Nature Foundation South Australia, and the Australian Wildlife Society. I acknowledge the facilities and scientific and technical assistance of Microscopy Australia, at the University of South Australia, a facility that is funded by the University of South Australia and the State and Federal Governments.

I would like to thank Scientec Research Pty Ltd for providing samples of their hard-shell delivery vehicles for testing during my PhD. Thank you to Colorcon® for donating Suglet® samples, Microchips Australia Pty Ltd for donating mini radiofrequency identification microchips and syringe implanters, and the Foundation for Australia's Most Endangered Species for providing the spray coating infrastructure. I also wish to acknowledge The Advertiser for allowing me to reproduce their bilby, cat, and subcutaneous implantation illustrations in my thesis and publications.

Without these project and scholarship funding initiatives, and kind donations, my research would not have been possible.

Author Statement

This doctoral thesis is submitted as a Thesis Containing Published Research, in accordance with Academic Regulations for Higher Degrees by Research Clause 16.11.b. A conventional chapter format is used throughout this work, however **Chapter 1**, and **Chapters 3–7** contain material from original research articles accepted for publication in reputable, peer-reviewed academic journals. The research articles are published in journals from the American Chemical Society (ACS), Elsevier, and the Multidisciplinary Digital Publishing Institute (MDPI). Publications in all these journals may be reproduced (in part or full) in a thesis, where the thesis is for non-commercial applications. The publications are listed in the **Publication Status of Thesis Research** section, and detailed information regarding the publications and acknowledgement of authorship contributions, are provided in the **Statement of Authorship** section.

I was first author of all the research articles, and conducted most of all experimental work, data analysis and interpretation, and visualisation, under guidance from my primary supervisor A/Prof. Anton Blencowe, and in collaboration with the co-authors of the research articles. Where appropriate, experimental contributions from co-authors, and technical assistance provided by others, are acknowledged at the start of each chapter, as well as in the research articles in which they are reported.

Chapter 1: Introduction

1.1 The Impacts of Invasive Mammalian Predators

Globally, invasive mammalian predators are likely the greatest threat to biodiversity. The majority (142, 58%) of modern bird, mammal, and reptile extinctions have been linked to predation from only 30 invasive mammalian predators,[1] and these predators continue to threaten a further 596 species.[1] The impact of invasive mammalian predators causes a significant loss of global biodiversity, especially considering that evolutionarily distinct species are most impacted by this predation.[1]

This is best evidenced in Australia, where disproportionately, feral cats (*Felis catus*) and European red foxes (*Vulpes vulpes,* hereafter referred to as foxes) present the greatest predatory threat to most native Australian mammals.[1] Together, foxes and feral cats kill 2.1 billion reptiles, birds, and mammals annually, and the majority (1.2 billion, 56%) of the prey killed are mammals.[2] Almost all (87%) of Australia's 316 terrestrial mammal species are endemic, and 29 (11%) of these species have already been extinguished, primarily due to the impacts of foxes and feral cats, which constitutes 30% of modern-day global extinctions.[2–4] Feral cats are more prevalent and more damaging than foxes. There are at least 2.8 million feral cats across > 99.8% of Australia's land area,[2, 5] and they are responsible for 81% (452 million) of the native mammal species that are killed every year.[2, 5–8] Further, since the 1960s, more than $18 billion (AUD) has been spent managing the impacts of feral cats in Australia, with the majority of these costs associated with population control.[9] This is in staggering contrast to the $700 million spent on managing foxes. Such a discrepancy highlights the unique challenge that feral cats pose when attempting to control their populations.[10, 11] In addition, the biodiversity losses caused by feral cats are incalculable. Native Australian mammals are some of the most unique in the world,[12] contributing to the generation of an estimated $23 billion in annual economic benefit through nature-based tourism, which is threatened by the activity of feral cats.[13] Ongoing research into the effects of feral cats in Australia, their effective control, and the conservation of species threatened by their activity, is crucial to ensure the

preservation of biodiversity, and to mitigate the economic costs associated with their control.

1.1.1 Feral Cat Control Methods — An Overview

At present, there exists no singularly effective landscape-scale method of controlling feral cats. This is due in part to the inherent complexity of controlling invasive predator populations in landscapes across Australia, as well as the caveats associated with currently available control methods. Conventional control methods for invasive mammalian predators, and their respective advantages and disadvantages are summarised in **Table 1.1.** The control of feral cats is a complex task, and a one-size-fits-all approach is not possible. Generally, the control methods employed during a management program must be selected on a case-by-case basis, to maximise efficacy and cost effectiveness within a given landscape. Conventional control methods include poison baiting, shooting, trapping, canid pest ejectors, and exclosure fencing. For example, if a control program is undertaken near an urban area, this may preclude the use of poison baiting due to the risk of bait consumption or secondary poisoning, posed to domestic animals, such as dogs.[14–17] In addition, an unmodified landscape may make the establishment and ongoing maintenance of exclosure fencing cost prohibitive. As a result, multiple control methods are often employed within the same control program, as complementary techniques can compensate for the shortcomings of an individual method.[18] This use of a combination of lethal techniques has resulted in a number of successful eradications of feral cats from islands, globally.[19–25]

Table 1.1: Conventional methods for controlling invasive mammalian predator populations in Australia.

Control Method	Description	Advantages	Disadvantages	Ref.
Poison Baiting	Fresh or dried meat is injected with poison (commonly sodium fluoroacetate, 1080) and deployed manually or aerially within the target area. Bait burial is required in some states, to reduce the likelihood of off-target uptake. Frequent bait renewal (biweekly) is required due to 1080 degradation and bait decomposition.	Cost-effective, broad-scale deployment of baits is practical at small and large scales; feral cats are highly susceptible to 1080; choice of poison can somewhat limit off-target effects.	Off-target toxicity; frequent renewal of baits required; risk of sub-lethal dosing; bait avoidance; commonly used to target foxes with less focus on feral cats; effective against cats when prey availability is lowest; considered less humane than shooting.	26–30
Canid Pest Ejectors (CPEs or "M-44 Ejectors")	The CPE mechanism requires the biting and pulling motion of a canid upon a meat "bait head", which activates the spring-loaded release of a lethal dose of poison (commonly cyanide or 1080), contained within a sealed capsule. Replacement of the bait head is generally required following removal, or decomposition of the bait.	Greater canid-selectivity compared to meat baits; reduced off-target uptake; increased 1080 stability; more effective than traditional baits; semi-automatic ejectors don't require resetting.	Require "bait heads" and frequent renewal as a result; effective against a single animal before requiring bait renewal; semi-automatic ejectors still require bait renewal; not appropriate for feral cats (i.e., canid-specific).	31–34
Shooting	The target animal is hunted within the area it is sighted and is lethally shot in the head.	Considered the most humane control method; effective for problem individuals.	Opportunistic; impractical for large-scale population control; large input of time and effort; efficacy skewed to juveniles.	10, 27, 35–38
Trapping	A variety of traps can be deployed (e.g., cage traps), which are generally non-lethal and require the destruction of the animal following trapping. Traps are deployed within a target area and must be monitored frequently as a result.	Can be used to target foxes and cats; generally, most effective when prey is scarce.	Considered less humane than both shooting and poison baiting; requires costly/intensive daily monitoring of traps; animals can be 'trap-shy'.	37, 39, 40
Exclosure (i.e., fencing or translocation)	Native mammals can be translocated to a predator-free area, or predators can be removed from an area prior to fencing to establish an exclusion zone. Ongoing monitoring and maintenance are required to ensure the integrity of the fencing perimeter.	Effective for predator-free areas; affords long-lasting protection (when well maintained).	Incursion renders exclosure ineffective; large upfront and ongoing maintenance costs; impractical for large-scale natural environments.	41–43

Whilst success has been reported for the eradication of feral cats from small and large islands,[44, 45] eradication programs on the mainland have been considerably less successful and by some is considered impossible.[46] Islands present a unique landscape for feral cat activity and control. An island where feral cats (or other invasives) are not present, can be a haven for native species, since feral cats are unlikely to migrate.[47] However, if introduced to an island, feral cats can mediate the extensive depredation of a species, as both are confined to a relatively small area, and the prey species has no means of escape.[48] Eradication of feral cats from an island is likely comparatively easier to achieve, as it increases the chances of successful interactions between feral cats and applied control methods. For example, poison baits and traps are easier to apply to a smaller land area and may have a greater likelihood of visitation due to the restricted home range of feral cats within the same area. In addition, control methods that are highly targeted, such as shooting, require access to feral cats, and it is likely easier to track feral cats across smaller land areas.

The shortfalls of conventional control methods, and larger land areas, makes it far more challenging to achieve successful eradication of feral cats on the mainland. In general, it is more difficult to mediate the same control pressure on a population of feral cats that is dispersed across a continent. Feral cat populations can exhibit high reinvasion potential, and compensatory migration can occur in response to lethal control, as current methods often fail to sufficiently reduce feral cat populations within a sufficiently large area, and an appropriate timescale.[49] In addition, the persistence of pet cats in urban areas, their predation on native wildlife, and their tendency to ‘become feral’, creates additional predation pressure, and a potential source-sink dynamic, where even well controlled populations may be supplemented by abandoned pet cats.[50] The unique challenges posed by landscape-level control (on the mainland), drive the need for the use of combinations of control methods. Importantly, this also drives the development of innovative control technologies with improved effectiveness, to increase each control program’s likelihood of success.

1.1.2 Toxicants

In Australia, the contemporary lethal control of feral cats is achieved *via* poisoning and is primarily conducted using poison baits containing either 1080 or *para*-aminopropiophenone (PAPP). The former has been widely employed for vertebrate pest control following its first use in Australia in the 1950s to control introduced rabbit populations.[51] 1080 has since proven an effective means of controlling vertebrate pests such as foxes and feral pigs. In contrast, PAPP is a relatively modern toxicant, with investigation of its use in Australia, for the control of foxes, first reported in the early 2000s.[52] A range of formulated baits containing either 1080 or PAPP are commercially available, though these products are mostly aimed at the control of canids (foxes and wild dogs), and rabbits. Currently, there are only two poison baits specifically targeting feral cats that are registered for use in Australia (though not yet commercially available); Eradicat® (1080) and Curiosity® (PAPP) (Australian Pesticides and Veterinary Medicines Authority (APVMA), PubCRIS Database).

The poison baiting of foxes and feral cats is the most effective and common control method employed in Australia, due to its cost-effectiveness and suitability for deployment at scale.[36, 53–55] Generally, baiting involves the incorporation of 1080 into a dried meat bait, followed by the manual or aerial deployment of the baits over a target area. 1080 is by far the most common poison utilised in baiting in both research and commercially available baits owing to its potent lethality against foxes and feral cats (median lethal dose (LD_{50}) values of 0.15 $mg.kg^{-1}$ [56] and 0.28 $mg.kg^{-1}$,[57] respectively) compared to native species. Following a lethal dose of 1080, foxes and feral cats have been observed to perish within 6 h[58] and 12–24 h,[57] respectively, with symptoms often observed far earlier. As a result, the ability for dosed animals to continue predation is severely limited, making poison baiting a rapid control method. 1080 is also advantageous as many native animals exhibit considerable evolutionary resistance, thus decreasing the chances of native animals perishing following non-target uptake of poison baits. For example, the burrowing bettong (*Bettongia lesueur*) is an omnivorous native Australian mammal that is considered near-threatened[60] and is one such non-target species that often consumes poison baits laid for fox and feral cat control.[61] However, this species is 100 times less sensitive to 1080 than the fox,

exhibiting an LD_{50} of 15 $mg.kg^{-1}$. As a result, a single bait containing a lethal dose of 1080 for a fox (~ 3 mg) would pose little threat to a burrowing bettong. Many native animals in Australia exhibit considerable resistance to 1080, reducing the possibility of off-target effects. This innate resistance is due to a shared co-evolutionary history with native Australian plants (particularly in Western Australia) that naturally produce 1080.[62]

As discussed by Glen et al., it is important to note that whilst the sensitivity of many Australian animals to 1080 (i.e., their LD_{50} value) has been estimated, the real-world susceptibility (i.e., the likelihood of the non-target species consuming baits and a sufficiently lethal dose of 1080, as well as the LD_{50} itself) is often overlooked.[63] Meaning that the risks to non-target species can be exaggerated when a dearth of evidence exists regarding the real-world lethal uptake of poison baits during baiting programs. As a result, when considering the possibility of non-target uptake of poison baits, a focus on susceptibility and (where possible) evidence of uptake should be maintained. The toxicity of 1080 to many native and non-native animals in Australia has been known for decades, with many species having reported LD_{50} values.[56, 57, 59, 64–71] It is important to note that whilst many native animals may be considered at risk of ingesting 1080 baits (for a comprehensive analysis, see Buckmaster et al.[72]), a far smaller number have actually been reported doing so. Species that have evidenced uptake of 1080 baits should be of greatest concern when orchestrating baiting programs. In this manner, 1080 is an ideal poison for use in baiting programs, as sufficient LD_{50} data exists for many native Australian animals. A comparatively small amount of data is currently available for other toxicants, such as PAPP, so the management of non-target risks is considerably more difficult.[14, 73–75]

Despite its ubiquitous use for lethal control, poison baiting has been criticised due to its perceived inhumanness.[76–78] Shooting — when conducted effectively — is generally considered the most humane method of lethal control.[10, 38] However, poison baiting is the only cost-effective, large-scale method of feral cat control currently available.[79–84] Overall, the beneficence of poison baiting in comparison to other available control methods (e.g., shooting, trapping) is the primary reason for its continued use in Australia. There remains some contention regarding the severity of

the suffering caused by 1080,[78, 85–87] and to a lesser extent, PAPP, but it is generally accepted that PAPP is more humane than 1080.[73, 88, 89] However, the decision to use 1080 or PAPP is complex and context-specific, as both poisons have distinct advantages and disadvantages, which affect their suitability for particular landscapes, vertebrate pests, deployment methods (e.g., aerial or ground baiting), and non-target species.

The relative humaneness of PAPP (cf., 1080) is perhaps its major advantage. PAPP also exhibits selectivity towards mammalian carnivores, due to metabolic differences between taxa, which likely limits its off-target effects. The LD_{50} value for feral cats is 5.6 $mg.kg^{-1}$,[73] and baits targeting cats (e.g., Curiosity®), incorporate a 78 mg dose to ensure lethality.[84] These baits generally pose a low risk to native birds and herbivorous mammals.[73] However, reptiles (*Varanus sp.*) are comparatively sensitive to PAPP, with some exhibiting higher sensitivity than feral cats (*V. varius,* LD_{50} = 3 $mg.kg^{-1}$) or lower sensitivity but susceptibility to a single bait (*V. rosenbergis*, LD_{50} = 12 $mg.kg^{-1}$).[90] Baits containing PAPP could either be deployed seasonally when varanids are least active (i.e., winter) to limit potential off-target effects, or be restricted in areas where varanids are at risk.[91, 92]

In comparison, the relatively lower humaneness of 1080 is its biggest drawback. However, native non-target species in Australia — particularly herbivores[68, 93, 94] — exhibit a high resistance to 1080, due to a co-evolutionary history with fluoroacetate-bearing vegetation.[62, 95] 1080 is highly effective against invasive mammalian carnivores like the feral cat, due to their lack of this co-evolutionary history. Feral cats exhibit respective LD_{50} and LD_{90} values of 0.28 $mg.kg^{-1}$ and 0.35 $mg.kg^{-1}$,[57, 59] and poison baits targeting feral cats (e.g., Eradicat®) often contain a lethal dose of 4.5 mg of 1080 (i.e., a > LD_{90} dose).[96–98] These baits generally pose the greatest off-target risk to other mammalian carnivores, like the domestic dog (LD_{50} = 0.06–0.35 $mg.kg^{-1}$),[99–101] but vary in their risk to non-target native animals, with unadapted birds and reptiles being among the most resistant,[93, 94, 102] likely due to their metabolic differences.

Neither 1080 nor PAPP are considered to pose a risk of causing environmental contamination, as both poisons exhibit rapid degradation.[14–17, 103, 104] However, there

exists a potential for secondary poisoning, particularly for non-target animals that are highly sensitive to either poison, such as domestic dogs.[14–17] No antidote exists for 1080 poisoning. Whilst an antidote (methylene blue, MB) is available to treat PAPP poisoning, it requires intravenous administration, making use of the antidote for non-target native animals impractical.[73, 87]

1.1.3 Problem Individuals

Efforts to mitigate the catastrophic effects of feral cat predation generally involve the attempted removal of feral cats from a target landscape, and subsequent attempts to re-establish populations of threatened species through reintroduction (or translocation) programs within the area.[26, 105] However, there is no singularly effective landscape-scale method of controlling feral cats and these programs are marred by the inability to completely remove feral cats from a target landscape or their eventual incursion. Invariably, the presence of feral cats within a landscape in which a reintroduction program is occurring, is met with the swift predation and decline of the reintroduced mammals. In many cases, a single control-averse or incursive 'problem individual' has been responsible for the destruction of the majority or all the reintroduced mammals, and the failure of the program.[106–113] This highlights the need for a targeted means of controlling problem individuals, to protect vulnerable populations of reintroduced native mammals.

1.1.4 Population Protecting Implants

The Concept

The current work aims to selectively target problem individuals, through the development of a pH-responsive poison implant that is designed to be subcutaneously implanted into native mammals during reintroduction programs. As previously proposed,[114] this implant could be designed to exploit the pH differential existing between the subcutaneous and gastric environments of native mammals and feral cats, respectively (**Figure 1.1**).

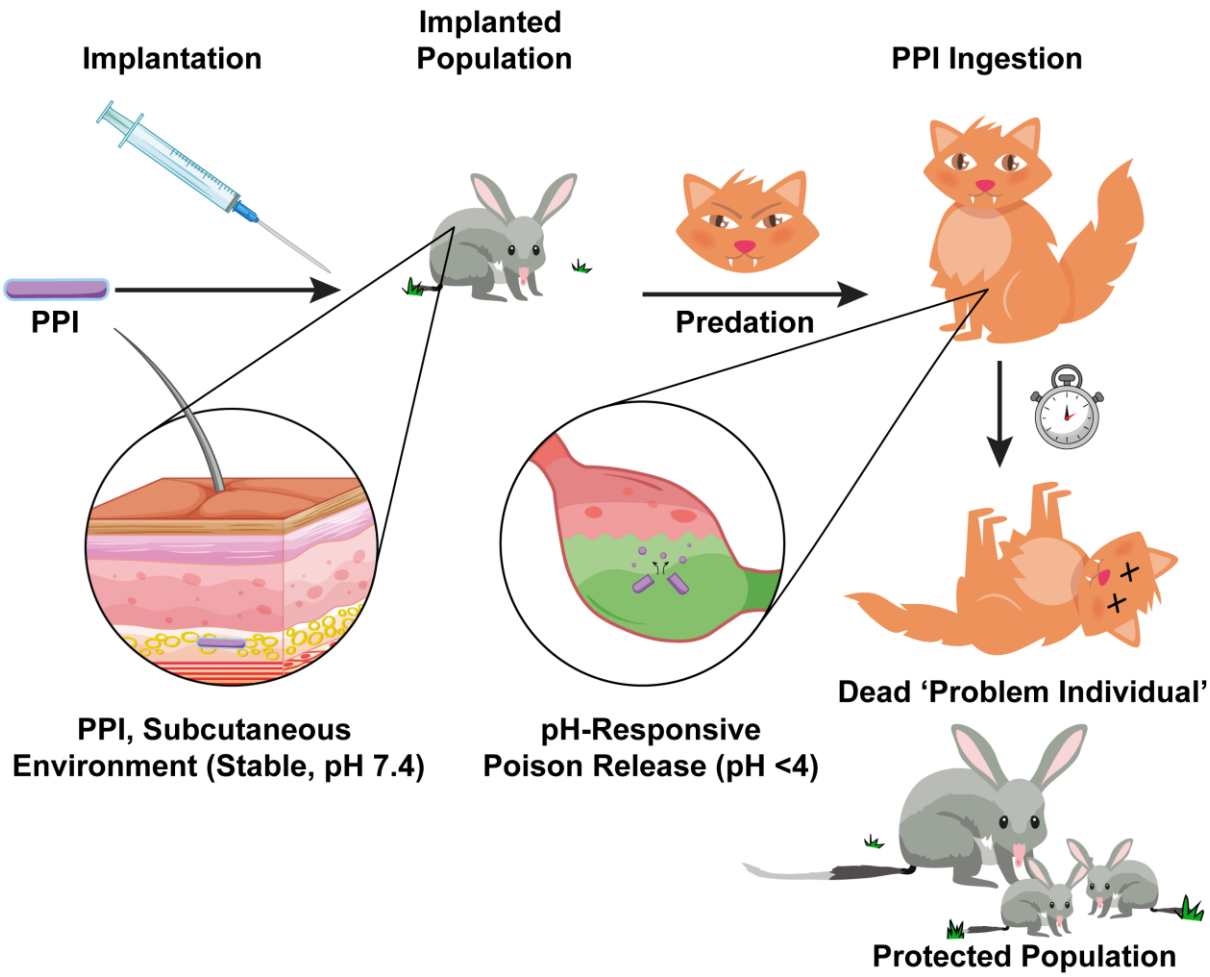


Figure 1.1: An illustrated overview of the population protecting implant concept.

The implant is designed to be inert within the subcutaneous environment, but rapidly dissolves and releases an encapsulated poison in the gastric environment. Hypothetically, the persistence of implanted native mammals (or 'toxic trojans') in a reintroduction area could ensure that problem individuals perish if they prey upon the native mammals. The death of the problem individuals would ensure that overall, most of the reintroduced population is protected from predation, hence we derive the term 'population protecting implant' (PPI) to describe the technology. This may mediate the extensive depredation caused by problem individuals and facilitate the survival of reintroduced populations of native mammals. Such an approach acknowledges and exploits the formidable predatory behaviour of feral cats, by artificially accelerating the much-needed evolution of anti-predator defences in prey naïve native mammals.

Design Considerations

In collaboration with South Australian ecologists (Drs. John Read, Katherine Moseby and David Peacock) and veterinary physiologist Dr. Todd McWhorter, several key design considerations were established for the PPI. Direct consultation with these experts during the design phase of the PPI development was considered crucial to ensure the technology would be compatible with modern ecological practices, and any unique behavioural or anatomical considerations regarding native Australian mammals. The key design considerations are outlined below:

i. Small size, to ensure no effects on mobility and ensure applicability to native animals/mammals of all sizes, and to increase the likelihood of consumption by a predator by minimising the chances of detection.
ii. Injectable, using conventional, minimally invasive methods.
iii. Contains a lethal dose (> LD_{90}) of poison for a feral cat.
iv. Must — where possible — minimise off-target effects by selectively targeting feral cats.
v. Biocompatible, with effective containment of poison in the subcutaneous environment.
vi. Stimuli-responsive, with rapid poison release in the gastric environment
vii. Facile, scalable manufacture to enable cost-effective, large batch production.

To address design consideration (*i)* and (*ii)*, the PPI dimensions were modelled on a standard radiofrequency identification (RFID) microchip (2.12 mm diameter × 12 mm length), to enable compatibility with conventional syringe implanters. RFID microchips are commonly used to identify and monitor mammals, which would enable the PPIs to be incorporated with minimal additional training or changes to current processes. In addition, the diminutive size of an RFID microchip or similarly sized PPI, would be unlikely to affect the movement of an implanted animal.

The incorporation of a 3 mg dose of 1080 would exceed the reported LD_{90} value (0.35 $mg.kg^{-1}$)[57] for a feral cat — likely constituting a LD_{99} dose — and thereby satisfy consideration (*iii).* 1080 exhibits an innate selectivity for invasive mammalian

predators (*vide supra*). As a result, PPIs containing 1080 would pose a reduced threat to non-target native species, and potentially minimise off-target effects as desired in consideration (*iv).*

1080 has a relatively low effective dose (cf., PAPP), which could enable its incorporation without significantly increasing the required size of the PPI. The small dose of 1080 (and by extension, the size of the PPI), may enable manufacture of a PPI to the desired size constraints, which would satisfy consideration (*i)*. In addition, small-sized implants are unlikely to be detected and subsequently rejected by feral cats, due to their unique feeding behaviour,[115] thereby satisfying consideration (*iv)*.

Considerations (*v)* and *(vi)* describe the performance of the PPI. Of high importance is the stability (i.e., containment of poison) in the subcutaneous environment, to prevent premature release and poisoning of the implanted animal. Though this is less problematic for implanted animals that have an innately high tolerance of 1080, some native species may not, and may be at risk if 1080 is released prematurely. The use of a reverse enteric 'barrier' coating was deemed most appropriate to afford a biocompatible coating that is insoluble at physiological pH, but soluble (rapidly) at gastric pH. Parallels can be drawn between conventional taste-masked pharmaceutical formulations that incorporate reverse enteric polymers, and the intended function of the PPI (*vide infra*). This approach could be adapted for the PPI design and would satisfy considerations (*v)* and (*vi).*

The final design consideration (*vii*) refers to targeting cost-effective, scalable manufacture for the PPIs. Minimising the cost per implant is important to ensure that PPIs can be incorporated into reintroduction or monitoring programs at low cost. The cost of a control method (and by extension, control program) is likely a key factor in determining its incorporation into new or ongoing programs. As such, only scalable, cost-effective manufacturing methods were investigated for the PPIs (*vide infra*).

In the context of the design considerations, a general PPI design was conceptualised, in which a rod-shaped PPI consisted of a poison-loaded 'core', encapsulated by a pH-responsive, reverse enteric coating (**Figure 1.2**).

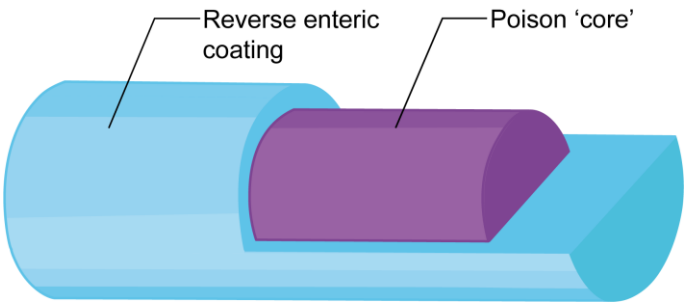


Figure 1.2: General PPI design, featuring a poison 'core' and a reverse enteric coating.

1.2 Subcutaneous Implants

1.2.1 Reservoir-type Implants for Drug Delivery

To date, subcutaneous implants (SIs) have primarily been investigated for use in controlled drug release applications, especially long-term drug release (days to years).[116] SIs are advantageous as they negate issues commonly encountered with the oral administration of drugs such as stability, release duration, dosage frequency and patient compliance.[117] Generally, SIs are millimetre-sized cylindrical devices that are implanted *via* specialised needles (i.e. syringe applicators) or surgery. Implantation within the subcutaneous tissue is ideal, as slow drug absorption is facilitated by the high fat content of the tissue and minimal immune reactivity occurs in the presence of foreign materials.[118] The most prominent and enduring examples of commercially available SIs are female contraceptive implants that deliver long-term dosing of hormonal medications (commercially available since the early 1990s).[116] Implants have also been investigated to deliver various therapeutics such as chemotherapeutics[119] and antibiotics.[120]

SIs can be designed as either biodegradable or non-biodegradable implants, in either case, SI design is predicated upon the release mechanism employed. The release mechanisms can be broadly classified as either diffusion controlled (i.e., matrix and non-biodegradable reservoir-type systems) or erosion/dissolution controlled (i.e., monolithic and biodegradable reservoir-type systems).[117, 121] In the context of the current work, erosion/dissolution-controlled release is most relevant, specifically

reservoir-type systems. In a reservoir-type system, a drug core is coated with a polymer membrane that controls drug release and determines the degradability of the system. If a non-biodegradable polymer is used, the thickness and permeability of the polymer controls drug release, whereas if a biodegradable polymer is used, the degradation of the polymer must also be considered.[117, 121]

To date, all SI designs have focussed upon implantation, then sustained drug release (using various drug release mechanisms[117, 121]) for the life of the implant at the site of implantation. However, no SI design has been predicated upon its removal from the implantation site to an alternate site (i.e., the gastric environment of another animal) to induce drug release. A SI of such a design would be operating as an inert reservoir-type implant without drug release, until the alternate site is reached, at which point drug release is induced – like a reverse enteric pharmaceutical dosage form.

1.3 Polymer Synthesis

1.3.1 Polymer Synthesis — A Brief Overview

An archetypal polymer can be described by the polymerisation mechanism underlying its synthesis — either a step-growth or chain-growth polymerisation mechanism. Step-growth polymerisation involves the stepwise combination of reactant pairs *via* their differing functional groups.[122, 123] Initially, some monomers react to form dimers, which can then react with another monomer unit to form trimers and so on. A defining feature of step-growth polymerisation is that any component (e.g., monomers, oligomers, and polymer chains) can react with any other throughout the polymerisation. Due to the stepwise nature of this process, polymers synthesised *via* step-growth polymerisation only reach high molecular weights at high monomer conversions (i.e., > 98%).[122, 123]

For chain-growth polymerisation, polymer chains can only grow by the addition of monomers to an active centre.[124] The active species is initially generated from an initiator to which monomers add to form a propagating polymer chain bearing an

active end-group. The polymerisation process generally continues until the monomer is consumed or the active polymer chains are terminated. In controlled chain-growth polymerisations the molecular weight of the polymer increases proportionally to the monomer conversion. For conventional free radical polymerisation (CFRP), a type of chain-growth polymerisation where there is poor control over the active species, high molecular weight polymers are formed immediately due to rapid polymerisation kinetics.[124]

Of these two broad classifications, chain-growth polymerisation represents the most employed and industrially relevant polymerisation mechanism. Globally, most of the widely available commercial synthetic polymers are prepared *via* chain-growth polymerisation.[124, 125] Chain-growth polymerisation processes can be further categorised by the type of active polymer chain (i.e., radical or ionic polymerisation for chains bearing radicals or ions), the absence of chain transfer and chain termination processes (living polymerisation), the presence of reversibly deactivated polymer chains (reversible-deactivation polymerisation), the use of a transition metal catalyst (coordination polymerisation), or the use of cyclic monomers (ring-opening polymerisation).[124] However, in the context of the current work, CFRP is the most relevant approach and is discussed further below.

1.3.2 Conventional Free Radical Polymerisation

In CFRP the active species has a radical centre that is initially generated from an initiator. Common initiators are azo or peroxide compounds which undergo thermally or photochemically induced homolytic cleavage of a covalent bond to produce primary radicals. An exemplar initiator of CFRP is 2,2'-azobisisobutyronitrile (AIBN), which undergoes thermally driven homolytic cleavage of its C-N bonds and produces a resonance stabilised tertiary radical which initiates polymerisation.[124, 126] An archetypal thermal decomposition of an azo initiator (I-I) into a radical initiator (I$^{\bullet}$) is shown in

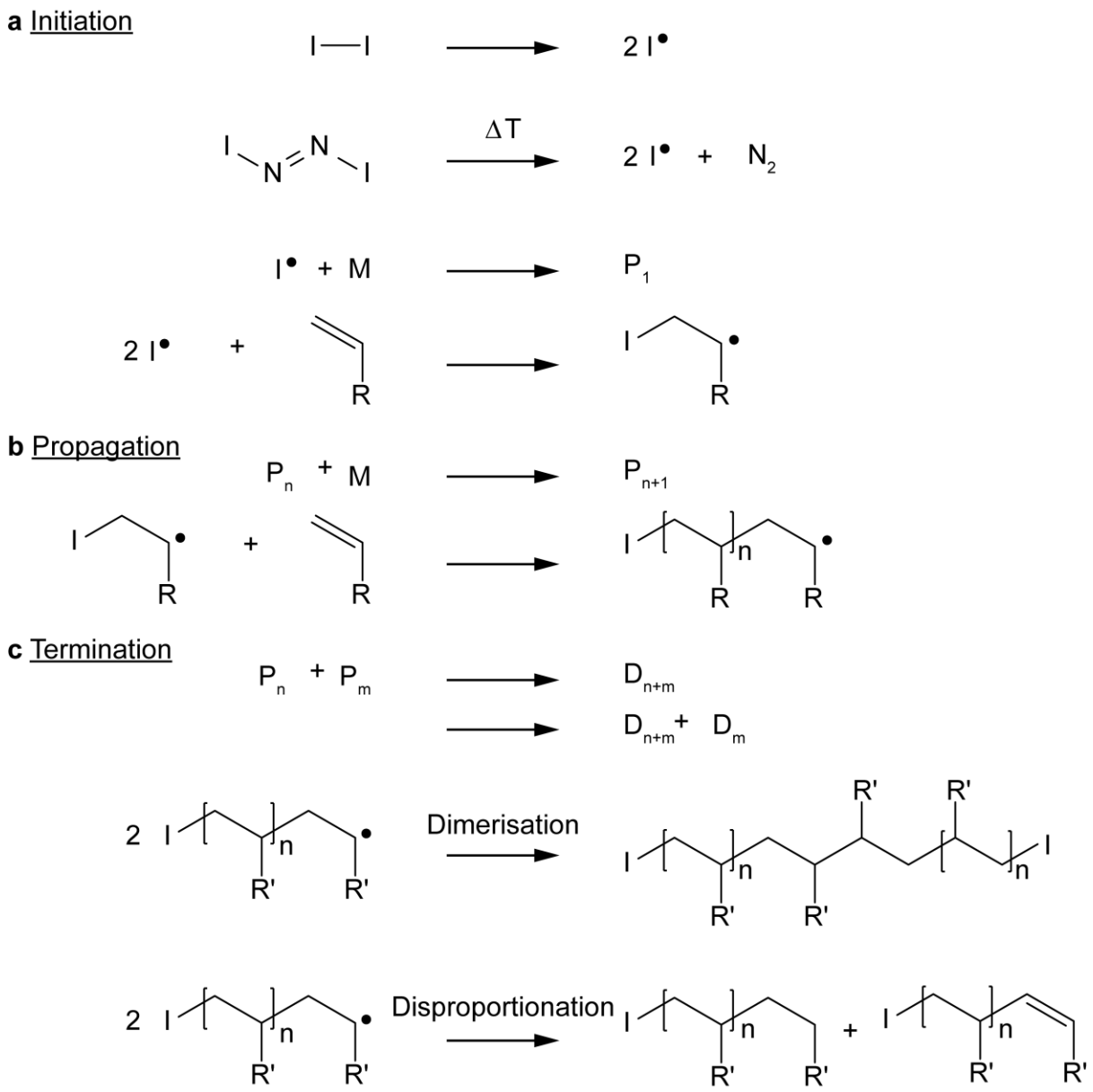
Figure 1.3a. The first stage in the CFRP mechanism — *initiation* — comprises primary radical generation ($I^{\bullet}$), which then adds across the first vinyl monomer (M) to form an initiating radical (P_1) (

Figure 1.3a).[124, 126, 127] In the second stage — *propagation* — monomer is then continually added to the newly generated radical species from the initiation step (P_n), which generates a radical terminated (or active) propagating polymer chain (P_{n+1}) (

Figure 1.3b).[124, 126, 127] Polymer chains continue to grow *via* propagation, until the third stage — *termination* — occurs, in which chain growth is terminated by either a dimerisation (also known as combination) or disproportionation reaction (

Figure 1.3c).[124, 126] When two growing chains combine (P_n and P_m) and lose two radicals, either one inactive polymer chain, D_{n+m} (i.e., termination *via* combination), or two inactive polymer chains, D_n and D_m (i.e., termination *via* disproportionation), are formed.

Figure 1.3: A general scheme describing the three stages of CFRP: a) *initiation* of polymerisation *via* the homolytic cleavage of an initiator to generate primary radicals and addition of a radical initiator to a monomer; b) *propagation* of the polymer chain



via the addition of a number of monomer units, and; c) *termination* of polymerisation by either dimerisation or disproportionation reactions.

Polymer chains can also be terminated by *chain transfer*, where a propagating polymer chain reacts with a transfer agent, thereby terminating the chain and producing a new radical centre capable of initiating a new chain.[128, 129] Transfer agents can include initiator, solvent, monomer, polymer, and impurities in the reaction mixture, or deliberately added chain transfer agents. Generally, the effects of transfer agents are negligible, with their presence only causing a decrease in molecular weight.[123] For example, chain transfer to an initiator is ineffectual given the extremely

low concentration of initiator compared to monomer. In contrast, chain transfer to the solvent can limit the molecular weight of the polymer. Though there are exceptions, termination still ultimately controls the molecular weight of the resultant polymer.

A significant advantage of CFRP (cf., step-growth, or controlled chain-growth polymerisation approaches) is the simplicity of the approach. In most cases, CFRPs can be achieved with low to moderate temperatures, can be conducted in bulk or most solvents including water, and only require short reaction times.[124, 126] The broad monomer compatibility of CFRP also enables facile copolymerisation, and therefore the synthesis of copolymers with tuneable physicochemical properties based on the chosen monomers. A caveat, however, is that CFRP does not mediate significant control over the molecular weight or dispersity of the resultant copolymer, and complex polymer architectures such as block copolymers cannot be achieved.[123] Other polymerisation techniques such as controlled/living polymerisation are required to achieve low dispersity polymers with complex structures. Therefore, CFRP is most suited to the synthesis of homopolymers, or statistical (also called random) copolymers, and unsurprisingly most of these polymers sold commercially are synthesised *via* CFRP.[124]

1.3.3 Plasticisers

Plasticisers are ubiquitously used to alter the properties of polymers and their formulations. Plasticisers can be classified based on their chemical structure and are broadly defined as low molecular weight compounds that cause a reduction in the glass transition temperature (T_g) of a polymer. Semi-crystalline and amorphous polymers exhibit glass transitions, which are characterised as reversible, temperature-dependent transitions from a hard, brittle, and ‘glassy’ solid, to a flexible, viscous, and ‘rubbery’ solid.[130] Below the T_g value, a polymer is glassy, while above the T_g value, it is rubbery. The free volume theory is most often used to describe this phenomenon, and the action of plasticisers. Briefly stated, the free volume theory postulates that there exists empty space (i.e., a “free volume”) between atoms in amorphous solids, that dictates the rate of molecular diffusion.[130] Long or asymmetric polymer side groups/chains cause the loose packing and plasticisation of bulk

structures, resulting in a greater free volume.[131] The specific volume of a polymer is linearly correlated with temperature. When cooling from a temperature greater than the T_g value, the specific volume decreases linearly. Once the T_g is reached, the specific volume continues to decrease at a reduced rate. This process causes a reduction in free volume.[130] Accordingly, the glass transition can be described in terms of this temperature-dependent change in free volume. That is, below the T_g the polymer segments have low mobility and are densely packed due to the reduced free volume.[130] The configuration of the segments is essentially 'frozen' at all temperatures below the T_g because of this, hence the polymer's glassy state. As the T_g is approached (or exceeded), the free volume increases, the polymer segments become more loosely packed, and their segmental mobility increases.[130] This enables the polymer segments to undergo changes in configurational arrangement relative to one another and maintain a rubbery state.[130] The properties of a given polymer (e.g., free volume, heat capacity, viscoelastic properties) change during glass transition as a result.[132]

According to the free volume theory, plasticisation is effectively the process of increasing the free volume of an amorphous solid.[133] Since the segmental mobility of polymer chains is directly related to the free volume, plasticisation can therefore be achieved by any process that increases segmental mobility.[133] For a given polymer structure, this means that increases in the mobility of its end groups and main or side chains, all cause an increase in free volume and therefore plasticisation.[133] Such an effect can be achieved by altering the chemical structure of the polymer itself (internal plasticisation), or *via* an additive (i.e., a plasticiser) that increases the free volume (external plasticisation).[130] Internal plasticisation can be achieved through the careful selection of monomer/comonomers that increase the number or length of side chains, or number of end groups.[130] Further, monomers/co-monomers that exhibit reduced steric hindrance or decreased intermolecular attraction can be incorporated, as they will increase the segmental mobility of the main polymer chain.[130] Similarly, external plasticisation can be achieved through the addition of a compound (i.e., a plasticiser) that causes the same effects.[130] A simple description of external plasticisation is that it creates plasticiser-polymer secondary interactions that decrease polymer-polymer secondary interactions.[134] This separates the polymer chains, increases the free

volume and segmental mobility of the polymer chains, thereby causing plasticisation.[134]

Addition of a plasticiser generally results in an increase in the flexibility, impact resistance, and processability of a given polymeric material.[130] Specialty plasticisers can also be used to confer comparatively exotic properties, such as improved conductivity, biodegradation resistance, or resistance to burning.[130] As a result, there is considerable interest in additive plasticisers, with countless reported polymer/plasticiser combinations. Some of the most common plasticisers are phthalates, oleates, ether-esters, and phosphates.[130] For a comprehensive discussion of plasticiser types, their effects and common applications, the reader is referred to Wypych et al.[130]

For external plasticisation, selection of a compatible and permanent plasticiser is paramount. However, the prediction of plasticiser compatibility and therefore selection of an appropriate plasticiser is complex. The compatibility of a polymer and plasticiser is directly related to the polarities of both compounds. A non-polar polymer and non-polar plasticiser (and vice versa) are likely to be miscible if they have similar polarities, due to the favourable secondary interactions between them (i.e., “like-dissolves-like”).[130] Various methods exist for predicting the compatibility of a plasticiser and polymer. For example, Hansen solubility parameters (HSP) can be calculated and used to predict the solubility (i.e., compatibility) of a plasticiser in a polymer, when appropriate data are available.[135] The structure of the plasticiser (e.g., molecular weight, chain length, aromaticity) and the conditions of its incorporation also effect its compatibility. Generally, higher molecular weight plasticisers (including monomeric and polymeric species) are more effective. A higher molecular weight often means the plasticiser exhibits low volatility and improved permanence, and therefore more effective and long-lived plasticisation.[136] The permanence of a plasticiser also depends on its rate of diffusion in a target polymer. While a high diffusion rate may facilitate the miscibility of the plasticiser and polymer, it can also reduce permanence due to diffusion out of the polymer matrix.[137]

1.3.4 Stimuli-responsive Polymers

The synthesis of stimuli-responsive homo- or random polymers can be facilely achieved using conventional free radical polymerisation, though comparatively complex polymers — such as block copolymers — can be synthesised *via* other polymerisation methods like reversible-deactivation radical polymerisation. As the name suggests, stimuli-responsive polymers undergo physical or chemical changes in response to one or more applied stimuli.[138] Exemplar stimuli include pH, temperature, light, and magnetic or electric fields.[138] These changes are generally reversible and alter the properties of the polymer in ways that can be exploited to develop “smart” materials.

In the case of polymers that are responsive to pH (i.e., pH-responsive polymers), weakly acidic or basic monomers, such as methacrylic acid or 2-(dimethylamino)ethyl methacrylate (respectively), confer pH-responsivity to a resultant copolymer that is similar to the p*K*a values of the constitutive monomers.[138,139] The ionisation of these groups, drives the responsive properties of the polymers. The protonation of basic monomers at low pH — or conversely the deprotonation of acidic monomers at high pH — changes the ionisation of the polymer and can lead to electrostatic repulsion, induce structural changes, and switches in hydrophilicity. Generally, the presence of relatively hydrophobic, neutral groups in the polymer backbone, creates a tight packing of polymer chains (also called a collapsed or tightly coiled state), due to the hydrophobic interactions between chains.[138,139] The ionisation of these groups following a change in solution pH induces a change to a loosely packed, expanded state — thereby increasing its hydrodynamic volume — due to the electrostatic repulsion afforded between charged groups in the polymer backbone. The extent and nature of these structural changes (i.e., the pH-responsivity) of the polymer can also be tuned *via* the incorporation of hydrophobic monomers, which alter the number and distribution of the pH-responsive groups, and therefore their electrostatic repulsion when ionised.[138,139]

For polymers with relatively simple structures, like random copolymers and homopolymers, ionisation induced structural changes can alter fundamental properties such as solubility. In contrast, the more complex architectures of block,

branched, or star-shaped copolymers, can undergo complex changes, such as self-assembly into ordered 3D structures (e.g., micelles, vesicles), swelling/deswelling, the formation of gels, or changes in surface activity.[138,139] For example, at physiological pH (7.4), block copolymers of poly(ethylene glycol)-*b*-poly(2-vinylpyridine) (PEG-*b*-PVP) self-assemble into micelles.[140–144] Due to the hydrophilicity differential that exists between the hydrophilic PEG and hydrophobic PVP blocks, micelles are formed that exhibit an inner hydrophobic PVP 'core' and an outer hydrophilic PEG 'shell'. When exposed to a lower pH environment (pH 5.5), the micelles disassemble, due to the electrostatic repulsion between the protonated — and consequently hydrophilic — pyridyl groups (pKa ~ 5). This pH-responsive behaviour could be exploited for the targeted delivery of hydrophobic drugs for the treatment of cancer.[144] Whereby a hydrophobic drug could be encapsulated in the micelles at physiological pH, and disassembly — and therefore drug release — triggered in the low-pH environment of cancer cell endo/lysosomes (pH 5.0–6.5).[144] Unsurprisingly, pH-responsive polymers and stimuli-responsive polymers in general, are of enormous interest within the scientific community.

1.4 Reverse Enteric Coatings

One of the most common applications of pH-responsive polymers, is in the formation of protective coatings of pharmaceutical formulations for oral delivery. Many pharmaceutical formulations require administration *via* the stomach or intestines and so formulations are designed to be highly soluble once the target environment is reached.[145] For example, the active drug may be acid labile and lose functionality if exposed to the low-pH gastric environment (pH 1.5–3.5), and so a pH-responsive coating is used to prevent release of the formulation until the higher pH of the intestines (pH 5–6) is reached.[146] These types of intestine-targeting polymer coatings are termed 'enteric' and commonly incorporate polyvinyl acetate and methacrylic acid-ethyl acrylate copolymers.[145–147] In contrast, when drug dissolution within the stomach is desired, 'reverse enteric' coatings are employed. Reverse enteric coatings prevent dissolution within the higher pH oral environment (pH 6.8–7.4),[148] but dissolve rapidly once the low-pH gastric environment is reached.[145] Generally, reverse enteric

coatings are used for taste-masking, to avoid patient non-compliance due to an unpalatable pharmaceutical formulation,[146] and employ tertiary amine-based acrylate copolymers. These polymers are commonly synthesised using CFRP.[149]

Prominent examples of commercially available reverse enteric formulations include the Eudragit® family (Eudragit® E 100, E 12.5, and E PO). Reviewed elsewhere,[150] these formulations are commonly used for immediate release applications that require taste-masking. Available in a range of forms, including granules (E 100), organic solutions (E 12.5), and powders (E PO), these Eudragit® formulations are soluble in the gastric environment (and up to pH 5) and insoluble at elevated pH (> pH 5).[150] Reverse enteric Eudragit® polymers have been used in the production of a range of taste-masked dosage forms, such as microparticles[151]/beads[152]/capsules,[153] and 3D printed[154] or pan coated[155] tablets (**Table 1.2**).

Often, taste-masking coatings or matrices are used in the preparation of multiparticulate formulations such as mini-tablets (containing microparticles/beads) or granules. Multiparticulate dosage forms are considered preferable to conventional tablets for paediatric patients, where palatability and swallowability are major barriers to patient compliance.[156, 157] However, the complete containment, and effective taste-masking of bitter active pharmaceutical ingredients (APIs) within the oral cavity remains challenging to mediate. Unique challenges are posed by the properties of reverse enteric copolymers (e.g., the swelling and permeability characteristics of Eudragit® copolymers), and the required dosage form.

Table 1.2: Overview of selected examples of reverse enteric dosage forms, and the processing methods used in their preparation.

Reverse enteric polymer	Product	API	Manufacture	Dosage Form	Notes	Ref.
Poly(butyl methacrylate-*co*-(2-dimethylaminoethyl) methacrylate-*co*-methyl methacrylate) (1:2:1)	Eudragit® E PO	Propranolol hydrochloride	Prilling	Microbeads	Most effective taste-masking at a ratio of 1:25 drug:matrix	152
	Eudragit® E PO and E 100	Prednisolone	Spray drying /tablet pressing or solvent casting	Microparticles alone or in an orodispersible tablet or film	Microparticles of E 100 (1:2 drug:polymer, ~ 33% loading) achieved 90% release in < 10 min (pH 1.2) and 3.8% in < 3 min (pH 6.8). Tablets (~ 98% loading) achieved 90% release in 30 min (pH 1.2) and released 58.5% in 3 min (pH 6.8). Films (91.8% drug loading) achieved 80% release in 30 min (pH 1.2) and 20.4% in 3 min (pH 6.8).	158
	Eudragit® E 100	Ondansetron hydrochloride	Spray drying	Microspheres	Eudragit® microspheres (1:2 drug:polymer, ~ 45% loading) achieved taste-masking at pH 6.8 (< 7.5 $\mu g.mL^{-1}$ i.e., bitterness threshold) and > 90% release at pH 1.0 in 15 min.	159
	Eudragit® E PO	Quinine sulphate	Extrusion-spheronisation and fluidised-bed spray coating	Pellets	Quinine release was reduced in water (pH ~ 7), within the first 5 min, from 9.2–2.1% when the E PO coating was increased from 10–30% $w.w^{-1}$. Complete release was achieved at pH 1.0 within 15 min at all coating levels.	160
Poly(methyl methacrylate-*co*-diethylaminoethyl methacrylate) (6:4)	Kollicoat® Smartseal 30D (aqueous dispersion)	Ornidazole	Fluidised-bed spray coating	Oral dry suspension	Ornidazole release limited to < 5% (5 min, pH 6.8), and < 15% (120 min), when coated with 40% $w.w^{-1}$ mass gain Kollicoat (top-spray). Achieved 90% release within 15 min. Comparable results (50% $w.w^{-1}$ mass gain) observed for bottom-spray approach.	161
		Cetirizine dihydrochloride	Spray drying	Microspheres	Microspheres containing drug:polymer ratios of 0.5:1, 0.75:1, 1:1, were found to release ~ 80% of contained drug within ~ 6 min at pH 6.8.	162

		Quinine sulphate dihydrate, diclofenac sodium	Fluidised-bed spray coating	Micropellets	Suglets® coated with both drugs at 10% or 50% w.w^{-1} weight gain, then coated with Kollicoat®. At pH 6.8, release was "negligible for several hours" and immediate in 0.1 M hydrochloric acid (HCl). In 24 h (pH 6.8) at coating levels of 10%, 20%, 30% and 40%, the amount of drug released was ~ 85%, ~ 65%, ~ 35%, and ~ 30%, respectively.	[163]
		Paracetamol	Modified tangential-spray fluidised-bed spray coating	Irregularly shaped particles	Particles coated with 15% w.w^{-1} weight gain limited paracetamol release to 5.5 ± 0.5 μg.mL^{-1} after 4 min (pH 7.4). Complete release achieved within 15 min at pH 1.2.	[164]
Poly(methyl methacrylate-*co*-diethylaminoethyl methacrylate) (7:3)	Kollicoat Smartseal 100P (organic solution)	Chlorpheniramine maleate (CPM)	Fluidised-bed spray coating	Film-coated multiparticulates	CPM multiparticulates coated with 10% w.w^{-1} weight gain released > 95% CPM in 30 min (pH 1.0), and impeded release (no release detected) for 15 min at pH 6.8.	[165]
Chitosan	-	Ferrous sulfate	Spray drying	Microparticles	Microparticles containing iron (25% w.w^{-1}) released ~10% iron at pH 7, and 90% at pH 1, both in 1 h	[166]
		Ondansetron hydrochloride	Spray drying	Microspheres	Chitosan microspheres (1:1 drug:polymer, ~ 83% loading) achieved taste-masking at pH 6.8 (< 7.5 μg.mL^{-1} i.e., bitterness threshold) and ~ 90% release at pH 1.0 in 25 min.	[159]

For dosage forms that do not prevent contact between the bitter API and the oral cavity (pH 6.8–7.4),[148] such as microbeads (or microparticles) which consist of a spherical matrix containing a mixture of the reverse enteric polymer and API, the encapsulated API is often prematurely released within the oral cavity.[167] As a result, the bitter taste of the API is only suppressed when relatively large amounts of the constitutive reverse enteric polymer are used, which limits the capacity for drug loading. For example, microbeads containing propranolol hydrochloride were prepared with Eudragit® E PO *via* prilling, to produce a taste-masked paediatric formulation for oral administration.[152] The greatest taste-masking was achieved with microbeads exhibiting a 1:25 ratio of propranolol:matrix (equivalent to ~ 96% matrix). The formulation limited the release of propranolol to 3.3% following 2.5 min at pH 6.8, and reached ~ 20% after 15 min.[152] However, a low drug loading of ~ 38 $mg.g^{-1}$ (mg of propranolol per g of microbead, equivalent to ~ 3.8% propranolol) was required for it to be achieved. Low drug loadings may be problematic for APIs that require high doses or dosage forms with size considerations, and the use of large amounts of reverse enteric polymer may raise concerns for patient safety (e.g., Gerogieva et al.[151]).

Dosage forms that provide a barrier between the bitter API and the oral cavity, such as microcapsules (also called micropellets) bearing reverse enteric film coatings, can exhibit more efficient taste-masking properties. For example, microcapsules containing the antiprotozoal drug ornidazole were film coated *via* fluidised-bed spray coating, with the reverse enteric polymer Kollicoat® Smartseal 30D, at a 40% $w.w^{-1}$ mass gain.[161] The microcapsules limited release of ornidazole to ≤ 5% following 5 min at pH 6.8, and only reached < 15 % after 120 min. Comparatively, similar performance to the Eudragit® E PO microbeads was achieved with significantly less of the Kollicoat® material. Further, when a similar ratio of Kollicoat® to drug was used (80% $w.w^{-1}$), superior taste-masking performance was achieved, as no ornidazole was released in 120 min. Whilst microcapsules are advantageous for improved taste-masking performance, microbeads can exhibit more rapid drug release within the gastric environment. In the previous examples, the Eudragit® microbeads achieved 100% drug release within 5 min (pH 1.2),[152] whereas the Kollicoat® microcapsules

achieved ~ 90% release within 15 and 45 min for the respective 40% and 80% w.w^{-1} coatings (pH 1.0).[161] In many cases, the selection of a currently available reverse enteric polymer and the dosage form it is incorporated into, requires a trade-off between taste-masking performance, and rapid release within the gastric environment. As a result, there remains a need for the development of reverse enteric coatings that effectively contain bitter APIs and mediate rapid release within the gastric environment.

1.5 Polymer Membranes/Films as Barrier Coatings

Polymer films have found widespread use in many industries, for applications such as food packaging,[168] drug delivery (*vide supra*), separation/filtration, protective coatings,[169] and paints.[170] No polymer film is completely impermeable, due to the presence of free spaces between polymer chains (i.e., the free volume),[171] meaning that the transport of liquids (e.g., water), gases (e.g., water vapour or oxygen), or ions (e.g., salts such as sodium chloride) generally occurs. Importantly, the extent to which a polymer film is permeable to one or more of these penetrants — whether innately for natural polymers or by design for synthetic polymers — determines its effectiveness for an application. In their application, polymer films can be broadly classified as either barrier coatings or semi-permeable membranes. Generally, these films are intended to either limit the permeation of water (barrier coating) or selectively promote the permeation of water but the sequestration of other molecules (semi-permeable membrane). Whilst the purposes of these membranes differ, the permeabilities of both are governed by the same transport processes. In the context of this work, polymer films designed as barrier coatings to prevent water permeation are most relevant and are discussed further.

The transport of water across a polymer film generally occurs *via* a three-step solution-diffusion mechanism: (*i*) water molecules are first adsorbed by the surface of the film, (*ii*) the water molecules then diffuse through the film down a concentration gradient, before (*iii*) desorption occurs at the interface between the film and the coated substrate.[172, 173] The permeability of the membrane can be quantified by the permeability coefficient (*P*), as a product of the solubility coefficient (*S*) — the amount

of penetrant sorbed by the polymer — and the diffusion coefficient (*D*) — the ability of the penetrant to diffuse through the polymer (**Equation 1.1**).[173]

$$P = [S][D]$$

Equation 1.1: Permeability coefficient equation.

There are numerous factors that affect the water permeability of a polymer film and its utility. Hydrophilic polymer films inherently have stronger interactions with water, and accordingly, exhibit greater water permeability.[174] However, polymer crystallinity can also affect both the water permeability and processability of the film. Crystalline polymers are generally less hydrophilic due to the strong intramolecular interactions between polymer chains, and the restricted access (and therefore reduced interactions) between water molecules and polar groups within the crystal structure.[174, 175] In contrast, the water permeabilities of amorphous polymers (and to an extent, semi-crystalline polymers) are impacted by their glass transition (T_g) values. The increase in segmental motion, characteristic of an amorphous polymer at elevated temperatures (i.e., T ≥ T_g °C), affords an increase in free volume.[170, 171, 174, 176] This increase in free volume enhances water permeability. However, as a penetrant, water can plasticise polymers and cause a depression of their T_g value and a further increase in free volume, thereby further enhancing water permeability.[170, 171, 174, 176] Polymer structure can also affect water permeability. Reductions in the segmental mobility of a polymer due to unsaturation or the presence of bulky side groups, can produce areas of free volume that enhance permeation.[171] In addition, the crosslinking of polymer chains prevents their solvation, and reduces segmental motion, due to the covalently cross-linked networks that form. As a result, water permeability of a polymer is negatively correlated with cross-linking density.[171, 174]

The design of a polymer film for an effective barrier coating requires consideration of the key factors affecting water permeability (*vide supra*), and therefore, careful tuning of the physicochemical and thermal properties of a candidate polymer is also required. In the context of this work, consideration of these factors is complexified by the antithetical properties of a polymer film that is meant to function as both a barrier coating and a reverse enteric coating. For example, reverse enteric coatings

generally employ basic amine-based functional groups, due to their pH-dependent ionisation and solubility switching (i.e., from hydrophobic (high pH) to hydrophilic (low pH)). However, common examples of these functional groups, such as pyridine, imidazole, or aminoalkyl methacrylate groups, — whilst hydrophobic — are relatively polar and still exhibit secondary interactions (e.g., hydrogen bonding) with water. As a result, water acts as a penetrant for these coatings when the polymers are in their neutral (i.e., hydrophobic) state, and undermines their barrier coating-like performance. The penetration of water is highly undesirable, however, attempts to mitigate the water permeability of a coating, will inherently reduce the water solubility of a film, thereby reducing its solubility at low pH and function as a reverse enteric coating. For example, increases in crystallinity, reductions in the number of polar functional groups (i.e., the mol% fraction of ionisable groups), or cross-linking of a polymer will likely all improve the barrier properties of a coating, but will decrease its water solubility. Invariably, unfettered changes to these physicochemical properties could lead to a lack of solubility of the polymer at the desired pH, and therefore, a loss of reverse enteric function. In the development of a polymer film that exhibits the properties of both barrier and reverse enteric coatings, a compromise of performance — as either type of coating — must be reached. Ultimately, this requires an experimental evaluation of a target pH-responsive polymer, with reference to the principles described herein.

1.6 Applicable Manufacturing Methods

Two manufacturing methods and their potential dosage forms are most relevant in the context of the current work — fluidised-bed spray coating and hot-melt extrusion (HME). These are generally considered to be scalable, cost-effective methods for the manufacture of solid pharmaceutical dosage forms. Other manufacturing methods were excluded based on the design criteria outlined in **Chapter 1.1.4** and are briefly discussed below.

Techniques such as wet/dry granulation, spray drying, and extrusion spheronisation, all produce small (< 10 mm), generally spherically shaped solid matrices impregnated with an API. As discussed earlier (*vide supra*), like microbeads/particles, these

dosage forms are likely to prematurely release the API *in vivo*. For a PPI, premature release of a poison *in vivo* could have negative effects on an implanted animal, which precludes the use of these techniques for implant development. It is possible to combine one of these approaches with a complementary technique such as fluidised-bed spray coating, to first produce the microbeads/particles containing the API and appropriate binders/excipients, then apply a reverse enteric coating. However, to afford a lethal dose, several microbeads/particles would be required, due to inherent restrictions to sizes compatible with conventional syringe implanters (i.e., < 2 mm diameter). It is possible that microbeads/particles could migrate *in vivo* following implantation. Currently, it is not known whether implant location will have a significant impact on implant consumption by a feral cat. It is plausible that if the lethal dose of poison is contained in microbeads/particles that are in sufficiently disparate locations, then consumption of select microbeads/particles may occur, and could therefore cause sublethal dosing. As a result, it is likely that a second encapsulation process would be required to prevent migration. Since this would add an additional dissolution process, and potentially reduce the rapidity of release *in vivo*, such an approach was deemed inappropriate.

Other conventional approaches to solid dosage form manufacture, such as tableting *via* direct compression have the same shortcomings as above (namely the lack of a barrier between the API and the *in vivo* environment). Again, even if a complementary coating technique was used, it would remain unfeasible given that direct compression of shaped tablets of the desired size (< 2 mm diameter, 10 mm length) is not possible.

Overall, hot-melt extrusion and fluidised-bed spray coating were considered the most appropriate manufacturing methods. Both approaches can be used to prepare solid dosage forms with highly customised dimensions and considerable accuracy (*vide infra*). However, whilst fluidised-bed spray coating and hot-melt extrusion have both been used to prepare dosage forms that incorporate reverse enteric polymers, neither method is universal. Important consideration must be given to the physicochemical and thermal properties of the API, pH-responsive polymer, and complete dosage form, to ensure their compatibility (*vide infra*).

1.6.1 Fluidised-bed Spray Coating

Film coating *via* spray atomisation is one of the most common and facile methods for coating pharmaceutical formulations.[177] This process involves dissolving the — generally polymeric — formulation in an organic solvent to afford a solution, or the preparation of an aqueous dispersion, before atomising the solution using compressed air. The droplets formed during atomisation deposit and spread across a coating substrate, and as the solvent evaporates a film is formed (**Figure 1.4**). The mechanism of film formation is relatively simple for organic solutions (**Figure 1.4a,b**) — polymer chains interpenetrate as the solvent evaporates, forming an intermediate gel state prior to film formation.[178] Chain interpenetration occurs at a concentration equal to the reciprocal of the intrinsic viscosity of the solution,[179, 180] whereas effective film adhesion is related to greater end-to-end distances of polymer chains.[181] The primary parameter determining effective film formation is the rate of evaporation of the organic solvent, which can be a single or mixed solvent system. If the evaporation rate is too fast, dried polymer particles are deposited on the surface of the coating substrate (often called 'dusting'), and a discontinuous film may form. If the evaporation rate is too slow, coating substrates bearing partially formed films become wet and tacky and agglomerate. An ideal evaporation rate prevents both the former and latter processes from occurring.[178]

The mechanism of film formation is comparatively complex for aqueous dispersions (**Figure 1.4c**). Following deposition on the coating substrate surface, the evaporation of water causes the polymer particles to pack together, then deform to fill the void spaces once occupied by water. As further drying occurs, a film is produced due to the coalescence of the polymer particles.[178]

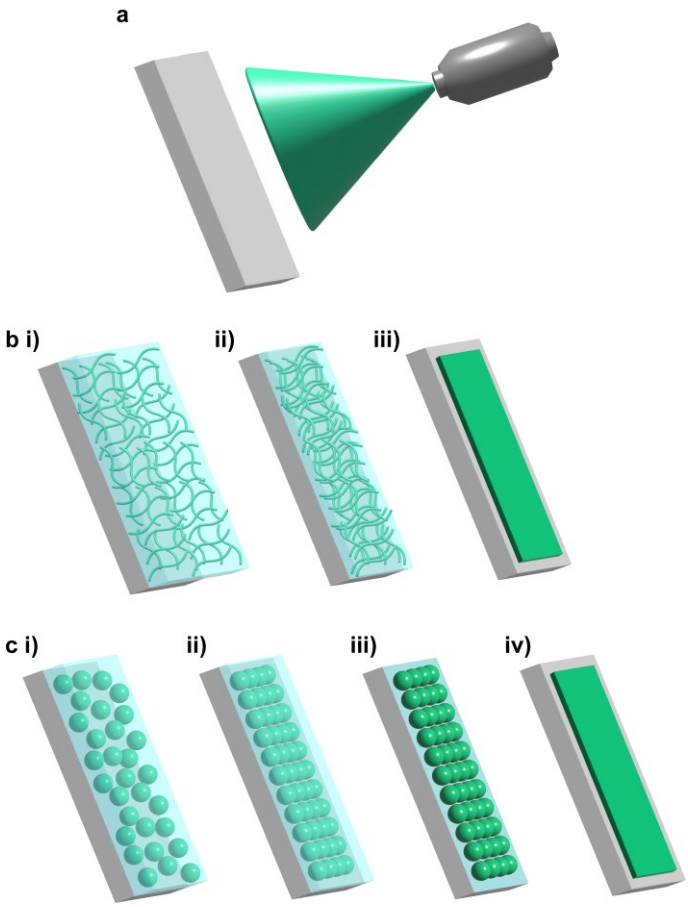


Figure 1.4: A conceptual illustration of a) spray coating of a substrate and film formation from b) an organic solution, wherein i) the polymer chains begin to interpenetrate as the solvent evaporates, ii) an intermediate gel state is formed as evaporation continues, before iii) film formation occurs. In contrast spray coating from c) an aqueous dispersion, involves i) deposition of aqueous droplets containing polymer particles, ii) stratification of the particles during evaporation, iii) deformation and tight packing of the particles following continued evaporation, and finally iv) coalescence of the polymer particles to form a film.

The processes underlying particle deformation and coalescence are disputed,[182] and discussion of these fall outside the scope of the current work. However, an important aspect of coating with aqueous polymer dispersions is the minimum film-forming temperature (MFFT). Coating above the MFFT enables the deformation and cohesion of the polymer particles and the formation of a continuous film.[183] Though distinct from the T_g, the MFFT is generally close to the T_g, as both are dependent on the same secondary interactions. For example, the incorporation of a low-T_g polymer or plasticiser will decrease the T_g and MFFT.[183] The higher heat of vaporisation of water

necessitates elevated spray coating temperatures, and therefore MFFTs that are appropriate under these conditions.

Though mechanistically complex, understanding film formation for aqueous polymer dispersions is important as the pharmaceutical industry generally favours the use of aqueous dispersions over organic solvents. In addition, the inherent flammability and toxicity risks associated with processes involving organic solvents, and the health risks posed by their incomplete evaporation, has elevated aqueous dispersions as the preferred choice.[172, 184] Historically, organic solutions were favoured in film coating processes, as they readily evaporated during coating. However, later advances in coating instrumentation increased the efficiency of drying processes and increased the accessibility of aqueous dispersions.[178]

Although various types of equipment can be used, in the context of the current work, processing utilising a fluidised bed is most relevant (**Figure 1.5**).[185, 145] Fluidised-bed spray coating instruments exhibit high drying efficiency and are compatible with both aqueous and organic solvents. Furthermore, the diminutive size of 'benchtop' fluidised bed instruments makes them suitable for laboratory-scale prototyping, as small batches (< 500 g) can be produced.[186]

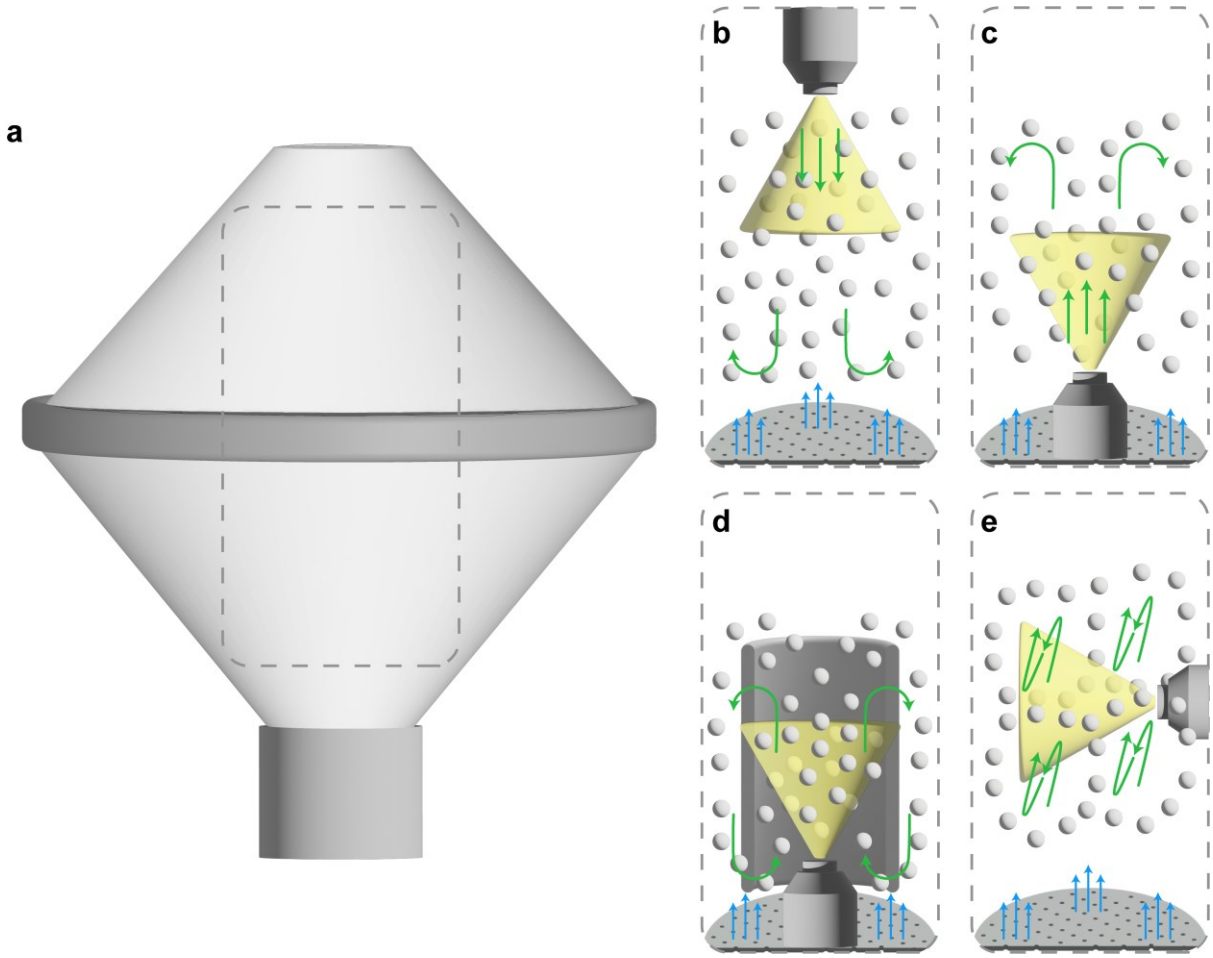


Figure 1.5: Illustration of a) a fluidised-bed spray coating chamber and archetypal spray configurations for b) top-down spray coating, c) bottom-up spray coating, d) bottom-up spray coating with a Wurster column insert, and e) tangential spray coating. Note the fluidisation air flow (blue arrows), spray formulation (yellow), and trajectory of spray coating substrate (green arrows).

1.6.2 Hot-melt Extrusion

In a typical HME process, a formulation containing a thermoplastic carrier, API, and any required processing aids or excipients (i.e., plasticisers, stabilising agents, or solubility enhancers) is heated, mixed, and extruded through a die *via* one or more rotating feeder screws (**Figure 1.6**).[187, 188] The temperature at which extrusion is performed is dependent on the melting point (T_m) and/or T_g of the polymeric carrier, and the thermal stability of the API and excipients. Generally, HME is primarily suitable for APIs that exhibit low-to-moderate sensitivity to thermal degradation. Many

polymeric carriers require heating to temperatures above the T_g or T_m, to enable mechanical mixing within the extruder, and risk thermally degrading the APIs in the formulation.[189] However, lipid carriers can overcome this limitation, as lipidic matrices can be processed close to room temperature (i.e., ~ 25 °C).[153, 190]

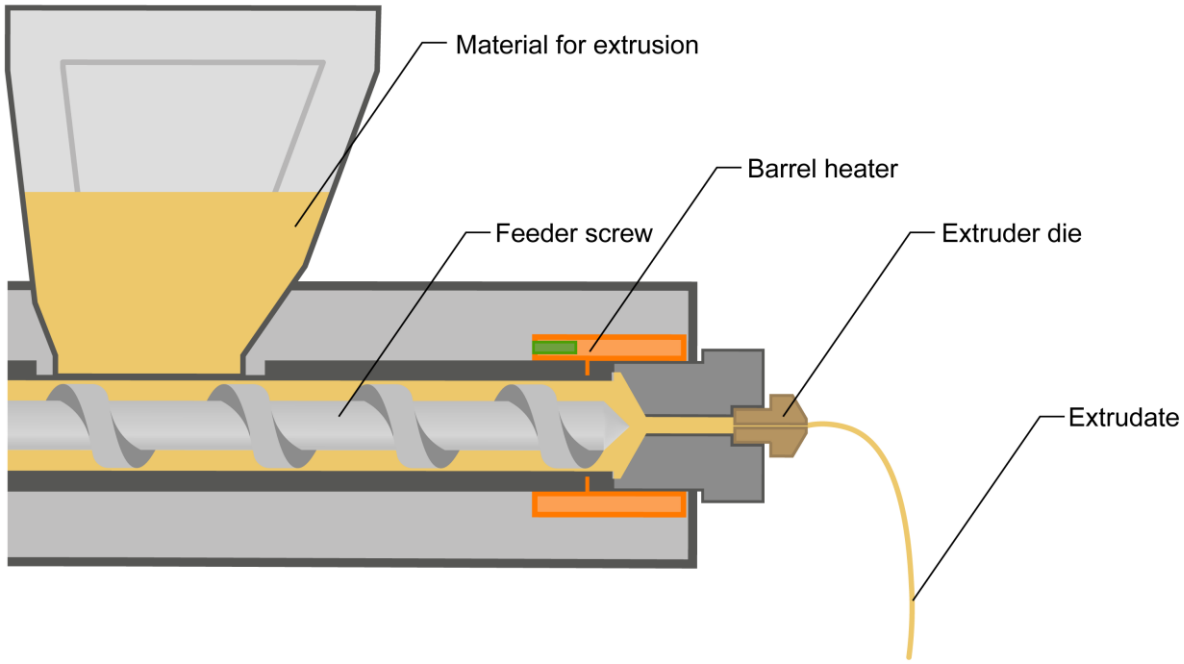


Figure 1.6: Simplified illustration of a hot-melt extruder, showing how the material for extrusion (a combination of thermoplastic carrier, API, and processing aids and/or excipients) is extruded through a die, *via* a heated barrel and rotating feeder screw.

HME produces solid pharmaceutical formulations that afford improved solubility of poorly water-soluble drugs,[191] controlled release,[192] taste-masking,[193] and targeted release.[194, 195] A range of delivery systems with these properties including tablets,[196] implants,[197] capsules,[195] films,[198] and granules,[199] can be prepared *via* single or multi-layered HME systems (i.e., *via* co-extrusion[200]). Through HME, pharmaceutical formulations with tailored sizes, shapes, and release properties can be prepared. This approach is scalable, solvent-less, and enables continuous manufacturing. In addition, materials produced *via* HME can undergo downstream processing to produce more complex or tailored systems. For example, HME granules can be film coated, to afford abuse-deterrent delivery systems[201], or HME filaments can be 3D printed into various dosage forms *via* fused-filament fabrication (FFF).[202]

Many thermoplastic carriers have been shown to be compatible with HME.[197, 203–205] Jaeghere et al. were able to tune the T_g values of extrudates containing polyvinyl alcohol (PVA) 4-88 (whereby, "4" is the viscosity (mPa.s) of a 4% aqueous solution at 20 °C, and "88" is the degree of hydrolysis of polyvinyl acetate (mol%)), *via* plasticisation with sorbitol. Incorporation of sorbitol from 0 to 40% w.w^{-1} reduced the T_g value of PVA 4-88 from 67.0 to 13.1 °C and enabled the solubilisation of the nonsteroidal anti-inflammatory drug celecoxib (15% w.w^{-1}) in a 40% w.w^{-1} sorbitol/PVA 4-88 formulation. Most relevant to the current work however, are poly(ethylene glycol) (PEG)-based HME formulations that are compatible with high API loadings, such as those required in the diminutive PPI design. PEG HME formulations have been investigated for a range of controlled release and 3D printing applications, and exhibit favourable mechanical, rheological, and solubility (both drug and formulation) properties. The release rate of an incorporated drug is dependent on both the type of drug and its loading, and the molecular weight of PEG used.[192, 206] The molecular weight of PEG incorporated into a formulation can also determine its mechanical and rheological properties when extruded, which can be tuned for specific applications such as 3D printing.[203] In addition, the unique physicochemical properties of PEG make it an effective thermoplastic carrier for applications requiring high API loadings.[206–208] For example, extrudates of PEG (molecular weight 300–7000 kDa) have been obtained with metoprolol tartrate, ibuprofen, or theophylline loadings as high as 60% w.w^{-1}.[206] Most notably, Isreb et al. reported a PEG-based HME formulation in which higher molecular weight PEG 600 kDa was plasticised with lower molecular weight PEG 6 kDa (1:1 w.w^{-1}). The resultant HME formulation required a relatively low extrusion temperature (80 °C), and successfully solubilised theophylline — a phosphodiesterase inhibiting drug used to treat various respiratory conditions — at a drug loading of 30% w.w^{-1}.

It should be noted that while most injectable drug-eluting implants are prepared through simple hot-melt extrusion processes,[209–212] this method alone is not appropriate to produce a reverse enterically coated implant. An archetypal drug-eluting implant is composed of a matrix containing the API, which is slowly released as the polymeric component(s) of the matrix erode (generally due to biodegradation).[197] This is akin to a reverse enteric microbead/particle (*vide supra*),

which in the context of a PPI, would result in the premature release of poison within the subcutaneous environment. One method of overcoming this limitation is to perform a co-axial extrusion, a process through which a multi-layered extrudate can be produced. However, whilst co-axial extrusion can provide multiple layers and hypothetically afford a reverse enterically coated implant, the core is not sealed at the ends by the outer-most layer. Therefore, extruded implants would need to be sealed in an additional process, limiting high-throughput manufacture, and potentially introducing a point of failure if sealing is not effective (e.g., see **Chapter 2.4**). As a result, HME would need to be combined with a complimentary manufacturing method (e.g., fluidised-bed spray coating), to enable the application of a reverse enteric coating following extrusion.

1.6.3 Implant Manufacture

Two approaches to implant manufacture were explored in this work. First, a solely fluidised-bed spray coating method was employed. Whereby, a solid ABS filament substrate was sequentially spray coated with a ‘core’ formulation, followed by a reverse enteric coating (**Figure 1.7a**). The second approach utilised HME to produce a solid core (equivalent to the combined size of the ABS filament and spray coated core), that was then spray coated with the reverse enteric coating (**Figure 1.7b**).

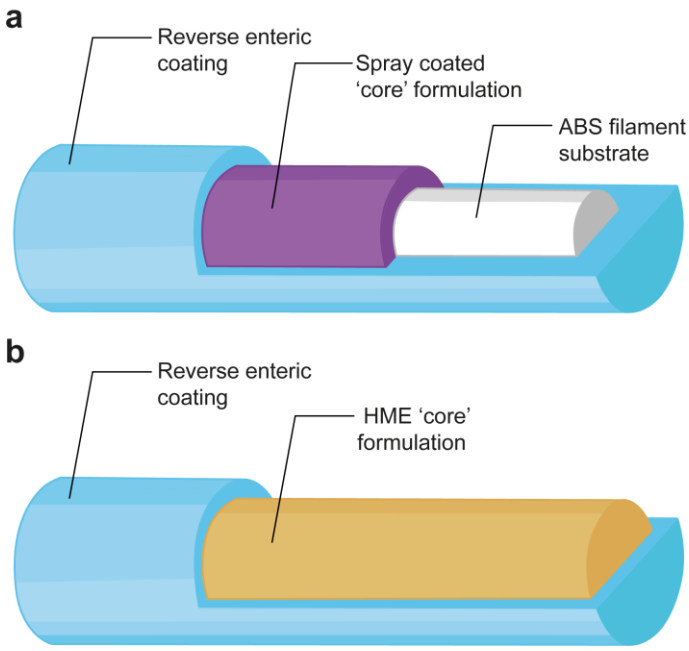


Figure 1.7: Conceptual illustrations of the two approaches to PPI manufacture. a) The ABS filament substrate-based fluidised-bed spray coating approach and b) the hot-melt extrusion and fluidised-bed spray coating approach.

1.7 Thesis Scope

1.7.1 Hypothesis

A pH-responsive (reverse enteric), subcutaneous implant can be developed that is stable at physiological pH (7.4) under the skin of a native mammal, but rapidly releases an encapsulated poison at gastric pH (< 2) in the stomach of a feral cat, for use as a targeted method of feral cat control.

1.7.2 Research Objectives

Objective 1: Synthesise a library of 2-vinylpyridine-based pH-responsive copolymers to explore the effects of copolymer composition on the physicochemical and thermal properties of the copolymer and select a lead copolymer exhibiting suitability for use as a reverse enteric coating.

Objective 2: Optimise the fluidised-bed spray coating of a reverse enteric formulation using the lead pH-responsive copolymer.

Objective 3: Investigate and optimise the manufacture of PPIs utilising the reverse enteric formulation developed in Objective 3.

Objective 4: Investigate the stability, release, and mechanical properties of manufactured implants *in vitro.*

Objective 5: Investigate the performance of manufactured implants *in vivo.*

1.7.3 Thesis Outline

Chapter 1 presents a review of literature relevant to the development of the PPI. The current work is contextualised by outlining the impacts of invasive mammalian predators — namely the feral cat — and the techniques and challenges associated with attempts to control them in Australia. The PPI concept is then introduced as a potential solution, and key design considerations are outlined for its effective performance. Additional literature is discussed in the context of these design considerations, and the chemistries necessary to achieve them. Parts of the literature review presented in Chapter 1 are taken from a series of publications that describe the work outlined in this thesis, as listed in **Chapter 9.1**.[213–215]

Chapter 2 introduces the only comparable technology to the proposed PPI, the hard-shell delivery vehicle (HSDV) developed by Scientec Research Pty Ltd. HSDVs are the current state-of-the-art, in terms of reverse enterically coated, toxic formulations for invasive predator control. In collaboration with Scientec, the HSDV and a series of custom manufactured derivatives are evaluated for their potential use as implants.

Chapter 3 describes the preliminary development of the PPI. The synthesis, characterisation, and reverse enteric performance of a series of copolymers of 2-vinylpyridine and butyl methacrylate is discussed. The manufacture of non-toxic PPIs *via* fluidised-bed spray coating is then described, with implants bearing a reverse enteric coating developed from a lead copolymer in the series. The *in vitro*

performance of the implants is then investigated, and implants with favourable performance are further evaluated in a preliminary *in vivo* study.

Based on the performance of the reverse enteric coating evaluated in Chapter 3, Chapter 4 focusses on the optimisation of coating performance. The synthesis of a library of pH-responsive copolymers *via* the copolymerisation of 2-vinylpyridine and butyl methacrylate, with methyl methacrylate or isobornyl methacrylate, is reported. The composition-property relationships of the synthesised copolymers are discussed and used to identify a lead copolymer for further investigation.

The development of the copolymers described in Chapters 3 and 4 is reported in a publication that investigates the copolymers as reverse enteric coatings for the taste-masking of pharmaceutical dosage forms (**Figure 1.8**).[214]

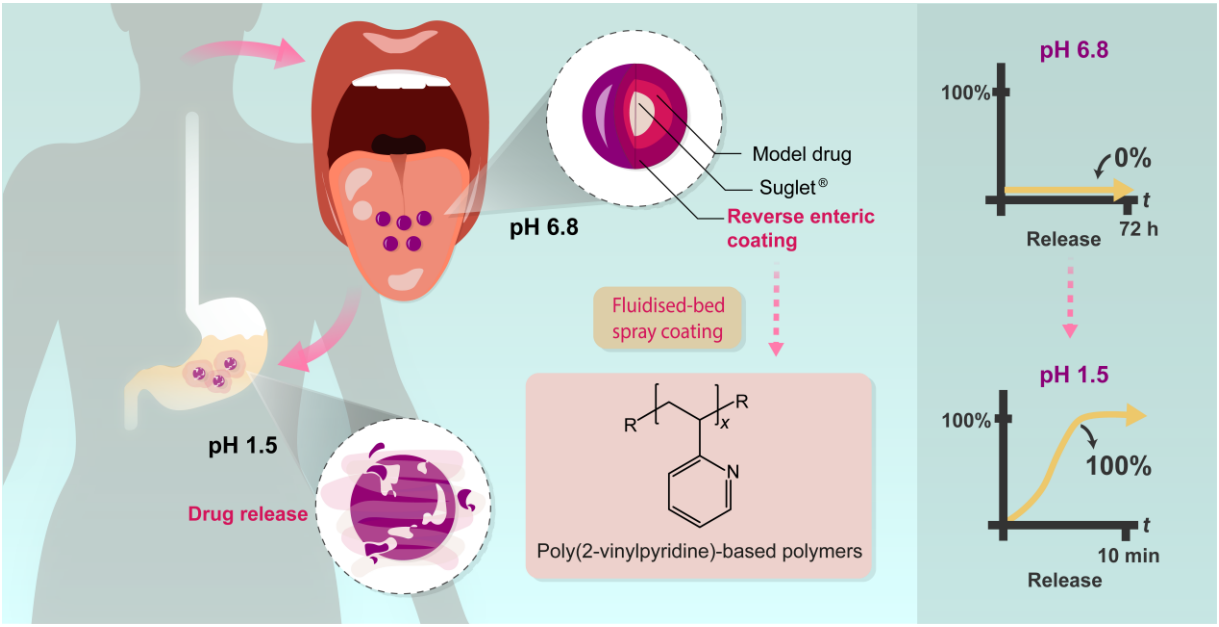


Figure 1.8: Graphical abstract illustrating the investigation of the copolymers synthesised in Chapters 3 and 4, as reverse enteric coatings for the taste-masking of pharmaceutical dosage forms.[214]

In Chapter 5, a reverse enteric formulation is prepared from the lead copolymer described in Chapter 4. The manufacture of non-toxic PPIs bearing this coating is reported, and their performance is evaluated both *in vitro* and *in vivo.* The intrabatch quality of the implants is interrogated and the performance of the implants is evaluated *in vitro*, regarding their stability and release properties. Implants with the

most favourable performance *in vitro* are investigated further for their stability *in vivo* in a murine model. The development and performance evaluation of the non-toxic, PPIs is published (**Figure 1.9**).[215]

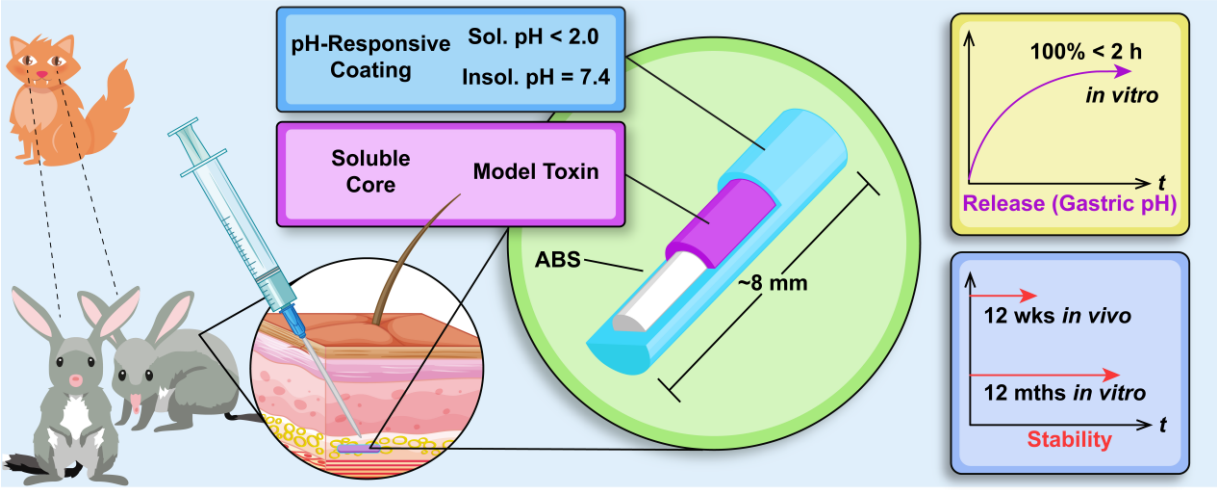


Figure 1.9: Graphical abstract illustrating the investigation of the non-toxic PPIs described in Chapter 5.[215]

Based on the favourable performance of non-toxic PPIs in Chapter 5, Chapter 6 reports the manufacture and performance evaluation of toxic PPIs containing 1080. The performance of the toxic PPIs is compared to the non-toxic PPIs, in both *in vitro* and *in vivo* experiments. Importantly, in this chapter, the ABS filament-based core of both PPIs, is found to significantly reduce implant stability *in vivo* and is identified as needing redesign. The development and performance evaluation of the toxic PPIs is published (**Figure 1.10**).[213]

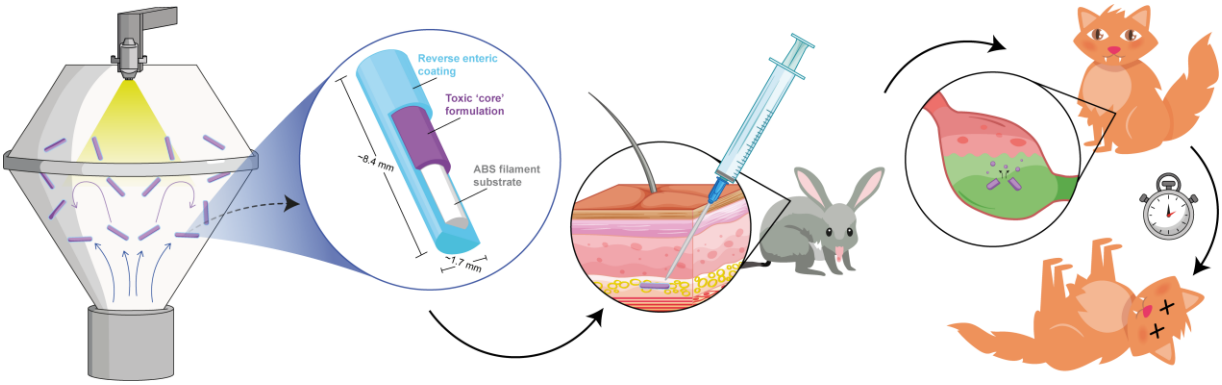


Figure 1.10: Graphical abstract illustrating the development of the toxic PPIs described in Chapter 6.[213]

Due to the poor performance of the toxic PPIs in Chapter 6, Chapter 7 proposes the replacement of the ABS filament core, with a soluble core, prepared *via* HME. A PEG-based formulation is employed to manufacture PPIs bearing a non-toxic and soluble core. The *in vitro* performance of the implants is evaluated and discussed in terms of the future development of the PPIs. The development and performance evaluation of the non-toxic PPIs manufactured using HME is published (**Figure 1.11**).[216]

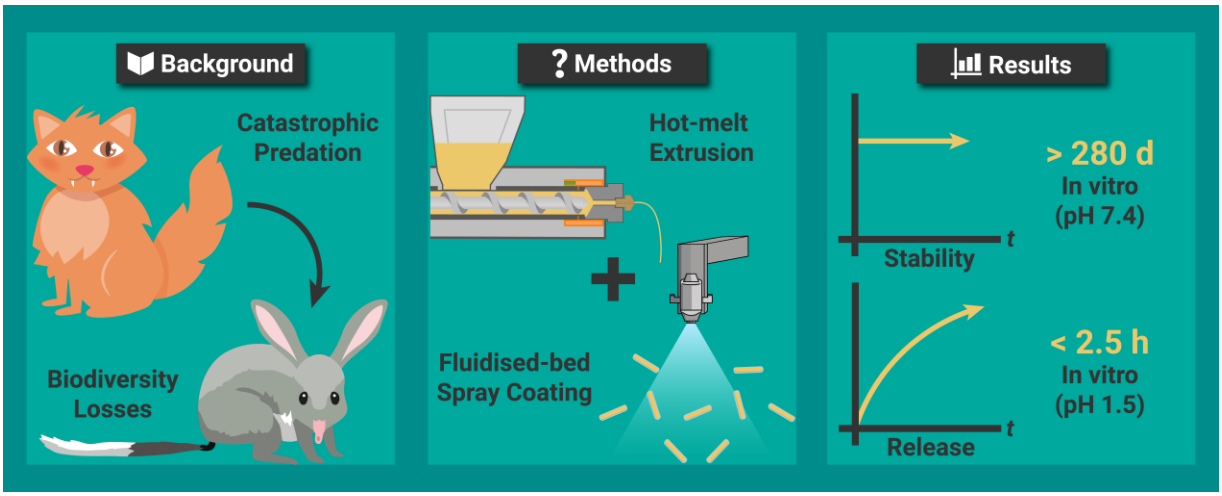


Figure 1.11: Graphical abstract illustrating the development of the non-toxic PPIs containing a HME core, and a fluidised-bed spray coated pH-responsive coating.[216]

In Chapter 8, a summary of the findings of this work is provided. These findings are discussed in the context of their ramifications for the future development of the PPI, and a series of future directions are proposed. Finally, the potential application of the current PPI designs and the pH-responsive copolymers developed in this work, within the conservation and pharmaceutical sectors, is discussed.

1.8 References

1. T. S. Doherty, A. S. Glen, D. G. Nimmo, E. G. Ritchie and C. R. Dickman, *Proc Natl Acad Sci U.S.A.*, 2016, **113**, 11261–11265.

2. A. M. Stobo-Wilson, B. P. Murphy, S. M. Legge, H. Caceres-Escobar, D. G. Chapple, H. M. Crawford, S. J. Dawson, C. R. Dickman, T. S. Doherty, P. A. Fleming, S. T. Garnett, M. Gentle, T. M. Newsome, R. Palmer, M. W. Rees, E. G. Ritchie, J. Speed, J.-M. Stuart, A. F. Suarez-Castro, E. Thompson, A. Tulloch, J. M. Turpin and J. C. Z. Woinarski, *Divers Distrib*, 2022, **28**, 976–991.

3. J. Q. Radford, J. C. Z. Woinarski, S. Legge, M. Baseler, J. Bentley, A. A. Burbidge, M. Bode, P. Copley, N. Dexter, C. R. Dickman, G. Gillespie, B. Hill, C. N. Johnson, J. Kanowski, P. Latch, M. Letnic, A. Manning, P. Menkhorst, N. Mitchell, K. Morris, K. Moseby, M. Page and J. Ringma, *Wildl Res*, 2018, **45**, 645–657.

4. J. C. Z. Woinarski, A. A. Burbidge and P. L. Harrison, *Proc Natl Acad Sci U.S.A.*, 2015, **112**, 4531–4540.

5. S. Legge, B. P. Murphy, H. McGregor, J. C. Z. Woinarski, J. Augusteyn, G. Ballard, M. Baseler, T. Buckmaster, C. R. Dickman, T. Doherty, G. Edwards, T. Eyre, B. A. Fancourt, D. Ferguson, D. M. Forsyth, W. L. Geary, M. Gentle, G. Gillespie, L. Greenwood, R. Hohnen, S. Hume, C. N. Johnson, M. Maxwell, P. J. McDonald, K. Morris, K. Moseby, T. Newsome, D. Nimmo, R. Paltridge, D. Ramsey, J. Read, A. Rendall, M. Rich, E. Ritchie, J. Rowland, J. Short, D. Stokeld, D. R. Sutherland, A. F. Wayne, L. Woodford and F. Zewe, *Biol Conserv*, 2017, **206**, 293–303.

6. B. P. Murphy, L.-A. Woolley, H. M. Geyle, S. M. Legge, R. Palmer, C. R. Dickman, J. Augusteyn, S. C. Brown, S. Comer, T. S. Doherty, C. Eager, G. Edwards, D. A. Fordham, D. Harley, P. J. McDonald, H. McGregor, K. E. Moseby, C. Myers, J. Read, J. Riley, D. Stokeld, G. J. Trewella, J. M. Turpin and J. C. Z. Woinarski, *Biol Conserv*, 2019, **237**, 28–40.

7. J. C. Z. Woinarski, B. P. Murphy, R. Palmer, S. M. Legge, C. R. Dickman, T. S. Doherty, G. Edwards, A. Nankivell, J. L. Read and D. Stokeld, *Wildl Res*, 2018, **45**, 247–266.

8. J. C. Z. Woinarski, B. P. Murphy, S. M. Legge, S. T. Garnett, M. J. Lawes, S. Comer, C. R. Dickman, T. S. Doherty, G. Edwards, A. Nankivell, D. Paton, R. Palmer and L. A. Woolley, *Biol Conserv*, 2017, **214**, 76–87.

9. C. J. A. Bradshaw, A. J. Hoskins, P. J. Haubrock, R. N. Cuthbert, C. Diagne, B. Leroy, L. Andrews, B. Page, P. Cassey, A. W. Sheppard and F. Courchamp, *NeoBiota*, 2021, **67**, 511–550.

10. P. Fisher, D. Algar, E. Murphy, M. Johnston and C. Eason, *Appl Anim Behav Sci*, 2015, **173**, 88–96.

11. P. E. S. Christensen, B. G. Ward and C. Sims, *Ecol Manag Restor*, 2013, **14**, 47–53.

12. B. G. Holt, J.-P. Lessard, M. K. Borregaard, S. A. Fritz, M. B. Araújo, D. Dimitrov, P.-H. Fabre, C. H. Graham, G. R. Graves, K. A. Jønsson, D. Nogués-Bravo, Z. Wang, R. J. Whittaker, J. Fjeldså and C. Rahbek, *Science*, 2012, **339**, 74–78.

13. *Nature like nowhere else. Activating nature-based tourism in South Australia*, Department of Environment, Water & Natural Resources and South Australian Tourism Commission, Adelaide, South Australia, 2017.

14. S. Mallick, M. Pauza, C. Eason, N. Mooney, R. Gaffney and S. Harris, *Wildl Res*, 2016, **43**, 140–152.

15. M. Gentle, J. Speed, B. L. Allen, S. Harris, H. Haapakoski and K. Bell, *Environ Sci Pollut Res*, 2017, **24**, 12338–12346.

16. G. Saunders, S. McLeod and B. Kay, *Wildl Res*, 2000, **27**, 129–135.

17. C. T. Eason, J. Ross and A. Miller, *N Z J Zool*, 2013, **40**, 217–225.

18. F. Courchamp, J.-L. Chapuis and M. Pascal, *Biol Rev*, 2003, **78**, 347–383.

19. S. Robinson and L. Gadd, *Pap Proc R Soc Tasman*, 2020, **154**, 47–50.

20. S. A. Robinson and G. R. Copson, *Ecol Manag Restor*, 2014, **15**, 34–40.

21. D. Algar, G. Angus and M. Onus, *J R Soc West Aust*, 2011, **94**, 439.

22. D. Algar, G. Angus, R. Brazell, C. Gilbert and G. Withnell, *J R Soc West Aust*, 2010, **93**, 133.

23. S. Robinson, L. Gadd, M. Johnston and M. Pauza, *N Z J Ecol*, 2015, **39**, 316–322.

24. J. Parkes, P. Fisher, S. Robinson and A. Aguirre-Muñoz, *N Z J Ecol*, 2014, **38**, 307–314.

25. K. J. Campbell, G. Harper, C. Hanson, D. Algar, B. Keitt and S. Robinson, in *Island invasives: Eradication and Management: Proceedings of the International Conference on Island Invasives*, IUCN, Centre for Biodiversity and Biosecurity, New Zealand, 2011, pp. 37–46

26. T. S. Doherty, C. R. Dickman, C. N. Johnson, S. M. Legge, E. G. Ritchie and J. C. Z. Woinarski, *Mammal Rev*, 2017, **47**, 83–97.

27. G. R. Saunders, M. N. Gentle and C. R. Dickman, *Mammal Rev*, 2010, **40**, 181–211.

28. K. E. Moseby, J. Stott and H. Crisp, *Wildl Res*, 2009, **36**, 422–435.

29. S. E. Allsop, S. J. Dundas, P. J. Adams, T. L. Kreplins, P. W. Bateman and P. A. Fleming, *Pac Conserv Biol*, 2017, **23**, 240–257.

30. J. Short, B. Turner, D. A. Risbey and R. Carnamah, *Wildl Res*, 1997, **24**, 703–714.

31. C. A. Marks, F. Busana and F. Gigliotti, *Wildl Res*, 1999, **26**, 101–109.

32. C. A. Marks, F. Gigliotti and F. Busana, *Wildl Res*, 2003, **30**, 601–609.

33. F. Busana, F. Gigliotti and C. A. Marks, *Wildl Res*, 1998, **25**, 209–215.

34. C. A. Marks and R. Wilson, *Wildl Res*, 2005, **32**, 151–156.

35. L. J. McLeod, G. R. Saunders and A. Miners, *Ecol Manag Restor*, 2011, **12**, 224–226.

36. T. S. Doherty, C. R. Dickman, C. N. Johnson, S. M. Legge, E. G. Ritchie and J. C. Z. Woinarski, *Mammal Rev*, 2016, **47**, 83–97.

37. B. Kay, E. Gifford, R. Perry and R. van de Ven, *Wildl Res*, 2000, **27**, 547–552.

38. T. Sharp, Model code of practice for the humane control of feral cats. Code of Practice, https://pestsmart.org.au/toolkit-resource/code-of-practice-feral-cats, (accessed 2022).

39. J. Short, B. Turner and D. Risbey, *Wildl Res*, 2002, **29**, 475–487.

40. P. J. S. Fleming, L. R. Allen, M. J. Berghout, P. D. Meek, P. M. Pavlov, P. Stevens, K. Strong, J. A. Thompson and P. C. Thomson, *Wildl Res*, 1998, **25**, 327–338.

41. K. E. Moseby and J. L. Read, *Biol Conserv*, 2006, **127**, 429–437.

42. K. E. Moseby, B. M. Hill and J. L. Read, *Austral Ecol*, 2009, **34**, 156–169.

43. P. J. de Tores and N. Marlow, in *Fencing for Conservation: Restriction of Evolutionary Potential or a Riposte to Threatening Processes?*, eds. M. J. Somers and M. Hayward, Springer New York, 2012, pp. 21–42.

44. K. J. Campbell, G. Harper, C. Hanson, D. Algar, B. Keitt and S. Robinson, in *Island invasives: Eradication and Management: Proceedings of the International Conference on Island Invasives*, IUCN, Centre for Biodiversity and Biosecurity, New Zealand, 2011, pp. 37–46

45. D. R. Spatz, N. D. Holmes, D. J. Will, S. Hein, Z. T. Carter, R. M. Fewster, B. Keitt, P. Genovesi, A. Samaniego, D. A. Croll, B. R. Tershy and J. C. Russell, *Sci Rep*, 2022, **12**, 13391.

46. E. A. Denny and C. Dickman, *Review of Cat Ecology and Management Strategies in Australia*, Invasive Animals Cooperative Research Centre, Canberra, 2010.

47. S. Legge, J. C. Z. Woinarski, A. A. Burbidge, R. Palmer, J. Ringma, J. Q. Radford, N. Mitchell, M. Bode, B. Wintle, M. Baseler, J. Bentley, P. Copley, N. Dexter, C. R. Dickman, G. R. Gillespie, B. Hill, C. N. Johnson, P. Latch, M. Letnic, A. Manning, E. E. McCreless, P. Menkhorst, K. Morris, K. Moseby, M. Page, D. Pannell and K. Tuft, *Wildl Res*, 2018, **45**, 627–644.

48. J. Woinarski, S. Ward, T. Mahney, J. Bradley, K. Brennan, M. Ziembicki and A. Fisher, *Wildl Res*, 2011, **38**, 307–322.

49. B. T. Lazenby, N. J. Mooney and C. R. Dickman, *Wildl Res*, 2015, **41**, 407–420.

50. S. Legge, J. C. Z. Woinarski, C. R. Dickman, B. P. Murphy, L.-A. Woolley and M. C. Calver, *Wildl Res*, 2020, **47**, 523–539.

51. A. Tomlinson, C. Marshall and C. Gooding, *J Dep Agric West Aust*, 1954, **3**, 82–87.

52. C. Marks, F. Gigliotti, F. Busana, M. Johnston and M. Lindeman, *Anim Welf*, 2004, **13**, 401–408.

53. N. J. Marlow, N. D. Thomas, A. A. E. Williams, B. Macmahon, J. Lawson, Y. Hitchen, J. Angus and O. Berry, *Ecol Manag Restor*, 2015, **16**, 131–141.

54. S. R. McLeod and G. Saunders, *Ecol Modell*, 2014, **273**, 1–10.

55. S. Comer, P. Speldewinde, C. Tiller, L. Clausen, J. Pinder, S. Cowen and D. Algar, *Sci Rep*, 2018, **8**, 5335.

56. J. C. McIlroy and D. R. King, *Wildl Res*, 1990, **17**, 11–13.

57. C. T. Eason and C. M. Frampton, *Wildl Res*, 1991, **18**, 445–449.

58. C. A. Marks, C. Hackman, F. Busana and F. Gigliotti, *Wildl Res*, 2000, **27**, 483–494.

59. J. C. McIlroy, *Wildl Res*, 1981, **8**, 385–399.

60. IUCN, The IUCN Red List of Threatened Species, http://www.iucnredlist.org/, (accessed 2018).

61. K. E. Moseby, J. L. Read, B. Galbraith, N. Munro, J. Newport and B. M. Hill, *Wildl Res*, 2011, **38**, 350–358.

62. R. J. Mead, A. J. Oliver, D. R. King and P. H. Hubach, *Oikos*, 1985, **44**, 55–60.

63. A. S. Glen, M. N. Gentle and C. R. Dickman, *Mammal Rev*, 2007, **37**, 191–205.

64. L. E. Twigg, G. R. Martin, A. F. Eastman, t. l. D. R. King and W. E. Kirkpatrick, *Aust J Zool*, 2003, **51**, 515–531.

65. L. E. Twigg and D. R. King, *Oikos*, 1991, **61**, 412–430.

66. J. C. McIlroy, *Wildl Res*, 1982, **9**, 505–517.

67. J. C. McIlroy, *Wildl Res*, 1983, **10**, 507–512.

68. J. C. McIlroy, *Wildl Res*, 1982, **9**, 487–503.

69. J. C. McIlroy, *N Z J Ecol*, 1983, **6**, 125–131.

70. J. C. McIlroy, D. R. King and A. J. Oliver, *Wildl Res*, 1985, **12**, 113–118.

71. J. C. McIlroy, *Wildl Res*, 1984, **11**, 373–385.

72. T. Buckmaster, C. R. Dickman and M. J. Johnston, *PLoS ONE*, 2014, **9**, e107788.

73. C. T. Eason, A. Miller, D. B. MacMorran and E. C. Murphy, *N Z J Ecol*, 2014, **38**, 177–188.

74. C. T. Eason, E. Murphy, S. Hix, R. Henderson and D. MacMorran, *Susceptibility of four bird species to para-aminopropiophenone,* Department of Conservation, Wellington, New Zealand, 2010.

75. P. J. Savarie, H. P. Pan, D. J. Hayes, J. D. Roberts, G. J. Dasch, R. Felton and E. W. Schafer, Jr., *Bull Environ Contam Toxicol*, 1983, **30**, 122–126.

76. G. E. Garrard, A. M. Kusmanoff, R. Faulkner, C. L. Samarasekara, A. Gordon, A. Johnstone, I. R. Peterson, N. Torabi, Y. Wang and S. A. Bekessy, *Wildl Res*, 2020, **47**, 698–708.

77. M. Sherley, *Anim Welf*, 2007, **16**, 449–458.

78. L. E. Twigg and R. W. Parker, *Anim Welf*, 2010, **19**, 249–263.

79. D. Algar and N. Burrows, *Conserv Sci West Aust*, 2004, **5**, 131.

80. R. Hohnen, J. Smith, J. Mulvaney, T. Evans and T. Mooney, *Wildl Res*, 2022, **49**, 637–645.

81. R. Palmer, H. Anderson, B. Richards, M. D. Craig and L. Gibson, *PLoS ONE*, 2021, **16**, e0251304.

82. M. Johnston, L. Bould, M. O'Donoghue, M. Holdsworth, P. Marmion, R. Bilney, A. Reside, D. Caldwell, R. Gaborov and T. Gentles, *Field efficacy of the Curiosity® bait for management of a feral cat population at Roxby Downs, South Australia*, Department of Environment and Primary Industries, Heidelberg, Victoria, 2014.

83. D. Algar, M. Johnston and S. Hilmer, in *Island invasives: Eradication and Management: Proceedings of the International Conference on Island Invasives*, IUCN, Centre for Biodiversity and Biosecurity, New Zealand, 2011, pp.10–16.

84. M. Johnston, D. Algar, M. O'Donoghue and J. Morris, in *Island invasives: Eradication and Management: Proceedings of the International Conference on Island Invasives*, IUCN, Centre for Biodiversity and Biosecurity, New Zealand, 2011, pp. 182–187.

85. C. Booth and J. Sampson, *1080: A Weighty Ethical Issue*, Invasive Species Council, Katoomba, 2020.

86. C. Eason, A. Miller, S. Ogilvie and A. Fairweather, *N Z J Ecol*, 2011, **35**, 1–20.

87. B. Warburton, C. Eason, P. Fisher, N. Hancox, B. Hopkins, G. Nugent, S. Ogilvie, T. A. A. Prowse, J. Ross and P. E. Cowan, *N Z J Zool*, 2022, **49**, 79–121.

88. C. T. Eason, E. C. Murphy, S. Hix and D. B. Macmorran, *Integr Zool*, 2010, **5**, 31–36.

89. M. Johnston, D. Algar, M. O'Donoghue, J. Morris, T. Buckmaster and J. Quinn, *Wildl Res*, 2020, **47**, 686–697.

90. L. McLeod and G. Saunders, *Pesticides used in the management of vertebrate pests in Australia: A review*, NSW Department of Primary industries, 2013.

91. T. S. Jessop, M. R. Kearney, J. L. Moore, T. Lockwood and M. Johnston, *Biol Invasions*, 2013, **15**, 1653–1663.

92. M. Johnston, F. Gigliotti and J. Trezise, *Vic Nat*, 2019, **136**, 203–207.

93. J. C. McIlroy, *Wildl Res*, 1986, **13**, 39–48.

94. J. C. McIlroy, *Proc Vertebr Pest Conf*, 1992, **54**, 356–359.

95. S. T. Lee, D. Cook, J. A. Pfister, J. G. Allen, S. M. Colegate, F. Riet-Correa and C. M. Taylor, *J Agric Food Chem*, 2014, **62**, 7345–7354.

96. C. A. Hetherington, D. Algar, H. Mills and R. Bencini, *Wildl Res*, 2007, **34**, 467–471.

97. D. Algar, G. J. Angus, M. Williams and A. Mellican, *Conserv Sci West Aust*, 2007, **6**, 109–149.

98. D. Algar, N. Hamilton, M. Onus, S. Hilmer, S. Comer, C. Tiller, L. Bell and J. Pinder, *Field trial to compare baiting efficacy of Eradicat® and Curiosity® baits*, Department of Environment and Conservation, 2018.

99. A. Tomlinson and C. Gooding, *J Dep Agric West Aust,* 1971, **12**, 268–270.

100. W. Tourtellotte and J. Coon, *J Pharmacol Exp Ther*, 1951, **101**, 82–91.

101. E. R. Kalmbach, *Science*, 1945, **102**, 232–233.

102. G. R. Martin and L. E. Twigg, *Wildl Res*, 2002, **29**, 75–83.

103. G. Northcott, D. Jensen, L. Ying and P. Fisher, *Environ Toxicol Chem*, 2014, **33**, 1048–1058.

104. D. H. Wong, W. E. Kirkpatrick, J. E. Kinnear and D. R. King, *Wildl Res*, 1991, **18**, 539–545.

105. B. Reddiex, D. M. Forsyth, E. McDonald-Madden, L. D. Einoder, P. A. Griffioen, R. R. Chick and A. J. Robley, *Wildl Res*, 2006, **33**, 691–709.

106. B. Hardman, D. Moro and M. Calver, *Ecol Manag Restor*, 2016, **17**, 152–158.

107. K. Moseby, D. Peacock and J. Read, *Biol Conserv*, 2015, **191**, 331–340.

108. K. E. Moseby, J. L. Read, D. C. Paton, P. Copley, B. M. Hill and H. A. Crisp, *Biol Conserv*, 2011, **144**, 2863–2872.

109. K. Tuft, T. May, E. Page and S. Legge, *Translocation of the pale field rat (Rattus tunneyi) to Wongalara (NT) from Mornington (WA)*, Australian Wildlife Conservancy, 2014.

110. D. Gibson, G. Lundie-Jenkins, D. Langford, J. Cole, D. Clarke and K. Johnson, *Aust Mammal*, 1994, **17**, 103–106.

111. J. Short, S. D. Bradshaw, J. Giles, R. I. T. Prince and G. R. Wilson, *Biol Conserv*, 1992, **62**, 189–204.

112. J. Short, *Wildl Res*, 2016, **43**, 38–50, 13.

113. C. N. Greenwell, M. C. Calver and N. R. Loneragan, *Animals*, 2019, **9**, 445.

114. J. Read, D. Peacock, A. Wayne and K. Moseby, *Wildl Res*, 2016, **42**, 689–696.

115. C. A. Marks, M. J. Johnston, P. M. Fisher, K. Pontin and M. J. Shaw, *J Wildl Manage*, 2006, **70**, 1119–1124.

116. A. Kumar and J. Pillai, in *Nanostructures for the Engineering of Cells, Tissues and Organs*, Elsevier, 2018, pp. 473–511.

117. E. M. Martín del Valle, M. A. Galan and R. G. Carbonell, *Ind Eng Chem Res,* 2009, **48**, 2475–2486.

118. Y. Fumimoto, A. Matsuyama, H. Komoda, H. Okura, C. M. Lee, A. Nagao, T. Nishida, T. Ito and Y. Sawa, *Tissue Eng Part C Methods*, 2009, **15**, 437–444.

119. M. Mohamed, G. Borchard and O. Jordan, *J Drug Deliv Sci Technol*, 2012, **22**, 393–408.

120. G. Schmidmaier, M. Lucke, B. Wildemann, N. P. Haas and M. Raschke, *Injury*, 2006, **37**, S105–S112.

121. N. Rajgor, M. Patel and V. Bhaskar, *Surg Neurol Int*, 2011, **2**, 473–511.

122. G. Odian, *Principles of polymerization*, John Wiley & Sons, 2004.

123. E. Vivaldo-Lima and E. Saldívar-Guerra, *Handbook of polymer synthesis, characterization, and processing*, John Wiley & Sons, 2013.

124. W.-F. Su, *Principles of polymer design and synthesis*, Springer, 2013.

125. H. R. Kricheldorf, O. Nuyken and G. Swift, *Handbook of polymer synthesis: second edition*, CRC Press, 2nd edn., 2004.

126. T. Meyer and J. T. Keurentjes, *Handbook of polymer reaction engineering*, Wiley-VCH Verlag, 2005.

127. C. S. Brazel and S. L. Rosen, *Fundamental principles of polymeric materials*, John Wiley & Sons, 2012.

128. G. Moad and D. H. Solomon, *The chemistry of radical polymerization*, Elsevier, 2006.

129. C. E. Carraher Jr, *Introduction to polymer chemistry*, CRC Press, 2017.

130. G. Wypych, *Handbook of plasticizers*, ChemTec Publishing, 4th edn., 2023.

131. R. Pan, R. Shanks, Q. Yang and H. Luo, *Comput Mater Sci*, 2018, **152**, 78–84.

132. M. L. Williams, R. F. Landel and J. D. Ferry, *J Am Chem Soc*, 1955, **77**, 3701–3707.

133. J. Kern and K. R. Darby, *The technology of plasticisers*, John Wiley & Sons, 1982.

134. J. D. Menczel and R. B. Prime, *Thermal analysis of polymers: fundamentals and applications*, Wiley, 2009.

135. C. M. Hansen, *Hansen solubility parameters: a user's handbook*, CRC Press, 2007.

136. E. Langer, K. Bortel, M. Lenartowicz-Klik and S. Waskiewicz, *Plasticizers derived from post-consumer PET*, Elsevier, 2019.

137. R. Sothornvit and J. M. Krochta, in *Innovations in Food Packaging*, ed. J. H. Han, Academic Press, London, 2005, pp. 403–433.

138. M. R. Aguilar and J. S. Román, *Smart polymers and their applications*, Woodhead Publishing, 2019.

139. G. Kocak, C. Tuncer and V. Bütün, *Polymer Chemistry*, 2017, **8**, 144–176.

140. X. Li, H. Yang, L. Xu, X. Fu, H. Guo and X. Zhang, *Macromol. Chem. Phys.*, 2010, **211**, 297–302.

141. L. I. Atanase and G. Riess, *J. Colloid Interface Sci.*, 2013, **395**, 190–197.

142. T. J. Martin, K. Procházka, P. Munk and S. E. Webber, *Macromolecules*, 1996, **29**, 6071–6073.

143. J.-F. Gohy, S. Mores, S. K. Varshney, J.-X. Zhang and R. Jérôme, *e-Polymers*, 2002, **2**.

144. K. Brewer, F. Bai and A. Blencowe, *Pharmaceutics*, 2023, **15**, 977.

145. L. A. Felton and S. C. Porter, *Expert Opin Drug Deliv*, 2013, **10**, 421–435.

146. E. T. Cole, R. A. Scott, A. L. Connor, I. R. Wilding, H.-U. Petereit, C. Schminke, T. Beckert and D. Cadé, *Int J Pharm*, 2002, **231**, 83–95.

147. C. N. Patra, R. Priya, S. Swain, G. Kumar Jena, K. C. Panigrahi and D. Ghose, *Future J Pharm Sci*, 2017, **3**, 33–45.

148. D. Aframian, T. Davidowitz and R. Benoliel, *Oral Dis*, 2006, **12**, 420–423.

149. M. G. Kulkarni and A. R. Menjoge, *pH sensitive polymer and process for preparation thereof,* United States, Patent No., US7531612B2, 2009.

150. K. Nollenberger and J. Albers, *Int J Pharm*, 2013, **457**, 461–469.

151. Y. Georgieva, M. Kassarova, V. Kokova, E. Apostolova and B. Pilicheva, *Pharmazie*, 2020, **75**, 61–69.

152. A. Lopalco, N. Denora, V. Laquintana, A. Cutrignelli, M. Franco, M. Robota, N. Hauschildt, F. Mondelli, I. Arduino and A. Lopedota, *Int J Pharm*, 2020, **574**, 118922.

153. J. Breitkreutz, M. Bornhöft, F. Wöll and P. Kleinebudde, *Eur J Pharm Biopharm*, 2003, **56**, 247–253.

154. H. Wang, N. Dumpa, S. Bandari, T. Durig and M. A. Repka, *AAPS PharmSciTech*, 2020, **21**, 243.

155. C. S. Leopold and D. Eikeler, *J Drug Target*, 1998, **6**, 85–94.

156. J. Walsh, S. R. Ranmal, T. B. Ernest and F. Liu, *Int J Pharm*, 2018, **536**, 547–562.

157. D. Khan, D. Kirby, S. Bryson, M. Shah and A. Rahman Mohammed, *Int J Pharm*, 2022, **616**, 121501.

158 W. Brniak, E. Maślak and R. Jachowicz, *Eur J Pharm Sci*, 2015, **75**, 81–90.

159. D. Bora, P. Borude and K. Bhise, *AAPS PharmSciTech*, 2008, **9**, 1159–1164.

160. P. C. Kayumba, N. Huyghebaert, C. Cordella, J. D. Ntawukuliryayo, C. Vervaet and J. P. Remon, *Eur J Pharm Biopharm*, 2007, **66**, 460–465.

161. A. Chivate, V. Sargar, P. Nalawade and V. Tawde, *Drug Dev Ind Pharm*, 2013, **39**, 1091–1097.

162. M. Wesoły, M. Zabadaj, A. Amelian, K. Winnicka, W. Wróblewski and P. Ciosek, *Sens Actuators B Chem*, 2017, **238**, 1190–1198.

163. A. Dashevskiy, V. Mohylyuk, A. R. Ahmed, K. Kolter, F. Guth and R. Bodmeier, *Drug Dev Ind Pharm*, 2017, **43**, 1548–1556.

164. M. Xu, P. W. S. Heng and C. V. Liew, *Expert Opin Drug Deliv*, 2015, **12**, 1597–1606.

165. M. Ghimire, Z. N. Mahmoudi, J. Teckoe and A. Rajabi-Siahboomi, *Int J Pharm*, 2018, **536**, 498.

166. V. Dueik and L. L. Diosady, *J Food Process Eng*, 2017, **40**, e12376.

167. L. A. Felton, *Drug Dev Ind Pharm*, 2018, **44**, 1049–1055.

168. P. Tyagi, K. S. Salem, M. A. Hubbe and L. Pal, *Trends in Food Sci Technol*, 2021, **115**, 461–485.

169. N. Jadhav, J. Byrom, A. Suryawanshi and V. Gelling, in *Active Protective Coatings: New-Generation Coatings for Metals*, eds. A. E. Hughes, J. M. C. Mol, M. L. Zheludkevich and R. G. Buchheit, Springer Netherlands, 2016, pp. 299–312.

170. F. N. Jones, M. E. Nichols and S. P. Pappas, *Organic coatings: science and technology*, John Wiley & Sons, 2017.

171. R. Wilson, S. C. George, A. K. S and S. Thomas, in *Transport Properties of Polymeric Membranes*, eds. S. Thomas, R. Wilson, A. K. S and S. C. George, Elsevier, 2018, pp. 3–13.

172. Q. Yang, F. Yuan, L. Xu, Q. Yan, Y. Yang, D. Wu, F. Guo and G. Yang, *Pharmaceutics*, 2019, **11**, 436.

173. E. Mwesigwa, G. Buckton and A. W. Basit, *Drug Dev Ind Pharm*, 2005, **31**, 959–968.

174. N. S. Sangaj and V. C. Malshe, *Prog Org Coat*, 2004, **50**, 28–39.

175. H. Sumitomo and K. Hashimoto, *Polymer Membranes (Advances in Polymer Science, 64)*, Springer-Verlag, 1985.

176. O. Bley, J. Siepmann and R. Bodmeier, *Eur J Pharm Biopharm*, 2009, **73**, 146–153.

177. R. E. Kirk, D. F. Othmer, J. I. Kroschwitz, M. Howe-Grant, *Kirk-Othmer Encyclopedia of Chemical Technology: Volume 1 - A to Alkaloids*, John Wiley and Sons, New York, 4 edn., 1996.

178. L. A. Felton, *Int J Pharm*, 2013, **457**, 423–427.

179. K. H. Bauer, *Coated Pharmaceutical Dosage Forms: Fundamentals, Manufacturing Techniques, Biopharmaceutical Aspects, Test Methods, and Raw Materials*, CRC Press, 1998.

180. P. D. Nadkarni, D. O. Kildsig, P. A. Kramer and G. S. Banker, *J Pharm Sci*, 1975, **64**, 1554–1557.

181. L. A. Felton and J. W. McGinity, *Eur J Pharm Biopharm*, 1999, **47**, 3–14.

182. P. A. Steward, J. Hearn and M. C. Wilkinson, *Adv Colloid Interface Sci*, 2000, **86**, 195–267.

183. A. R. Nair, Y. D. Lakshman, V. S. K. Anand, K. S. N. Sree, K. Bhat and S. J. Dengale, *AAPS PharmSciTech*, 2020, **21**, 309.

184. K.-S. Seo, R. Bajracharya, S. H. Lee and H.-K. Han, *Pharmaceutics*, 2020, **12**, 853.

185. E. Teunou and D. Poncelet, *J Food Eng*, 2002, **53**, 325–340.

186. A. M. Mehta, *Processing and equipment considerations for aqueous coatings*, CRC Press, 3rd edn., 2008.

187. M. A. Repka, S. K. Battu, S. B. Upadhye, S. Thumma, M. M. Crowley, F. Zhang, C. Martin and J. W. McGinity, *Drug Dev Ind Pharm*, 2007, **33**, 1043–1057.

188. M. Crowley, F. Zhang, M. Repka, S. Thumma, S. Upadhye, S. K. Battu, J. McGinity and C. Martin, *Drug Dev. Ind. Pharm.*, 2007, **33**, 909–926.

189. S. Tambe, D. Jain, Y. Agarwal and P. Amin, *J Drug Deliv Sci Technol*, 2021, **63**, 102452.

190. J. Breitkreutz, F. El-Saleh, C. Kiera, P. Kleinebudde and W. Wiedey, *Eur J Pharm Biopharm*, 2003, **56**, 255–260.

191. M. A. Repka, S. Bandari, V. R. Kallakunta, A. Q. Vo, H. McFall, M. B. Pimparade and A. M. Bhagurkar, *Int J Pharm*, 2018, **535**, 68–85.

192. O. Cantin, F. Siepmann, F. Danede, J. F. Willart, Y. Karrout and J. Siepmann, *J Drug Deliv Sci Technol*, 2016, **36**, 130–140.

193. M. Maniruzzaman, J. S. Boateng, B. Z. Chowdhry, M. J. Snowden and D. Douroumis, *Drug Dev Ind Pharm*, 2014, **40**, 145–156.

194. M. Fukuda, N. A. Peppas and J. W. McGinity, *J Control Release*, 2006, **115**, 121–129.

195. E. Mehuys, J.-P. Remon and C. Vervaet, *Eur J Pharm Sci*, 2005, **24**, 207–212.

196. M. M. Crowley, B. Schroeder, A. Fredersdorf, S. Obara, M. Talarico, S. Kucera and J. W. McGinity, *Int J Pharm*, 2004, **269**, 509–522.

197. C. Dharmayanti, T. A. Gillam, D. B. Williams and A. Blencowe, *Polymers*, 2020, **12**, 2930.

198. M. B. Pimparade, A. Vo, A. S. Maurya, J. Bae, J. T. Morott, X. Feng, D. W. Kim, V. I. Kulkarni, R. Tiwari, K. Vanaja, R. Murthy, H. N. Shivakumar, D. Neupane, S. R. Mishra, S. N. Murthy and M. A. Repka, *Eur J Pharm Biopharm*, 2017, **119**, 81–90.

199. A. Gryczke, S. Schminke, M. Maniruzzaman, J. Beck and D. Douroumis, *Colloids Surf B*, 2011, **86**, 275–284.

200. A. K. Vynckier, L. Dierickx, L. Saerens, J. Voorspoels, Y. Gonnissen, T. De Beer, C. Vervaet and J. P. Remon, *Int J Pharm*, 2014, **464**, 65–74.

201. N. Jedinger, S. Schrank, J. M. Fischer, K. Breinhälter, J. Khinast and E. Roblegg, *AAPS PharmSciTech*, 2016, **17**, 68–77.

202. J. Zhang, X. Feng, H. Patil, R. V. Tiwari and M. A. Repka, *Int J Pharm*, 2017, **519**, 186–197.

203. A. Isreb, K. Baj, M. Wojsz, M. Isreb, M. Peak and M. A. Alhnan, *Int J Pharm*, 2019, **564**, 98–105.

204. J. dos Santos, G. S. da Silva, M. C. Velho and R. C. Beck, *Pharmaceutics*, 2021, **13**, 1424.

205. L. Viidik, J. Vesala, R. Laitinen, O. Korhonen, J. Ketolainen, J. Aruväli, K. Kirsimäe, K. Kogermann, J. Heinämäki, I. Laidmäe and T. Ervasti, *Eur J Pharm Sci*, 2021, **158**, 105619.

206. O. Cantin, F. Siepmann, J. F. Willart, F. Danede, J. Siepmann and Y. Karrout, *J Drug Deliv Sci Technol*, 2021, **61**, 102238.

207. S. Omari, E. A. Ashour, R. Elkanayati, M. Alyahya, M. Almutairi and M. A. Repka, *J Drug Deliv Sci Technol*, 2022, **74**, 103505.

208. O. A. Abu-Diak, D. S. Jones and G. P. Andrews, *J Pharm Sci*, 2012, **101**, 200–213.

209. S. Funk, M. M. Miller, D. R. Mishell, D. F. Archer, A. Poindexter, J. Schmidt and E. Zampaglione, *Contraception*, 2005, **71**, 319–326.

210. B. J. A. Furra and F. G. Hutchinsonb, *J Control Release*, 1992, **21**, 117–127.

211. N. J. London, A. Chiang and J. A. Haller, *Adv Ther*, 2011, **28**, 351–366.

212. J. A. H. van Laarhoven, M. A. B. Kruft and H. Vromans, *Int J Pharm*, 2002, **232**, 163–173.

213. K. Brewer, T. J. McWhorter, K. Moseby, J. L. Read, D. Peacock and A. Blencowe, *Polymers*, 2023, **15**, 878.

214. K. Brewer and A. Blencowe, *Pharmaceutics*, 2023, **15**.

215. K. Brewer, T. J. McWhorter, C. Sloper, K. Moseby, J. L. Read, D. Peacock and A. Blencowe, *ACS Appl Polym Mater*, 2022, **4**, 6687–6699.

216. K. Brewer, T. J. McWhorter, K. Moseby, J. L. Read, D. Peacock and A. Blencowe, *J Drug Deliv Sci Technol*, 2023, 104277.

Chapter 2: Scientec Research Pty Ltd and the Hard-Shell Delivery Vehicle — A State of the Art

2.1 Overview

In Chapter 2, the hard-shell delivery vehicle (HSDV) a state-of-the-art pH-responsive poison delivery technology used in poison baits, to control feral cats, is described. Being the only comparable technology to the proposed population protecting implant (PPI), a critical evaluation of the HSDV and several derivative designs, is provided in collaboration with the company responsible for their development — Scientec Research Pty Ltd (hereafter referred to as Scientec). The intrabatch variation of the HSDV samples is interrogated using a dimensional analysis and optical microscopy. Whereas the *in vitro* stability and release properties of the HSDVs are evaluated in the context of their performance as implants, using a hydrogel model of the subcutaneous environment, and a simulated gastric environment, respectively. The HSDVs were found to exhibit poor stability and release properties, due to a combination of the poor sealing afforded by the manufacturing method employed by Scientec, and the polymer coatings used in their manufacture. While these results demonstrated that the HSDVs were unsuitable for use *in vivo*, they also highlighted the need for the development of pH-responsive coatings with low solubility above gastric pH, and a manufacturing method that eliminated sealing defects.

2.2 Introduction

As discussed previously, there is a dearth of pH-responsive polymers that exhibit appropriate pH-responsivity for use as subcutaneous implants. This is possibly due to the few applications requiring such properties, and a resultant lack of research interest. We argue that long-term subcutaneous stability and rapid release within the gastric environment cannot be achieved *via* delivery systems based on current pH-responsive polymers, including both those reported in the literature and those that are commercially available. Accordingly, we sought to evaluate the performance of

technologies that use current pH-responsive polymers, that are in development for similar applications as the PPI.

Hisstory® and Curiosity® baits were developed to afford improved control of feral cats compared to conventional poison baits. Generally, poison baits are small sausage-like pieces of meat that are injected with an aqueous solution of sodium fluoroacetate (1080).[1] In contrast, Hisstory® and Curiosity® baits utilise the same bait medium but contain a HSDV[2–5] consisting of a poison capsule containing a lethal dose of either 1080 (Hisstory®) or para-aminopropiophenone (PAPP, Curiosity), with rhodamine B (RhB), and encapsulated in a pH-responsive polymer. Whilst the same bait medium is used, baits are buffered to pH 7.5 prior to HSDV insertion.[6] The HSDV is intended to avoid the dispersal of the toxicant throughout the bait and ensure the entire dose of 1080 (4.5 mg) or PAPP (80 mg) is ingested by the feral cat and rapidly released in the gastric environment.

In addition, the HSDV exploits the differences in feeding behaviour between feral cats and native Australian animals, to reduce non-target uptake.[2, 7–9] Feral cats generally tear food items into swallowable portions and are unlikely to detect — nor then reject — the HSDV. For many other animals, feeding is more laborious and food items are reduced to much smaller portions with extensive chewing, thereby greatly increasing the chances of detecting and rejecting the HSDV. Curiosity baits have undergone considerable field testing to determine their effectiveness and safety (i.e., for non-target species), and are registered by the Australian Pesticides and Veterinary Medicines Authority (APVMA) for use throughout Australia (APVMA Product No. 81864).[3, 6, 10–19] In contrast, Hisstory® baits are at an earlier stage of development and so are not currently registered but have been field tested.[4]

2.3 HSDV Samples Received for Testing

There is a clear parallel between the HSDV used in the Hisstory® and Curiosity® baits, and the proposed PPI. Both bear pH-responsive coatings designed to afford insolubility/stability in one medium (i.e., a meat bait and the subcutis of a native animal, respectively), and rapid dissolution in the gastric environment of a feral cat.

To the author's knowledge, the HSDV was the only technology both commercially available and in development, with similarity to the PPI, and so was investigated further. The performance of the HSDVs was investigated in collaboration with Scientec — the Australian biotech company responsible for its research and development. Scientec provided samples of the original, spherical-shaped HSDV (HSDV-A, **Figure 2.1a**) and a new cylindrical-shaped design (HSDV-B, **Figure 2.1b**), that both contained 1080 (i.e., a Hisstory® bait HSDV). HSDV-A and HSDV-B were both manufactured with Eudragit® E 100, a commercially available reverse enteric copolymer (soluble pH < 5), using the same general composition and processes used in the production of the Curiosity® bait HSDVs. The HSDV-B design was intended to enable the evaluation of the suitability of both Eudragit® E 100 and Scientec's proprietary hot-melt extrusion (HME)-based manufacturing process, to the production of implantable HSDVs for use as PPIs.[20]

In addition, three additional cylindrical-shaped HSDVs (HSDV-C–E) were provided that utilised the commercially available polyesters Resomer® L 206 S and L210 S, and Biopol® (**Figure 2.1c–e**). In the context of implants, polyester coatings could be disrupted *via* enzymatic degradation (i.e., biodegradation) or acid-catalysed hydrolysis (i.e., of the ester groups). Scientec had previously developed delayed-release implants — called "Tik Toks" — bearing a polyester coating. Designed to be subcutaneously implanted into dingoes, the coating on the Tik Tok implants was engineered to fail after a predetermined period, and release an encapsulated, lethal dose of 1080 within the subcutaneous environment, to kill the implanted dingoes.[21] It was hypothesised that dingoes bearing Tik Toks could be used to eradicate a population of feral goats on Pelorus, a small island off the north Queensland coast. Following implantation and eradication of the feral goats, if the dingoes could not be removed *via* other control methods, the implants would fail, and prevent the translocated dingoes from depredating native wildlife on the island.[21] Ultimately, the Pelorus experiment was ended prematurely, due to significant political and public criticism,[22, 23] and it is unclear whether the Tik Tok implants were effective. The Tik Tok implants were designed to fail after ~ 600 d but were still 'active' after ~ 720 d.[21] Further monitoring of the implanted dingoes was not possible due to the battery failure of the global positioning satellite (GPS) collars used to track the dingoes during

the experiment. Evaluation of the polyester HSDVs in this work, would — in part — indicate whether dissolution within the gastric environment was possible for these common commercially available polymers.

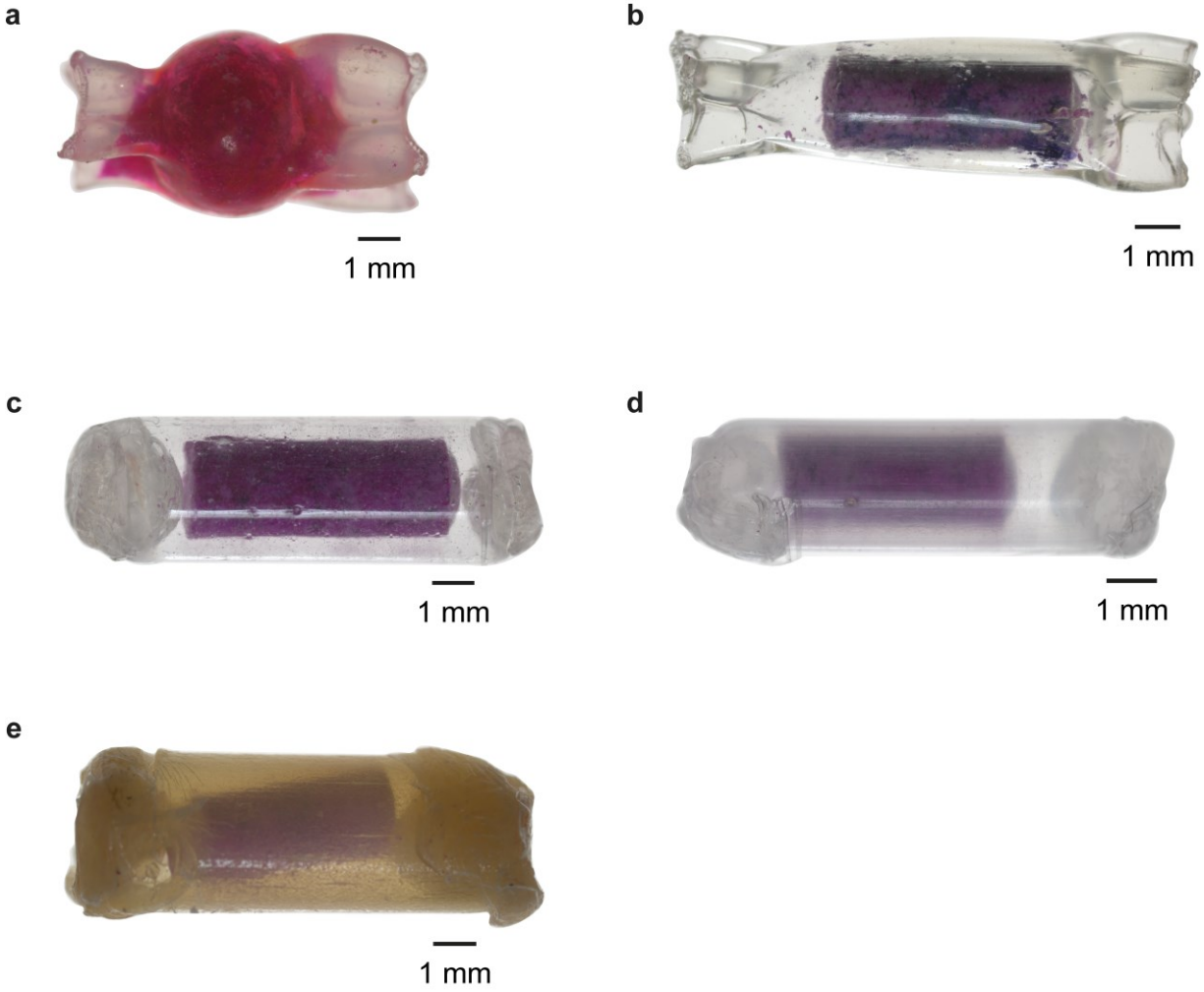


Figure 2.1: Representative images of the HSDVs supplied by Scientec: a) HSDV-A, b) HSDV-B, c) HSDV-C, d) HSDV-D, and e) HSDV-E.

2.4 Results and Discussion

2.4.1 Critical Evaluation of HSDV Design and Manufacture

A summary of the properties of the tested HSDVs are provided in **Table 2.1**. All the HSDVs were manufactured using a proprietary HME process developed by Scientec.[20, 24] This process is described as involving the HME of the coating material, during which a compressed core 'pellet' is inserted, followed by the sealing, and cutting of each end using a heated press. As shown in **Figure 2.1**, this process afforded HSDVs with 'pinched' (e.g., HSDV-A and B) or 'curved' (e.g., HSDV-C–E) ends, and spherical (HSDV-A) or cylindrical (HSDV-B–E) shaped outer morphologies, depending on the shape of the heated press that was used.

The HSDVs were generally found to exhibit the most intrabatch variability regarding their lengths, as indicated by the higher percentage relative standard deviation (%RSD) values for the length measurements, compared to the diameter and mass. However, when inspected qualitatively, the sealed ends of the HSDVs were found to be highly inconsistent, in length, width and shape, which likely contributed to the higher %RSD values of the HSDV length measurements. The inconsistent end-shapes of the HSDVs were partially obfuscated in the recorded measurements, as the %RSD values of the width measurements were comparatively lower. The measurements were made at the midpoint (diameter) and across the middle of the ends (length) of the HSDVs and did not account for the irregularities in HSDV shape. In addition, several of the received HSDVs exhibited broken cores (though intact polymer coatings), and core material compressed between the pinched ends. Together, these observations suggested that the ends of the sealed HSDVs presented a potentially significant quality control issue. If the sealing of the coating was ineffective for a HSDV, it could fail *in vivo*, and pose a risk to the implanted animal if they were to be used as PPIs.

Table 2.1: Summary of HSDV designs and properties.

HSDV Design	Core	1080 (mg)	Core Mass (mg) [a]	Length (mm) [b]	Width (mm) [b]	Mass (mg) [b]	pH-Responsive Polymer	Polymer Mass (mg) [c]
A (n = 20)	1080:Lactose:RhB 15:150:1	4.5	49.8	8.28 ± 0.4 (4.8)	4.61 ± 0.3 (6.5)	81.48 ± 2.4 (2.9)	Eudragit® E 100	31.7
B (n = 27)	1080:Lactose:RhB 15:150:1	3.0	33.2	13.78 ± 0.3 (2.2)	3.72 ± 0.1 (2.7)	106.54 ± 3.5 (3.3)	Eudragit® E 100	73.3
C (n = 8)	1080:Lactose:RhB 15:150:1	4.5	49.8	11.55 ± 1.1 (9.5)	3.05 ± 0.1 (3.3)	77.64 ± 6.4 (8.2)	Resomer® L 206 S	27.8
D (n = 13)	1080:Lactose:RhB 15:150:1	4.5	49.8	12.55 ± 0.9 (7.2)	3.21 ± 0.1 (3.1)	95.42 ± 7.4 (7.8)	Resomer® L L210 S	45.6
E (n = 3)	1080:Lactose:RhB 15:150:1	4.5	49.8	11.59 ± 1.7 (14.7)	5.10 ± 0.2 (3.9)	151.07 ± 19.4 (12.8)	Biopol	101.3

[a] Determined from the mass ratios of the core components and the quoted mass of 1080 per HSDV. [b] Values represented as mean ± std. dev. (%RSD).

[c] Determined from the core mass and HSDV total mass values.

The overall sizes and shapes of the HSDVs, (except for HSDV-A) were generally akin to a standard radiofrequency identification (RFID) microchip (2.12 mm diameter × 12 mm length). However, the diameters of the HSDVs were generally 1.5–2.5× greater, and weighed 80–150 mg. It is possible that these dimensions could preclude their use as subcutaneous implants for some small mammals. The thicknesses of the polymer coatings were not interrogated, though qualitatively the coatings appeared to be 0.5–1 mm thick. It is likely that the HME process limited the manufacture of the HSDVs to those with coatings > 0.5 mm in thickness, due to the challenges inherent to the co-axial extrusion of polymeric materials.

2.4.2 HSDV *In Vitro* Performance Evaluation

The coatings used in HSDV-A and B were manufactured from Eudragit® E 100, which is a pH-responsive polymer often employed in taste-masking coatings for pharmaceutical formulations as it exhibits dissolution at pH < 5 and swelling and permeability at pH > 5.[25, 26] The pH-responsiveness of Eudragit® E 100 and its commercial availability make it an attractive choice for poison encapsulation in both the HSDV and PPI. HSDV-A and B were subjected to *in vitro* experiments evaluating their stability and release properties. The release properties of the HSDVs were investigated in a pH 1.5 (37 °C) solution, to mimic the gastric environment of a feral cat. The dissolution of the Eudragit® E 100 coatings and subsequent release of the HSDV core contents, was determined qualitatively *via* the observed release of RhB. HSDV-A samples (n = 3) were found to begin release within 3.5 ± 0.4 min at pH 1.5 (37 °C), with release completed following 37.0 ± 4.2 min (**Figure 2.2a**). For the HSDV-B samples (n = 2) the initial release time was found to be 29.3 ± 9.3 min, with release completed following 148.0 ± 17.0 min. A third HSDV-B sample was tested (total n = 3), that only began releasing at 208.5 min, failed to complete release within a further 4 h, and was only found to have completed release after 16 h (i.e., complete release between 4–16 h) (**Figure 2.2b**).

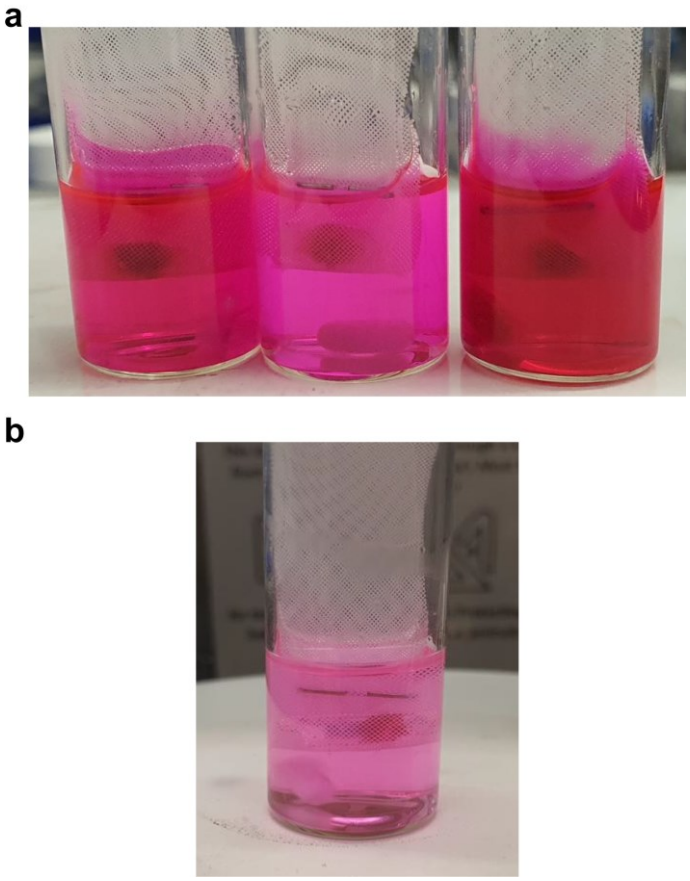


Figure 2.2: Example images of RhB release for a) HSDV-A after 10 min, and b) HSDV-B after 4 h, in a pH 1.5 (37 °C) release solution. Note the implants were removed from the 37 °C sample oven prior to imaging.

Overall, the HSDV-A and B samples were mostly found to complete release within the gastric half-emptying time (GET) of a feral cat (~ 2.5–4 h).[27] However, the delayed release (both initial and complete) of one HSDV-B sample was outside of the GET of a feral cat and was indicative of considerable intrabatch variation amongst the HSDV-B samples.

The stabilities of the HSDVs were investigated in a hydrogel model of the subcutaneous environment, prepared from 25% $w.w^{-1}$ Pluronics F127 (phosphate-buffered saline (PBS) pH 7.4, 37 °C). Failure was determined by the presence of RhB in the hydrogel. HSDV-A exhibited the poorest stability, with failure detected in all samples within 16 h (**Figure 2.3a**). In comparison, all HSDV-B samples failed within 10–17 d (**Figure 2.3b**), and therefore exhibited slightly better stability. In addition, all HSDV-B samples exhibited significant swelling during stability testing, which generally occurred within 2–3 d.

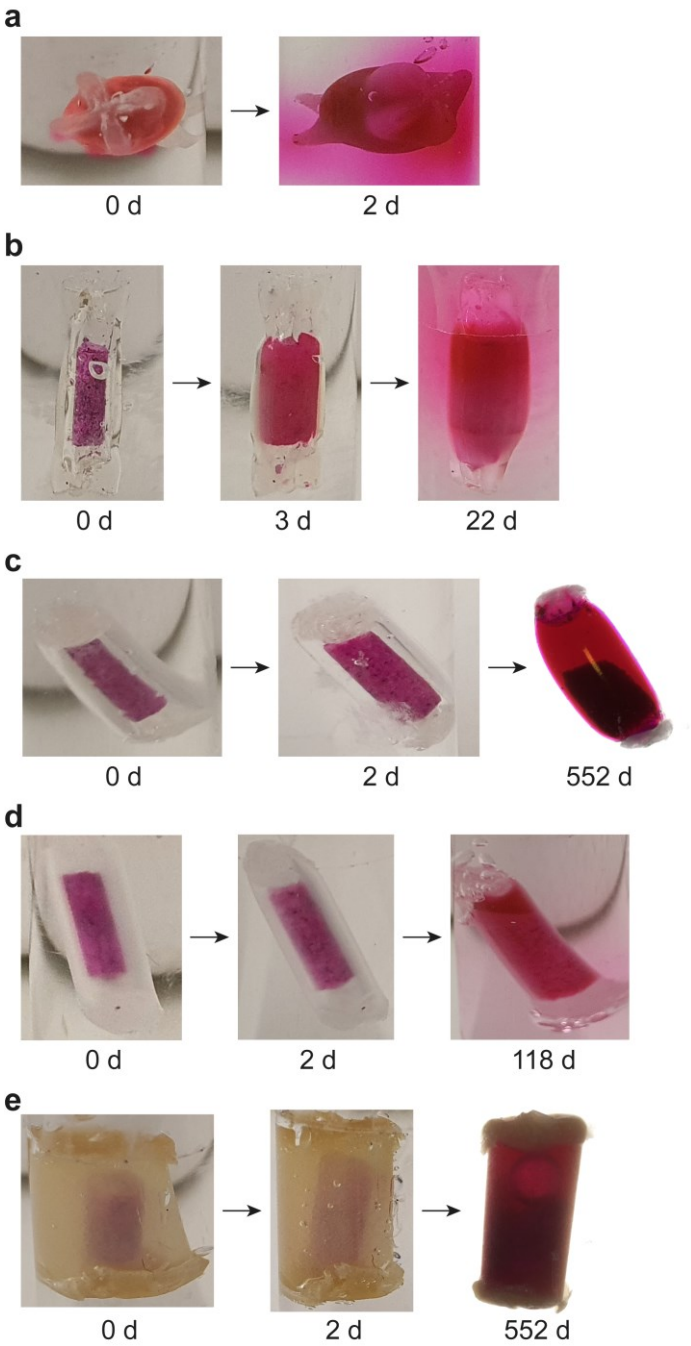


Figure 2.3: Digital images showing the swelling and/or failure of representative a) HSDV-A, b) HSDV-B, c) HSDV-C, d) HSDV-D, and e) HSDV-E samples, during stability testing in Pluronics F127 hydrogels (25% $w.w^{-1}$ in PBS) at pH 7.4 and 37 °C (n = 3).

During stability testing, RhB was observed on the surface of HSDV-A and B, which indicated that some core material was not contained within the implant (**Figure 2.4a,c**). This was possibly due to the surface contamination of the polymer coating during manufacture, or core material that was loosely trapped during the end-sealing process. However, it could also be indicative of an ineffective sealing process, particularly as HSDV-A samples were observed releasing core material

from the ends during the *in vitro* stability experiment (e.g., **Figure 2.4b**). Similarly, HSDV-B samples were observed swelling and releasing core material from the ends during the *in vitro* release experiment, and one sample exhibited significantly different release properties (**Figure 2.4d**). These results suggested that the end-sealing process used to produce both HSDVs was ineffective and resulted in considerable intrabatch variation.

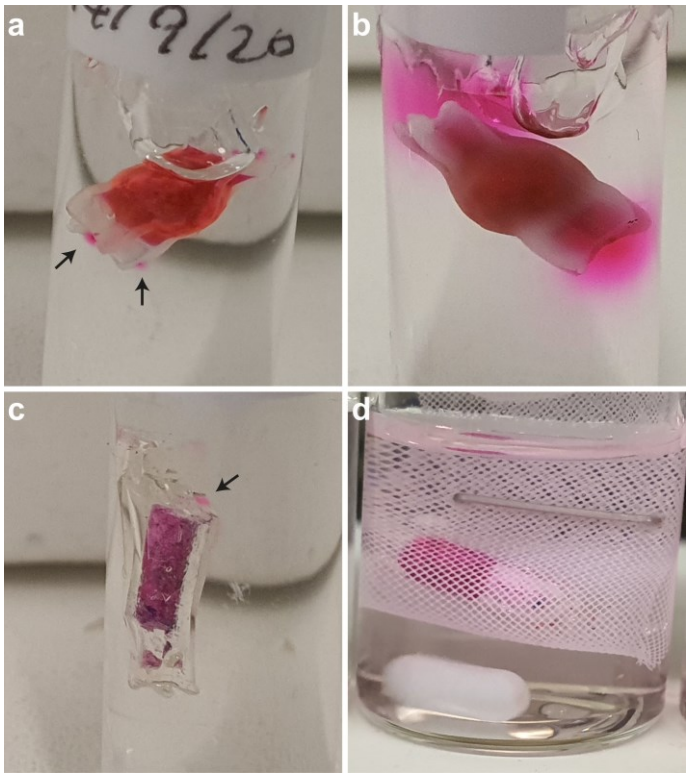


Figure 2.4: Images of a HSDV-A showing a) core material solubilised from the surface of HSDV-A immediately following immersion in Pluronics F127 (25% w.w^{-1} PBS pH 7.4, 37 °C) as indicated by the presence of RhB (black arrows) and b) failure caused by swelling and leakage of the core material from the ends after 16 h in Pluronics F127. Images of a HSDV-B showing c) core material solubilised from the surface of HSDV-B immediately following immersion in Pluronics F127 (black arrow), and d) swelling and release of the core material at one end, after 35 min in a pH 1.5 solution (25 °C).

In contrast to Eudragit® E 100, Resomer® L 206 S and L 210 S, are poly(L-lactide) (PLLA) homopolymers, where the former is ester terminated, and Biopol® is a poly(hydroxybutyrate) homopolymer. All three polymers are polyesters, with no reported pH-responsivity. Therefore, the primary release mechanism of HSDVs prepared from these polymers would be (bio)degradation and not pH-mediated dissolution. The possible degradation mechanisms of the polymers in the gastric

environment are acid-catalysed hydrolysis and enzymatic degradation.[28, 29] Both degradation processes would invariably be slower than the pH-mediated dissolution of Eudragit® E 100. However, it was considered possible (by Scientec) that coatings of these polyesters may degrade fast enough to achieve release following ingestion by a feral cat, either within the gastric or enteric environments. As such HSDV-C (Resomer L 206 S), D (Resomer L 210 S) and E (Biopol) samples (n = 3) were tested for the release (pH 1.5, 23 °C) and stability characteristics (pH 7.4, 37 °C), as previously described. It should be noted that these samples were tested for their release under conditions that would mediate acid-catalysed hydrolysis. No enzymes were present in the release solution, so enzymatic degradation was not tested in these experiments.

None of the polyester-based HSDVs released their core contents at gastric pH within the testing period (48 h). All tested samples exhibited significant swelling during the *in vitro* stability testing (**Figure 2.3c–e**). Samples of HSDV-C (n = 3) were stable for 17 d (×2) and 576 d (×1) and displayed considerable intrabatch variation (like the release properties of HSDV-B). In contrast, samples of HSDV-D (n = 3) exhibited more consistent stability, as samples were stable for 76, 97 and 118 d. The failures of the HSDV-C and D samples appeared to be due to swelling, and the release of core material from the ends of the HSDVs. In contrast, HSDV-E (n = 1), was found to be stable for 713 d, despite considerable swelling. Overall, the *in vitro* stabilities of the polyester-based HSDVs were inconsistent, and their lack of release at pH 1.5, suggested that acid-catalysed hydrolysis would not occur within an appropriate period. Whilst the exact cause of failure during stability testing could not be determined, it appeared to be due to the swelling of the HSDV, and the subsequent rupturing of the ends.

2.5 Conclusions

The poor stability of the HSDV-A and B samples at subcutaneous pH (7.4), and the poor release properties of the HSDV-C, D and E samples at gastric pH (1.5), demonstrated their lack of suitability for use as subcutaneous implants for invasive predator control. The considerable swelling exhibited by the HSDVs during testing appeared to cause premature failure of the implants, which was likely exacerbated by the poor end-sealing afforded by Scientec's proprietary HME manufacturing

process. The Eudragit® E 100 coating solubilised rapidly at pH 1.5, but in the context of a PPI, stability within the physiological environment is more important. This is highlighted by the need to buffer the Curiosity® and Hisstory® meat baits into which HSDV-As are inserted, to prevent the premature release of the core material (and hence, 1080 or PAPP), ostensibly due to the risk of coating dissolution or HSDV swelling. The HSDV-C–E samples generally exhibited improved stability but failed to release their core contents with a GET-relevant period. These data suggested that if a pH-responsive coating was used, it would require sufficient hydrophobicity to mitigate swelling and prolong stability *in vivo*, and that the use of a biodegradable polymer coating would not be possible, unless a sufficiently rapid degradation mechanism was available.

It is important to contextualise these results with the intended function of the original HSDV design. There is a considerable difference between the subcutaneous environment of a living animal, and the interior of a dried (and buffered) meat bait. The subcutaneous environment — and the *in vitro* testing conditions employed herein — invariably have higher moisture content than a dried meat bait, and likely exert greater osmotic pressure on the HSDVs. While the osmotic pressure exhibited *in vitro* may be sufficient to disrupt the sealed ends of the HSDVs, it is possible the pressure is reduced in a dried meat bait to such an extent that the HSDVs remain stable for the life of the bait. Further, buffering of dried meat baits to neutral pH values (i.e., pH 7.5)[19] likely reduces the protonation and hydrophilicity of the Eudragit® E 100 coating, and provides an additional barrier against swelling. The positive results reported in the field trials of Curiosity® baits, appear to support this assertion.[6, 10, 11, 14]

Therefore, these results suggested that while some of the HSDVs (namely HSDV-A and HSDV-B) are suitable for use in dried meat baits, they are all unsuitable for use *in vivo*. In addition, this study highlighted two additional considerations for the development of a PPI; (i) the need for a pH-responsive coating with a large differential between the pH values where it is soluble and insoluble, and (ii) a manufacturing process that produces uniform, defect-free implants. It was hypothesised that satisfying these two requirements would result in the production of implants that were soluble at low pH, but insoluble (with minimal swelling, if any) at physiological pH, and would exhibit long-lived stability due to the low intrabatch variation, respectively.

2.6 Experimental

2.6.1 Materials

Potassium chloride (KCl), hydrochloric acid (HCl, 36.5-38.0%), and Pluronics F127 were purchased from Sigma-Aldrich (St. Louis, United States). The pH 1.5 solutions were prepared from 0.2 M KCl and 0.2 M HCl. PBS tablets were purchased from Sigma and PBS solutions were prepared following the manufacturer's guidelines. High-purity water with a resistivity of > 18 MΩ.cm was obtained from an Arium Pro Ultrapure Water System (Sartorius, Goettingen, Germany).

2.6.2 Instrumentation

Images of the HSDV samples were captured using an Olympus SZ61 stereomicroscope fitted with a Gryphax Arktur (Jenoptik AG, Jena, Germany) camera module, using the Gryphax software (v2.2.0.1234).

2.6.3 Procedures

In Vitro Stability Experiments

A 25% $w.w^{-1}$ Pluronics F127 hydrogel was prepared by solubilising Pluronics F127 (25 g) in PBS (pH 7.4, 75 mL) at 4 °C under stirring. While fluid, the hydrogel was aliquoted (1.5 mL) into a series of 12 × 50 mm soda glass vials and allowed to gel at ambient temperature (23 °C). Immediately following gelation, a HSDV was inserted into each hydrogel, such that half of the HSDV remained unsubmerged. The exposed half of the HSDV was then covered in a further aliquot (2 mL) of the F127 hydrogel solution, which was also allowed to gel at ambient temperature. This resulted in a HSDV that was completely submerged in a total volume of 3.5 mL of the hydrogel. All samples were stored at 37 °C immediately following preparation, and for the duration of the experiment.

In Vitro Release Experiments

The pH 1.5 release solution was prepared from 0.2 M solutions of HCl and KCl. 50 mL of KCl was combined with 41.4 mL of HCl and diluted to 200 mL with high-purity water. The pH values of all release solutions were adjusted to within ± 0.02 units of the target pH using an NIST standard-calibrated pH 700 benchtop meter (Oakton Instruments, Illinois, United States). In a 16 × 50 mm soda glass vial, implants were suspended in 3.5 mL of a pH 1.5 (37 °C) release solution using a polyester mesh. The release of RhB was monitored qualitatively, by the appearance of the pink RhB dye in the receiving solution. The start of core release was defined as the time at which RhB was first observed in the receiving solution, and the end of core release was defined as the time at which no solid core material was observed in the HSDV.

2.7 References

1. D. Algar and N. Burrows, *Conserv Sci West Aust*, 2004, **5**, 131.

2. C. A. Hetherington, D. Algar, H. Mills and R. Bencini, *Wildl Res*, 2007, **34**, 467–471.

3. M. Johnston, D. Algar, M. O'Donoghue and J. Morris, in *Island invasives: Eradication and Management: Proceedings of the International Conference on Island Invasives*, IUCN, Centre for Biodiversity and Biosecurity, New Zealand, 2011, pp. 182–187.

4. D. Algar, M. Johnston, L. Clausen, M. O'Donoghue, J. Quinn, *Assessment of the hazard that the Hisstory®* bait for feral cats presents to a non-target species; northern quoll (*Dasyurus hallucatus*), Department of the Environment and Energy, 2017.

5. D. Algar, M. Johnston, M. O'Donoghue and J. Quinn, in *2015 National Feral Cat Management Workshop Proceedings*, Invasive Animals Cooperative Research Centre, Australia, 2015, pp. 80–84.

6. M. Johnston, L. Bould, M. O'Donoghue, M. Holdsworth, P. Marmion, R. Bilney, A. Reside, D. Caldwell, R. Gaborov and T. Gentles, *Field efficacy of the Curiosity® bait for management of a feral cat population at Roxby Downs, South Australia*, Department of Environment and Primary Industries, Heidelberg, Victoria, 2014.

7. C. A. Marks, M. J. Johnston, P. M. Fisher, K. Pontin and M. J. Shaw, *J Wildl Manage*, 2006, **70**, 1119–1124.

8. P. J. de Tores, D. R. Sutherland, J. R. Clarke, R. F. Hill, S. W. Garretson, L. Bloomfield, L. Strümpher, A. S. Glen and J. Cruz, *Wildl Res*, 2011, **38**, 39–50.

9. T. Buckmaster, C. R. Dickman and M. J. Johnston, *PLoS ONE*, 2014, **9**, e107788.

10. A. Robley, L. Cockman, M. Hoskins, E. Le Duc and A. Shiells, *Biol Conserv,* 2022, **180**, 262–269.

11. R. Hohnen, J. Smith, J. Mulvaney, T. Evans and T. Mooney, *Wildl Res*, 2022, **49**, 637–645.

12. M. Johnston, F. Gigliotti and J. Trezise, *Vic Nat*, 2019, **136**, 203-207

13. M. J. Johnston, F. Gigliotti, M. O'Donoghue, M. Holdsworth, S. Robinson, A. Herrod and K. Eklom, *Field assessment of the Curiosity® bait for management of feral cats in the semi-arid zone (Flinders Ranges National Park)*, Department of Sustainability and Environment, Heidelberg, Victoria, 2012.

14. D. Algar, N. Hamilton, M. Onus, S. Hilmer, S. Comer, C. Tiller, L. Bell and J. Pinder, *Field trial to compare baiting efficacy of Eradicat® and Curiosity®*

baits, Western Australian Department of Environment and Conservation, 2018

15. M. Johnston, D. Algar, M. O'Donoghue, J. Morris, T. Buckmaster and J. Quinn, *Wildl Res*, 2020, **47**, 686–697.

16. S. Robinson, L. Gadd, M. Johnston and M. Pauza, *N Z J Ecol*, 2015, **39**, 316–322.

17. M. Johnston, D. Algar, M. Onus, N. Hamilton, S. Hilmer, B. Withnell and K. Koch, *A bait efficacy trial for the management of feral cats on Dirk Hartog Island*, Department of Sustainability and Environment, 2010.

18. M. Johnston, M. O'Donoghue, M. Holdsworth, S. Robinson, A. Herrod, K. Eklom, F. Gigliotti, L. Bould and N. Little, *Field assessment of the Curiosity® bait for managing feral cats in the Pilbara*, Department of Sustainability and Environment, Heidelberg, Victoria, 2013.

19. M. Johnston, *Field assessment of the Curiosity® bait for the management of feral cats after fire at Wilsons Promontory National Park*, Department of Sustainability and Environment, Heidelberg, Victoria, 2012.

20. M. F. O'Donoghue and J. A. Morris, *Apparatus and method for coating a material,* Australia, Patent No., 1998078708, 1997.

21. B. L. Allen, L. R. Allen, M. Graham and M. Buckman, *Aust Zool*, 2021, **41**, 374–387.

22. R. Lennox and F. Probyn-Rapsey, *Borderlands Journal*, 2021, **20**, 49–88.

23. F. Probyn-Rapsey and R. Lennox, *Environ. Plan E Nat Space*, 2022, **5**, 362–380.

24. Scientec Research Pty Ltd, Controlled Release Delivery Technology, http://www.scientec-research.com/crd.html, (accessed 2022).

25. S. Thakral, N. K. Thakral and D. K. Majumdar, *Expert Opin Drug Deliv*, 2013, **10**, 131–149.

26. C. N. Patra, R. Priya, S. Swain, G. Kumar Jena, K. C. Panigrahi and D. Ghose, *Future J Pharm Sci*, 2017, **3**, 33–45.

27. C. A. Wyse, J. McLellan, A. M. Dickie, D. G. M. Sutton, T. Preston and P. S. Yam, *J Vet Intern Med*, 2003, **17**, 609–621.

28. E. Castro-Aguirre, F. Iñiguez-Franco, H. Samsudin, X. Fang and R. Auras, *Adv Drug Deliv Rev*, 2016, **107**, 333–366.

29. I. Manavitehrani, A. Fathi, H. Badr, S. Daly, A. Negahi Shirazi and F. Dehghani, *Polymers*, 2016, **8**, 20.

Chapter 3: Preliminary Implant Design and Manufacture

3.1 Overview

Chapter 3 describes the synthesis, characterisation, and evaluation of a series of addition copolymers of 2-vinylpyridine and butyl methacrylate, for use as pH-responsive population protecting implant (PPI) coatings. The physicochemical (i.e., water absorption and solubility) and thermal properties (i.e., glass transition and thermal degradation temperatures) of the copolymers were investigated in relation to the mol% fraction of their constitutive monomers. These results were related to their potential effects on PPI performance, importantly the need to reduce water absorption as highlighted in Chapter 2. A candidate copolymer was selected, and a preliminary investigation of PPI design and manufacture *via* fluidised-bed spray coating was undertaken, to afford implants with improved end-sealing, as proposed in Chapter 2. The *in vitro* release and stability, and *in vivo* performance of the manufactured implants were then evaluated. The results of these experiments showed that the physicochemical and thermal properties of the copolymers could be tuned, and water absorption reduced. Manufactured implants exhibited favourable stability and release properties *in vitro*, but exhibited swelling, which ultimately caused the implants to have moderate stability *in vivo*. These results highlighted the need to develop a pH-responsive copolymer exhibiting reduced water absorption.

The in vivo stability experiment described in this chapter was undertaken in collaboration with Dr. Todd McWhorter and Roxy Ackerman, who performed the experiment. Kyle Brewer assisted in the interpretation of the raw data and conducted all data reporting and visualisation.

3.2 Results and Discussion

3.2.1 Implant Core Preparation

To allow the administration of PPIs to native mammals *via* a non-invasive injection akin to microchipping, a rod-shaped implant was envisaged with a poison core and an encapsulating pH-responsive coating. Thus, the PPI dimensions were modelled on a standard microchip (2.12 mm diameter × 12 mm length) to enable implantation of the PPIs using conventional syringe implanters that are commonly used to subcutaneously implant radiofrequency identification (RFID) microchips into domestic animals and wildlife. This design consideration limited the available volume of the poison core. To ensure a > LD_{90} dose[1] for feral cats and eliminate the possibility of a sublethal dosing event, 3 mg of sodium fluoroacetate (1080) was required per implant. To meet the design specifications, the core needed to consist of 50% $w.w^{-1}$ 1080, with the remainder being a water-soluble binder. Poly(ethylene glycol) (PEG, 10 kDa) was selected as the binding compound, due to its considerable water solubility, ubiquitousness, safety, and commercial availability.[2]

To avoid excessive and unnecessary handling of poison during the initial stages of PPI development and testing, sodium acetate (NaOAc) — a non-toxic and analogous compound to the poison 1080 — was used in the core formulation. NaOAc exhibits similar physicochemical properties to 1080, is comparatively non-toxic, and commercially available. Two non-toxic, water-soluble dyes — methylene blue (MB) and rhodamine b (RhB) — were also incorporated into the core formulation at very low loadings. MB has been reported to stain the urine of small mammals,[3] and RhB is known to stain the vibrissae (whiskers) and faeces of cats.[4] It was hypothesised that the incorporation of both dyes may enable the confirmation of implant consumption by a feral cat (or implant failure in a native animal) following inspection of their body or bedding. The presence of the dyes would also enable the facile visual and spectrophotometric detection of core dissolution. An appropriate solvent system was investigated to ensure the complete dissolution of both NaOAc and PEG, whilst maximising the organic content to facilitate the evaporation of the solvent during coating. Ultimately, an optimised core formulation was prepared containing a 49:49:1:1 % $w.w^{-1}$ ratio of

NaOAc:PEG:MB:RhB dissolved in ethanol:water (EtOH:water, 70:30). To facilitate the evaporation of the binary EtOH:water solution, a fluidisation air temperature of 40 °C was required. The coating formulation was supplied to the instrument using a syringe pump with a flow rate of 15.2 $mL.h^{-1}$ and coated at an atomising air pressure of 5 psi. During coating, the fluidisation air flow velocity was gradually increased from 50–80% as the mass of the implants increased, to ensure adequate fluidisation.

The NaOAc core formulation was spray coated onto rod-shaped acrylonitrile butadiene styrene (ABS) filament substrates (n ≈ 850; 0.64 ± 0.03 mm diameter × 8.04 ± 0.08 mm length) (**Figure 3.1a**), until ~ 6 mg per implant had been deposited (**Figure 3.1b**). Optical microscopy (OM) and scanning electron microscopy (SEM) analysis of the NaOAc core formulation revealed uniform coatings of ~ 250 μm in thickness (**Figure 3.1b**). The NaOAc core coating exhibited pitting — a phenomenon generally attributed to the use of processing temperatures exceeding the melting point(s) of component(s) in the coating formulation[5] — which was not the case in this work. It is likely that during atomisation the quicker evaporation of ethanol resulted in the deposition of highly concentrated, predominantly aqueous droplets onto the implant surface. Continued evaporation of the water from these viscous droplets could have led to entrapped bubbles that collapsed and formed micropores, similar to those reported for ethyl cellulose films spray coated from EtOH:water.[6] Cracking was also observed in the core coating, which was attributed to the poor plasticisation and high crystallinity of the NaOAc core formulation (due to the high NaOAc content) and the contraction of the deposited material during evaporation. Importantly, the pitting and cracking defects in the core appeared to have no effect upon the friability of the resultant NaOAc cores, as no breakage or shedding was observed during handling and further coating. As a result, the NaOAc core formulation was considered suitable for implant manufacture and no further optimisation was undertaken.

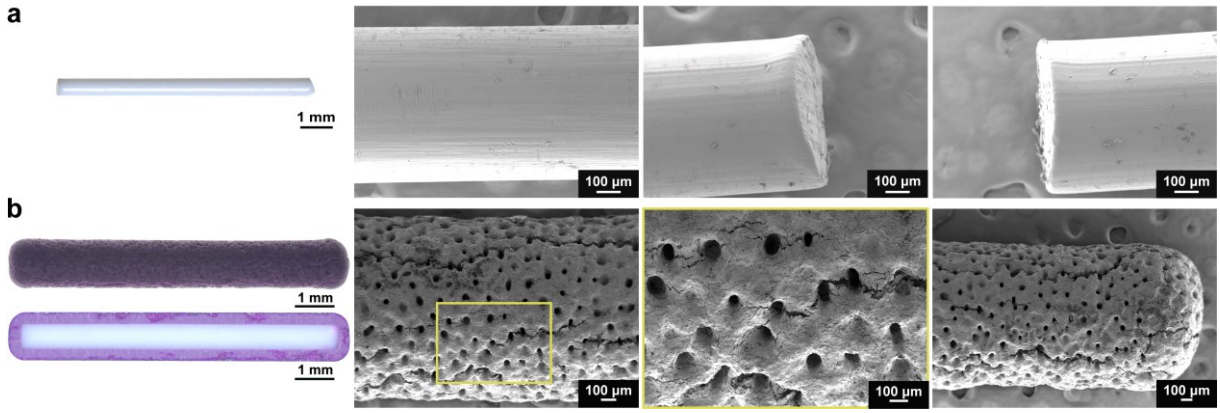


Figure 3.1: Representative digital images and scanning electron micrographs of a) an ABS filament substrate, b) a NaOAc core.

3.2.2 Synthesis and Characterisation of Poly[(2-vinylpyridine)$_x$-*co*-(butyl methacrylate)$_y$] (PVB) Copolymers

2-Vinylpyridine (VP) was selected as the pH-responsive moiety through which to develop an appropriately pH-responsive polymer. Given the reported pKa value of VP homopolymers (~ 4.5[7]), it was hypothesised that *via* addition polymerisation with a methacrylate monomer(s), a pH-responsive copolymer with suitable pH-responsiveness and compatibility with fluidised-bed spray coating, could be synthesised. To that end, a series of pH-responsive copolymers were synthesised with varying ratios of VP and butyl methacrylate (BMA). The physicochemical and thermal properties of these copolymers were investigated using the following selection criteria: (i) pH 7.4 insolubility and low water absorption; (ii) low pH (< 2) solubility, and (iii) a suitable glass transition temperature (T_g), that allowed processing, and provided a stable yet flexible coating at 37 °C. The physicochemical properties of the synthesised copolymers were investigated through solubility, water absorption, and thermal analysis experiments, and their compatibility with fluidised-bed spray coating was investigated following spray coating, *via* a combination of OM and SEM. Successfully coated implants were evaluated for their performance through the determination of their stability and release characteristics *in vitro* and *in vivo*.

Initially, a series of addition copolymers of VP and BMA were synthesised *via* conventional free radical polymerisation (CFRP) (**Figure 3.2a**), with varying ratios of the two monomers. The synthesised poly[(2-vinylpyridine)$_x$-*co*-(butyl methacrylate)$_y$] copolymers were designated as PVB x/y, where *x* and *y* refer to

their respective VP and BMA repeat unit (RU) mol% ratios. Polymerisation was initiated by 2,2'-azobisisobutyronitrile (AIBN), and monomer conversion was monitored *via* gas chromatography (GC). Additional volumes of AIBN were added hourly over 3 h, until monomer conversion was greater than 95%. The copolymer product was then purified *via* precipitation from hexanes. In all cases, the polymers were obtained as pale-yellow solids.

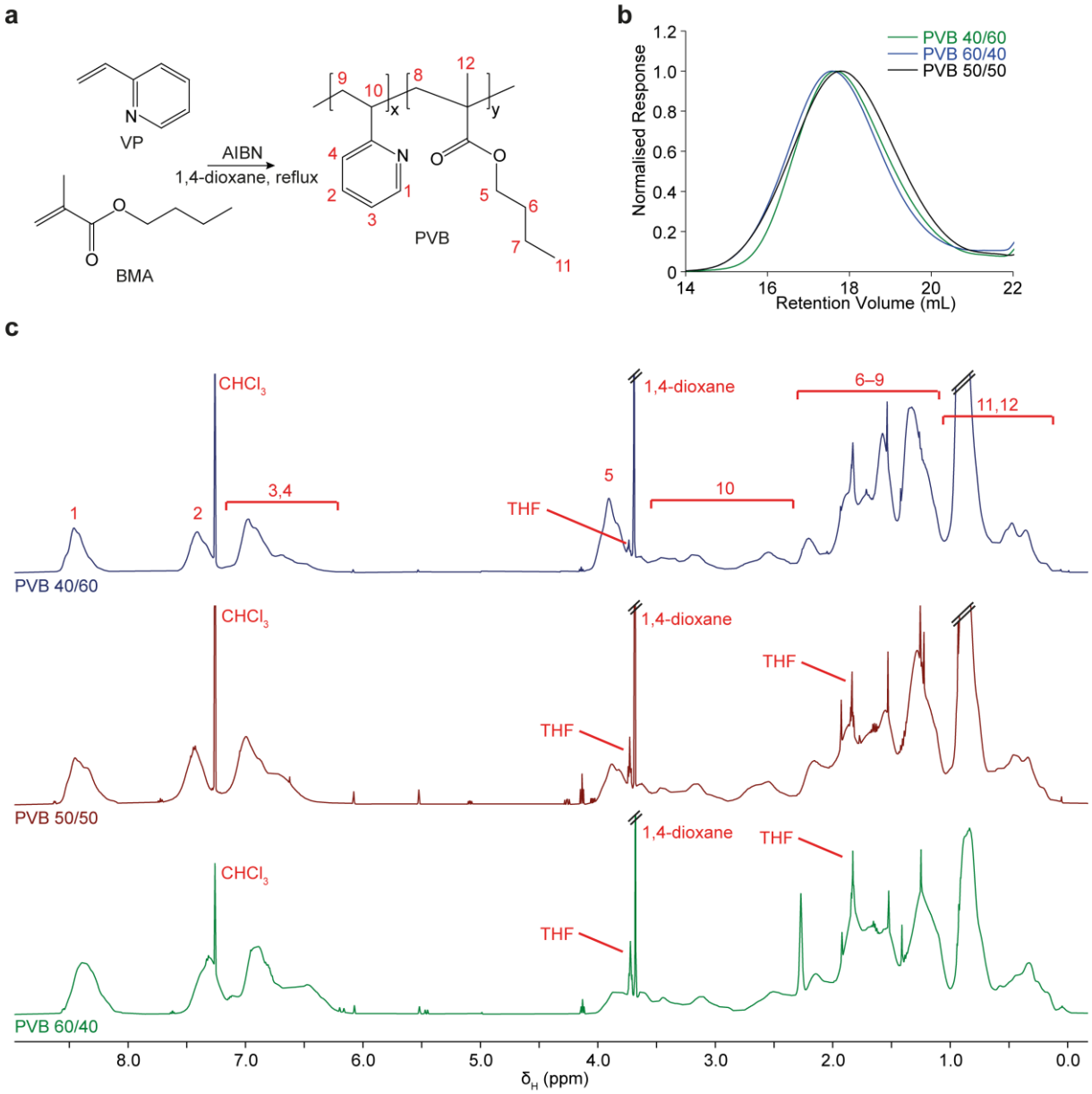


Figure 3.2: a) Synthesis of poly[(2-vinylpyridine)$_x$-*co*-(butyl methacrylate)$_y$] (PVB x/y) copolymers *via* CFRP. b) Gel permeation chromatography (GPC) differential refractive index (DRI) chromatograms and c) proton nuclear magnetic resonance (^{1}H NMR) spectra (500 MHz, deuterated chloroform ($CDCl_3$), 21 °C) of the PVB series.

Monomer conversion and the relative ratios (relative mol% of RUs) of the incorporated monomers were determined *via* GC with respect to their pre-polymerisation (t_0) concentrations, using the solvent (1,4-dioxane) as an internal reference. The targeted VP:BMA mol% ratios of 50:50, 60:40 and 40:60 were closely achieved using this approach (**Table 3.1**).

Table 3.1: Poly[(2-vinylpyridine)$_x$-*co*-(butyl methacrylate)$_y$] copolymer RU mol% ratios and molecular weight characteristics.

Copolymer code	Targeted mol% of RU	Calculated mol% of RU [a]	M_w [b] (kDa)	M_n [b] (kDa)	$Đ$ [b]	T_g [c] (°C)
PVB 60/40	60:40	63:37	35.3	21.0	1.7	58.9
PVB 50/50	50:50	51:49	37.1	21.1	1.8	53.1
PVB 40/60	40:60	41:59	30.1	17.5	1.7	43.3

[a] Monomer conversion and RU mole ratios determined by GC relative to t_0 using 1,4-dioxane as an internal reference. [b] Determined by GPC using a conventional column calibration of narrow molecular weight poly(methyl methacrylate) (PMMA) standards, where M_w is the weight-average molecular weight, M_n is the number-average molecular weight, and $Đ$ is the dispersity. [c] Determined by MDSC.

The synthesised copolymers were further characterised *via* GPC (**Figure 3.2b**) and ^{1}H NMR spectroscopy (**Figure 3.2c**). The broad, overlapping resonances obtained in the ^{1}H NMR spectra — typical of a random copolymer — precluded accurate determination of the monomer RUs to allow corroboration with the GC results. However, resonances characteristic of the VP RU aromatic protons between δ_H 8.40 and 6.75 ppm, and BMA RU ester methylene protons at δ_H 3.9 ppm, supported the successful incorporation of the two monomers in the PVB copolymers. The ^{1}H NMR spectra also showed the presence of trace amounts of solvents used during synthesis (1,4-dioxane (δ_H 3.67 ppm) and tetrahydrofuran (THF) (δ_H 3.75 and 1.70 ppm)). In some cases, trace amounts of unreacted monomers were observed (i.e., alkene proton resonances between δ_H 6.2 and 5.0 ppm). However, the presence of these impurities was considered inconsequential given their trace amounts, and the copolymers were used without further purification.

GPC analyses of the copolymers (**Figure 3.2b**) revealed similar weight-average molecular weight (M_w) values between 30–37 kDa, and broad, monomodal molecular weight distributions (dispersity ($Đ$) = 1.7–1.8, **Table 3.1**), consistent with dispersities that are typically observed for polymers synthesised by CFRP. It is important to note that the copolymer M_w values determined from the GPC analyses (**Table 3.1**) are relative to the poly(methyl methacrylate) (PMMA) standards used to calibrate the system and are not absolute. Together, the results from the GC and GPC analyses, and ^{1}H NMR spectra, demonstrated the successful synthesis of the copolymer series with excellent accuracy regarding the target RU mol% ratios and relatively consistent molecular weight profiles.

3.2.3 Thermal Characterisation of the PVB Copolymers

Modulated high-resolution thermogravimetric analysis (MTGA) and modulated differential scanning calorimetry (MDSC) analyses were conducted on the synthesised copolymers to investigate their thermal properties, namely their respective degradation temperatures (T_d) and T_g values. While the T_d values of the copolymers would inform the processing conditions that could be used, the T_g values would affect the copolymer's compatibility with spray coating and its performance if coated on a tablet or microparticle formulation.[8, 9]

From the MDSC analyses, none of the synthesised copolymers exhibited either a defined melting (T_m) or crystallisation (T_c) temperature, which demonstrated that all the copolymers were amorphous. The reversing heat flow curves from the MDSC analyses of the PVB copolymers (**Figure 3.3a**) revealed a positive correlation between the mol% fraction of VP and the T_g values of the copolymers. PVB 60/40 had the highest mol% fraction of VP and exhibited the highest T_g value of 58.9 °C, whereas PVB 40/60 had the lowest T_g value of 43.3 °C, and PVB 50/50 had an intermediate T_g value of 53.1 °C (**Figure 3.3a**). This relationship results from the contribution of the VP RUs to the T_g values of the resultant copolymers, as VP homopolymers generally exhibit high T_g values (cf., BMA) due to the stronger intermolecular forces between VP RUs, and the bulky nature of pendant VP RUs. Whereas BMA RUs are less bulky with weaker interactions, which causes BMA homopolymers to have lower T_g values.

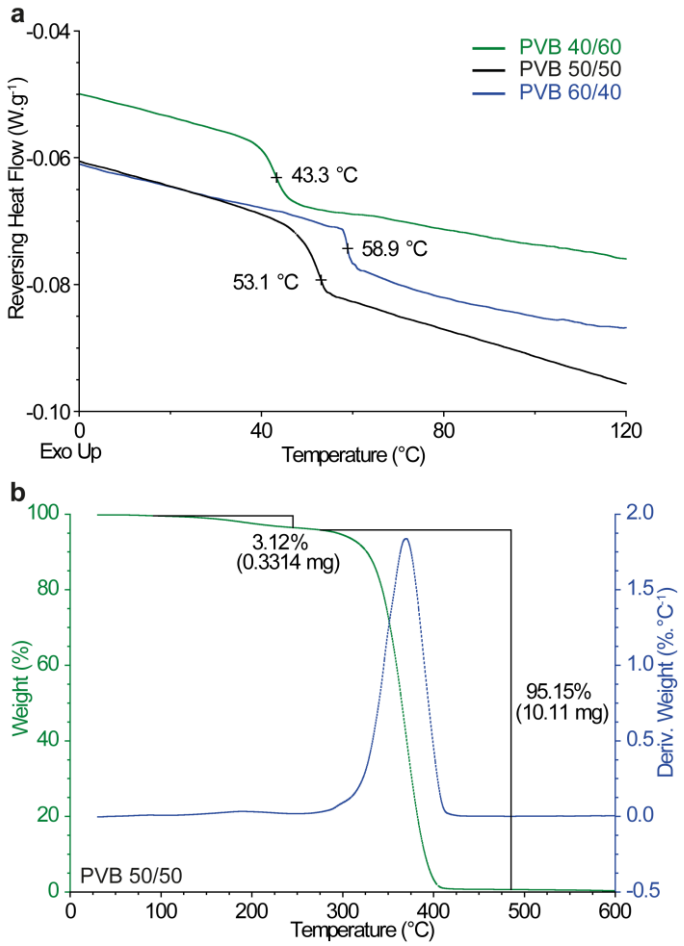


Figure 3.3: a) Reversing heat flow ($W.g^{-1}$) curves of the PVB copolymer series determined *via* MDSC. b) Weight (%) and derivative weight ($\%.°C^{-1}$) curve of PVB 50/50, representative of the PVB copolymer series.

A representative copolymer from the PVB series (PVB 50/50) was analysed *via* MTGA (**Figure 3.3b**), given the high likelihood of a shared degradation mechanism amongst copolymers from the same series. PVB 50/50 exhibited an onset value for thermal degradation of ~ 270 °C (**Figure 3.3b**), followed by a single degradation event involving a weight loss of ~ 95%. Homopolymers of VP and BMA thermally degrade predominantly *via* depolymerisation, with major degradation products being monomer and low molecular weight oligomers.[10, 11] In addition, when incorporated in a block copolymer of VP and polystyrene (i.e., poly(2-vinylpyridine-*co*-styrene)), the same degradation mechanism for the homopolymer of VP is observed for the VP block in the copolymer.[12] Therefore, the single decomposition event observed for PVB 50/50 suggested that degradation likely occurred predominantly *via* depolymerisation. Importantly, whilst the temperature of the major decomposition event has little implications within the context of fluidised-bed spray coating, the favourable thermal stability of the

synthesised copolymers may make them suitable for processing at elevated temperatures (i.e., up to 250 °C). For example, hot-melt extrusion (HME) has been successfully used to produce taste-masked orally disintegrating tablets, containing the reverse enteric copolymer Eudragit® E PO, and ibuprofen, with improved friability and release properties compared to a commercially available dosage form.[13] Extrusion was performed at 140 °C, which is an extrusion temperature and therefore a processing method, that is accessible to the PVB copolymers.

3.2.4 pH-dependent Solubility of the PVB copolymers

The pH-dependent solubility of a copolymer is integral to its performance as a conventional reverse enteric coating. Invariably, to effectively achieve stability within the oral cavity and rapid dissolution within the stomach for example, a significant solubility differential is required between both environments. To effectively compare the solubility of the synthesised PVB copolymers, their solubility was evaluated in solutions simulating the gastric environment (i.e., pH 1.0, 1.5 and 2.0). The solubility of each copolymer was calculated from its concentration, as determined *via* GPC analysis of the aqueous solution, using relevant standard curves (Appendix, Figure A3.1).

The solubility of the PVB copolymers was generally positively correlated with the mol% fraction of VP (Figure A3.1), and decreased with increasing pH (i.e., decreased protonation of the VP RUs). At pH 1.5, PVB 60/40 exhibited the greatest solubility (9.8 ± 1.2 $mg.mL^{-1}$), whilst PVB 50/50 and PVB 40/60 exhibited similar solubilities (7.5 ± 1.4 and 7.1 ± 0.3 $mg.mL^{-1}$).

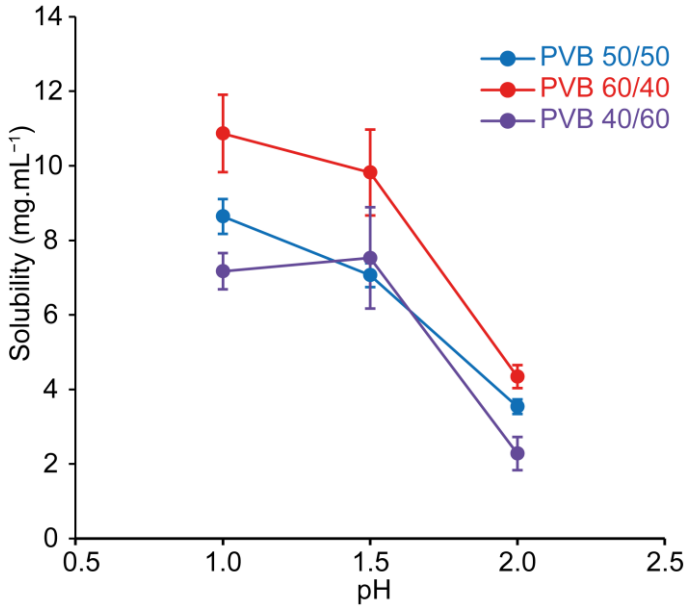


Figure 3.4: The effect of PVB copolymer composition on solubility at pH 1.0, 1.5 and 2.0 (37 °C). Values are reported as the mean ± std. dev. (n = 3).

3.2.5 Water Absorption Properties of the PVB Copolymers

It was important to determine the water absorption properties of the copolymers, as the absorption of water could affect the integrity of the implant following film coating. Commercially produced reverse enteric coatings experience significant dissolution or swelling at physiological pH and are unable to withstand long-term exposure to these environments. It was hypothesised that a copolymer or formulation that has maximal solubility at gastric pH, and minimal water absorption at physiological pH, would exhibit the greatest performance for the PPI. The water absorption (in % $w.w^{-1}$) of the copolymers in each series was evaluated gravimetrically by immersing polymer discs in phosphate-buffered saline (PBS, pH 7.4, 20 mL) at 37 °C and periodically recording their change in mass.

For the PVB copolymer series, the extent of water absorption was found to be proportional to the mol% fraction of VP in the copolymer, with PVB 60/40 resulting in the greatest water absorption after reaching an apparent equilibrium between 30–40 d (~ 4.5% $w.w^{-1}$). PVB 50/50 exhibited a slightly lower water absorption (~ 4.4% $w.w^{-1}$), and PVB 40/60 showed the lowest water absorption (~ 2.1% $w.w^{-1}$) within the same period (**Figure 3.5**). Such a relationship is reasonable given the relatively higher hydrophilicity of VP and is supported by the demonstrated

proportional relationship between the solubility of a copolymer and its mol% fraction of VP.

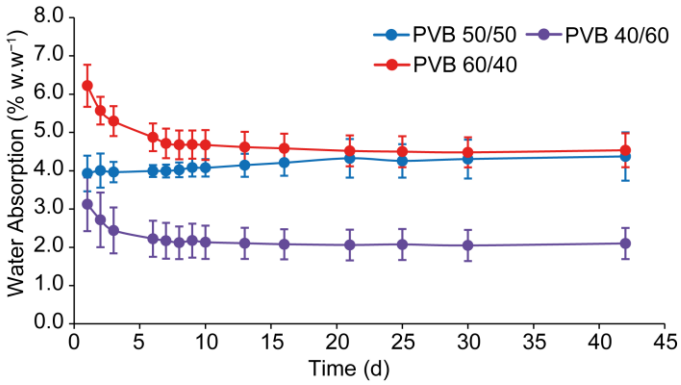


Figure 3.5: Water absorption (% w.w^{-1}) as a function of time from PBS (pH 7.4, 37 °C) for the PVB copolymer series.

The incorporation of a series of hydrophobic excipients, and their effects on water absorption, were also investigated. However, when the PVB 50/50 copolymer was combined with the excipients micronised talc or octadecanol, the effects were inconsistent, and prevented film formation during coating. These results are briefly summarised in **Appendix 3.5.2** but will not be discussed further. Of the three PVB copolymers, PVB 50/50 showed the most appropriate physicochemical and thermal properties i.e., favourable solubility (7.5 ± 1.4 mg.mL^{-1}, pH 1.5), water absorption (~ 4.5% w.w^{-1}), and T_g value (53.1 °C), and was investigated for the manufacture of implants. PVB 60/40 and PVB 40/60, while considered to show less favourable properties (e.g., namely lower solubility at pH 1.5 and 2), were thought to potentially be suitable for use as reverse enteric, taste-masking coatings of pharmaceutical formulations. As a result, a preliminary investigation of these two copolymers as taste-masking coatings was conducted and is provided in **Appendix 3.5.3**.

3.2.6 Manufacture and Evaluation of the PVB Implants

The NaOAc cores (n ≈ 900; 1.13 ± 0.04 mm diameter × 8.56 ± 0.1 mm length) were separated into sub-batches and spray coated with PVB-based coating formulations. Small batches of ~ 25 NaOAc cores were coated with a series of trial PVB 50/50 formulations, prepared using different organic solvents (e.g., EtOH, dichloromethane (DCM), and acetone). A copolymer concentration of 10% w.v^{-1} was used in all the trial formulations, as prior coating with the NaOAc core

formulation suggested this might provide the best balance between copolymer content and viscosity. The optimised spray coating parameters for the NaOAc core formulation were then used to evaluate the PVB 50/50 formulations. Both DCM and acetone were too volatile, resulting in dusting of the implants, which could not be mitigated by reducing the fluidisation air temperature or atomisation air pressure, or by increasing the syringe pump flow rate. Dusting did not occur with EtOH, however, the fluidisation air temperature was reduced to ambient temperature (23 °C). Higher fluidisation air temperatures (e.g., 40 °C, used for the core coating) caused the copolymer to become tacky and the implants to adhere to one another — a phenomenon caused by the fluidisation air temperature approaching the T_g value of PVB 50/50. The atomisation air and syringe pump flow rate were both found to be compatible with the PVB 50/50 formulation, and alterations to these parameters did not achieve a noticeable change in coating performance. Implants coated with the 10% $w.v^{-1}$ PVB 50/50 (EtOH) formulation qualitatively exhibited a film coating and indicated that EtOH was the most appropriate solvent.

As a result, a larger batch of implants (n ≈ 200) bearing the PVB 50/50 coating (i.e., PVB implants) was prepared. After each coat, implants were briefly dried in a vacuum desiccator to ensure all the coating solvent had been removed (0.02 mbar, 15 min, 23 °C). During coating, the dimensions and masses of the implants were monitored using digital callipers and an analytical balance, respectively. By monitoring the average change in diameter of a statistically relevant number of implants (n ≥ 10% of the batch size), the thickness of the copolymer coating was monitored. The implants were found to possess a 315 μm PVB 50/50 coating. OM and SEM analysis of the coated implants (**Figure 3.6**) revealed a cohesive and uniform copolymer coating. Light dusting was observed on the implant surface, however when the implant cross-section was viewed, it demonstrated that the dusting did not have any effect on the cohesiveness of the coating. These data suggested that the PVB 50/50 formulation was compatible with fluidised-bed spray coating and produced uniform and cohesive coatings. The performance of the PVB implants was then evaluated.

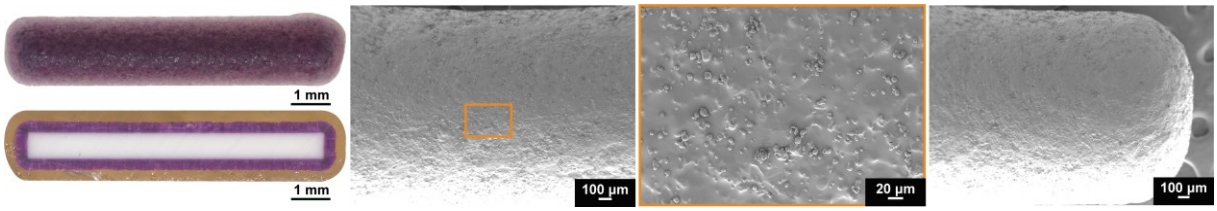


Figure 3.6: Representative digital images and scanning electron micrographs of a PVB implant.

3.2.7 *In Vitro* Evaluation of PVB Implant Performance

The dissolution of the copolymer coating and subsequent release of the core contents from PVB implants was investigated *in vitro* at pH 1.5 and 37 °C (**Figure 3.7a**), to mimic the gastric environment of a feral cat. The release of NaOAc was monitored *via* the concomitant release of MB (λ_{max} = 663 nm) present within the implant core, to enable inline monitoring *via* ultraviolet-visible (UV-vis) spectrophotometry. MB was selected for this purpose, as it was determined that a small degree of spectral overlap caused an inflated absorbance for the RhB signal ($\lambda_{max.}$ = 557 nm) when both dyes were present in solution (data not shown). Future core preparations contained only MB to mitigate this spectral overlap issue. 1080 could not be directly monitored using this method due to overlapping absorbances exhibited by 1080 and the PVB copolymers. It should also be noted that the high-performance chromatography method described in **Chapter 6.2.5** was not suitable for monitoring release in these experiments, due to the high concentrations of copolymer (~ 3–4 mg.mL^{-1}) present in the receiving solution, and the required manual sampling and offline measurement of the release solutions.

Release was observed after 15.4 ± 2.2 min, and the core contents had completely released after 27.7 ± 2.6 min. Given the variability of the reported gastric pH in cats, it is challenging to infer whether the release of the implant core contents at pH 1.5 *in vitro* would be sufficient to result in release *in vivo*. However, the gastric half-emptying time (GET) of feral cats has been reported as ~ 2.5–4 h.[14] Therefore, it is reasonable to suggest that the relatively rapid release (cf. GET) at pH 1.5, may only require the gastric pH to reach 1.5 transiently. Effectively, only a small fraction of the PVB 50/50 copolymer coating needs to solubilise to expose the core and initiate release, as the hydrophilic core contents would continue to release irrespective of gastric pH. In addition, maintaining a large pH-differential between stability and release conditions is preferable, as significant solubility at pH

> 2 may cause the coating to become permeable to the core contents in the subcutaneous environment. Though further investigation of implant dissolution *in vivo* (e.g., in pen trials) was considered necessary to ensure release occurs within a sufficient period, the release conditions established during this preliminary experiment were considered sufficient.

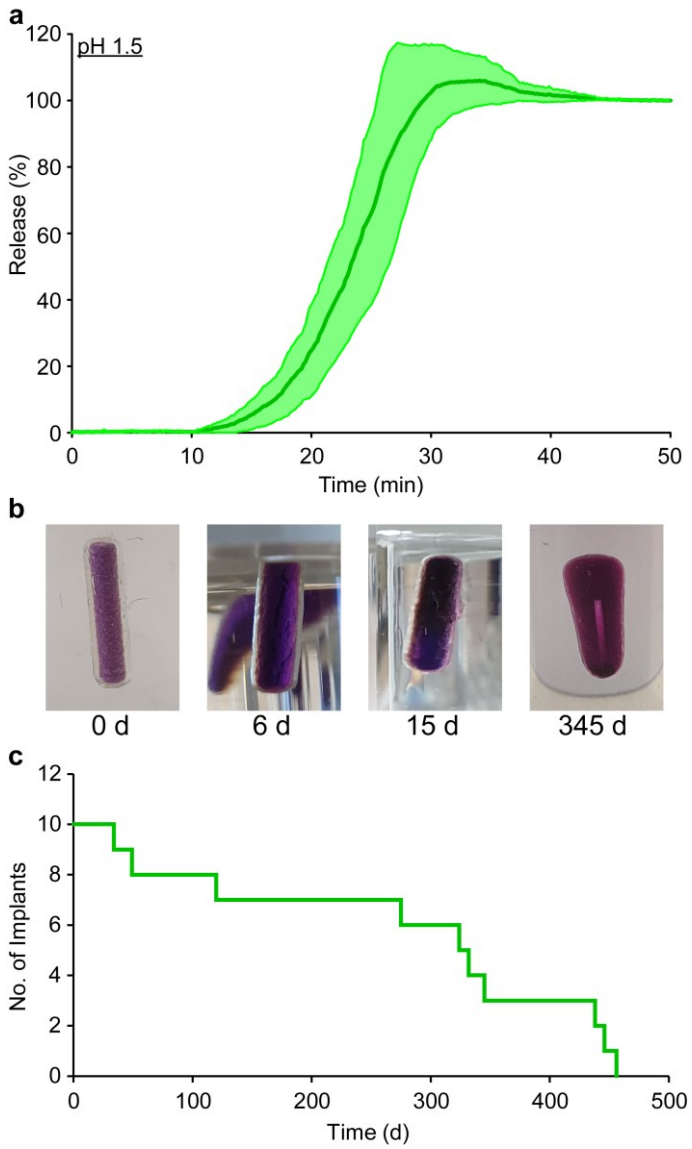


Figure 3.7: a) Release monitoring profile of MB ($\lambda_{max.}$ = 663 nm) from PVB implants, at 37 °C, in a pH 1.5 solution (3.5 mL). Traces are reported as the mean (solid line) ± std. dev. (shaded area) (n = 5). b) Stability results of PVB implants in Pluronics F127 (25% w.w^{-1}, in PBS) at pH 7.4 and 37 °C (n = 10), over ~ 500 d. c) Representative images of a PVB implant during the stability experiment. Note the failure of the pictured implant following 345 d in Pluronics F127, as indicated by the presence of RhB and MB in the surrounding hydrogel.

The stability of the implants was assessed *in vitro* using a hydrogel model to mimic the subcutaneous environment. PVB Implants were completely submerged in Pluronics F127 hydrogels in PBS (25% $w.w^{-1}$, pH 7.4) and stored at 37 °C. This enabled the interrogation of implant stability at physiological pH (7.4), temperature (37 °C), and hydration (75%)[15, 16] with failure indicated by the observed release of MB and RhB from the PVB implant core. It was noted that over several days the core would slowly darken in colour indicating the permeation of water through the coating and dissolution of the core (**Figure 3.7b**). As discussed in **Chapter 1.5**, like all nonporous polymer films submerged in water or exposed to water vapour,[17, 18] the polymer coating was found to act as a semi-permeable membrane, leading to ingress of the surrounding water, dissolution of the implant core and swelling over longer periods. At physiological pH, the slightly polar functional groups (neutral pyridine and ester moieties) in the copolymer structure may have facilitated the movement of water through the coating. Of the tested PVB implants, 30% were observed to fail in the first ~ 100 d of the experiment, with the remaining 70% stable for more than ~ 250 d (**Figure 3.7c**). Generally, the failure of the implants correlated to the swelling phenomenon. The PVB 50/50 coating would likely be stretched and thinned by the osmotic pressure during swelling, and if the coating was unable to withstand this process, it would rupture and cause implant failure. At this stage it was unclear why a relatively longer stability was exhibited by some implants (~ 450 d, 30%) during testing. Nevertheless, it was evident that the hydrophilicity and water absorption exhibited by the PVB 50/50 coating was responsible for the rapid swelling observed in the simulated subcutaneous environment. This highlighted the need to achieve a significant reduction in the water absorption properties of the copolymer coating to increase the stability of the implants.

3.2.8 *In Vivo* Evaluation of PVB Implant Performance

Whilst it was determined that it was likely necessary to improve the stability of the PVB implants by reducing the hydrophilicity (and therefore water absorption) of the pH-responsive coating, it was not known if the *in vitro* model of the subcutaneous environment was sufficiently representative of the comparatively complex *in vivo* subcutaneous environment. For biomaterials, the foreign body response (FBR) represents a significant challenge to long-term function, primarily due to the

formation of a fibrous tissue capsule (FTC) during the encapsulation phase of the immune response.[19] Unlike conventional biomaterials, it was hypothesised that the FTC might be of benefit to the implants. For example, the FTC may effectively restrict the movement of the implant shortly after implantation and prevent its migration to other locations in the implanted animal, which may be important if successful implant consumption by feral cats is discovered to be location dependent. Importantly, reductions in the transport of small molecules (e.g., nutrients, oxygen)[20] have been reported between implanted biomaterials and surrounding tissues, when the biomaterial is encapsulated by a FTC. It was hypothesised that the formation of a FTC around the PPI, might confer a reduction in water transport from surrounding tissues, and potentially reduce the rate of water absorption. In addition, the FTC may constrain the swelling of the polymer coating, thereby providing some mechanical support and a reduced likelihood of coating rupture and implant failure.

To test this hypothesis and determine the stability of the implants *in vivo* during the development of the pH-responsive coating, a short-term stability trial was conducted. The *in vivo* stability of the PVB implants was investigated over 4 weeks using a murine model. Where, in reverse time order, male Sprague-Dawley rats (n = 3) were injected with three implants to assess stability at 4, 2, and 1 weeks (n = 3). A RFID microchip was also implanted for identification and as a control. The first PVB implant was implanted superficial to the left scapula, ~ 1 cm left of the spine, with subsequent implants positioned caudally along the animal (**Figure 3.8a**, top). In all cases the RFID microchip was implanted superficial to the right scapula, adjacent to the first PVB implant. Once the final time point was reached (i.e., 1 week), the integrity of the implants was assessed qualitatively prior to euthanasia, *via* computed tomography (CT) (Appendix, **Figure A3.2**), and again following post-mortem explantation and visual examination (**Figure 3.8b**).

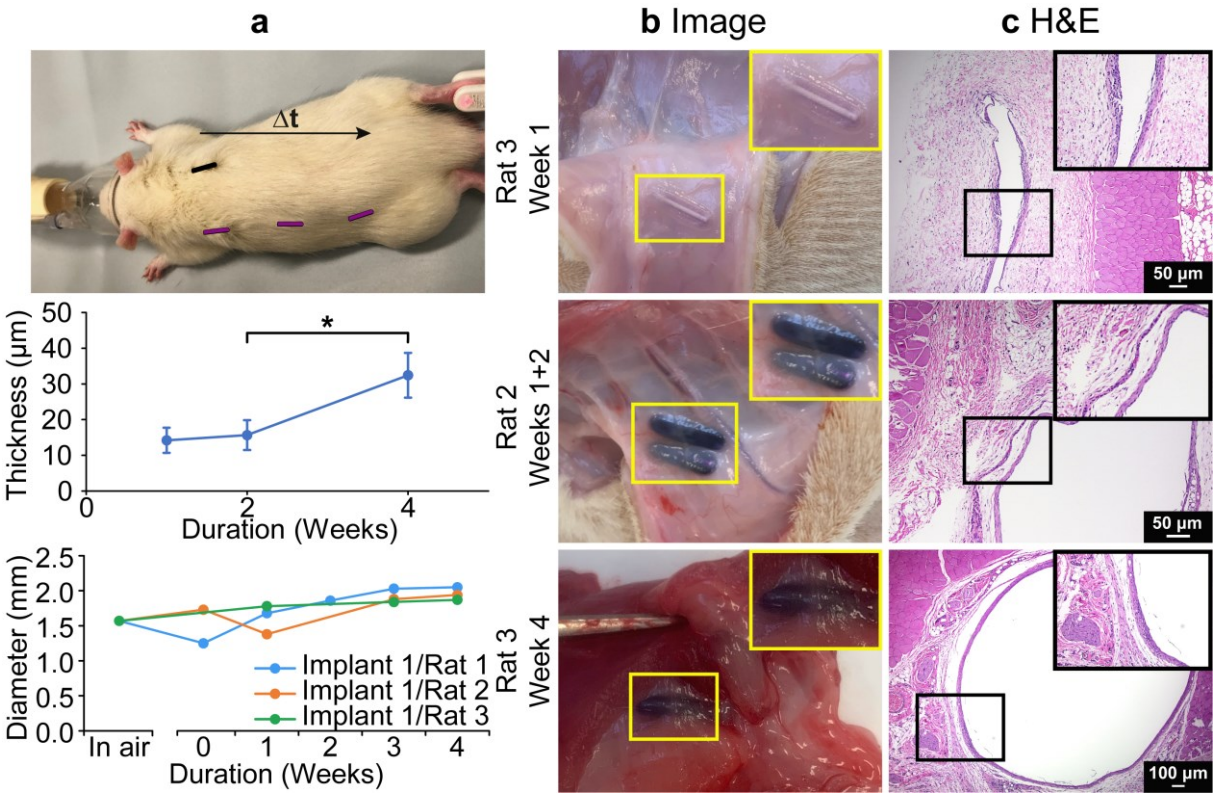


Figure 3.8: a) PVB Implant (purple) and RFID microchip (black) implantation locations (top). FTC thickness (µm) as measured from tissue explants using point-to-point measurements with values reported as mean ± std. dev. of n = 5 (week 1), and n = 15 (weeks 2 and 4) measurements *p < 0.05 x t-test of difference = 0 (vs ≠) (middle). PVB implant diameter measurements obtained from CT scans of implants immediately after implantation and *in situ* during the study (bottom). b) Macroscopic images (post-mortem) of PVB implants *in situ*, captured prior to explantation — note the swelling of the implants and the containment of the core material. c) Haematoxylin and eosin (H&E)-stained samples of the explanted tissue, revealing the fibrous capsule surrounding the PVB implants.

Like the *in vitro* stability experiment, all PVB implants exhibited osmosis-driven swelling *in vivo*, as shown in the post-mortem examination (**Figure 3.8b**) and CT images (Appendix, **Figure A3.2**). Weekly CT scans were performed on the implanted rats, and point-to-point measurements were used to determine whether a change in PVB implant diameter had occurred *in situ* (**Figure 3.8a, bottom**). All implants increased in diameter due to swelling during the study and reached a plateau ~ 3–4 weeks following implantation, with PVB implants reaching ~ 2 mm in diameter (**Figure 3.8a, bottom**). This suggested that an osmotic equilibrium had been reached within ~ 4 weeks following implantation. An apparent increase in RFID microchip diameter was also observed *via* CT (Appendix, **Figure A3.3a**),

which most likely resulted from measurement of the FTC that formed around the RFID microchips. Notably, two 1-week PVB implants had failed, as observed by the loss of their core contents (**Figure 3.8b**). However, no MB or RhB staining was observed in the bedding or vibrissae (respectively) of either rat, likely due to an insufficient dose of both dyes. The PVB implants and the surrounding tissues were collected, sectioned, and stained with haematoxylin and eosin (H&E) to assess FTC formation, and compare implant biocompatibility with the RFID microchips. Tissue sections were also stained with Masson's trichrome to determine the amount of type 1 collagen (see **Chapter 3.4.3** and **Figure A3.3**).

Histological analysis of the surrounding tissues revealed the formation of a FTC for the PVB implants at all time points (**Figure 3.8c**). Qualitative observations of the tissue samples showed the maturation of the tissue into a less cellular and more striated and collagenous fibrous capsule (**Figure 3.8c**). In addition, an increase in collagen — though not significant — was observed in week 4 (cf. week 1) (Appendix, **Figure A3.3b**). The observed changes in cell populations and increases in collagen that occurred in the tissue surrounding the implant (i.e., the formation of granulation tissue and its maturation into a collagenous, fibrous capsule)[21] were consistent with the FBR and the formation of a FTC. FTCs were well-defined at weeks 2 and 4 for all implants (n = 3), however only one of the three 1-week implants exhibited a measurable FTC (n = 1) (**Figure 3.8c**). The inconsistency of FTC formation for the PVB implants at week 1 was not correlated with failure, and as a result, was considered likely due to the implants being in the early stages of the FBR. Of the measured FTCs, there was no significant increase in thickness from week 1 to 2 (14.2 ± 3.5 μm to 15.7 ± 4.2 μm), though this was likely due to the inconsistent FTC formation at week 1, resulting in an insufficient sample size (**Figure 3.8a,** middle). However, FTC thickness increased significantly from weeks 2 to 4 (15.7 ± 4.2 to 32.4 ± 6.3 μm) (**Figure 3.8a,** middle). No rats exhibited marked inflammation at any time point, just fibrosis with occasional mononuclear cell infiltrate that decreased over time as collagen fibres became aligned and compacted. This tissue reaction was indistinguishable from that observed in response to conventional microchips (not shown), suggesting comparable biocompatibility.

FTC formation, a well-documented process for implanted non-degradable biomaterials, was expected as the coating — and by extension the implant — was

designed to be non-degradable in the mammalian subcutaneous environment. Although FTC formation was hypothesised to impede implant swelling, qualitatively there was no observable difference in the rate or extent of swelling. Overall, the PVB implants demonstrated moderate stability, with all the implants at weeks 2 and 4 found to be stable, though in a swollen state. However, two 1-week implants failed. Both 1-week implants were located most-caudally, where the subcutis is generally thinner and more restrictive. It was considered likely that this region imparted greater mechanical stress upon the implants and — coupled with the swelling and thinning of the PVB 50/50 coating resulting from osmosis — caused the ABS filament substrate to puncture the coating and the implant to prematurely fail. This combination of factors was likely not experienced by the 2- or 4-week implants because comparatively thick, and loose skin is present superficial to the left scapula, subjecting the 4- and 2-week implants to reduced mechanical stress and enabling the implants to reach an osmotic equilibrium during swelling, without failure.

These results indicated that whilst the PVB implants exhibited favourable stability *in vivo*, there was a need to mitigate swelling, and confine implantation to regions where lesser mechanical stress was likely to be exerted on the implants (i.e., superficial to the left scapula). Hypothetically, these changes could increase the stability of the implants, and ensure long-term stability *in vivo*.

3.3 Conclusions

It was hypothesised that the ratio of the two monomers VP and BMA could be varied to afford a copolymer with the desired physicochemical and thermal properties. The pH-responsiveness of the copolymer could be controlled by the proportion of VP, and to a lesser extent, BMA. The comparative hydrophobicity of BMA, and it's lower T_g value (20 °C) (cf. VP, T_g = 104 °C) could modulate the pH-responsiveness, and the T_g value of the resultant copolymer. A PVB copolymer with a VP:BMA ratio of 50:50 (PVB 50/50) exhibited the most favourable combination of T_g value (53.1°C) and solubility at pH 1.5 (7.1 ± 0.3 mg.mL^{-1}) and was compatible with fluidised-bed spray coating. Implants coated with a 315 µm-thick PVB 50/50 coating exhibited rapid release *in vitro* (27.7 ± 2.6 min) but exhibited failures within 100 d during *in vitro* stability testing. Similarly, the PVB

implants were stable *in vivo* in rats following subcutaneous implantation, for up to 4 weeks. However, implant failures were observed within the first week following implantation, likely due to a combination of swelling and mechanical stress, respectively, associated with the PVB 50/50 coating and implant location. These results highlighted the need to mitigate implant swelling observed *in vitro* and *in vivo*, to improve the stability of the implants. In addition to confining implantation to the left scapula, to minimise potential mechanical stresses caused by the thinner subcutis present in more caudal regions of the animals. As a result, further investigation of the VP-based pH-responsive system was undertaken, to produce a reverse enteric coating with reduced swelling and potentially superior stability.

3.4 Experimental

3.4.1 Materials

The materials described in Chapter 3 are the same as **Chapter 2.6.1**, unless stated below.

All reagents were used as received unless otherwise specified. VP (97%) and BMA (99%) were purchased from Sigma-Aldrich (St. Louis, United States) and passed through basic aluminium oxide to remove inhibitors immediately prior to use. Analytical grade 1,4-dioxane, DCM, hexanes, EtOH (100% undenatured), NaOAc, and high-performance liquid chromatography (HPLC) grade dimethylformamide (DMF) and THF were purchased from ChemSupply (Gillman, Australia). AIBN (12% $w.w^{-1}$ in acetone), PEG (M_n = 10 kDa), MB (≥ 82%), RhB (≥ 95%), basic aluminium oxide, $CDCl_3$, and lithium chloride (LiCl, technical grade) were purchased from Sigma-Aldrich (St. Louis, United States). PMMA standards for gel permeation chromatography were purchased from PSS Polymer Standards Service GmbH (Mainz, Germany). pH 1.0, 1.5 and 2.0 solutions were prepared from 0.2 M potassium chloride (KCl) and 0.2 M hydrochloric acid (HCl). Cylindrical ABS rods (0.55 mm × 250 mm) were purchased from BNA Model World (Moorabbin, Australia). Sterile standard microchip (2.12 × 12 mm) syringe implanters were purchased from Faread Technology Co. Ltd. (Jiaxing, Zhejiang) and used as received or with modification (*via* the replacement of the microchip with an implant). Mini microchip (1.4 × 8.5 mm) syringe implanters were donated

by Microchips Australia Pty Ltd. (Keysborough, Victoria). Ultra-high purity nitrogen (N_2) and argon (Ar) were purchased from BOC Ltd. (North Ryde, Australia). Polylite™ Polylactic acid (PLA) 3D printing filament (1.75 mm) (Polymaker, Shanghai, China) was purchased from 3D Printing Solutions (Para Hills West, Australia). Suglets® sugar spheres (12/14 mesh, 1.4–1.7 mm diameter) were provided by Colorcon® (Scoresby, Victoria, Australia).

3.4.2 Instrumentation

The instrumentation details are as outlined in **Chapter 2.6.1**, unless stated below.

Gas Chromatography

Polymer syntheses were monitored, and the composition of the copolymers determined by GC using a Shimadzu GC-2010 gas chromatograph (St. Louis, MI, United States), equipped with a flame ionisation detector (FID), and fitted with a Supelco SPB-35 (Supelco, Bellefonte, United States) stationary phase column (30.0 m × 0.25 mm, 0.25 µm). The GC was operated in linear velocity mode with nitrogen as the carrier gas, at a linear velocity of 56.5 $cm.s^{-1}$. Sample port and FID temperatures of 250 °C were utilised. A split injection volume of 1.0 µL (split ratio 50:1) and a temperature program of 40 °C (1 min) to 180 °C (2 min) at 22.50 $°C.min^{-1}$ was employed for each analysis. At predetermined timepoints, a 50 µL aliquot of the polymerisation solution was diluted in DCM (1.5 mL) and analysed to determine the consumption of the monomers with respect to their t_0 concentrations, using the solvent (1,4-dioxane) as an internal reference.

Proton Nuclear Magnetic Resonance Spectroscopy

^1H NMR spectroscopy was performed at 298 K (25 °C) using a Bruker Avance III HD 600 MHz spectrometer (Billerica, United States) operating at 600 MHz. Samples were dissolved in $CDCl_3$, and the residual chloroform solvent peak was used as an internal reference ($CHCl_3$; δ_H 7.26 ppm).

Gel Permeation Chromatography

The molecular weight characteristics of the copolymers were determined by GPC, using a Shimadzu Prominence liquid chromatography system fitted with a DRI detector (Shimadzu, RID-20A) and two Shimadzu columns (GPC-80MD and GPC-804D) connected in series (Shimadzu Corporation, Kyoto Japan). Operating at 40 °C, THF was used as the eluent at a flow rate of 1 $mL.min^{-1}$, with a sample concentration of 5 $mg.mL^{-1}$ and an injection volume of 50 µL. All samples were filtered through a 0.45 µm nylon syringe filter prior to injection. LabSolutions software (v5.93) (Shimadzu, Kyoto, Japan) was used to determine molecular weight characteristics with reference to a conventional column calibration of narrow molecular weight PMMA standards. The solubility of the copolymers was determined using the same system operating at 70 °C with 0.1 M LiCl in DMF as the mobile phase.

Modulated Differential Scanning Calorimetry

MDSC was performed on a Discovery DSC250 (TA Instruments, New Castle, United States) under nitrogen flow (cell purge flow rate, 50 $mL.min^{-1}$). Samples (≈ 10 mg) were heated from −80 to 250 °C at a ramp rate of 3 $°C.min^{-1}$, with a modulation period and modulate temperature amplitude of 40 s and ± 0.64 °C, respectively. Standard Tzero aluminium pans (TA Instruments, New Castle, DE, United States) were used for all copolymer and coating formulation samples. Copolymer glass transition temperatures were determined at the point of inflection between the onset and end temperatures of the transition from the reversing heat flow ($W.g^{-1}$) signal, using Universal Analysis software (v4.5A) (TA Instruments, New Castle, United States).

Modulated Thermogravimetric Analysis

Modulated high-resolution thermogravimetric analysis (MTGA) was performed on a Discovery TGA5500 (TA Instruments, New Castle, DE, United States) under nitrogen flow (sample purge flow rate, 25 $mL.min^{-1}$). In aluminium pans, samples (≈ 10 mg) were analysed from 30 to 600 °C at a ramp rate of 5 $°C.min^{-1}$, with a modulation period and modulate temperature amplitude of 200 s and ± 5.00 °C, respectively. A sensitivity value of 1 and a resolution number of 6 was used for all

analyses. The weight loss and decomposition temperatures were determined from the step change in the weight (%) and peak maximum of the derivative weight (%.°C^{-1}) signals, respectively, using Universal Analysis software (v4.5A) (TA Instruments, New Castle, DE, United States).

Fluidised-bed Spray Coating

Implant spray coating was conducted using a benchtop Mini Coater/Drier 2 (Caleva Process Solutions Ltd., Dorset, England). The formulation being spray coated was supplied to the instrument using a NE-1000 Programmable Single Syringe Pump (New Era Pump Systems, Inc., Farmingdale, New York) fitted with a disposable Luer lock syringe containing the formulation. All the coating formulations were pumped at a flow rate of 15.2 mL.h^{-1} with an atomising air pressure of 5 psi. The temperature-controlled fluidisation air was set to either ambient temperature (23 °C) or 40 °C for coating at these temperatures. The fluidisation air flow velocity was selected based on the size of the batch being coated to ensure adequate fluidisation and was generally 50–80% during core coating and 80–100% during copolymer coating.

Scanning Electron Microscopy

SEM was performed on a Merlin Field Emission Scanning Electron Microscope (FE-SEM) (Zeiss, Oberkochen, Germany), through the detection of type II secondary electrons (SE2). SEM samples were adhesively mounted on carbon tape coated stubs, then sputter coated with platinum using an Agar High Resolution Sputter Coater (Agar Scientific, Essex, United Kingdom) immediately prior to analysis. Micrographs were acquired at an accelerating voltage of 2 kV, and a working distance of ~ 5 mm.

Ultraviolet-visible Light Spectrophotometry

UV-vis spectrophotometry was performed on an Evolution 260 Bio spectrophotometer fitted with a single cell Peltier system (Thermo Scientific, Massachusetts, United States). All analyses were performed using a quartz cuvette (10 mm path length) fitted with a stirrer bar, under maximum stirring, at 25 or 37 °C.

3D Printing.

The 3D printed mounting block (Appendix, **Figure A3.4**) was designed in Solidworks (2020 SP5.0) and printed from PLA 3D printing filament, using a Prusa i3 MK3S+ 3D printer (Prusa Research, Prague, Czech Republic).

3.4.3 Procedures

The procedures in Chapter 3 were conducted as outlined in **Chapter 2.6.3** and **Chapter 3.4.3**, unless stated below.

Synthesis of Poly[(2-vinylpyridine)$_x$-co-(butyl methacrylate)$_y$]

The copolymers of poly[(2-vinylpyridine)$_x$-*co*-(butyl methacrylate)$_y$] (PVB x/y) were synthesised with x:y ratios of 40:60, 50:50, and 60:40 mol% (VP:BMA). A representative description of the synthesis of PVB 50/50 is provided.

Inhibitor-free VP (25.6 mL, 238 mmol) and BMA (37.8 mL, 238 mmol) (mol% VP:BMA 50:50), and AIBN solution (6.51 mL, 4.8 mmol)) were combined ([total monomer]:[initiator] 100:1 mole ratio) in 1,4-dioxane (50% v.v^{-1}) under an inert atmosphere (Ar) and heated at reflux with stirring. Additional AIBN solution (6.51 mL, 4.8 mmol) was added after 1 and 2 h to maximise monomer conversion. After 3 h, the reaction was cooled (~ 25 °C), the crude reaction mixture (CRM) was diluted with THF (~ 20% v.v^{-1}), and the copolymer product precipitated from hexanes (1:10 v.v^{-1} CRM:hexanes) in a conical flask. The supernatant was decanted, and the precipitate was redissolved in THF (~ 75 mL), transferred to a round-bottomed flask, concentrated *in vacuo* (40 °C, 10 mbar), and then dried *in vacuo* (23 °C, 0.02 mbar) to afford the polymer as a pale-yellow solid. The percentage of monomer conversion (determined by GC) was 95% and the isolated yield was > 99%. GPC M_n = 16.2 kDa, M_w = 31.9 kDa, $Đ$ = 1.97. ^{1}H NMR (600 MHz, 21 °C, $CDCl_3$) δ_H 8.45 (br s, CH, VP RU), 7.44 (br s, CH, VP RU), 6.99–6.50 (m, CH, VP RU), 3.87 (br s, OCH_2, BMA RU), 3.53–2.32 (m, CH, VP RU), 2.32–1.02 (m, CH_2, BMA and VP RUs), 1.02–0.16 (m, CH_3, BMA RU) ppm (**Figure 3.2**).

Preparation of Implant Coating Formulations

Implant NaOAc Core Formulation (MB and RhB)

The NaOAc core formulation was prepared by dissolving PEG 10 kDa (15 g), NaOAc (15 g) and MB (200 mg) and RhB (200 mg) in 70/30 $v.v^{-1}$ EtOH/water under stirring. The temperature-controlled fluidisation air flow was set to 40 °C throughout the coating of the NaOAc core formulation.

Implant Reverse Enteric Coating Formulation (PVB)

The pH-responsive, reverse enteric copolymer formulation was prepared by dissolving PVB 50/50 (10 g) in EtOH (100 mL) under stirring to afford a 10% $w.v^{-1}$ solution. The fluidisation air flow was at ambient temperature (23 ± 1 °C) throughout the coating of the pH-responsive copolymer formulation.

Copolymer Solubility

Powdered copolymer samples (~ 10 mg) were combined with 1 mL of a pH 1.0, 1.5, or 2.0 solution, in microcentrifuge tubes. The tubes were rotary mixed for 48 h at 37 °C, then centrifuged (15 krpm, 3 min), to separate the solubilised copolymer in the supernatant solution, and the insoluble copolymer solid. A 50 µL aliquot of the supernatant was removed, diluted (1:10) in GPC mobile phase (0.1 M LiCl in DMF) and analysed *via* GPC. The peak area of the copolymer was correlated to a calibration curve (*vide infra*), to determine the concentration of the copolymer in the sample, and therefore, its solubility.

Seven-point calibration curves were prepared for each copolymer by correlating the known mass of a copolymer standard to its peak area value obtained *via* GPC analysis (Appendix, Figure A3.1). Copolymer standards were prepared by vortex mixing (2 krpm) a 10 mg sample in a pH 1.0 solution (1 mL, 10 $mg.mL^{-1}$) until homogeneity, and conducting a 1:10 dilution in the mobile phase. Each copolymer standard was analysed *via* GPC at injection volumes from 10–100 µL, to afford a seven-point calibration curve.

Copolymer Water Absorption Testing

A 15-ton hydraulic press was used to prepare powdered copolymer samples (~ 150 mg) as discs (13 mm diameter × 1.2 mm height). The copolymer discs were dried for 72 h *in vacuo* (0.01 mbar, 23 °C), then weighed and submerged in PBS (20 mL, pH 7.4) in sealed vials and stored at 37 °C. The copolymer discs were removed periodically from the solution and any solution present on the disc surface was removed using lint-free tissue paper (Kimwipes™) prior to weighing. The mass of the absorbed PBS solution was then calculated from the increase in disc mass. The copolymer discs were monitored for 40–60 d. All copolymers were analysed in triplicate, and water absorption values were reported as the mean ± std. dev.

Implant Manufacture

ABS filament substrates were prepared by cutting cylindrical ABS rods into pieces of 0.59 ± 0.07 mm diameter and 7.55 ± 0.03 mm length (n = 900), using a cutting jig and a scalpel. A statistically relevant number of implant substrates (n = 100) were measured using digital callipers and weighed. The substrates were then coated with a core formulation. A sequential coating process was employed, with each coating cycle having a duration of 45 min. Following each coating cycle, the implant cores were dried (0.1 mbar, 23 °C) for a minimum of 20 min, then measured and weighed. From the increase in the average mass of the implant cores, the mass of the core coating was determined. In this way, the coating mass was tracked throughout the coating process, until ~ 6 mg of the core formulation had been deposited. Following the final coating, the implant cores were dried for a further 16 h (0.1 mbar, 23 °C) prior to storage in a desiccator. Similarly, implant cores were coated with the pH-responsive copolymer coating formulation until a desired coating thickness was reached, as determined by the change in the average measured implant diameter (using digital callipers) following coating. The implant cores bearing a copolymer coating were dried after the intermediate and final coatings.

Implant Embedment and Microtoming

Implant samples were embedded in Araldite 5 Minute Epoxy Adhesive (Selleys, Sydney, Australia) prepared as per the manufacturer's instructions, in a 5 × 13 × 5 mm silicone mould, then affixed to a 29 × 42 × 8 mm 3D-printed mounting block using the same adhesive (Appendix, **Figure A3.4**). Sections (5–10 µm-thick) were cut from the embed using a Microm HM 325 (Thermo Scientific, Massachusetts, United States) microtome, until the midpoint of the implant was reached, and a cross-section was obtained. Implant cross-sections were imaged under an Olympus SZ61 stereomicroscope fitted with a Gryphax Arktur (Jenoptik AG, Jena, Germany) camera module, using the Gryphax software (v2.2.0.1234). In the obtained images, a series of point-to-point measurements were made from the outer perimeter of the polymer coating to that of the core coating using ImageJ software (v1.53g). A total of 12 measurements were made across the sides of the implant, and 10 across the ends. These data were used to determine the average coating thickness at the sides and ends, and an overall coating thickness. Representative images of implants with point-to-point measurements at each coating thickness are available in the Appendix, **Figure A3.5**.

In Vitro Stability Experiments

In vitro stability studies were conducted as described in **Chapter 2.6.3**, using an as-prepared implant, instead of a HSDV.

In Vitro Release Experiments

The pH 1.0 release solution was prepared from 0.1 M HCl, and the pH 1.5 release solution was prepared as described in **Chapter 2.6.3**. The pH values of all release solutions were adjusted to within ± 0.02 units of the target pH as described in **Chapter 2.6.3.** Implant release was monitored inline using UV-vis spectrophotometry. In a quartz cuvette, implants were suspended in 3.5 mL of either pH 1.0 or 1.5 release solution using a polyester mesh, and under stirring, the presence of MB in the release solution was monitored *via* its absorbance at 664 nm (λ_{max}). In all release experiments, the start of implant core release was defined as the time at which 5% of the maximum absorbance had been reached (initial release). Meanwhile, the end of implant core release was defined as the

time at which 90% of the maximum absorbance had been reached (complete release).

In Vivo Stability Experiments

Animal work was conducted under approval S-2015-176 from the University of Adelaide Animal Ethics Committee.

PVB 50/50 coated, NaOAc core implants were sterilised using an ultraviolet-C light source (30 min exposure), then manually loaded into sterile syringe implanters (2 mm) and stored in vacuum sealed storage bags until immediately prior to use. All processing was conducted in a laminar flow cabinet using aseptic techniques. Male Sprague-Dawley rats (10–11 weeks of age, n = 3) were each subcutaneously implanted with a mini microchip for identification (superficial to the right scapula) and three implants (superficial to the left scapula and two locations caudally, approximately 1 cm left of the spine). Sterilised implants and microchips were administered under general anaesthesia *via* syringe implanters (Appendix,

Figure A3.6). Anaesthesia was induced using a combination of intraperitoneally administered medetomidine (0.1 $mg.kg^{-1}$) and fentanyl (100–200 $\mu g.kg^{-1}$), and maintained with isoflurane (1–2%, oxygen flow 300–600 $mL.min^{-1}$). All rats were held on a warming pad during recovery. Implants intended for different durations *in situ* (i.e., 4, 2, 1 week(s)) were implanted in reverse time order. Rats were scanned using computed tomography (Toshiba Alexion Advance Edition 16 slice) at each implantation and at the conclusion of the experiment. Rat body weights were recorded every 2–5 d, throughout the study and are summarised in the Appendix, (**Figure A3.3c**). Rats were euthanised using carbon dioxide (CO_2) and a post-mortem examination conducted where implants were exposed and photographed prior to tissue samples being collected in 10% neutral buffered formalin (ThermoFisher Scientific). Tissue samples were trimmed, dehydrated, and embedded in paraffin, and subsequent sections stained using H&E.

Histological Analysis via Optical Microscopy

Images of the FTC surrounding implants were taken at 400× magnification on an Olympus BX53 microscope (Olympus Corporation, Tokyo, Japan) with a DP25

camera and Olympus LabSens software (v1.1). Optimising contrast within the LabSens software was the only post-production alteration. To measure FTC thickness, an average thickness was calculated from five point-to-point measurements made around the circumference of each FTC section.

FTC composition (% type I collagen) was measured through colour thresholding, using ImageJ software. Each image was duplicated, then all images were cropped to obtain sections showing the full width of the fibrous capsule, without any surrounding tissue. Image analysis methods were based on those tested by Hong et al.[22] for determining dermal microstructure. Settings for colour thresholding were adapted to suit the colour range in the images for this study. RGB levels were used to select all possible collagen (stained by aniline blue in MT). Specific settings were chosen by adjusting the RGB parameters to suit 15 trial images and using the average of these values to reduce any discrepancies when collecting data from images with variable stain colour saturation. The ImageJ thresholding parameters were as follows: Thresholding method: Moments, Thresholding colour: Black, Colour space: RGB, Dark background: Not selected, Selection of collagen area only: Red 0–154; Green 74–227; Blue 182–255, Selection of total capsule area: Red 0–255; Green 0–225; Blue 0–255.

Computed Tomography

CT scans were used to determine implant integrity and measure implant diameter *in vivo*. Scans were reconstructed using the bone 0.5 volume settings (resolution 0.172 × 0.172 × 0.5 mm). To determine the diameter of each implant, an average diameter was calculated from measurements made at three points along the length of the implant. For visual demonstration purposes, the CT images were adjusted (*via* exposure, offset, and gamma correction parameters) in Adobe Photoshop (v22.4.1), to provide the best contrast for the implant.

Statistical Analyses

All results are expressed as mean ± std. dev. The mean values of fibrous tissue capsule thickness, and type 1 collagen content were compared between two groups using unpaired two-tailed Student's t-tests. Only p-values < 0.05 were considered significant. All statistical tests were performed using the Minitab 17

(v17.1.0) software package. Exact p-values, t-values, and degrees of freedom (DF) are summarized in the Appendix (**Table A3.1**).

3.5 Appendix

3.5.1 Supplementary Figures

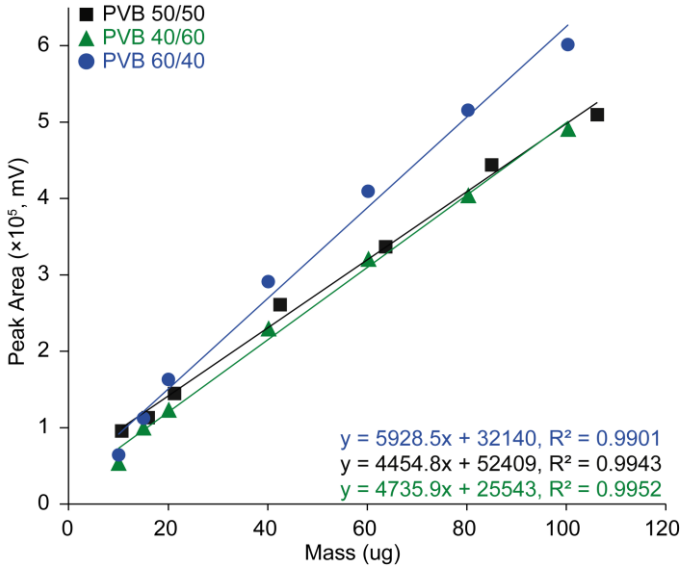


Figure A3.1: GPC calibration curves prepared for the copolymer series, from aqueous solutions of each copolymer (10 mg.mL^{-1}, pH 1.0), injected at volumes between 10–100 µL.

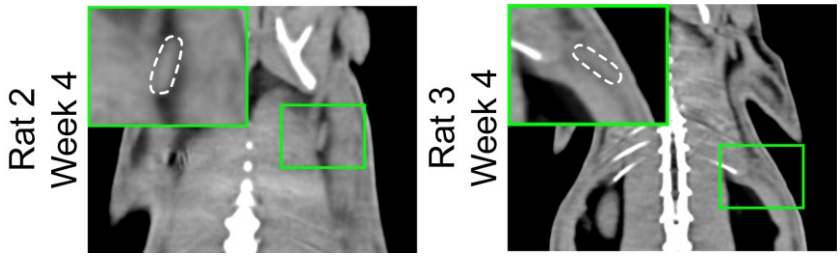


Figure A3.2: CT scans of intact PVB implants captured prior to euthanasia, with implants outlined with dashed white lines.

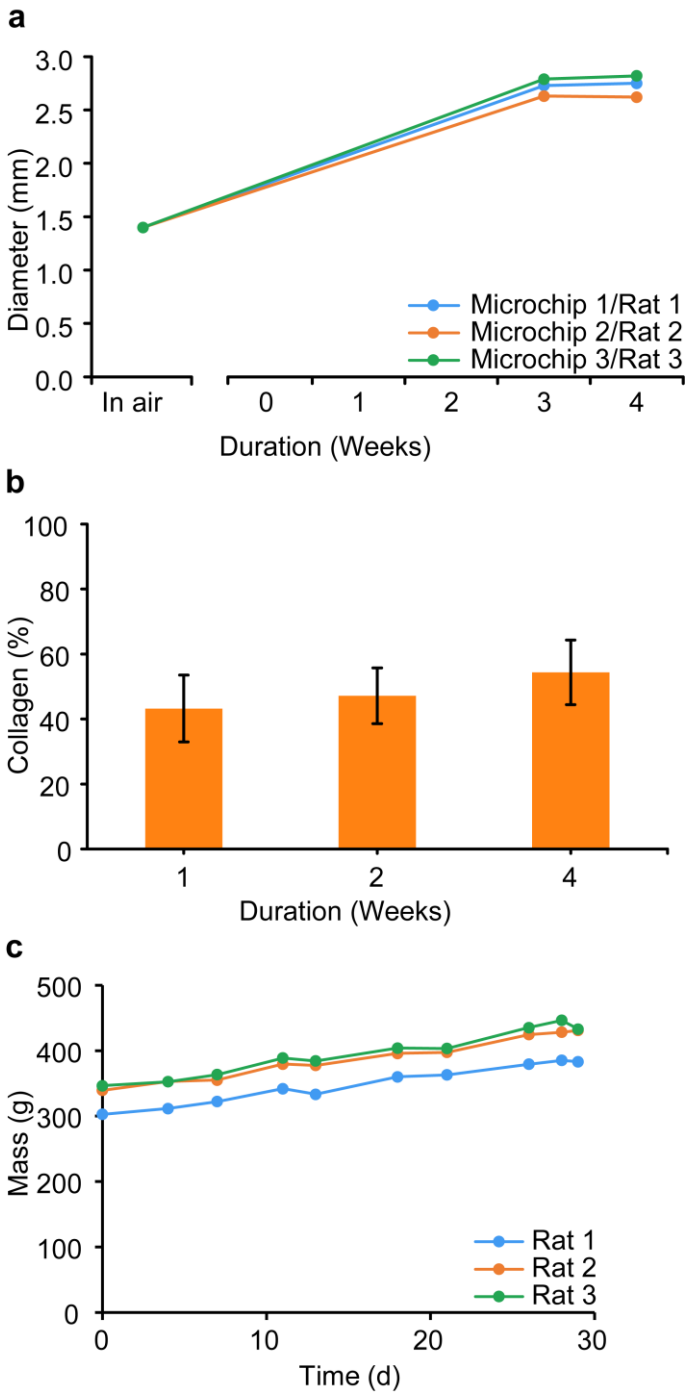


Figure A3.3: Graphs showing a) diameter measurements of the implanted control RFID microchips (n = 3), before (in air) and after (weeks 3 and 4) encapsulation in a FTC, obtained from CT scans during the *in vivo* stability study, b) histological analysis results of type I collagen content as measured from tissue explants using colour thresholding in ImageJ, with values reported as mean ± std. dev. from n = 6 (week 1), n = 2 (week 2) and n = 9 (week 4) measurements, and c) male Sprague-Dawley rat body masses (n = 3), recorded during the *in vivo* stability study (~ 30 d).

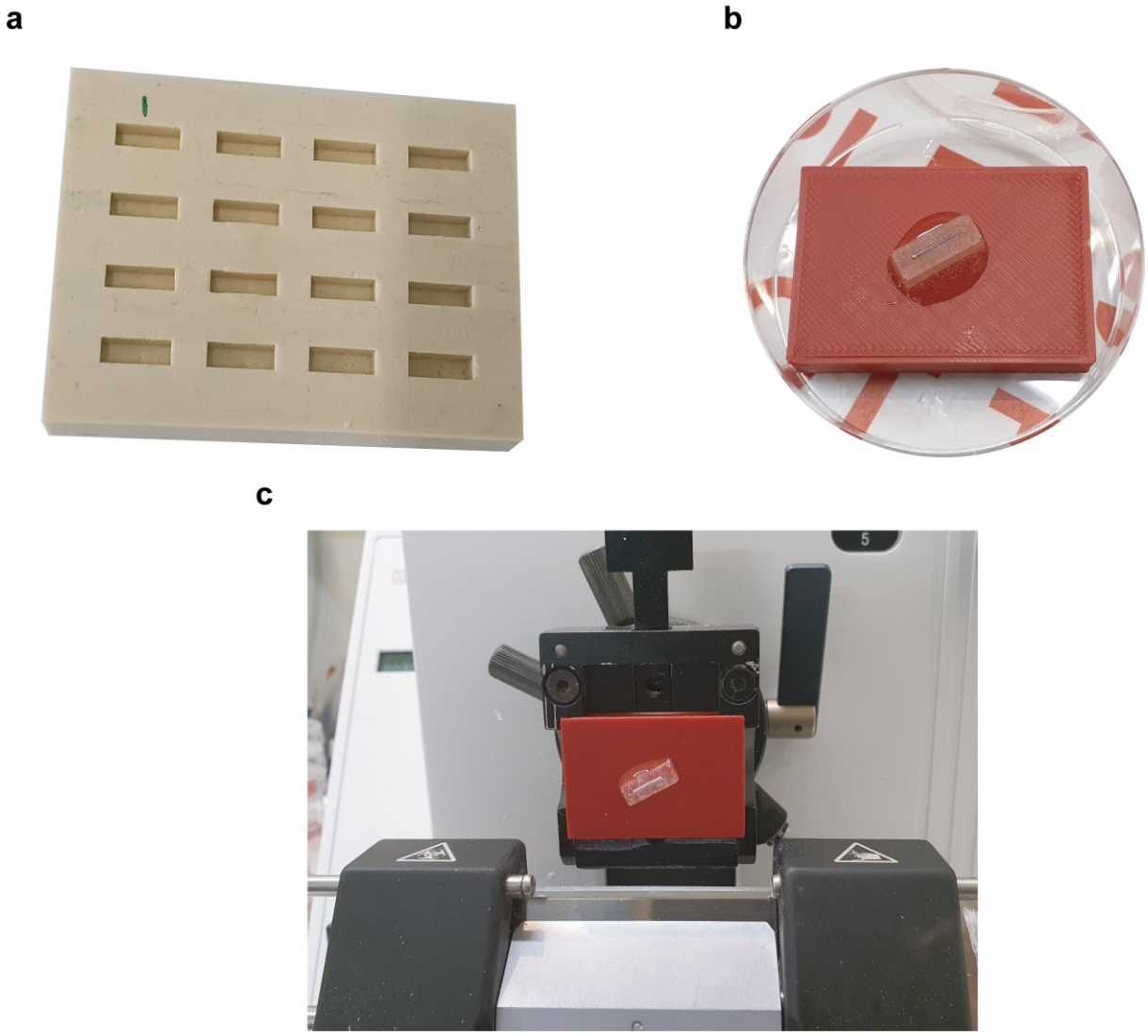


Figure A3.4: a) The silicon mould used for embedding implants in two-part epoxy. b) An embed affixed to a 3D-printed mounting block. c) The mounted embed fitted in a Thermo Scientific Microm HM 325 microtome.

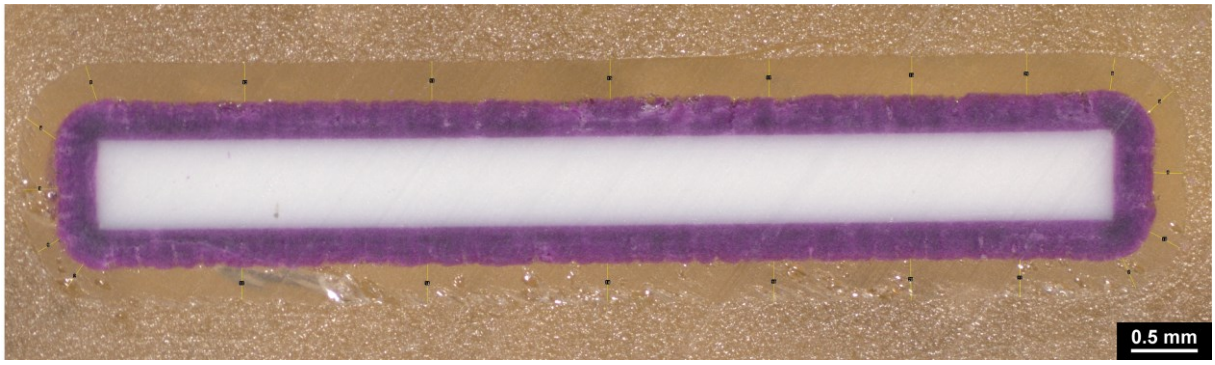


Figure A3.5: Example of an epoxy-embedded and microtomed PVB implant, and point-to-point measurements used to determine the thickness of the copolymer coating.

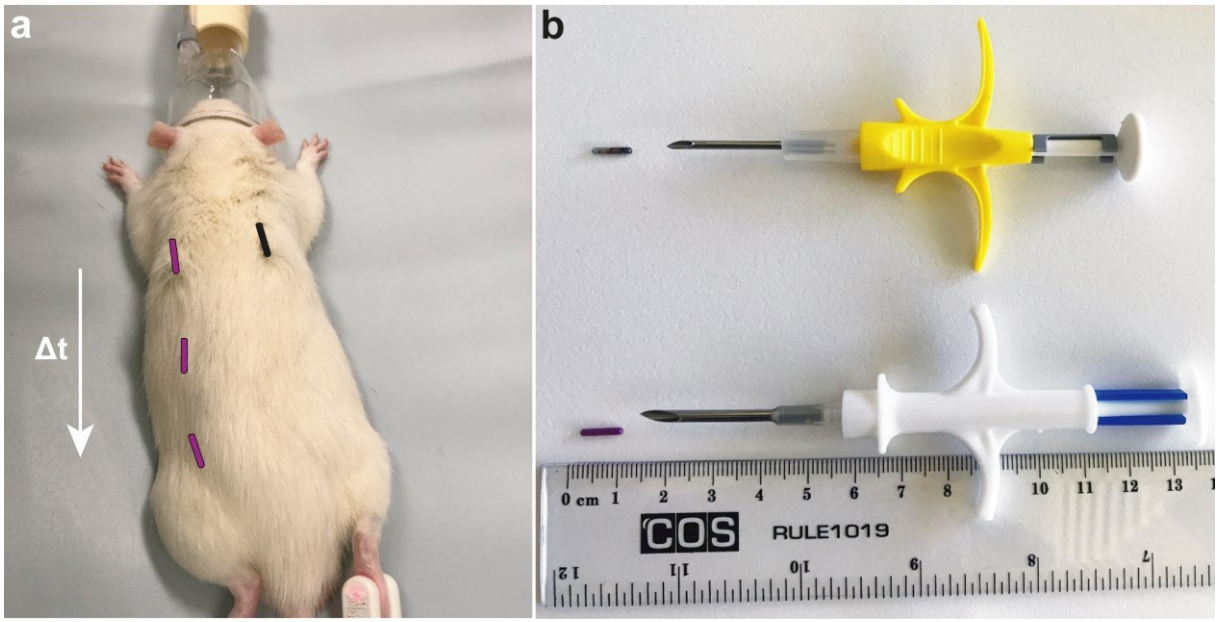


Figure A3.6: Images showing a) the locations of the PVB implants (purple) and the mini microchip (black) (superimposed over an image of a rat) for the *in vivo* stability study. b) A mini microchip and syringe implanter (1.4 × 8.5 mm) (top), and a PVB implant and syringe implanter (2.12 × 12 mm, bottom), both used during the *in vivo* stability study.

Table A3.1: Summary of two-tailed Student's t-test results. Tests were performed utilising a t-test of difference = 0 (vs. ≠).

Test of Mean	t-value	DF	p-value
Collagen (%) Week 1 versus Week 2	-0.70	7	0.507
Collagen (%) Week 2 versus Week 4	-8.31	24	<0.01
Collagen (%) Week 1 versus Week 4	-2.03	11	0.067

3.5.2 Copolymer Water Absorption: Effect of Excipients

To determine whether water absorption could be further minimised without altering the copolymer composition, or reducing the solubility of the copolymer, the addition of common hydrophobic excipients was investigated. Due to the favourable solubility and T_g value of PVB 50/50, it was selected as the target copolymer to determine the effects of hydrophobic excipients octadecanol and micronised talc. To prepare homogeneous mixtures, samples of PVB 50/50 were separately solubilised with 12.7, 22.5, and 30.3% w.w^{-1} octadecanol (N.B., based

on total mass of polymer and excipient) in DCM, then concentrated *in vacuo* to afford a homogenous solid. The solid was then ground into a fine powder and compressed into polymer discs. Due to the insolubility of talc in common organic solvents, it was physically mixed with powdered PVB 50/50 to afford talc concentrations of 10, 20, and 30% w.w^{-1}, and compressed into polymer discs.

Initially, the water absorption of the PVB 50/50 octadecanol samples fluctuated slightly before reaching a more constant value after 40 d (**Figure A3.7a**). Overall, the addition of octadecanol reduced the extent of water absorption when present in a concentration of 22.5 and 30.3% w.w^{-1}, decreasing water absorption to ~ 1.7% w.w^{-1} and 1.6% w.w^{-1}, respectively. The incorporation of 12.7% w.w^{-1} octadecanol had no measured effect on water absorption compared to neat PVB 50/50. In contrast, the incorporation of 10% w.w^{-1} talc greatly increased the extent of water absorption (**Figure A3.7b**) from ~ 2.5% to ~ 10% w.w^{-1}. However, samples containing 20 and 30% w.w^{-1} talc were found to be extremely fragile with almost all samples breaking during handling and as a result no data was recorded.

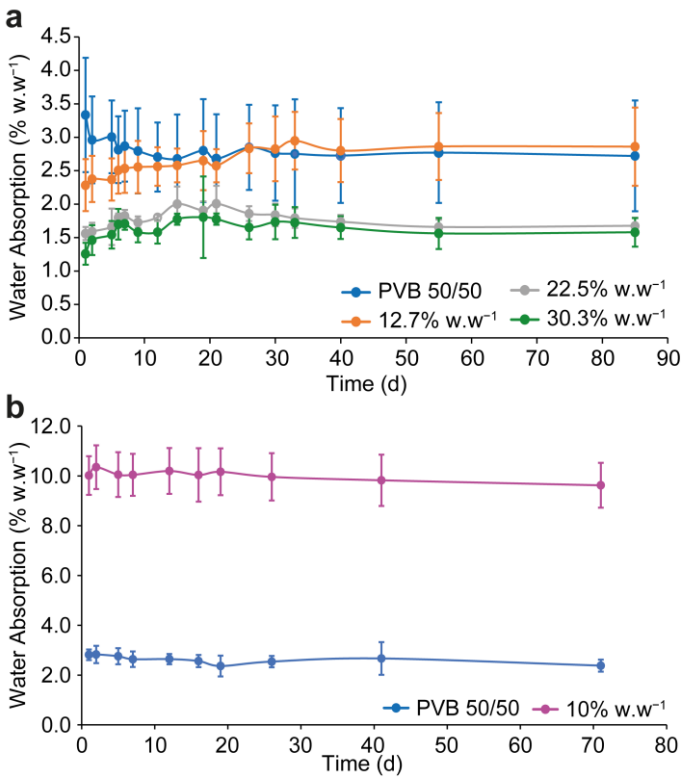


Figure A3.7: Water absorption exhibited by PVB 50/50 without and with the addition of the hydrophobic excipients a) octadecanol (12.7, 22.5, and 30.3% w.w^{-1}) and b) micronised talc (10% w.w^{-1}). All values are reported as mean ± std. dev. (n ≥ 4).

These data showed that — to an extent — the water absorption of PVB could be tuned further *via* the incorporation of the hydrophobic excipient octadecanol. In contrast, the addition of talc increased water absorption. Though this was an undesired outcome, it was hypothesised that talc may serve as an effective anti-adherent during the coating process. Considering this, neat PVB 50/50, PVB/octadecanol (22.5% $w.w^{-1}$) and PVB/talc (10% $w.w^{-1}$) formulations were investigated for their compatibility with fluidised-bed spray coating.

Initially, EtOH was also found to be the most effective solvent for the PVB/octadecanol (22.5% $w.w^{-1}$), and PVB/talc (10% $w.w^{-1}$) formulations, forming a solution and a dispersion (respectively). However, using the same formulation concentration (10% $w.v^{-1}$) and spray coating parameters as the PVB 50/50 formulation, spray coating was unsuccessful. The PVB/octadecanol (22.5% $w.w^{-1}$) formulation was found to evaporate too slowly and caused agglomeration, resulting in the failure of the trial batches. As shown in **Figure A3.8a**, investigation of an PVB/octadecanol (22.5% $w.w^{-1}$) coated implant *via* SEM, revealed a thin, incomplete coating with pores. The observed agglomeration could not be mitigated through the optimisation of the spray coating parameters and appeared to be caused by the presence of octadecanol in the formulation. In contrast, the PVB/talc (10% $w.w^{-1}$) formulation appeared to produce an adequate film coating. SEM analysis of a PVB/talc (10% $w.w^{-1}$) coated implant (**Figure A3.8b**) showed a comparatively cohesive film coating, with particles of a few microns present on the implant surface. It was unclear whether these particles were indicative of slight dusting of the copolymer, or talc, though it was possibly a combination of both. The presence of talc in the formulation caused repeated nozzle blockages during coating, and significantly increased the frequency of required cleaning. This drastically reduced the efficiency of the spray coating process but could not be rectified through optimisation of the coating parameters. The evaporation and nozzle blockage issues encountered when coating with octadecanol and talc respectively, precluded their continued investigation.

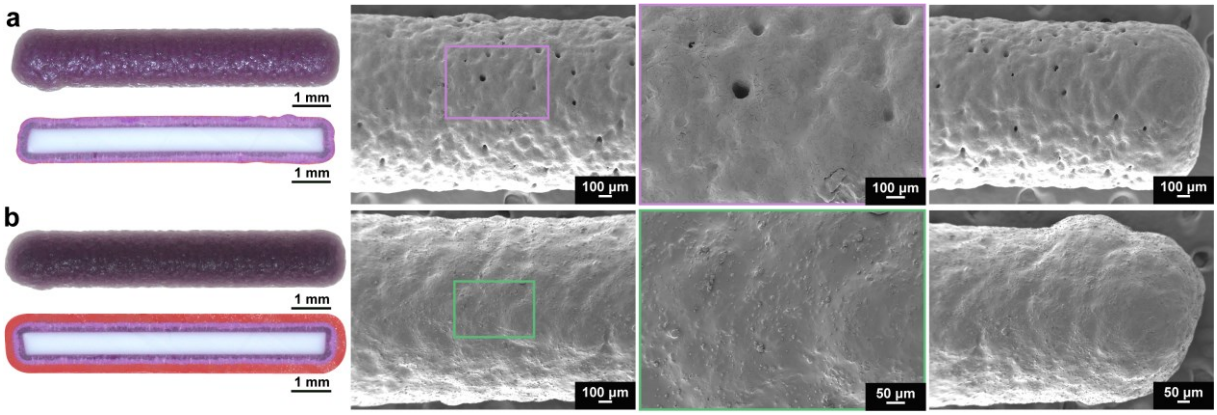


Figure A3.8: Representative digital images and scanning electron micrographs of a) a NaOAc core and PVB/octadecanol (22.5% w.w^{-1}) coated implant and b) a NaOAc core and PVB/talc (10% w.w−^{1}) coated implant.

3.5.3 Evaluation of the PVB Copolymers 60/40 and 40/60 as Reverse Enteric, Taste-masking Coatings

Methods

Suglet® Fluidised-Bed Spray Coating

A model drug formulation was prepared by solubilising PEG 10 kDa (7.5 g) and RhB (1.3 g) in 70:30% v.v^{-1} EtOH:water (170 mL). The model drug formulation was introduced to the spray coater *via* a syringe pump operating at a flow rate of 15.2 mL.h^{-1} and atomised using an atomising air pressure of 5 psi. Suglets® (n = 1800) were fluidised with a fan speed of 90% and fluidisation air temperature of 40 °C, throughout the coating. The formulation was applied in a single coating cycle (45 min), after which the coated Suglets® were dried *in vacuo* (0.02 mbar, 23 °C, 16 h), and stored in a desiccator prior to use.

Reverse enteric copolymer coating formulations were prepared by solubilising PVB 40/60 or PVB 60/40 in EtOH (50 mL). Reverse enteric copolymer coatings were applied using the same parameters as the model drug formulation, except the fluidisation air temperature was set to ambient temperature (23 °C). Suglets® (n = 340) were coated in two cycles (45 min each, 90 min total) for each copolymer, to afford weight gains of 5.2–5.4% w.w^{-1}. The coated Suglets® were dried *in vacuo* after the first cycle (0.02 mbar, 23 °C, 20 min), and again after the second (16 h), then stored in a desiccator prior to use.

Suglet® Reverse Enteric Coating Performance (In Vitro)

A simulated salivary fluid (phosphate-buffered, pH 6.8 solution) was prepared from a pH 7.4 PBS solution, *via* the addition of 0.1 M HCl. Suglets® coated with both the model drug formulation and a reverse enteric copolymer coating were submerged in the pH 6.8 solution (3.0 mL) and stored at 37 °C, to mimic human salivary conditions. Samples were monitored periodically, and taste-masking failure was determined qualitatively, by the presence of RhB in the receiving solution.

Suglets® coated with both the model drug formulation and a reverse enteric copolymer coating were suspended in a pH 1.5 solution (3.5 mL) at 37 °C, under stirring, to mimic the human gastric environment. The presence of RhB in the receiving solution was monitored inline by UV-vis spectrophotometry (λ_{max} = 556 nm), to determine the initial and complete release times of RhB.

Results and Discussion

Fluidised-Bed Spray Coating

A model drug formulation and reverse enteric copolymer coatings were applied to Suglets® sugar spheres, to evaluate the performance of the copolymers as taste-masking formulations (**Table A3.2**).

Table A3.2: Summary of Suglet® batch properties before and after coating with model drug and copolymer formulations.

Coating	$n_{Suglets®}$	Mass Gain (% w.w^{-1})	Mass Coated (µg per Suglet®)
PEG/RhB	1805	6.2	209
PVB 60/40	335	5.2	186
PVB 40/60	332	5.4	193

Initially, Suglets® (dia.$_{avg}$ = 1.52 ± 0.08 mm, m_{avg} = 3.36 mg, n ≈ 1800) were coated with a PEG/RhB model drug formulation (6:1 PEG:RhB mass ratio) (**Figure A3.9**). A single coating cycle afforded a 6.2% w.w^{-1} mass gain (equiv. to ~ 209 µg per Suglet®), which applied enough of the model drug, RhB (~ 31 µg per Suglet®) to enable inline monitoring of release *via* UV-vis spectrophotometry. RhB was incorporated as the model drug in the formulation to enable the facile determination of its release, and therefore, the effectiveness of the reverse enteric copolymer coatings applied thereafter.

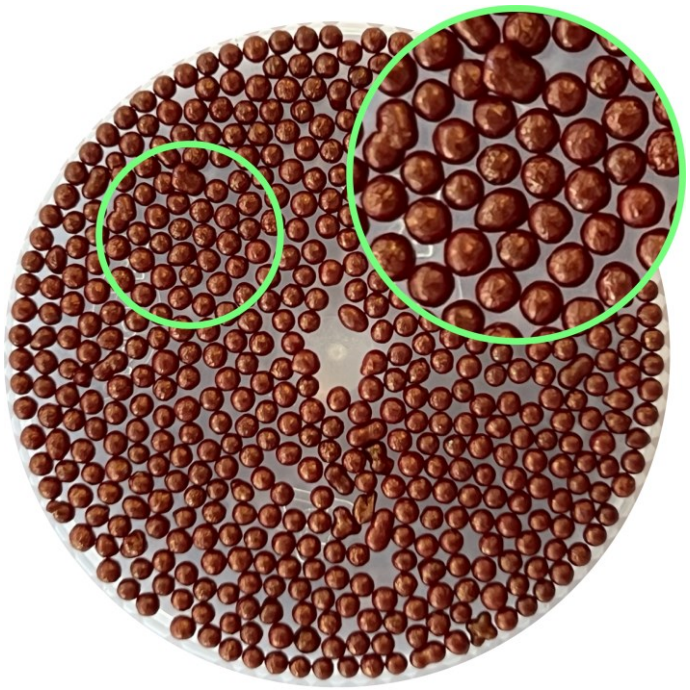


Figure A3.9: Suglets® coated with the model drug formulation containing PEG and RhB, coated at a mass gain of 6.2% w.w^{-1}.

Two sub-batches of Suglets® coated with the model drug formulation (n ≈ 340) were then each coated with a 10% w.v^{-1} (in EtOH) reverse enteric PVB 60/40 or PVB 40/60 copolymer formulation (**Figure A3.10**). The PVB 60/40 and PVB 40/60 copolymers exhibited the highest and lowest mol% fraction of VP, respectively. Consequently, the PVB 60/40 and PVB 40/60 copolymers also exhibited the highest and lowest T_g and water absorption values, respectively. By evaluating these two copolymers, the effects of copolymer composition on their physicochemical properties and commensurate performance as taste-masking coatings, could be evaluated. Each sub-batch was coated using two coating cycles, to afford total mass gains of ~ 5.2–5.4% w.w^{-1}, which were equivalent to ~ 186–193 µg per Suglet®. The same formulation and coating parameters were used

for each copolymer formulation, to enable the comparison of their relative performance. Generally, Suglets® coated with the PVB copolymer formulations did not exhibit any significant signs (qualitatively) of ineffective coating. Twinning was observed between Suglets® following coating with either formulation, however it is highly likely that this could be mitigated in the future, by further optimisation of the coating parameters. It should be noted that extensive optimisation of the coating parameters and the coated mass of each copolymer was not undertaken.

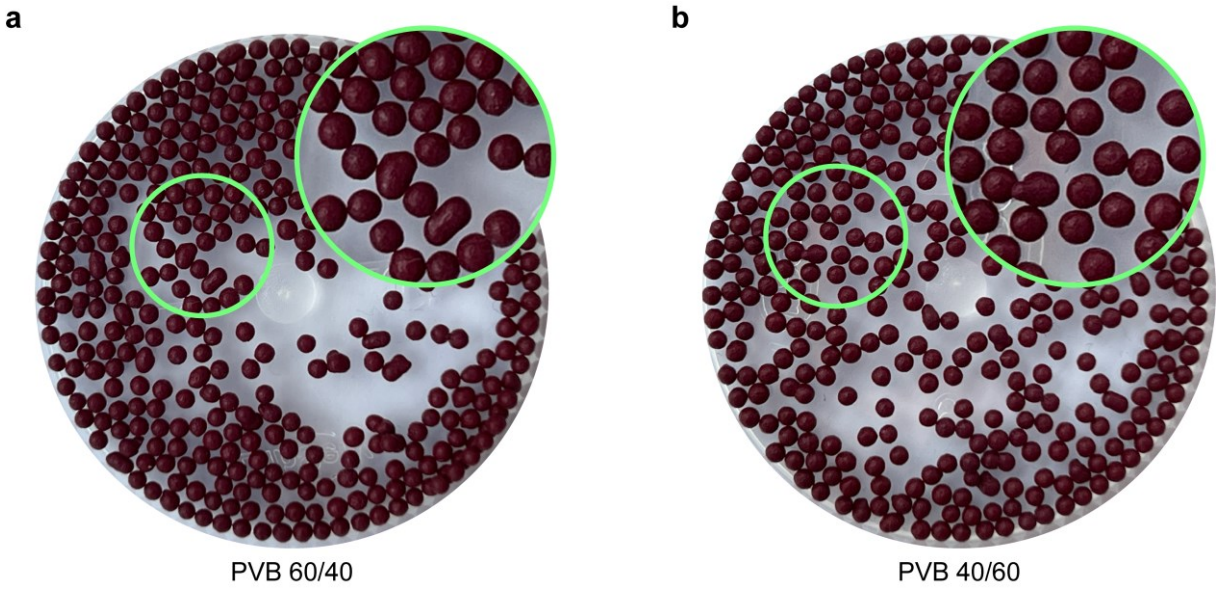


Figure A3.10: Suglets® coated with a) PVB 60/40 (5.2% w.w^{-1} mass gain), b) PVB 40/60 (5.4% w.w^{-1} mass gain).

In Vitro Evaluation of the Taste-masking Performance of PVB 60/40 and 40/60

To evaluate the performance of PVB copolymers as reverse enteric coatings, copolymer coated Suglets® (n = 6) were immersed in a pH 6.8 solution at 37 °C to mimic the human salivary environment. The coatings were determined to have effectively contained the RhB formulation until RhB was observed in the receiving solution. It should be noted that the integrity of the polymer coating was considered the primary determinant for effective taste-masking in these experiments, since the active pharmaceutical ingredient (API, i.e., RhB) does not diffuse through the coating (*vide supra*). Moderate stability was observed for the PVB 60/40 copolymer formulation, as sporadic failures for 3/6 Suglets® were observed for up to 30 min, with the remaining Suglets® observed to prevent the release of RhB within the same period. In contrast, the most effective copolymer formulation was PVB 40/60 which effectively contained RhB in all 6 Suglets® for 30

min. Considering the short period of taste-masking generally targeted for most oral pharmaceutical formulations (< 5 min),[23, 24] PVB 40/60 showed excellent reverse enteric, taste-masking properties. Additional monitoring revealed continued containment of RhB for 72 h, in 5/6 Suglets® for the PVB 40/60 (cf., only 1/6 Suglets® for PVB 60/40). In conjunction with the low mass gain required to mediate such prolonged insolubility (cf., 40% or 80% $w.w^{-1}$ for taste-masking formulations as reported by Chivate et al.),[24] PVB 40/60 demonstrated the excellent taste-masking properties of the copolymers and their potential suitability for reverse enteric pharmaceutical formulations.

The dissolution of the copolymer coatings in a simulated gastric environment (pH 1.5 solution, 37 °C) was investigated to determine whether the PVB formulations would rapidly release an encapsulated drug following ingestion. The presence of RhB in the receiving solution was monitored inline *via* UV-vis spectrophotometry (λ_{max} = 556 nm), to determine the initial and complete release times. The results of the release experiments are summarised in **Table A3.3** and release profiles are provided in **Figure A3.11.**

Table A3.3: Summary of *in vitro* release results of model drug and copolymer coated Suglets®.

Coating	Initial Release [a] (min)	Complete Release [b] (min)
PVB 60/40	1.3 ± 0.1 (10)	2.1 ± 0.3 (15)
PVB 40/60	3.6 ± 1.5 (43)	7.2 ± 2.4 (33)

[a] Initial release was defined as 5% of the total release of RhB. [b] Complete release was defined as 90% of the total release of RhB. All values are reported as mean ± std. dev. (%RSD) for n = 5 samples.

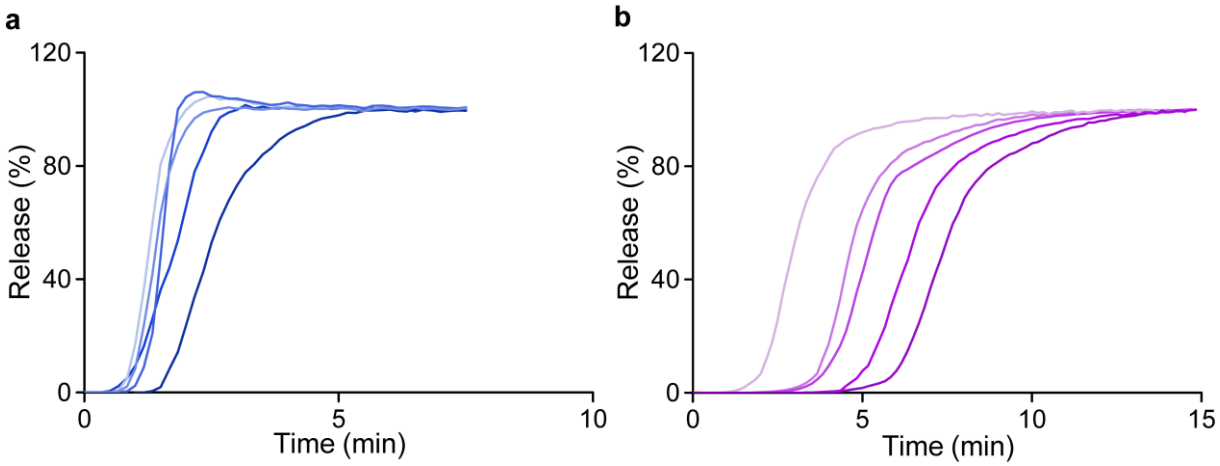


Figure A3.11: Release profiles obtained of Suglets® coated with a PEG/RhB model drug formulation (6.2% w.w^{-1} mass gain), and a) PVB 60/40 (5.2% w.w^{-1} mass gain), or b) PVB 40/60 (5.4% w.w^{-1} mass gain), during dissolution in a pH 1.5 solution (37 °C), under stirring. Traces represent individual samples (n = 5), monitored *via* the absorbance maximum of RhB (λ_{max} = 556 nm). Note that in a) two samples show a > 100% release peak maximum, which was caused by a local increase in dye concentration, due to a lag in stirring during analysis.

In all cases, the release of RhB occurred within 5 min, and was completed within 10 min. Both the initial and complete release times for Suglets® coated with PVB 60/40 and 40/60, were positively correlated with their taste-masking properties at pH 6.8. For example, only 50% of the tested Suglets® with a PVB 60/40 coating were taste-masked for 30 min, which also exhibited the shortest initial (1.3 ± 0.1 min) and complete release times (2.1 ± 0.3 min). In contrast, all the tested PVB 40/60 coated Suglets® were effectively taste-masked at pH 6.8 and exhibited the longest initial (3.6 ± 1.5 min) and complete release (7.2 ± 2.4 min) times at pH 1.5.

This behaviour was likely due to the T_g values of the copolymers. PVB 40/60 exhibited a T_g value (43.3 °C), lower than that of PVB 60/40 (58.9 °C). The comparatively lower T_g value of PVB 40/60 likely facilitated the interpenetration of polymer chains[25] during spray coating — due to greater chain mobility — resulting in more effective (i.e., cohesive) and uniform film formation when coated at ambient temperature (23 °C). Coatings that were more cohesive would invariably withstand the artificial salivary environment — which could induce coating-disrupting processes such as water absorption and swelling — better than less cohesive coatings. Similarly, in the gastric environment, cohesive coatings would effectively delay the release of an encapsulated API, due to the necessary

dissolution of the coating prior to release. The higher T_g value of PVB 60/40 likely reduced the effectiveness of film formation, leading to thinner and less cohesive coatings that were rapidly disrupted at pH 6.8, and sufficiently solubilised at pH 1.5. Suglets® coated with PVB 40/60 were shown to mediate the rapid release of RhB within the simulated gastric environment. Whilst further investigation was required to determine if this performance was conserved at scale, these preliminary experiments suggested that the PVB 40/60 formulation demonstrated an excellent capacity for use as a reverse enteric, taste-masking coating.

3.6 References

1. C. T. Eason and C. M. Frampton, *Wildl Res*, 1991, **18**, 445–449.
2. A. A. D'souza and R. Shegokar, *Expert Opin Drug Deliv*, 2016, **13**, 1257–1275.
3. S. R. Heise and F. M. Rozenfeld, *J Chem Ecol*, 1999, **25**, 1671–1685.
4. P. Fisher, D. Algar and J. Sinagra, *Wildl Res*, 1999, **26**, 281–285.
5. A. N. Zaid, *Drug Des Devel Ther*, 2020, **14**, 4613–4623.
6. N. Shinji, Y. Hiroyuki, H. Yoshiyuki and N. Kazuo, *Int J Pharm*, 1994, **104**, 95–106.
7. N. Tantavichet, M. D. Pritzker and C. M. Burns, *J Appl Polym Sci*, 2001, **81**, 1493–1497.
8. S. Y. Lin, K. S. Chen and L. Run Chu, *J Control Release*, 2000, **68**, 343–350.
9. H. Wen and K. Park, *Oral controlled release formulation design and drug delivery: theory to practice*, John Wiley & Sons, 2011.
10. A. Elmaci and J. Hacaloglu, *Polym Degrad Stab*, 2009, **94**, 738–743.
11. S. Özlem and J. Hacaloglu, *J Anal Appl Pyrolysis*, 2013, **104**, 161–169.
12. T. Orhan and J. Hacaloglu, *Polym Degrad Stab*, 2013, **98**, 356–360.
13. A. Gryczke, S. Schminke, M. Maniruzzaman, J. Beck and D. Douroumis, *Colloids Surf B*, 2011, **86**, 275–284.
14. C. A. Wyse, J. McLellan, A. M. Dickie, D. G. M. Sutton, T. Preston and P. S. Yam, *J Vet Intern Med*, 2003, **17**, 609–621.
15. R. F. Reinoso, B. A. Telfer and M. Rowland, *J. Pharmacol. Toxicol. Methods*, 1997, **38**, 87–92.
16. N. Nakagawa, M. Matsumoto and S. Sakai, *Skin Res Technol*, 2010, **16**, 137–141.
17. S. Joshi and H. U. Petereit, *Int J Pharm*, 2013, **457**, 395–406.
18. A. Jonquières, R. Clément and P. Lochon, *Prog Polym Sci*, 2002, **27**, 1803–1877.
19. T. R. Kyriakides, H.-J. Kim, C. Zheng, L. Harkins, W. Tao and E. Deschenes, *Biomed Mater*, 2022, **17**, 022007.
20. D. Zhang, Q. Chen, C. Shi, M. Chen, K. Ma, J. Wan and R. Liu, *Adv Funct Mater*, 2021, **31**, 2007226.
21. R. Klopfleisch and F. Jung, *J Biomed Mater Res A*, 2017, **105**, 927–940.

22. J. H. Hong, D. H. Kim, I. J. Rhyu, Y. C. Kye and H. H. Ahn, *Skin Res Technol*, 2020, **26**, 132–136.

23. A. Lopalco, N. Denora, V. Laquintana, A. Cutrignelli, M. Franco, M. Robota, N. Hauschildt, F. Mondelli, I. Arduino and A. Lopedota, *Int J Pharm*, 2020, **574**, 118922.

24. A. Chivate, V. Sargar, P. Nalawade and V. Tawde, *Drug Dev Ind Pharm*, 2013, **39**, 1091–1097.

25. L. A. Felton, *Int J Pharm*, 2013, **457**, 423–427.

Chapter 4: Synthesis and Characterisation of pH-responsive Copolymers for Reverse Enteric Coatings

4.1 Overview

Chapter 4 describes the synthesis, characterisation, and evaluation of a series of addition copolymers of 2-vinylpyridine (VP), butyl methacrylate (BMA), and methyl methacrylate (MMA) or isobornyl methacrylate (IBMA). As described in **Chapter 3.2**, the synthesised copolymers were evaluated for their physicochemical and thermal properties, to identify a candidate copolymer that exhibited reduced water absorption and improved PPI performance following fluidised-bed spray coating. Like those described in **Chapter 3.2**, the physicochemical and thermal properties of the copolymers could be tuned by modifying the mol% fraction of their constitutive monomers. A copolymer of VP, BMA and IBMA was identified as a lead copolymer and used to manufacture PPIs. However, poor film formation was observed due to its high glass transition temperature (T_g). The results of Chapter 4 demonstrated the need to reduce the T_g value of the lead copolymer to facilitate film formation, whilst retaining the copolymers favourable physicochemical properties.

4.2 Results and Discussion

4.2.1 Copolymers of 2-Vinylpyridine and Butyl Methacrylate, and Methyl Methacrylate or Isobornyl Methacrylate

The swelling observed for the PVB 50/50 implants described in **Chapter 3.2.7** was attributed to the slightly polar functional groups (neutral pyridine and ester moieties) in the copolymer structure, which likely facilitated the movement of water through the coating. It was hypothesised that *via* addition polymerisation with a methacrylate monomer(s), of greater hydrophobicity or crystallinity (cf., BMA), the water absorption of the resultant copolymer could be decreased, whilst retaining sufficient pH-responsivity. Two additional, high T_g value (cf., BMA) monomers — MMA and IBMA — were selected as additional target monomers to make a range

of T_g values accessible, as homopolymers of MMA or IBMA generally exhibit higher T_g values than homopolymers of BMA or VP (i.e., poly(methyl methacrylate) (PMMA) T_g = 38–150 °C[1] and poly(isobornyl methacrylate) (PIBMA) T_g = 170–206 °C).[2] Further, the mol% fraction of VP in the copolymer structure, and incorporation of comparatively hydrophobic monomers, would also alter the hydrophilicity of the resultant copolymer and enable the tuning of water absorption and solubility of a coating as a result. To that end, a library of pH-responsive copolymers was prepared with varying ratios of VP and BMA, and MMA or IBMA. The physicochemical and thermal properties of these copolymers were investigated, to determine which copolymers exhibited favourable solubility (insoluble at pH 7.4, soluble at pH < 2), low water absorption, and a suitable T_g value to enable spray coating. These properties were considered necessary to afford a uniform and cohesive coating following spray coating.

4.2.2 Synthesis and Characterisation of Poly[(2-vinylpyridine)$_x$-*co*-(butyl methacrylate)$_y$-*co*-(methyl methacrylate)$_z$] (PVBM) Copolymers

As outlined in **Table 4.1**, a series of addition copolymers of VP, BMA, and MMA were synthesised using conventional free radical polymerisation (CFRP) (**Figure 4.1a**), using the previously described approach (**Chapter 3.2.2**). The synthesised poly[(2-vinylpyridine)$_x$-*co*-(butyl methacrylate)$_y$-*co*-(methyl methacrylate)$_z$] copolymers were designated as PVBM x/y/z, where *x*, *y*, and *z* refer to their respective VP, BMA and MMA repeat unit (RU) mol% ratios. While the PVB copolymers were purified *via* precipitation to remove residual monomer, the PVBM copolymers were purified *in vacuo* (10 mbar, 80 °C), to afford the copolymer product. The removal of residual solvent and monomer *via* evaporation simplified the purification process, negating the need for a more complex and lengthy precipitation, particularly when the scale of future syntheses was increased. In addition, the yields of the PVBM copolymers were ~ 10% greater than the PVB copolymers, likely owed to a decrease in transfer losses incurred when precipitation was used. In all cases the targeted mol% ratios were closely achieved using this approach (**Table 4.1**).

Table 4.1: Summary of copolymer RU mol% ratios, molecular weight characteristics, and thermal properties.

Copolymer code	Targeted mol% of RU	Calculated mol% of RU [a]	M_w [b] (kDa)	M_n [b] (kDa)	$Đ$ [b]	T_g [c] (°C)
PVBM 40/50/10	40:50:10	40:50:10	32.4	14.8	2.2	45.3
PVBM 30/50/20	30:50:20	30:50:20	34.5	16.2	2.1	50.2
PVBM 30/40/30	30:40:30	31:39:30	35.4	17.2	2.1	59.7
PVBM 40/40/20	40:40:20	41:39:20	36.0	18.6	1.9	57.1

[a] Monomer conversion and RU mole ratios determined by gas chromatography (GC) relative to their pre-polymerisation concentrations (t_0) using 1,4-dioxane as an internal reference. [b] Determined by gel permeation chromatography (GPC) using a conventional column calibration of narrow molecular weight poly(methyl methacrylate) (PMMA) standards, where M_w is the weight-average molecular weight, M_n is the number-average molecular weight, and $Đ$ is the dispersity of the copolymer. [c] Determined by modulated differential scanning calorimetry (MDSC).

As previously described for the PVB series, the syntheses of PVBM copolymers were monitored *via* gas chromatography (GC) to determine the relative mol% fraction of the VP, BMA and MMA RUs, and the resultant copolymers were further characterised *via* gel permeation chromatography (GPC) (**Figure 4.1b**) and proton nuclear magnetic resonance (^{1}H NMR) spectroscopy (**Figure 4.1c**), as described in **Chapter 3.2.2**. Resonances characteristic of the VP RU aromatic protons between δ_H 8.40 and 6.75 ppm, and the characteristic methoxy proton resonance of the MMA RU at δ_H ~ 3.6 ppm, confirmed the successful incorporation of MMA in the PVBM copolymers (**Figure 4.1c**). Like the PVB series, the ^{1}H NMR spectra also showed the presence of trace amounts of solvents used during synthesis (1,4-dioxane (δ_H 3.67 ppm), and water (δ_H 1.52 ppm) — attributed to the use of solvents that were not anhydrous. In some cases, trace amounts of unreacted monomers were observed (i.e., alkene proton resonances between δ_H 6.2 and 5.0 ppm). However, as previously mentioned the presence of these impurities was considered inconsequential given their trace amounts, and no further purification was undertaken.

GPC analyses of the copolymers (**Figure 4.1b**) revealed similar weight-average molecular weight (M_w) values between 32–36 kDa (PVBM series) and broad, monomodal molecular weight distributions (dispersity, $Đ$ = 1.9–2.2), (**Table 4.1**).

Together, the results from the GC and GPC analyses, and ^{1}H NMR spectra, demonstrated the successful synthesis of the copolymer series with excellent accuracy regarding the target RU mol% ratios and relatively consistent molecular weight profiles.

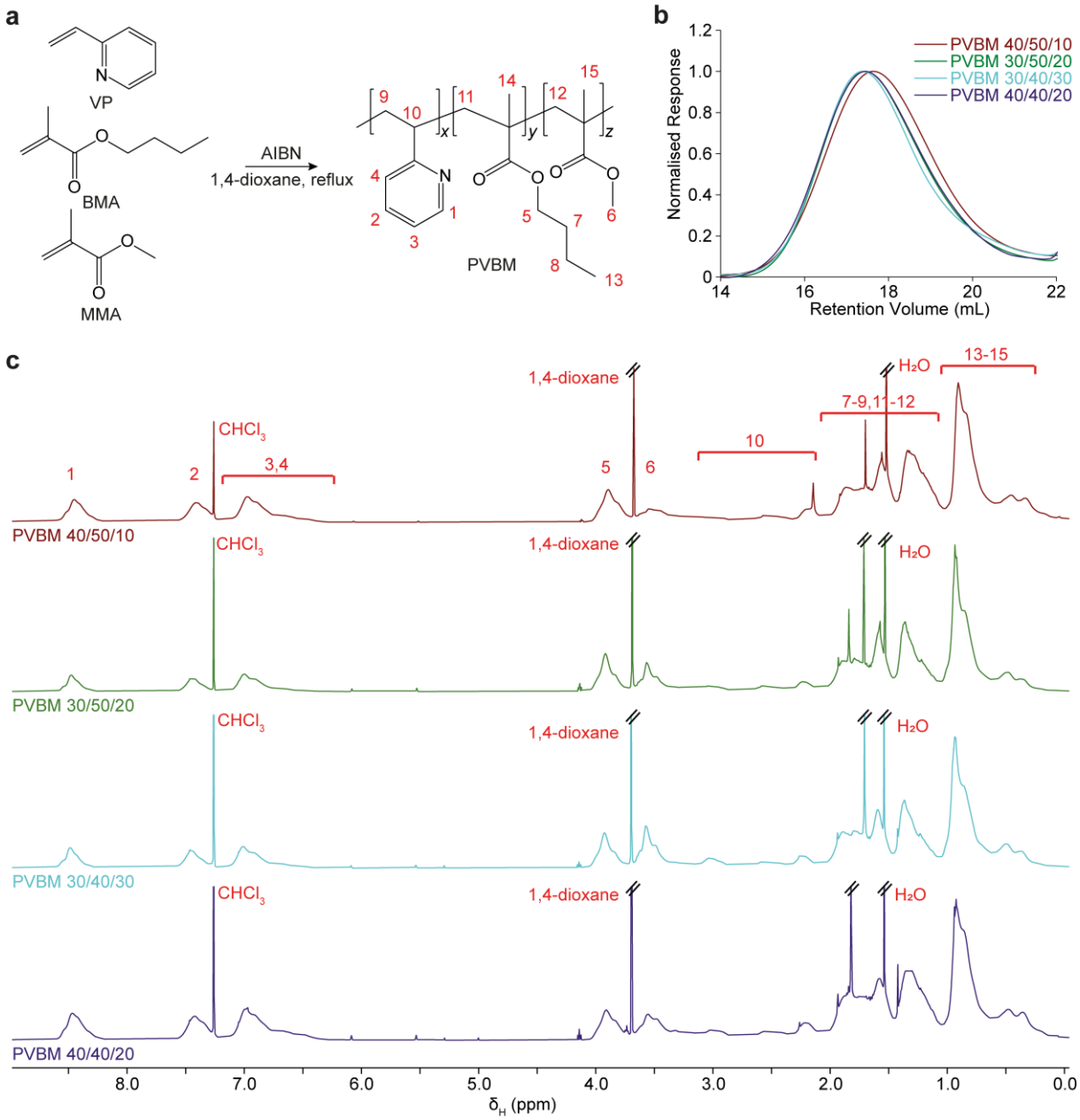


Figure 4.1: a) Synthesis of the poly[(2-vinylpyridine)$_x$-*co*-(butyl methacrylate)$_y$-*co*-(methyl methacrylate)$_z$] (PVBM) copolymers *via* CFRP. b) GPC differential refractive index (DRI) chromatograms and c) ^{1}H NMR spectra (500 MHz, deuterated chloroform ($CDCl_3$), 21 °C) of the PVBM copolymer series.

Negligible difference in dispersity or the accuracy of the feed *versus* product RU mol% fractions was observed (**Table 4.1**) for the PVBM series. The synthesised

PVBM copolymers were then subjected to the same selection criteria experiments as the PVB series.

4.2.3 Thermal Characterisation of the PVBM Copolymers

Modulated differential scanning calorimetry (MDSC) analysis of the PVBM copolymers revealed that an increase in the mol% fraction of MMA by ~ 10% and a commensurate reduction in BMA at a constant fraction of VP (~ 40%) (i.e., PVBM 40/40/20 versus PVBM 40/50/10) resulted in a ~ 12 °C increase in T_g value (**Figure 4.2a**). This suggested that there was a greater contribution to the T_g value from MMA in the resultant copolymer (cf., BMA). Which was supported by previous reports of the dependence of the T_g values of MMA copolymers, on the proportion of MMA.[3–7] In contrast, when the mol% fraction of VP was lowered to ~ 30%, and the proportion of MMA increased commensurately in PVBM 30/50/20 (cf., PVBM 40/50/10), an increase in T_g value of ~ 5 °C was observed. Additionally, when the proportion of MMA was increased further (and the mol% fraction of BMA reduced, in PVBM 30/50/30), a further ~ 10 °C increase in the T_g value was observed. The relative increase in T_g value despite a reduction in the mol% fraction of VP, demonstrated that there was a strong positive relationship between the proportion of MMA and the T_g value of the resultant copolymer.[3–7] This is likely due to the tendency of MMA to form syndiotactic homopolymers exhibiting higher T_g values, due to the stronger interactions afforded by the relatively polar MMA RUs (cf., BMA).[1, 8]

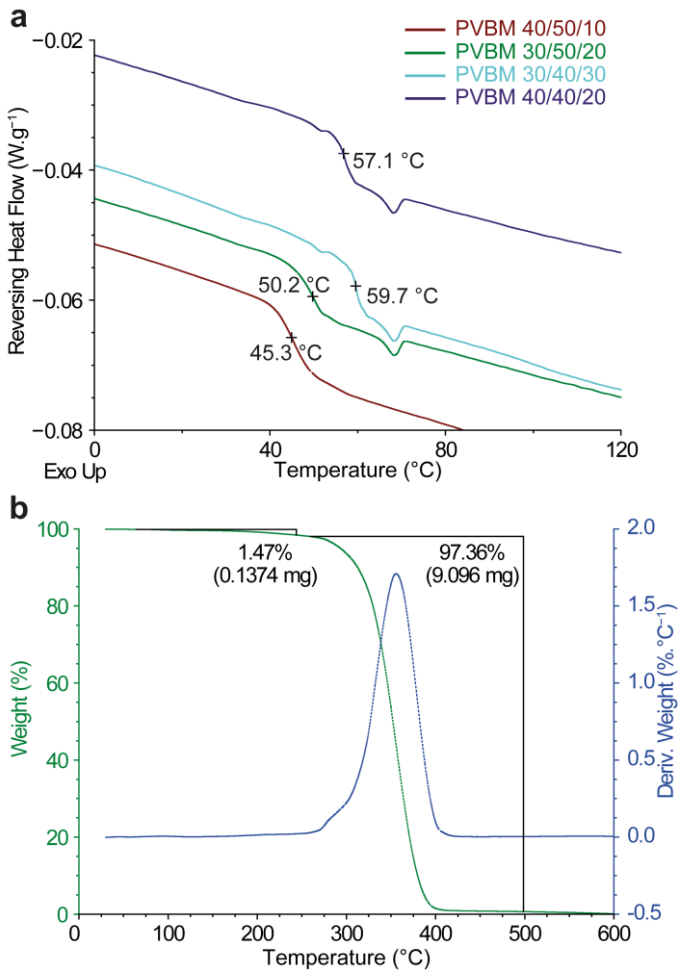


Figure 4.2: a) Reversing heat flow ($W.g^{-1}$) curves of the PVBM copolymer series obtained *via* MDSC. b) Weight (%) and derivative weight ($\%.°C^{-1}$) curves of PVBM 30/40/30 — representative of the PVBM copolymer series — obtained *via* modulated thermogravimetric analysis (MTGA).

A representative copolymer from the PVBM series was analysed *via* modulated high-resolution thermogravimetric analysis (MTGA), given the high likelihood of a shared degradation mechanism amongst copolymers from the same series. PVBM 30/40/20 exhibited a similar onset value for thermal degradation to PVB 50/50 (~ 270 °C) (**Figure 4.2b**), followed by a single degradation event involving a weight loss of ~ 97%. This suggested a similar depolymerisation degradation mechanism for both copolymers. Like VP and BMA homopolymers, both homo- and copolymers of MMA (e.g., poly[(methyl methacrylate)-*co*-(benzyl methacrylate)][9, 10] thermally degrade *via* depolymerisation.

4.2.4 pH-dependent Solubility of the PVBM copolymers

In the PVBM series, PVBM 30/50/20 and 30/40/30 exhibited poor solubility (< 5 $mg.mL^{-1}$), and precluded the analysis of their solubility, as the detector response fell below the limit of quantification (i.e., exhibited a signal-to-noise ratio < 10:1). PVBM 40/50/10 and PVBM 40/40/20 exhibited pH-dependent solubility (**Figure 4.3**), with similar solubilities determined for all the test solutions (pH 1.0, 1.5, and 2.0). Overall, the solubilities of PVBM 40/50/10 and PVBM 40/40/20 at pH 1.5 (5.4 ± 0.6 and 5.6 ± 0.3 $mg.mL^{-1}$, respectively) were lower than all of the copolymers in the PVB series. The lowered solubility of the PVBM copolymers (cf., PVB), was likely due to both the reduction in VP mol% fraction (cf., PVB 50/50), and the glassy MMA segments within the copolymer structures. The relative hydrophilicity of MMA (cf., BMA) was not sufficient to overcome this reduction in solubility. This effect was even more pronounced for PVBM 30/50/20 and 30/40/20, which exhibited even lower solubility.

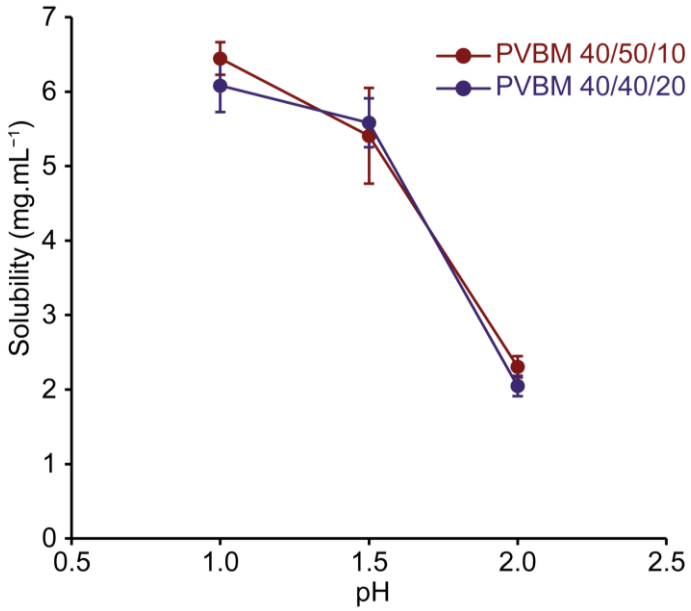


Figure 4.3: The pH-dependent solubility of the PVBM copolymers (37 °C), as determined by GPC. Values are reported as the mean ± std. dev. (n = 3). Note the absence of PVBM 30/40/30 and 30/50/30, due to their low solubility at pH 1.0. Standard curves used in the GPC analysis of copolymer solubility samples are provided in the Appendix **(Figure A4.1)**.

4.2.5 Water Absorption Properties of the PVBM Copolymers

Consistent with the PVB series, the water absorption exhibited by the PVBM copolymers was correlated with the mol% fraction of VP (**Figure 4.4**). The copolymer with the lowest proportion of VP, PVBM 30/50/20, showed the lowest water absorption (42 d, −0.1% ± 0.84 w.w^{-1}). The apparent negative water absorption at later time points (30–40 d), was likely due to a combination of the copolymer's low water uptake, and the limitations inherent to determining water absorption on a bulk sample gravimetrically. Regardless, when compared to PVBM 40/50/10, which had the greatest water absorption (42 d, 2.4% ± 0.2 w.w^{-1}), the extent of water absorption was positively correlated with the mol% fraction of VP. When the mol% fraction of BMA was reduced in favour of a higher MMA mol% fraction (with the same VP mol% fraction) (e.g., PVBM 40/50/10 cf. 40/40/20) no significant difference in water absorption was observed. This suggested that water absorption was not correlated with the mol% fraction of MMA and was predominantly dependent on the mol% fraction of VP in the copolymer.

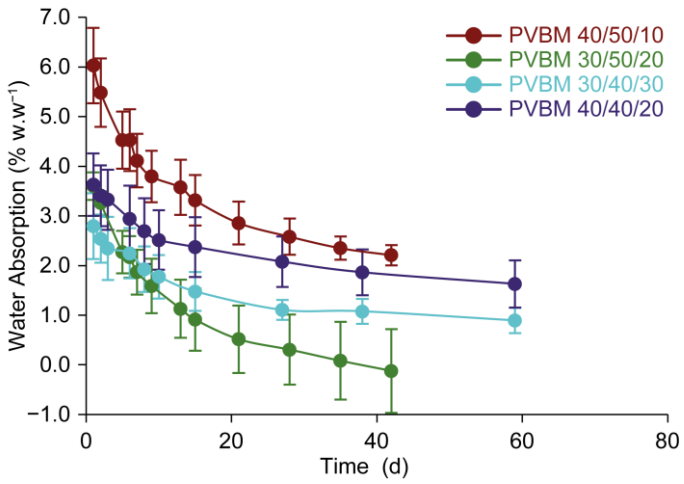


Figure 4.4: Water absorption (% w.w^{-1}) determined at pH 7.4 and 37 °C for the PVBM copolymer series. All values are reported as mean ± std. dev. (n = 8).

4.2.6 Poly[(2-vinylpyridine)$_x$-*co*-(butyl methacrylate)$_y$-*co*-(isobornyl methacrylate)$_z$]

IBMA was selected to further investigate the tuning of the physicochemical properties of the VP-based copolymer. The incorporation of a comparatively hydrophobic monomer would reduce the hydrophilicity of the resultant copolymer and thereby reduce its water absorption and solubility properties. The differing

hydrophobicities of BMA and IBMA monomers (logP = 1.34[11] and 3.69 (est. ChemDraw v20.0.0.41, PerkinElmer Informatics), respectively), could potentially enable the hydrophilicity of the copolymers to be reduced (cf., the PVB and PVBM series), whilst maintaining high T_g values due to the inherently higher T_g values of IBMA homopolymers (T_g = 170–206 °C).[2]

4.2.7 Synthesis and Characterisation of Poly[(2-vinylpyridine)$_x$-*co*-(butyl methacrylate)$_y$-*co*-(isobornyl methacrylate)$_z$] (PVBI) Copolymers

A series of addition copolymers of VP, BMA and IBMA were synthesised using CFRP (**Figure 4.5a**). The synthesised poly[(2-vinylpyridine)$_x$-*co*-(butyl methacrylate)$_y$-*co*-(isobornyl methacrylate)$_z$] copolymers were designated as PVBI x/y/z, where *x*, *y*, and *z* refer to their respective VP, BMA and IBMA RU mol% ratios. The dispersity, product RU mol% fractions and yields of the PVBI syntheses were comparable to the PVBM series (**Table 4.2**), further suggesting the robustness of the chosen synthetic approach. In all cases the targeted mol% ratios were closely achieved using this approach (**Table 4.2**).

Table 4.2: Summary of copolymer RU ratios, molecular weight characteristics, and thermal properties.

Copolymer code	Targeted mol% of RU	Calculated mol% of RU [a]	M_w [b] (kDa)	M_n [b] (kDa)	$Đ$ [b]	T_g [c] (°C)
PVBI 50/45/5	50:45:5	49:46:5	25.2	13.2	1.9	40.0
PVBI 50/40/10	50:40:10	50:40:10	25.0	12.1	2.1	52.6
PVBI 50/35/15	50:35:15	51:34:16	27.2	14.2	1.9	64.1
PVBI 50/30/20	50:30:20	51:30:20	34.2	16.4	2.1	73.7
PVBI 40/40/20	40:40:20	40:40:20	43.4	22.3	2.0	70.2

[a] Monomer conversion and mole ratios determined by GC relative to t_0 using 1,4-dioxane as an internal reference. [b] Determined by GPC using a conventional column calibration of narrow molecular weight PMMA standards. [c] Determined by MDSC.

The PVBI copolymer syntheses were monitored *via* GC, and the resultant copolymers further characterised *via* GPC (**Figure 4.5b**) and ^{1}H NMR spectroscopy

(**Figure 4.5c**), as previously described (**Chapter 3.2.2**), which demonstrated the successful synthesis of all the copolymers.

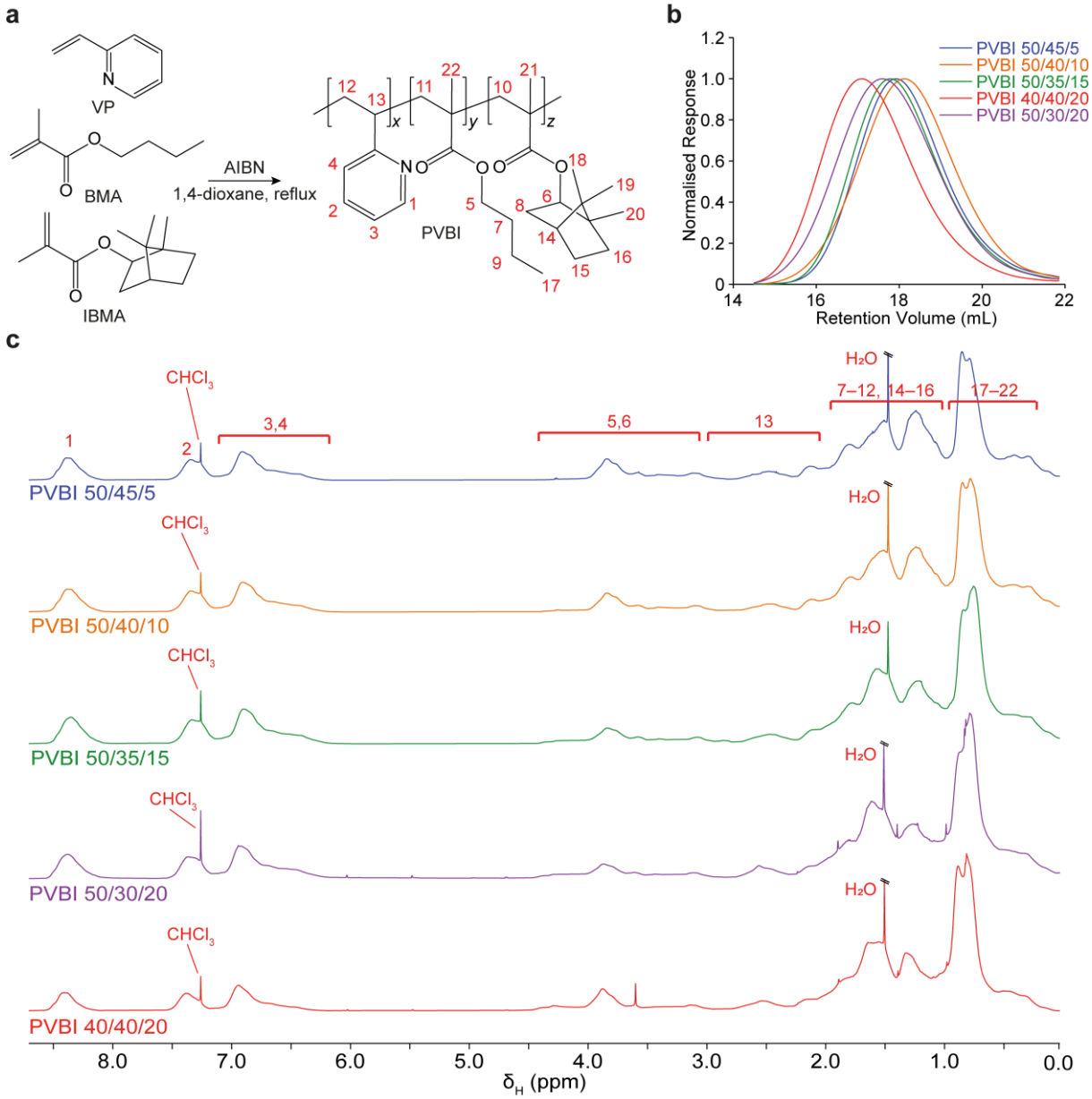


Figure 4.5: a) Synthesis of poly[(2-vinylpyridine)$_x$-*co*-(butyl methacrylate)$_y$-*co*-(isobornyl methacrylate)$_z$] (PVBI) copolymers *via* CFRP. b) GPC DRI chromatograms and c) ^{1}H NMR spectra (500 MHz, $CDCl_3$, 21 °C) of the PVBI copolymer series. Carbon-13 nuclear magnetic resonance (^{13}C NMR) spectra are provided in the Appendix **(Figure A4.2)**.

Resonances characteristic of the VP RU aromatic protons between δ_H 8.40 and 6.75 ppm, and the resonance observed at 0.75 ppm corresponding to the methyl groups of the IBMA RUs, confirmed successful incorporation of IBMA in the copolymer. The ^{1}H NMR spectra also showed the presence of trace amounts of

water (δ_H 1.52 ppm) attributed to the use of solvents that were not anhydrous. However, the presence of water was considered inconsequential given its trace amounts, and the copolymers were used without further purification. GPC analyses of the copolymers (**Figure 4.5b**) revealed similar M_w values between 25–43 kDa, and broad, monomodal molecular weight distributions ($Đ$ = 1.9–2.1, **Table 4.2**).

4.2.8 Thermal Characterisation of the PVBI Copolymers

The T_g values of the PVBI copolymers showed that a higher proportion of IBMA (e.g., PVBI 40/40/20) or VP (e.g., PVBI 50/30/20) resulted in a commensurate increase in the T_g value (**Figure 4.6a**). Particularly, an increase in the IBMA content from ~ 5–20% (i.e., PVBI 50/45/5 cf., PVBI 50/30/20) with a constant proportion of VP (~ 50%) and a reduction in BMA content (from ~ 45–30%) resulted in a ~ 35 °C increase in the T_g value of the resultant copolymer. The increase in the T_g value likely results from the bulky and rigid pendant isobornyl groups of the IBMA RUs, which reduce chain mobility.[2, 12, 13] In comparison, the flexible and less bulky aliphatic chain of the BMA RUs, lowers the T_g value of the resultant copolymer. The reported T_g values of the homopolymers of the monomers support this reasoning.[2, 14] These results supported the hypothesised ability to tune the T_g values of the copolymers in each series by changing the RU ratios of the constituent monomers. Copolymers with T_g values from 40–74 °C are easily accessible in these series, potentially providing compatibility with a range of processing conditions.

Unlike BMA and MMA homopolymers, the major thermal degradation pathway for IBMA homopolymers is γ-H transfer from the isobornyl ring to the carbonyl group.[15, 16] However, the single decomposition event observed for PVBI 50/30/20 (**Figure 4.6b**), suggested that degradation occurred predominantly *via* depolymerisation, likely due to the high mol% fraction of VP and BMA in the copolymer.

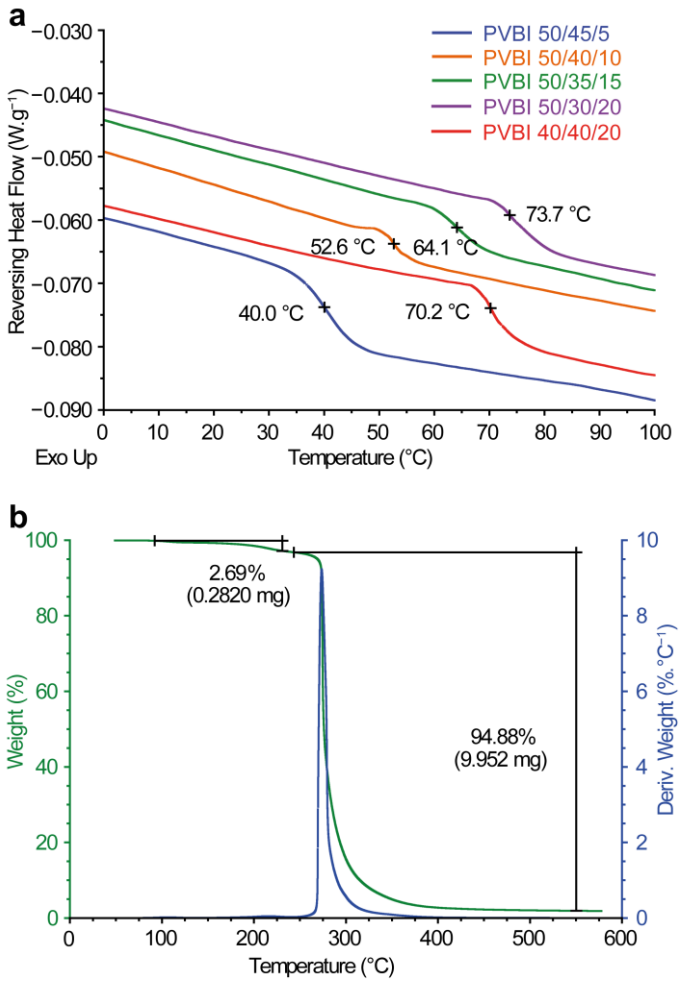


Figure 4.6: a) Reversing heat flow ($W.g^{-1}$) curves of the PVBI copolymer series obtained *via* MDSC. b) Weight (%) and derivative weight ($\%.°C^{-1}$) curves of PVBI 50/30/20 — representative of the PVBI copolymer series — obtained *via* MTGA.

4.2.9 pH-dependent Solubility of the PVBI Copolymers

Except for PVBI 40/40/20, all of the copolymers in the PVBI series were soluble at pH 1.5 ($\geq \sim 4$ $mg.mL^{-1}$) (**Figure 4.7**). Given that PVBI 40/40/20 contained the lowest and highest proportions of VP (40%) and IBMA (20%) respectively, it follows that it exhibited the poorest aqueous solubility due to its relatively greater hydrophobicity. As the mol% fraction of IBMA was decreased to 5%, at pH 1.5, the solubilities of the copolymers increased from 3.7 ± 0.4 mg/mL^{-1} (PVBI 50/30/20) to 6.3 ± 0.1 $mg.mL^{-1}$ (PVBI 50/45/5), which indicated that the solubility of the copolymers was proportional to the IBMA mol% fraction, when the mol% fraction of VP was held constant at 50%. Overall, these results demonstrate that the VP mol% fraction of the copolymers mediates their solubilities, but solubility can be

further tuned — in a proportional manner — through the incorporation of relatively hydrophobic monomers at a constant VP mol% fraction.

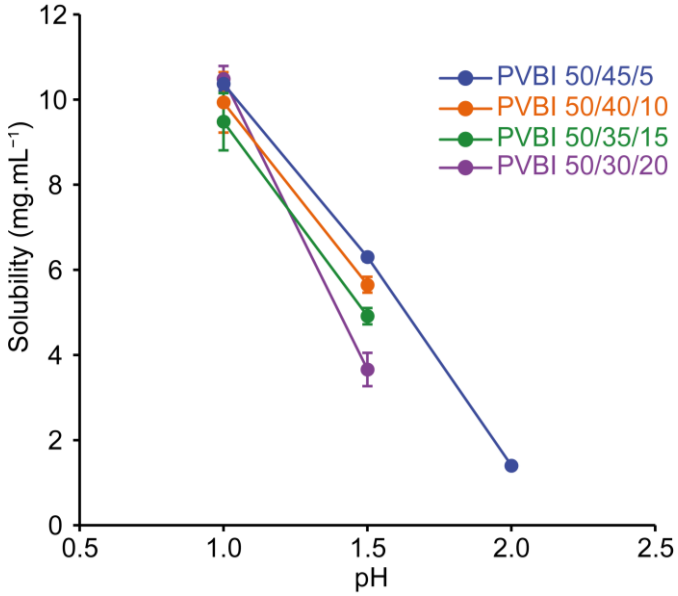


Figure 4.7: The effect of PVBI copolymer composition on solubility at pH 1.0, 1.5, and 2.0 (37 °C). Values are reported as the mean ± std. dev (n = 3). Standard curves used in the GPC analysis of copolymer solubility samples are provided in the Appendix (**Figure A4.3**).

4.2.10 Water Absorption Properties of the PVBI Copolymers

The water absorption exhibited by the PVBI copolymers was found to be proportional to the mol% fraction of IBMA and — unlike the PVB and PVBM series — appeared to be independent of the mol% fraction of VP (**Figure 4.8**). No considerable change in water absorption was observed when the VP mol% fraction was reduced from 50–40%, whilst the IBMA mol% fraction was unchanged at 20% (PVBI 50/30/20 cf., PVBI 40/40/20). However, when the VP mol% fraction was kept at 50%, and the IBMA mol% fraction increased from 10 to 15%, water absorption decreased from 2.4% ± 0.6 w.w^{-1} to 1.8% ± 0.5 w.w^{-1} (52 d) (PVBI 50/40/10 cf., PVBI 50/35/15) (**Figure 4.8**). The water absorption for PVBI 50/45/5 appeared to maintain an increasing trend (> ~ 5% w.w^{-1} after 40 d) (**Figure 4.8**), which was attributed to the low T_g value of the copolymer (T_g = 40.0 °C). The resultant increase in chain mobility likely enabled swelling of the copolymer disc in the presence of water, leading to increased water absorption over time. Importantly, these data demonstrate that PVBI copolymers could be prepared with

a relatively high mol% fraction of VP (50%), and their water absorption properties tuned *via* the incorporation of IBMA.

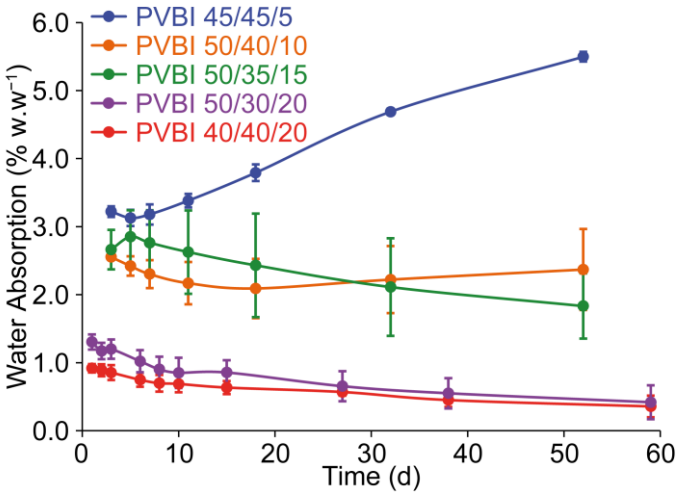


Figure 4.8: Water absorption (% w.w^{-1}) determined at pH 7.4 and 37 °C for the neat PVBI copolymer series.

4.2.11 Manufacture and Evaluation of the PVBI Implants

As discussed in **Chapter 3.2.8**, the osmotic water absorption of the PVB 50/50 coating impeded the stability of the PVB 50/50 coated implants. A reduction in water absorption was targeted, to produce implants that exhibited reduced water absorption, and potentially, increased stability as a result. Therefore, the synthesised PVBM and PVBI copolymers were compared *via* their physicochemical and thermal properties, to select a copolymer that exhibited reduced water absorption, for fluidised-bed spray coating. Of the two copolymer series, PVBM 40/40/20 and PVBI 50/30/20 were identified as candidate copolymers. However, PVBI 50/30/20 was ultimately selected, due to its lower water absorption, moderate solubility at pH 1.5 and observed insolubility at pH 2.0, and higher T_g value. A batch of NaOAc core implants was prepared, as described in **Chapter 3.2.6**. However, two changes were made to the core and reverse enteric copolymer coatings. The NaOAc core formulation was altered to contain only methylene blue (MB), whilst the same total composition was maintained (i.e., 1:1:0.027 NaOAc:poly(ethylene glycol) (PEG):MB, by weight). This was due to the lack of detection of metabolised rhodamine b (RhB) in the vibrissae of rats, and the spectral overlap described in **Chapter 3.2**. It was determined that the dose of RhB incorporated into each implant was likely to also be undetectable in feral cats, and so was not an appropriate tool for confirming implant consumption.

During initial small-scale testing — performed as described in **Chapter 3.2.6** — it was found that a more non-polar solvent was required to effectively solubilise, and spray coat a 10% w.v^{-1} formulation of PVBI 50/30/20. Toluene (cf., ethanol (EtOH), dichloromethane (DCM), acetone, and hexanes) was found to effectively solubilise the copolymer and produce a film coating under the optimised coating parameters established in **Chapter 3.2.6**. This was likely due to the greater hydrophobicity of PVBI 50/30/20, afforded by the incorporation of IBMA. Using the previously described approach (**Chapter 3.2.6**), a batch of NaOAc core and PVBI 50/30/20 coated implants (PVBI implants) was prepared (n = 300). Initially, the PVBI implants appeared to exhibit a cohesive film coating. However, after short-term storage at room temperature (23 °C), the implants exhibited large fractures in the film coating. Inspection of the coating of PVBI implants bearing a 300 µm-thick coating using optical microscopy (OM) and scanning electron microscopy (SEM) (**Figure 4.9**), confirmed the presence of the fractures. Further, though the coating appeared uniform (**Figure 4.9**) when an implant cross-section was inspected, whole PVBI coated implants appeared to exhibit dusting, and a non-cohesive, particulate coating, which suggested that while some film formation occurred, it was not sufficient to form a cohesive coating.

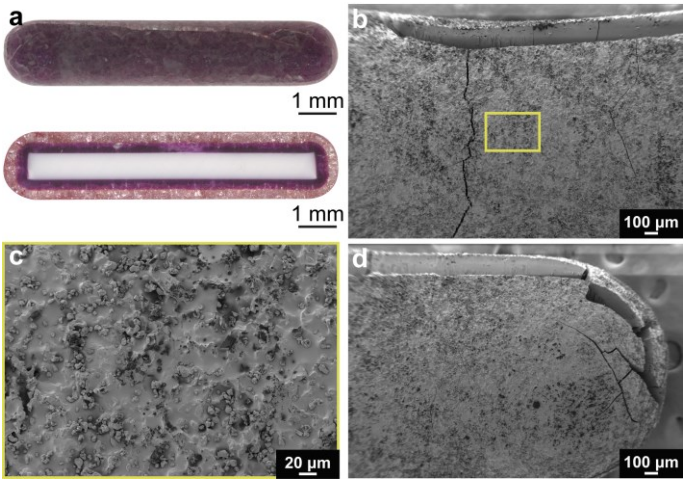


Figure 4.9: Representative a) OM images of PVBI implants, whole (top) and cross-sectioned (bottom). SEM micrographs of a whole PVBI implant showing b) the centre of the implant exhibiting dusting and large fractures in the coating, c) a magnified view of the dusted PVBI 50/30/20 particles, and d) the end of the implant, exhibiting large fractures and dusting.

It was hypothesised that the lack of cohesive film formation was due to the high T_g value of PVBI 50/30/20 (T_g = 73.7 °C). At room temperature (23 °C), the

glassiness of the copolymer could have prevented autoadhesion as the coating solvent (i.e., toluene) evaporated. However, due to the promising properties of PVBI 50/30/20, the use of a plasticiser was proposed as a means of reducing the T_g value of the copolymer, whilst maintaining the desired solubility at pH 1.5, and minimal water absorption.

4.3 Conclusions

A series of pH-responsive copolymers were synthesised *via* CFRP, to produce copolymers with reduced water absorption properties. VP constituted the pH-responsive moiety, and was copolymerised with BMA and MMA, or BMA and IBMA, in varying mol% fractions, to investigate the effects on key physicochemical and thermal properties (T_g value, solubility, and water absorption) of the resultant copolymers. For all the synthesised copolymers, the mol% fraction of VP mediated their solubilities and water absorption properties. Such a result was expected, considering VP was the only pH-responsive moiety incorporated into the copolymers. The mol% fraction of VP was also positively correlated with the T_g values of the PVB copolymers (**Chapter 3.2.2**). Similarly, when the mol% fraction of VP was constant, the mol% fraction of MMA in the PVBM copolymers was positively correlated with their T_g values. However, this appeared to have little effect on the solubility and water absorption properties of the PVBM copolymers. In contrast, the mol% fraction of IBMA in the PVBI copolymers (with the same VP mol% fraction) was found to have a strong positive correlation with the T_g values, water absorption properties and solubilities of the copolymers. Therefore, these properties could be tuned by fixing the mol% fraction of VP and altering the mol% fraction IBMA. While the copolymer PVBI 50/30/20 exhibited the most favourable physicochemical properties (i.e., low water absorption, moderate solubility at pH 1.5, and low solubility at pH ≥ 2.0), its high T_g value prevented cohesive film formation during fluidised-bed spray coating. As a result, the need to plasticise PVBI 50/30/20 to lower the T_g value of the copolymer while retaining its favourable physicochemical properties, was highlighted.

4.4 Experimental

4.4.1 Materials

The materials described in Chapter 4 are the same as **Chapter 2.6.1** and **Chapter 3.4.1**, unless stated below.

All reagents were used as received unless otherwise specified. MMA (99%) and IBMA (92.5%) were purchased from Sigma-Aldrich (St. Louis, United States) and passed through basic aluminium oxide to remove inhibitors immediately prior to use. Analytical grade toluene was purchased from Chem-Supply (Gillman, Australia).

4.4.2 Instrumentation

Instrument details are as outlined in **Chapter 2.6.2** and **Chapter 3.4.2**.

Nuclear Magnetic Resonance Spectroscopy

Carbon-13 nuclear magnetic resonance (^{13}C NMR) spectroscopy was performed at 298 K using a Bruker Avance III HD 600 MHz spectrometer (Billerica, United States) operating at 150 MHz. Samples were dissolved in deuterated chloroform ($CDCl_3$), and the residual chloroform solvent peak was used as an internal reference ($CHCl_3$; δ_C 77.2 ppm).

4.4.3 Procedures

The procedures in Chapter 4 were conducted as outlined in **Chapter 2.6.3** and **Chapter 3.4.3**, unless stated below.

Synthesis of Poly[(2-vinylpyridine)$_x$-co-(butyl methacrylate)$_y$-co-(methyl methacrylate)$_z$]

The copolymers of poly[(2-vinylpyridine)$_x$-*co*-(butyl methacrylate)$_y$-*co*-(methyl methacrylate)$_z$] (PVBM x/y/z) were synthesised with x:y:z ratios of 40:50:10,

30:50:20, 30:40:30, and 40:40:20 mol% VP:BMA:MMA. A representative description of the synthesis of PVBM 40:50:10 is provided.

Inhibitor-free VP (20.5 mL, 190 mmol), BMA (37.8 mL, 238 mmol) and MMA (5.07 mL, 47 mmol) (mol% VP:BMA:MMA 40:50:10), and 2,2'-azobisisobutyronitrile (AIBN) solution (6.51 mL, 4.8 mmol)) were combined ([total monomer]:[initiator] 100:1 mole ratio) in 1,4-dioxane (50% $v.v^{-1}$) under an inert atmosphere (Ar) and heated at reflux with stirring. Additional AIBN solution (6.51 mL, 4.8 mmol) was added after 1 and 2 h to maximise monomer conversion. After 3 h, the reaction was cooled (~ 25 °C), the crude reaction mixture (CRM) was diluted with tetrahydrofuran (THF) (~ 20% $v.v^{-1}$), transferred to a round-bottomed flask, and the copolymer product was obtained by drying the CRM *in vacuo* (10 mbar, 80 °C). The copolymer product was obtained as a pale-yellow solid. The percentage monomer conversion (determined by GC) was 99% and the isolated yield was > 98%. GPC M_n = 14.8 kDa, M_w = 32.4 kDa, $Đ$ = 2.19. ^{1}H NMR (600 MHz, 21 °C, $CDCl_3$) δ_H 8.45 (br s, CH, VP RU), 7.41 (br s, CH, VP RU), 6.97–6.50 (m, CH, VP RU), 3.90 (br s, OCH_2, BMA RU), 3.54 (br s, OCH_3, MMA RU), 3.25–2.07 (m, CH, VP RU), 2.07–1.01 (m, CH_2, VP, BMA and MMA RU), 1.01–0.13 (m, CH_3, BMA RU) ppm (**Figure 4.1**).

Synthesis of Poly[(2-vinyl pyridine)$_x$-co-(butyl methacrylate)$_y$-co-(isobornyl methacrylate)$_z$]

The copolymers of poly[(2-vinylpyridine)$_x$-*co*-(butyl methacrylate)$_y$-*co*-(isobornyl methacrylate)$_z$] (PVBI x/y/z) were synthesised with x:y:z ratios of 50:45:5, 50:40:10, 50:35:15, 50:30:20, and 40:40:20 mol% VP:BMA:IBMA. A representative synthesis of the PVBI 50:30:20 copolymer is given below.

Inhibitor free VP (20.50 mL, 190 mmol), BMA (18.00 mL, 113 mmol), and IBMA (17.25 mL, 76. mmol), and AIBN solution (5.25 mL, 3.1 mmol) were combined ([total monomer]:[initiator] 122:1 mole ratio) in 1,4-dioxane (50% $v.v^{-1}$) under an inert atmosphere (Ar) and heated at reflux with stirring. AIBN (5.25 mL, 3.1 mmol) was added again after 1 and 2 h to maximize monomer conversion. After 3 h, the reaction was cooled (~ 25 °C), and the solvent was removed *in vacuo*. Further drying was conducted at 80 °C *in vacuo* (0.01 mbar) to afford the polymer as a pale-yellow solid. The percentage conversion (determined by GC) was > 99%, and

the isolated yield was > 98%. GPC M_n = 17.7 kDa, M_w = 34.0 kDa, $Đ$ = 1.92. ^{1}H NMR (600 MHz, 21 °C, $CDCl_3$): δ_H 8.40 (br s, CH, VP RU), 7.39 (br s, CH, VP RU), 7.10–6.20 (m, CH, VP RU), 4.45−3.05 (m, OCH_2, BMA RU; OCH, IBMA RU), 3.00–2.05 (m, CH, VP RU), 1.97–1.0 (m, CH_2, VP, BMA and IBMA RU; CH, IBMA RU), 0.97–0.45 (m, CH_3, BMA and IBMA RU) ppm (**Figure 4.5**). ^{13}C NMR (150 MHz, 21 °C, $CDCl_3$): δ_C 176.4, 164.6, 149.1, 135.5, 124.3, 120.9, 64.0, 48.4, 46.8, 45.6, 45.1, 38.9, 33.8, 30.3, 27.0, 23.4, 20.1, 19.2, 18.3, 13.8, 11.5 ppm (**Figure A4.2**).

Preparation of Implant Coating Formulations

Implant NaOAc Core Formulation (MB Only)

The NaOAc core formulation was prepared by dissolving PEG 10 kDa (15 g), NaOAc (15 g), and MB (400 mg) in 70/30% v.v^{-1} EtOH/water under stirring. The temperature-controlled fluidisation air flow was set to 40 °C throughout the coating of the NaOAc core formulation.

Implant Reverse Enteric Coating Formulation (PVBI)

The pH-responsive copolymer formulation was prepared by dissolving poly[(2-vinylpyridine)$_x$-*co*-(butyl methacrylate)$_y$-*co*-(isobornyl methacrylate)$_z$] with an x:y:z ratio of 50:30:20 (PVBI 50/30/20, 10 g) in toluene (100 mL) under stirring to afford a 10% w.v^{-1} solution. The fluidisation air flow was at ambient temperature (23 ± 1 °C) throughout the coating of the PVBI 50/30/20 copolymer formulation.

4.5 Appendix

4.5.1 Supplementary Figures

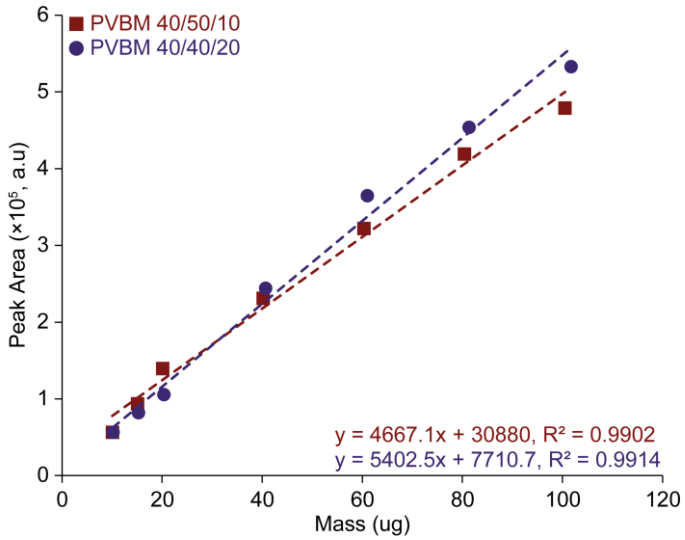


Figure A4.1: GPC standard curves for the PVBM 40/50/10 and 40/40/20 copolymers. Standards were prepared from an aqueous solution of each copolymer (pH 1.0, ~ 10 mg.mL^{-1}) and analysed at injection volumes of 10–100 µL (equivalent to 10–100 ug of copolymer on column).

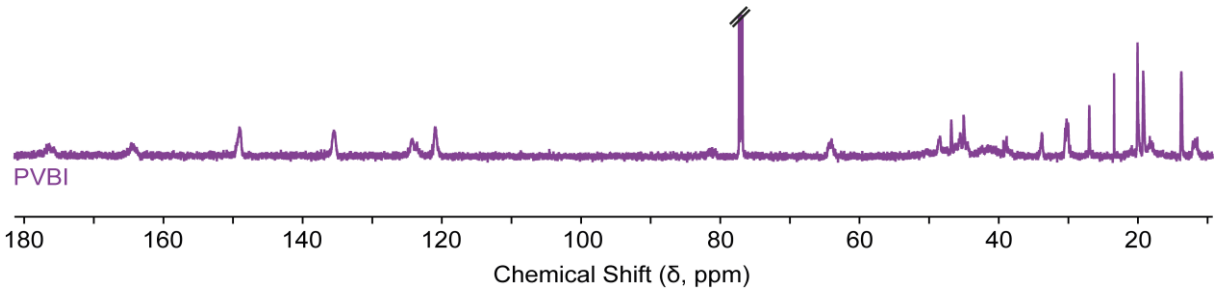


Figure A4.2: ^{13}C NMR spectrum (150 MHz, $CDCl_3$, 21 °C) of PVBI 50/30/20.

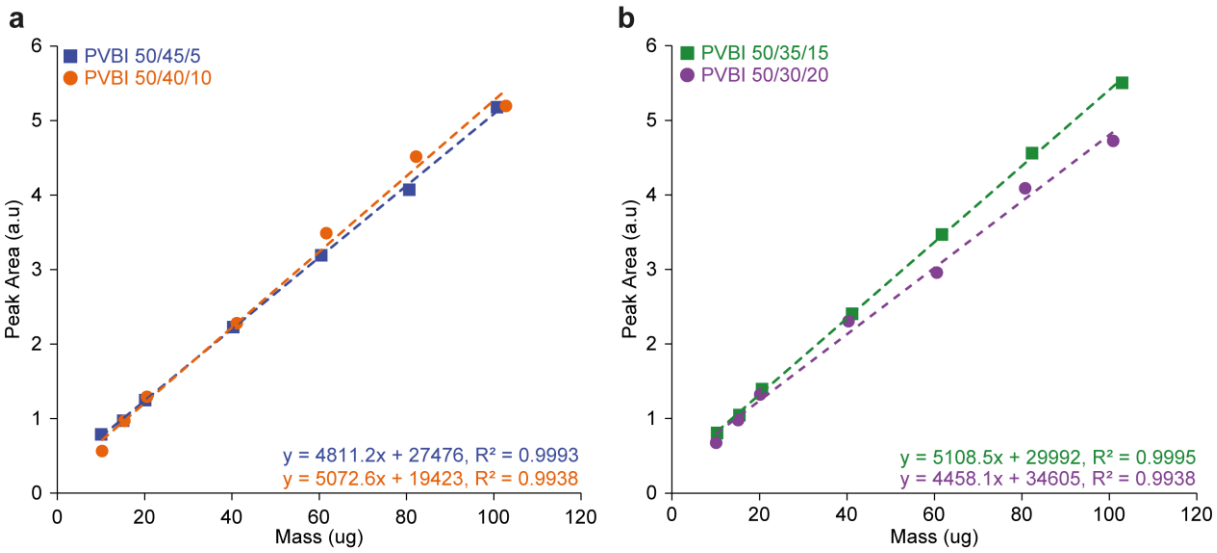


Figure A4.3: GPC standard curves for a) the PVBI 50/45/10 and 50/40/10 copolymers, and b) the PVBI 50/35/15 and 50/30/20 copolymers. Standards were prepared from an aqueous solution of each copolymer (pH 1.0, ~ 10 mg.mL^{-1}) and analysed at injection volumes of 10–100 µL (equivalent to 10–100 ug of copolymer on column).

4.5.2 Evaluation of the PVBM Copolymers 30/50/20 and 40/50/10 as Reverse Enteric, Taste-masking Coatings

Fluidised-bed Spray Coating

Two sub-batches of Suglets® coated with the model drug formulation containing PEG and RhB (n = ~ 340) (**Chapter 3.2.6, Figure A3.9**) were each coated with a 10% w.v^{-1} (in EtOH) reverse enteric PVBM copolymer formulation (**Table A4.1**). Each sub-batch was coated using two coating cycles, to afford total mass gains of ~ 4.9–6.5% w.w^{-1}, which were equivalent to ~ 175–232 µg per Suglet®. The same formulation and coating parameters were used for each copolymer formulation, to enable the comparison of their relative performance. Generally, Suglets® coated with the PVBM copolymer formulations did not exhibit any significant signs (qualitatively) of ineffective coating (**Figure A4.4**). Twinning was observed between Suglets® following coating with either formulation, though it was most pronounced with the PVBM 30/50/20 formulation (**Figure A4.4b**). However, it is highly likely that this could be mitigated in the future, by optimisation of the coating parameters.

Table A4.1: Summary of Suglet® batch properties before and after coating with model drug and copolymer formulations.

Coating	$n_{Suglets}$®	Mass Gain (% w.w^{-1})	Mass Coated (µg per Suglet®)
PEG/RhB	1805	6.2	209
PVBM 40/50/10	340	6.5	232
PVBM 30/50/20	338	4.9	175

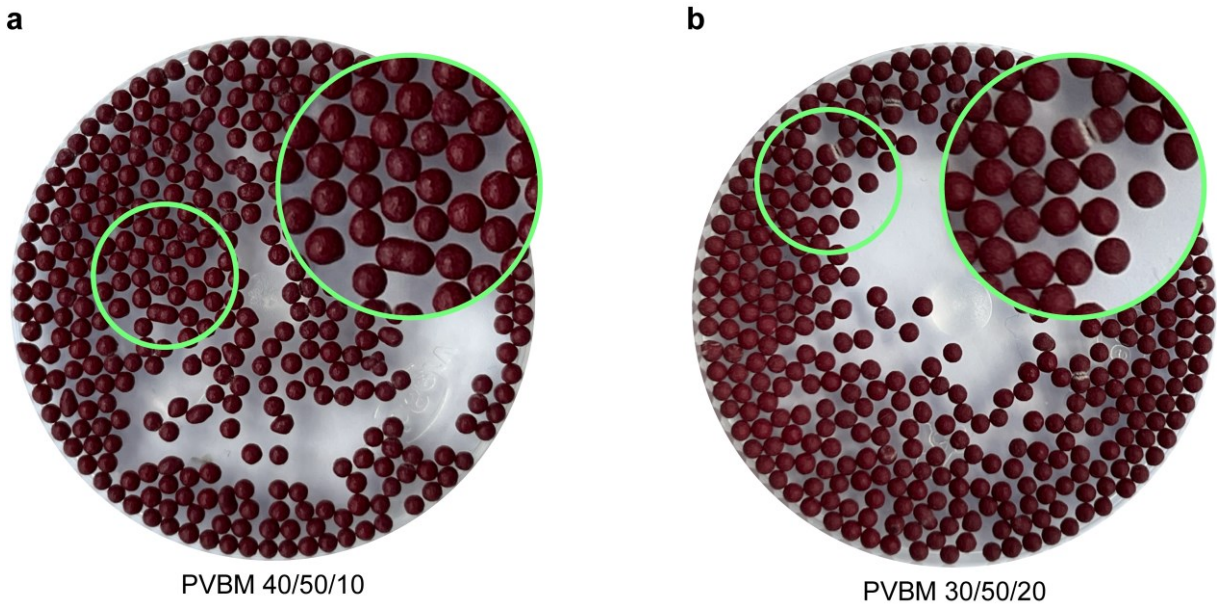


Figure A4.4: Suglets® coated with a) PVBM 40/50/10 (6.5% w.w^{-1} mass gain), b) PVBM 30/50/20 (4.9% w.w^{-1} mass gain).

In Vitro Evaluation of the Taste-masking Performance of PVBM 30/50/20 and 40/50/10

As described previously (**Chapter 3.5.3**) the stability of Suglets® (n = 6) bearing each of the tested PVBM copolymer coatings was assessed at pH 6.8 (37 °C). The least effective copolymer formulation was PVBM 30/50/20, where all the tested Suglets® (n = 6) released RhB immediately following immersion in the pH 6.8 solution. In contrast, the most effective copolymer formulation was PVBM 40/50/10, which effectively contained RhB in all 6 Suglets® for 30 min. Additional monitoring revealed continued containment of RhB for 72 h, in 6/6 Suglets® for the PVBM 40/50/10 coatings, respectively.

The results of the release experiments conducted at pH 1.5 are summarised in **Table A4.2**. Suglets® coated with the PVBM 30/50/20 formulation could not be monitored inline *via* Uv-Vis spectrophotometry, as no delayed release was exhibited at pH 1.5 (i.e., RhB was immediately released upon contact with the solution). Both the initial and complete release times for Suglets® coated with the PVBM 40/50/10 formulation, were positively correlated with its stability at pH 6.8. The tested PVBM 40/50/10 coated Suglets® rapidly released RhB, with short initial (4.6 ± 1.4 min) and complete release (8.5 ± 2.0 min) times, respectively (**Figure A4.5**).

Table A4.2: Summary of *in vitro* release results of model drug and copolymer coated Suglets®.

Coating	Initial Release [a] (min)	Complete Release [b] (min)
PVB 60/40	1.3 ± 0.1 (10)	2.1 ± 0.3 (15)
PVB 40/60	3.6 ± 1.5 (43)	7.2 ± 2.4 (33)
PVBM 40/50/10	4.6 ± 1.4 (32)	8.5 ± 2.0 (23)
PVBM 30/50/20	-	-

[a] Initial release was defined as 5% of the total release of RhB. [b] Complete release was defined as 90% of the total release of RhB. All values are reported as mean ± std. dev. (percentage relative standard deviation, %RSD) for n = 5 samples.

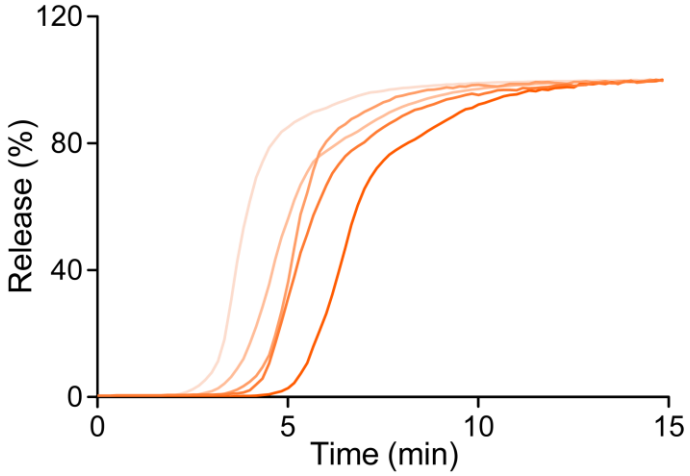


Figure A4.5: Release profiles obtained of Suglets® coated with a PEG/RhB model drug formulation (6.2% w.w^{-1} mass gain), and PVBM 40/50/10 (6.5% w.w^{-1} mass gain), during dissolution in a pH 1.5 solution (37 °C), under stirring. Traces

represent individual samples (n = 5), monitored *via* the absorbance maximum of rhodamine b (λ_{max} = 556 nm).

Compared to Suglets® coated with the PVB 40/60 formulation, the PVBM 40/50/10 formulation appeared to exhibit superior performance as a reverse enteric formulation. Moderately increased stability over 72 h of testing at pH 6.8 was observed for Suglets® coated with PVBM 40/50/10 (6/6 Suglets®) compared to those coated with PVB 40/60 (5/6 Suglets®). The similar stabilities of the two copolymers attributed to their T_g values. PVB 40/60 and PVBM 40/50/10 exhibited similar T_g values (T_g = 43.3 °C and 45.3 °C, respectively), which were lower than that of PVB 60/40 (58.9 °C) and PVBM 30/50/20 (T_g = 50.2 °C). The comparatively lower T_g values of PVB 40/60 and PVBM 40/50/10, likely facilitated the interpenetration of polymer chains[17] and ultimately film formation. Incomplete film formation is likely to have occurred for the PVBM 30/50/20 coated Suglets®, due to its moderately high T_g value (T_g = 50.2 °C).

Whilst these results are preliminary — given the small batch sizes employed — with further evaluation the reported copolymers may enable the preparation of reverse enteric pharmaceutical formulations with improved taste-masking properties, using relatively low proportions of the copolymers in the resultant dosage form.

4.6 References

1. J. Brandrup, E. H. Immergut, E. A. Grulke, A. Abe and D. R. Bloch, *Polymer Handbook*, Wiley New York, 4th edn., 1999.

2. J. M. Yu, P. Dubois and R. Jérôme, *Macromolecules*, 1996, **29**, 7316–7322.

3. M. Fernández–García, R. Cuervo–Rodriguez and E. L. Madruga, *J Polym Sci, Part B: Polym Phys*, 1999, **37**, 2512–2520.

4. G. Nguyen, D. Nicole, M. Matlengiewicz, D. Roizard and N. Henzel, *Polym Int*, 2001, **50**, 784–791.

5. S. K. Ooi, W. D. Cook, G. P. Simon and C. H. Such, *Eur Polym J*, 2002, **38**, 903–910.

6. I. Šoljić, A. Jukić and Z. Janović, *Polym Int*, 2009, **58**, 1014–1022.

7. D. Neugebauer, K. Bury and M. Wlazło, *J Appl Polym Sci*, 2012, **124**, 2209–2215.

8. L. M. Smith and M. L. Coote, *J Polym Sci, Part A: Polym Chem*, 2013, **51**, 3351–3358.

9. S. Özlem-Gundogdu, E. A. Gurel and J. Hacaloglu, *J Anal Appl Pyrolysis*, 2015, **113**, 529–538.

10. B. J. Holland and J. N. Hay, *Polymer*, 2001, **42**, 4825–4835.

11. K. Li, W. Ma, H. Han, C. Xu, Y. Han, D. X. Wang, W. Ma and Z. Zhang, *Desalin Water Treat*, 2019, **170**, 46–54.

12. N. Hadjichristidis, J. Mays, W. Ferry and L. J. Fetters, *J Polym Sci B Polym Phys*, 1984, **22**, 1745–1751.

13. K. Y. Ko and S. H. Hwang, *J Ind Eng Chem*, 2018, **59**, 50–55.

14. J. E. Mark, *Physical Properties of Polymers Handbook*, Springer, New York, 2nd edn., 2006.

15. S. Ozlem, E. Aslan-Gürel, R. M. Rossi and J. Hacaloglu, *J Anal Appl Pyrolysis*, 2013, **100**, 17–25.

16. A. Matsumoto, K. Mizuta and T. Otsu, *J Polym Sci, Part A: Polym Chem*, 1993, **31**, 2531–2539.

17. L. A. Felton, *Int J Pharm*, 2013, **457**, 423–427.

Chapter 5: Manufacture and Evaluation of Implants with an Optimised Reverse Enteric Coating

5.1 Overview

As highlighted in **Chapter 4.2.11**, Chapter 5 describes the plasticisation of the lead copolymer of 2-vinylpyridine (VP), butyl methacrylate (BMA) and isobornyl methacrylate (IBMA), using the hydrophobic plasticiser ethyl oleate (EO). Using a plasticised coating formulation containing the lead copolymer (PVBI/EO_{10}), non-toxic PVBI/EO_{10} implants are then prepared using the same approach as described in **Chapter 3.2**. The performance of the PVBI/EO_{10} implants is investigated both *in vitro* and *in vivo*, as previously described in **Chapter 3.2**, with additional *in vitro* testing of the mechanical properties of the PPIs, and a longer duration *in vivo* stability study. The glass transition temperature (T_g) and water absorption properties of the plasticised copolymer were both found to exhibit proportional relationships with the concentration of EO. An EO concentration of 10% $w.w^{-1}$ afforded the most appropriate glass transition temperature, whilst only affording a moderate increase in water absorption. Manufactured PVBI/EO_{10} implants were found to exhibit low intrabatch variation, and excellent *in vitro* stability and release properties. While swelling was not mitigated, the PVBI/EO_{10} implants showed favourable stability *in vivo*, with most implants remaining stable for 12 weeks. In addition, the PVBI/EO_{10} implants were found to exhibit comparable biocompatibility with conventional radiofrequency identification (RFID) microchips. These results were considered a proof-of-concept demonstration of the function of the population protecting implant (PPI) and highlighted the need to determine whether such performance was conserved when PPIs were manufactured with a toxic core formulation.

The mechanical testing apparatus described in this chapter was designed and printed by Jarrod Kohlhagen, while Kyle Brewer conducted all mechanical testing experiments, and interpreted and reported all the resulting data. The in vivo stability experiment was conducted by Dr. Todd McWhorter, with technical assistance from Dr. Anthony Nicholson, and Julie Olson. Kyle Brewer assisted in

the interpretation of the raw data and conducted all data reporting and visualisation. Dr. Todd Gillam and Dr. Nobuyuki Kawashima provided technical assistance with the scanning electron microscopy experiments described in this chapter, while Kyle Brewer acquired most of the micrographs, performed all interpretation of the results and conducted all data reporting and visualisation. Dr. Todd Gillam provided technical assistance with the electrospray ionisation-mass spectrometry experiment described in this chapter, while Kyle Brewer conducted all interpretation, reporting, and visualisation of the results.

5.2 Results and Discussion

5.2.1 Plasticisation of Poly[(2-vinylpyridine)$_x$-*co*-(butyl methacrylate)$_y$-*co*-(isobornyl methacrylate)$_z$] (PVBI 50/30/20)

While many pH-responsive polymers are used commercially and have been reported in the literature,[1–3] none have been designed for long-term stability in the subcutaneous environment. This is likely due to a considerable challenge posed by reverse enteric coatings — water absorption. In **Chapter 4.2**, PVBI 50/30/20 was determined to have physicochemical properties that may limit water absorption, namely, insolubility at pH 7.4 with low water absorption (< 0.5% w.w^{-1}) and solubility at pH < 2 (3.7 ± 0.4 mg.mL^{-1} at pH 1.5). However, when this copolymer was applied to the implants, it produced coatings that were ‘dusted’, brittle, and prone to fracture, both during processing and storage, which was attributed to the high glass transition temperature (T_g) value (~ 74 °C) of the copolymer. To maintain the favourable physical attributes of the PVBI copolymer and simultaneously reduce its T_g value, the plasticisation of PVBI 50/30/20 was investigated.

The plasticiser ethyl oleate was selected to plasticise the PVBI copolymer, as it satisfies many of the criteria outlined in **Chapter 1.3.3**. Ethyl oleate was selected due to the relative hydrophobicity of oleate plasticisers (i.e., log K_{ow} = 9.21–9.49) — and therefore likely similar non-polarity to PVBI/EO_{10}.[4] In addition, ethyl oleate has a high boiling point (357 °C)[5] and low vapour pressure common of oleate plasticisers (0.13–0.5 kPa at 200 °C).[4] Ethyl oleate also has similar structural features (i.e., an ester functional group and long alkyl chain) that are amenable to

secondary interactions with PVBI/EO_{10} (e.g., Van der Waals interactions). Ethyl oleate is also known to be an effective plasticiser for coating and film applications.[4] Finally, ethyl oleate is a cost-effective choice, as it can be purchased commercially or facilely synthesised from readily available precursors (i.e., ethanol and oleic acid) (*vide infra*).

To interrogate the effects of EO on PVBI 50/30/20, the physicochemical properties of PVBI 50/30/20 in combination with 0 to 15% $w.w^{-1}$ EO, were evaluated. An increase in the concentration of EO from 0 to 15% $w.w^{-1}$ resulted in a significant reduction of the T_g value by as much as ~ 54 °C (

Figure 5.1a). Additionally, modulated thermogravimetric analysis (MTGA) of the plasticised formulations revealed a characteristic decomposition event at ~ 150 °C corresponding to EO, which increased proportionally from 7.6 to 17.2% consistent with the EO loading (

Figure 5.1b). In comparison, the PVBI copolymer was thermally stable up to ~ 280 °C.

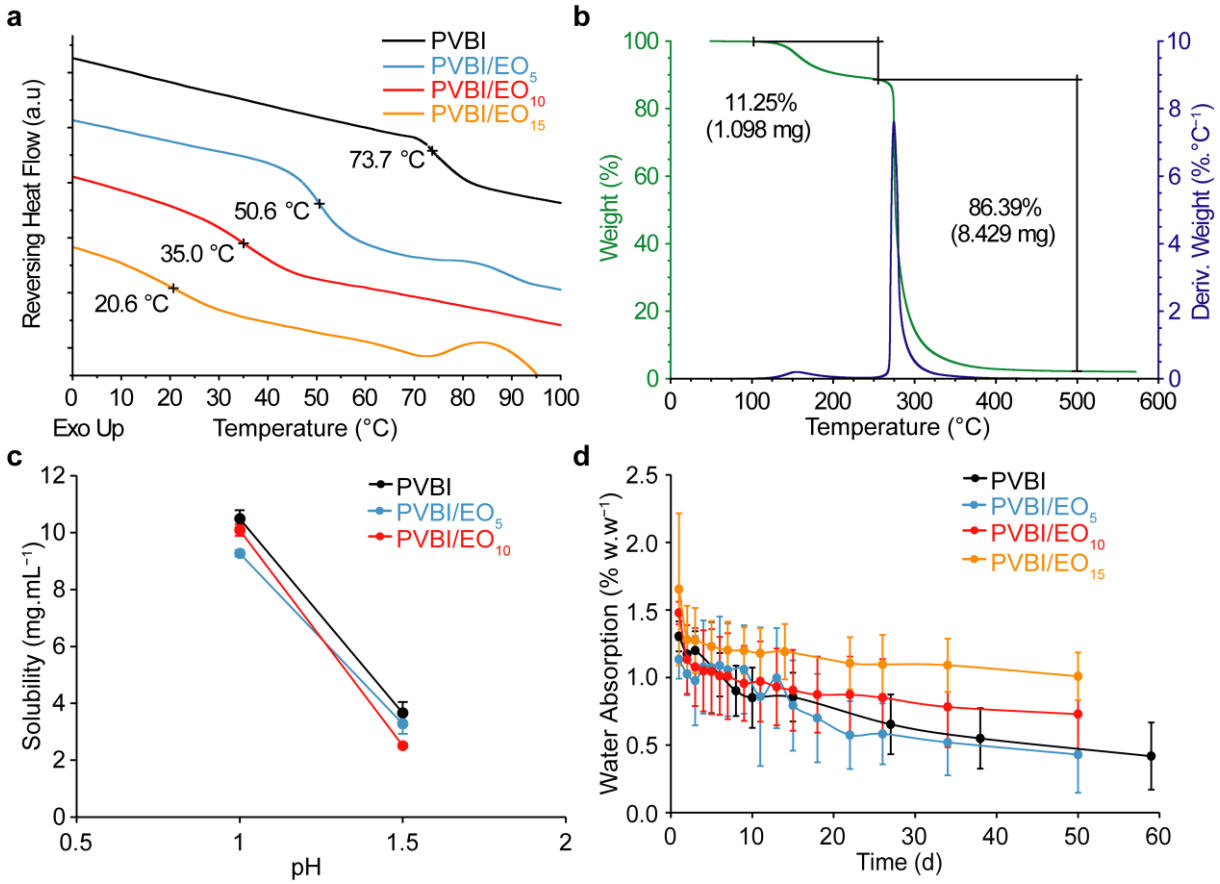


Figure 5.1: a) Overlay of the reversing heat flow curves (in arbitrary units, a.u.) from modulated differential scanning calorimetry (MDSC) of PVBI, with 0, 5, 10, and 15% w.w^{-1} EO, showing their respective glass transitions and T_g values. b) Weight (%) and derivative weight (%.°C^{-1}) curves from the MTGA analysis of PVBI/EO$_{10}$. c) Effect of plasticisation with EO on the solubility of PVBI in pH 1.0, 1.5, and 2.0 solutions; values are reported as the mean ± std. dev. (n = 3), and the solubility results are also tabulated in the Appendix (**Figure A5.1**). d) Effect of plasticisation with 5, 10, and 15% w.w^{-1} EO on the water absorption of PVBI at pH 7.4 and 37 °C; values are reported as the mean ± std. dev. (PVBI n = 8, PVBI/EO$_5$ n = 5, PVBI/EO$_{10}$ n = 5, and PVBI/EO$_{15}$ n = 4), and the water absorption results are also tabulated in the Appendix (**Table A5.2**).

The presence of EO did not have a significant effect on the solubility of the copolymer (

Figure 5.1c). Importantly, water absorption testing of the EO-containing formulations revealed only a slight increase in water absorption with increasing EO, which remained < 1.5% $w.w^{-1}$ for all formulations (

Figure 5.1d). Considering these results, the copolymer formulation containing 10% $w.w^{-1}$ EO and solubilised in toluene (10% $w.v^{-1}$) ($PVBI/EO_{10}$) was selected

for implant manufacture as it exhibited the most appropriate physicochemical and thermal properties. Namely, PVBI/EO_{10} exhibited a T_g value close to physiological temperature, that would likely allow the coating to remain flexible *in vivo*, and therefore withstand swelling.

5.2.2 Manufacture and Evaluation of the PVBI/EO_{10} Implants

As previously described (**Chapter 4.2.11**), the core formulation containing sodium acetate, poly(ethylene glycol), and methylene blue (NaOAc:PEG:MB, 1:1:0.027 weight ratio) dissolved in ethanol (EtOH):water (70:30) was spray coated onto rod-shaped acrylonitrile butadiene styrene (ABS) filament substrates (n ≈ 1000; 0.63 ± 0.06 mm diameter × 7.38 ± 0.08 mm length) (

Figure 5.2a) until ~ 6 mg per implant had been deposited (

Figure 5.2b). The resulting NaOAc implant cores (n ≈ 500; 1.14 ± 0.06 mm diameter × 7.76 ± 0.2 mm length) were then spray coated with the optimal copolymer formulation (PVBI/EO_{10}) to afford implants with coating thicknesses of 100, 200, and 300 μm (

Figure 5.2c). By varying the thickness of the copolymer coating, its effect upon implant stability, release and the flexural properties could be assessed, enabling the selection of an optimised implant design.

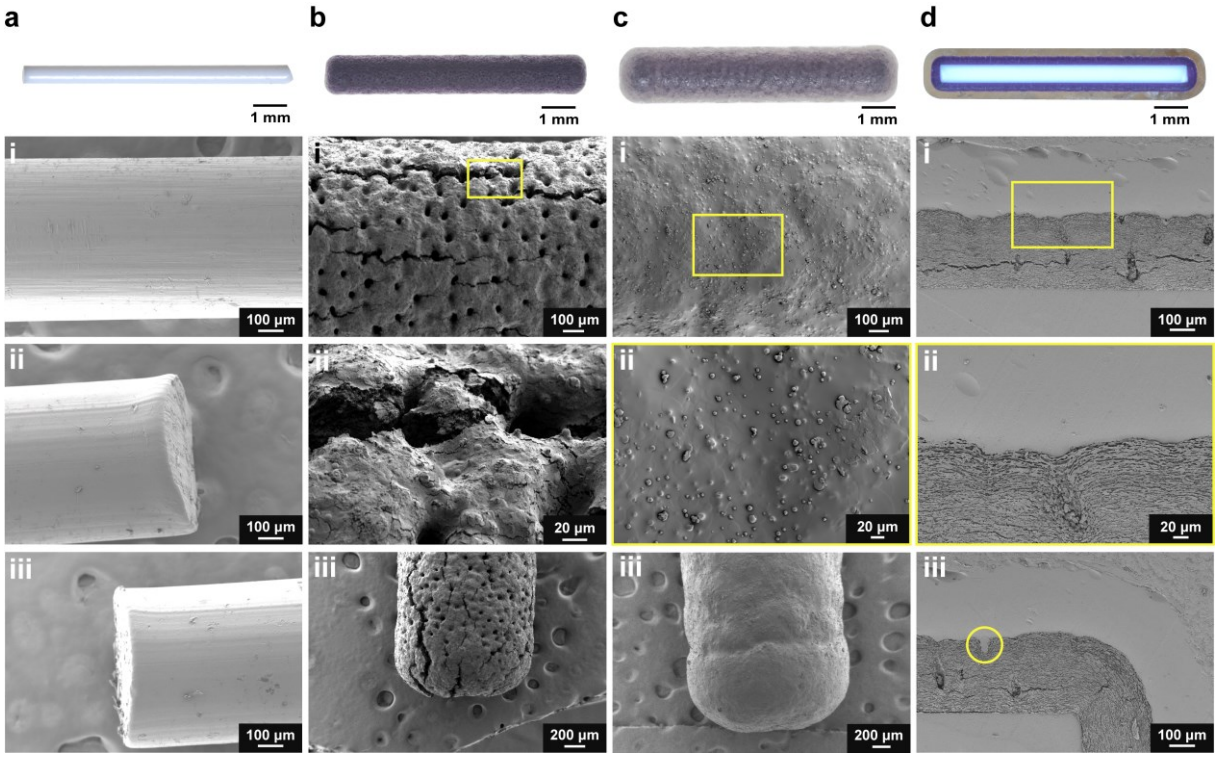


Figure 5.2: Representative digital images and scanning electron micrographs of a) an ABS filament substrate, b) a NaOAc core, c) a NaOAc core and PVBI/EO_{10} coated (300 µm) implant, and d) an epoxy-embedded and microtomed NaOAc core and PVBI/EO_{10} coated (300 µm) implant, note the filled-in pit encircled in yellow.

Once the desired coating mass (core formulation) or thickness (copolymer formulation) was reached, statistically relevant samples of implants (n = 75 (15% batch size)) were weighed measured using digital callipers, and the final coating mass and thickness were determined (**Table 5.1**). In addition, implants were

embedded in epoxy resin (n = 6 from each coating thickness) and microtomed to afford a longitudinal cross section of the implant at the midpoint (

Figure 5.2d). The resultant microtomed samples were imaged under an optical microscope and inspected for coating uniformity and the presence of any coating defects. Point-to-point measurements were then made of the PVBI/EO_{10} coatings to further interrogate the coating uniformity (**Table 5.1**).

Calliper measurements were generally found to be ~ 20% higher than the point-to-point measurements of the microtomed samples but exhibited the same trend of increasing coating thickness (relative to the number of coating cycles) and low percentage relative standard deviations (RSD% < 10%). However, there was greater variation in the coating thicknesses determined from calliper measurements made across the length of the implants. This may be due to a slight variation in the length and shape of the substrates, rather than a disproportionate coating thickness at the ends (compared to the sides). This is supported by the comparatively low variation in both the calliper measurements at the sides, and the point-to-point measurements made at the ends and sides. In addition, inspection of the coatings following microtoming, revealed uniform and defect-free PVBI/EO_{10} coatings around the perimeter of the implant, supporting this reasoning (

Figure 5.2d).

Implants from each stage of coating were also analysed *via* scanning electron microscopy (SEM) to interrogate the morphology of the coatings, particularly the presence of coating artifacts (i.e., fractures and dusting) not easily observed *via* optical microscopy (OM). Such artifacts could affect the integrity of the coatings and their performance *in vivo*. Micrographs of the substrates revealed smooth surfaces with slight deformation at each end, caused when cutting the filament (

Figure 5.2a); however, the deformation did not result in any observable defects in either the core (

Figure 5.2b) or PVBI/EO_{10} coatings (

Figure 5.2c). The NaOAc core coatings exhibited pitting (

Figure 5.2b), as previously observed in **Chapter 3.2.1** which was unlikely to be due to the processing temperatures used,[6] but rather the formation of micropores due to the slower evaporation of water (cf., EtOH) during coating.[7] Cracking was also observed in the core coating, due to the high NaOAc content and the contraction of the deposited material during evaporation, as described in **Chapter 3.2.1**. Importantly, the pitting and cracking defects in the core appeared to have no effect on implant storage and handling, or subsequent performance.

Table 5.1: Summary of implant dimensions following coating with the lead PVBI/EO_{10} formulation.

Coating Thickness (μm)	Diameter (mm) [a]	Length (mm) [a]	Mass (mg) [a]	Coating Thickness (Calliper) (μm) [a]		Coating Thickness (Microtomed) (μm) [b]			
				Side Midpoint	End	Overall [c]	Ends [d]	Sides [e]	Side Midpoint [f]
100	1.37 ± 0.05	7.99 ± 0.19	12.74 ± 0.87	115 ± 9	116 ± 30	99 ± 9	101± 10	97 ± 8	98 ± 8
200	1.57 ± 0.06	8.17 ± 0.25	16.98 ± 1.19	218 ± 10	206 ± 35	170 ± 13	169 ± 15	169 ± 10	181 ± 6
300	1.75 ± 0.05	8.28 ± 0.27	20.97 ± 0.94	307 ± 8	256 ± 38	237 ± 17	242 ± 20	233 ± 12	243 ± 10

[a] Determined from n = 75 digital caliper measurements. [b] Determined from n = 6 epoxy-embedded, microtomed implants. [c] Determined from 22 point-to-point measurements. [d] Determined from 10 point-to-point measurements. [e] Determined from 12 point-to-point measurements. [f] Determined from 2 point-to-point measurements. All results are reported as the mean ± std. dev.

The effects of the pitting and cracking were negligible, as micrographs of the implant cross-section (

Figure 5.2d) revealed that the pits were mostly superficial, with depths of less than ~ 50 μm (< 17% of the core coating thickness). In addition, once coated with PVBI/EO_{10}, these pits were filled, as evidenced by the cohesive film observed in the micrographs of the PVBI/EO_{10} implant (

Figure 5.2c) and the presence of a filled pit in the implant cross-section (

Figure 5.2d). The presence of PVBI/EO_{10} particles (< 10 μm) was also observed on the surface of the PVBI/EO_{10} implant (

Figure 5.2c), indicating that minor dusting had occurred during coating. However, given the clear evidence of droplet spreading and adhesion on the NaOAc core, and the absence of any coating defects in the implant cross-section (

Figure 5.2d), these particles did not have any effect upon the uniformity of the coating. These data demonstrated that cohesive film formation was achieved for both core and copolymer coatings, with low intrabatch variation and tuneable coating thicknesses. The implants were also able to be manufactured at a diminutive size (< 2 mm diameter × < 9 mm length) with a mass of payload equivalent to a lethal (> LD_{90}) dose of sodium fluoroacetate (1080), while maintaining compatibility with commercial syringe implanters.

5.2.3 Investigation of the Mechanical Properties of the PVBI/EO_{10} Implants

While the soft tissue of the animal is likely to dampen any mechanical forces experienced by an implant, increased physical activity (e.g., fighting and mating) may cause flexural deformation and implant failure. The mechanical integrity of the PPIs was assessed *via* three-point flexural testing, where the flexural strength (σ_F) is defined as the maximum stress at failure experienced during bending and the flexural modulus (E_f) relates to the resistance to bending (i.e., stiffness).[8] In the context of the PPIs, σ_F and E_f relate to how much bending the implants can

withstand before fracture and how resistant the implants are to bending, respectively. Flexural testing was conducted on as-prepared implants with different thickness coatings of the lead copolymer, with and without EO for comparison (Appendix, **Figure A5.1**). σ_F and E_f for each sample were calculated based on a fixed diameter equal to that of the implant core. This was conducted to minimise the influence of the overall implant diameter upon the calculated values and instead constrain the analysis to the physical properties of the plasticised and unplasticised coatings. There was a small increase in σ_F when the thickness of the polymer coating was increased, for both coatings. However, σ_F significantly increased when the coating was plasticised in PVBI/EO_{10}, regardless of the coating thickness (**Figure 5.3a**). The increase in σ_F was attributed to the lower T_g value of the plasticised coating, compared to the unplasticised coating (35 °C *versus* 74 °C), which made it more ductile and less brittle, enabled it to withstand greater flexure, and resulted in a higher measured flexural strength. Together, these results showed that σ_F was primarily dependent on the ductility of the plasticised PVBI/EO_{10} coating and, to a lesser extent, the thickness of the coating itself. Conversely, E_f was found to be similar for implants with and without plasticised coatings, indicating a similar stiffness and resistance to deformation (**Figure 5.3a**). Thus, it was likely that the composition of the implant core (namely, the ABS filament substrate) was the major determinant for E_f. Overall, the plasticised PVBI/EO_{10} coating produced implants with improved mechanical properties, as it is probable that an implant that exhibits a degree of flexibility would be best suited for subcutaneous implantation. This would allow some flexing, which is likely to be experienced in the subcutaneous environment of native mammals. These results highlighted the importance of the core and copolymer coatings in preparing implants with desired mechanical properties.

5.2.4 *In Vitro* Release Properties of the PVBI/EO_{10} Implants

The dissolution of the copolymer coating and subsequent release of the core contents from implants were investigated *in vitro* at pHs 1.0 and 1.5 (**Figure 5.3b**), to mimic the gastric environment of a feral cat. The release of NaOAc (analogous to 1080) was monitored *via* the concomitant release of MB ($\lambda_{max.}$ = 664 nm) present within the implant core, to enable inline monitoring *via* UV-visible spectrophotometry. As expected, the time taken for the initial release was found to

be directly proportional to the thickness of the PVBI/EO_{10} coating at both pHs 1.0 and 1.5 (**Figure 5.3b** and **Table 5.2**). Similarly, an increase in coating thickness resulted in a commensurate increase in the time taken for complete release. From pH 1.0 to pH 1.5, the time taken for both initial and complete release approximately tripled, and implants with the thickest coating (300 µm) achieved complete release within ~ 100 min at pH 1.5 (27 min at pH 1.0). Importantly, for implants at each coating thickness and pH, core release occurred within the gastric half-emptying times (GET) reported for feral cats (~ 2.5–4 h).[9]

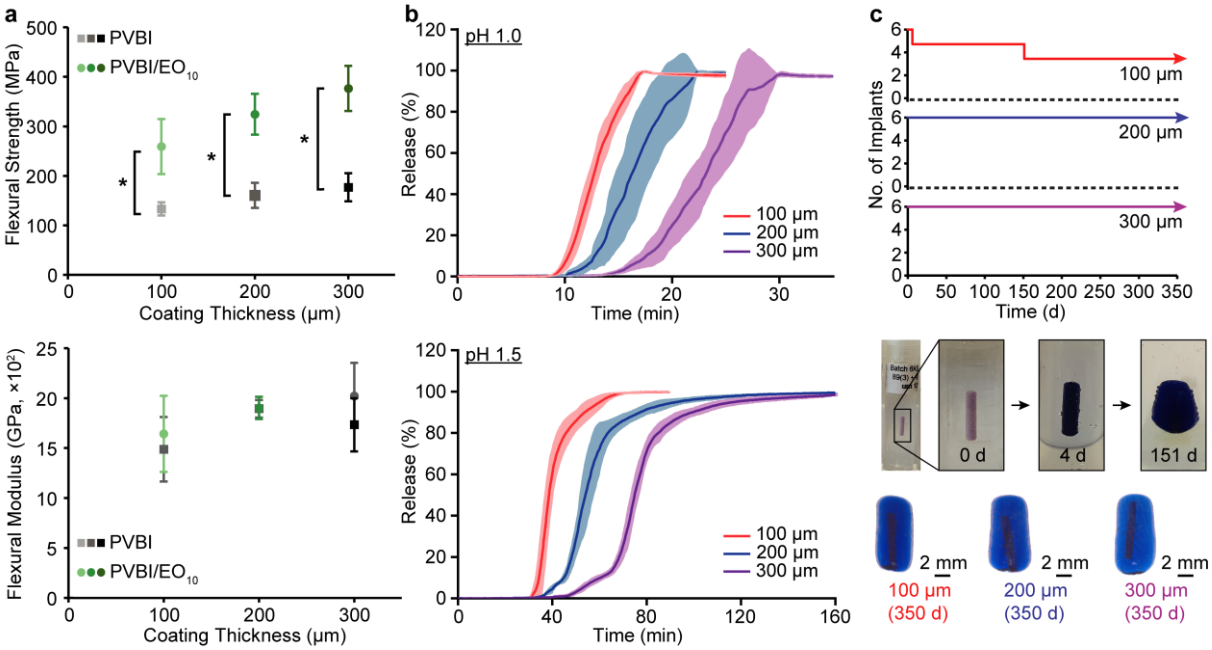


Figure 5.3: a) Flexural strength (σ_F) and flexural modulus (E_f) measurements of PVBI and PVBI/EO_{10} implants (n = 5), determined from force versus stroke curves generated through three-point flexural testing. All tests were conducted at ambient temperature (23 ± 1 °C), and all values were calculated for implants with fixed diameters (1.14 mm). σ_F and E_f values are reported as the mean ± std. dev. (n = 5), *p < 0.05 × 2-sample t-test of difference = 0 (vs ≠ 0). Force versus stroke curves from all tests are provided in the Appendix (**Figure A5.1**). b) Release monitoring profiles of MB from PVBI/EO_{10}-coated implants (100, 200, or 300 µm) at 37 ± 1 °C, in pH 1.0 or pH 1.5 (3.5 mL) release media. Traces are reported as the mean (solid line) ± std. dev. (shaded area) (n = 5). c) Stability results of PVBI/EO_{10} implants (100, 200, or 300 µm) in Pluronics F127 (25% $w.w^{-1}$,in PBS) at pH 7.4 and 37 °C (n = 6), over 350 days. Traces represent the number of stable implants (i.e., no failure of the PVBI/EO_{10} coating and release of the core material) for implants at each coating thickness. Images show the swelling and failure of a

100 µm PVBI/EO_{10} implant over 151 days and representative implants that were stable at 350 days.

Table 5.2: Summary of PVBI/EO_{10} implant *in vitro* release results.

Coating Thickness (µm) [a]	pH 1.0		pH 1.5	
	Initial Release (min) [b]	Complete Release (min) [c]	Initial Release (min)	Complete Release (min)
100	10.0 ± 0.5	15.9 ± 0.6	34. ± 1.4	54.2 ± 4.1
200	12.1 ± 0.9	19.6 ± 1.9	39.9 ± 1.3	77.4 ± 6.7
300	16.6 ± 1.2	26.78 ± 1.6	53.0 ± 2.6	99.3 ± 6.7

[a] NaOAc implants coated with the PVBI/EO_{10} formulation. [b] Initial release was defined as 5% of the total release of MB from the implant core. [c] Complete release was defined as 90% of the total release of MB from the implant core. All values are reported as the mean ± std. dev. (n = 5).

As described in **Chapter 3.2.7** though *in vivo* release experiments are required, implant release will likely occur even after only a small fraction of the PVBI/EO_{10} coating is solubilised. A video footage recorded of implant release (pH 1.5) supports this reasoning (Appendix, **Figure A5.2c**).

5.2.5 *In Vitro* Stability Properties of PVBI/EO_{10} Implants

The stability of the implants was assessed *in vitro* using a hydrogel model to mimic the subcutaneous environment. Implants with different coating thicknesses were completely submerged in Pluronics hydrogels in PBS (pH 7.4) and stored at 37 °C (**Figure 5.3c**). This enabled the interrogation of implant stability at physiological pH (7.4), temperature (37 °C), and hydration (75%),[10, 11] with failure indicated by the observed release of methylene blue from the implant core.

While the implants coated with PVBI/EO_{10} at coating thicknesses of 200 and 300 µm were found to be stable for at least 350 d, two 100 µm coated implants (40%) failed at 6 and 151 d (**Figure 5.3c**). The relatively rapid failure of the 100 µm coated implants implies that defects present in thinner coatings were not observed *via* microscopy of the microtomed samples; however, this may be due to the relatively small sample size. For all the implants, regardless of coating thickness, it was noted that over several days, the core would slowly darken in colour indicating the permeation of water through the coating and dissolution of the core (**Figure 5.3c**). Like all nonporous polymer films submerged in water or exposed to water vapour,[12, 13] and the PVB implants described in **Chapter 3.2.7**, the polymer coating was found to act as a semipermeable membrane. The lower water absorption of the PVBI/EO_{10} coating (cf., PVB 50/50) appeared (qualitatively) to limit permeability and prevent a rapid ingress of water that could have led to coating/implant failure. However, over longer periods, the implants were again found to gradually swell due to the ingress of water along the osmotic gradient.

The movement of water through the PVBI/EO_{10} coating (i.e., osmosis) caused the solubilisation of the core material, leading to a 'swelling' of the implant core, *via* the same process as described in **Chapter 3.2.7**. The two 100 µm PVBI/EO_{10} implant failures observed were likely due to this phenomenon; due to swelling, the PVBI/EO_{10} coating would be stretched and thinned by the osmotic pressure, and the thin 100 µm coatings were likely less able to withstand this process, leading to failure. Increasing the thickness of the copolymer coating did not appear to significantly reduce swelling, though the relative flexibility of the coating appeared to prevent rupture for the remaining 100 µm coated implants and all the 200 and 300 µm coated implants (**Figure 5.3c**). There was no observed release of the core material for implants that did not rupture following swelling, likely due to the charged nature of NaOAc and MB and the molecular weight of PEG 10 kDa, all preventing transport across the neutral PVBI/EO_{10} coating. While this suggested that 1080 would be effectively contained in the core of the implants despite swelling, it was important to consider that the swelling of implants *in vivo* could reduce their mechanical strength and impact their long-term stability in native mammals, as they will likely be exposed to moderate mechanical stresses. However, it was hypothesised that with the qualitatively more water-absorption-

resistant PVBI/EO_{10} coating, the PVBI/EO_{10} implants may exhibit impeded swelling and superior stability *in vivo*.

5.2.6 *In Vivo* Stability Properties of PVBI/EO_{10} Implants

In vivo stability of the 300 µm coated PVBI/EO_{10} implants was investigated over 12 weeks using a murine model, where, in a reverse time order, male Sprague-Dawley rats (n = 6) were injected with three implants to assess stability at 4, 2, and 1 week(s) (n = 3), or 12, 9, and 6 weeks (n = 3). A RFID microchip was also implanted for identification and as a control (

Figure 5.4a, top). The first implant in each series (i.e., t = 12 or 4 weeks) was implanted superficial to the left scapula, ~ 1 cm to the left of the spine, with subsequent implants positioned caudally along the animal (

Figure 5.4a). The results from the *in vivo* stability study of the PVB implants (**Chapter 3.2.8**) suggested that the PVBI/EO_{10} implants located most caudally (i.e., the 1- and 6-week(s) time points) would be subjected to greater mechanical stress due to the thinner and more restrictive subcutis. However, PVBI/EO_{10} implants were again placed at this location to provide a performance comparison between the two implant types — namely any changes in performance afforded by the PVBI/EO_{10} coating — and to maximise the beneficence of the experiment by evaluating implants at three time points for each rat. Each microchip was implanted superficial to the right scapula, adjacent to the first implant. Once the final time point was reached (i.e., 1 or 6 weeks), the integrity of the implants was assessed qualitatively prior to euthanasia *via* computed tomography (CT) and again by visual examination post-mortem.

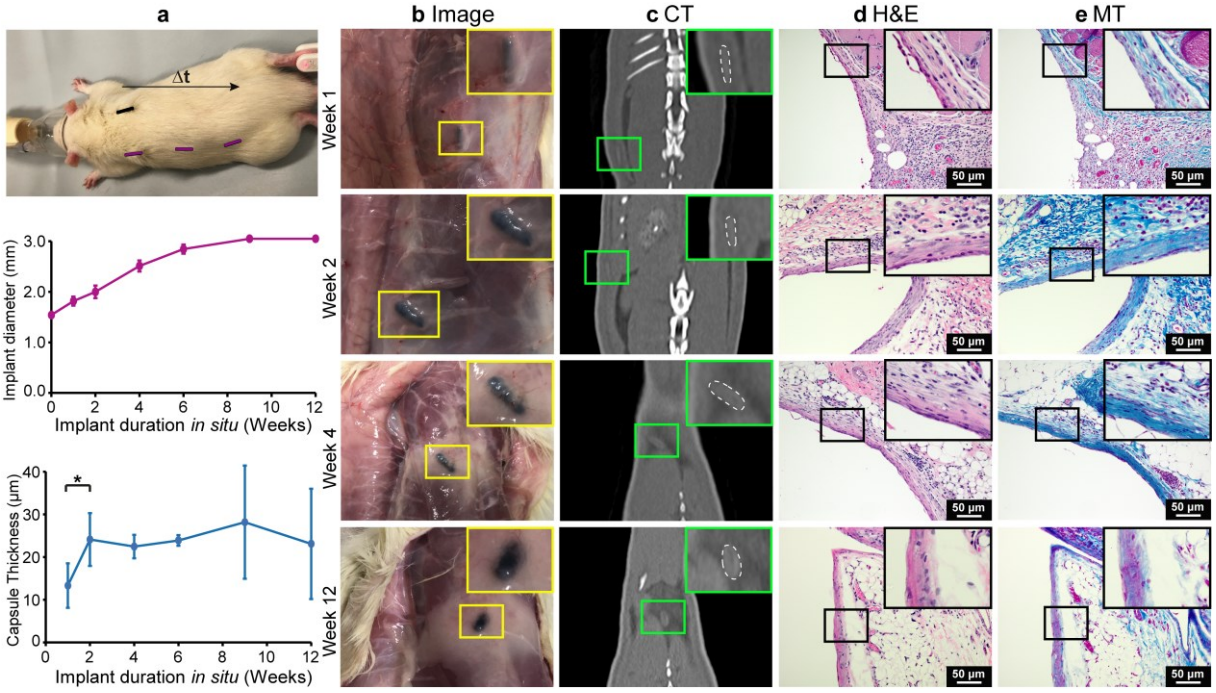


Figure 5.4: a) PVBI/EO$_{10}$ implant (purple) and microchip (black) locations (top), implant diameter measurements obtained from CT images of implants *in situ* (middle), and fibrous tissue capsule (FTC) thickness (µm) as measured from tissue explants using point-to-point measurements in Olympus LabSens (bottom); values are reported as the mean ± std. dev. (week 0, n = 6; weeks 1–4, n = 3; weeks 6–12, n = 2), *p < 0.05 × t-test of difference = 0 (vs <). b) Macroscopic images (post-mortem) of implants *in situ*, captured prior to explantation, note the

swelling of the implants and the containment of the core material. c) CT scans of intact implants captured prior to euthanasia, with implants encircled in white. d) Hematoxylin and eosin (H&E) and e) Masson's trichrome (MT) stained samples of the explanted tissue, revealing the FTC surrounding the implants; representative results for the 9-week implant are available in the Appendix (**Figure A5.3**).

As observed *in vitro*, all implants exhibited swelling *in vivo*, as shown in the post-mortem examination (

Figure 5.4b) and CT images (

Figure 5.4c). Implants increased in diameter due to swelling, until a plateau was reached 9 weeks following implantation at ~ 3 mm in diameter (

Figure 5.4a). Implants and the surrounding tissue were collected, sectioned, and stained with haematoxylin and eosin (H&E) and Masson's trichrome (MT) to assess biocompatibility and fibrous tissue capsule (FTC) formation. Histological analysis of the surrounding tissues revealed the formation of a FTC for all implants (

Figure 5.4d–e).

The thickness of the fibrous capsule developed at the implantation site increased significantly from week 1 to 2 (13.3 ± 5.2 to 24.1 ± 6.2 μm) *in situ* with no significant change occurring thereafter (

Figure 5.4a). Consistent with this were observed changes in cell populations occurring within the surrounding tissue (i.e., the formation of a granulation tissue and its maturation into a fibrous capsule).[14] In addition, significant increases in collagen were observed in the later time points (Appendix, **Figure A5.4**), and qualitative observations demonstrated the maturation of the tissue into a less cellular and more striated and collagenous fibrous capsule (

Figure 5.4d–e). An apparent reduction in the collagen content between weeks 4 and 6 and high variation in the FTC thickness for weeks 9 and 12 were both likely due to the reduced sample size (n = 2 because one rat did not recover from anaesthesia after the 9-week implantation) for the 6-, 9-, and 12-week samples. No rats exhibited marked inflammation at any time point, just fibrosis with occasional mononuclear cell infiltration that decreased over time as collagen fibres became aligned and compacted (as described in **Chapter 3.2.8**). This tissue reaction was indistinguishable from that observed in response to conventional RFID microchips (not shown) and suggested comparable biocompatibility, like the PVB implants reported in **Chapter 3.2.8**.

While FTC formation was shown in **Chapter 3.2.8** not to impede implant swelling, it was hypothesised that the comparatively hydrophobic PVBI/EO_{10} coating (cf., PVB 50/50) may impede implant swelling. Qualitatively, there was no observable difference in the rate or extent of swelling between the PVB and PVBI/EO_{10} implants. Overall, *in vivo* the PVBI/EO_{10} implants demonstrated favourable stability, with all implants from time points 1, 2, 4, 9, and 12 weeks remaining intact at the conclusion of the experiment. However, two implant failures were observed at 6 weeks (Appendix, **Figure A5.3**). Like the PVB implants that failed in **Chapter 3.2.8**, both PVBI/EO_{10} implants were located most caudally, and suggested that after 6 weeks *in situ* the PVBI/EO_{10} coating did not provide any greater resistance to the mechanical stressors this region imparted. In contrast, unlike the PVB implants, the 1-week time point PVBI/EO_{10} implants (also placed most-caudally) were found to be stable. This suggested that for the shorter time *in situ*, the PVBI/EO_{10} coating likely experienced less swelling, which imparted greater mechanical strength to the 1-week implants, and the ability to withstand the forces exerted by the thinner subcutis. This combination of factors was likely not experienced by the 4- or 12-week implants, due to the comparatively thick and loose skin that is present superficial to the left scapula.

These results highlighted that the replacement of the ABS filament substrate in the implant core with a soluble substrate might be necessary to reduce the chances of it puncturing the PVBI/EO_{10} coating when swollen and mechanically stressed. However, implants located superficial to the left scapula exhibited favourable stability, for both the PVB and PVBI/EO_{10} implants. This suggested that the location of implantation was a pertinent issue and could be solved by simply constraining the location of the implants to a less mechanically stressful region of the animal. Over greater timescales, enzymatic degradation of the PVBI/EO_{10} coating within the subcutaneous environment was also considered a possible mechanism of failure; however, implant swelling makes observing this challenging, and hence, should be considered for further investigation when manufactured implants show significant *in vivo* stability. Instead, in future experiments it was considered necessary to determine whether stability was maintained when PVBI/EO_{10} implants containing a toxic 1080 core were implanted superficial to the left scapula.

5.3 Conclusions

PVBI/EO_{10} implants exhibited cohesive, uniform film coatings, with low intrabatch variation, when prepared *via* fluidised-bed spray coating. Relatively large-batch production of implants was achieved, and the implants were suitably sized for compatibility with conventional microchip syringe implanters. This demonstrated the potential for such an approach to provide a scalable and cost-effective method of PPI manufacture. The flexural strength and modulus values of the implants suggested their favourable mechanical flexibility and ability to withstand moderate stress *in vivo*. The PVBI/EO_{10} coating resulted in long-lived implant stability in a simulated subcutaneous environment and rapid dissolution in a simulated gastric environment. In addition, the implants exhibited favourable biocompatibility and stability *in vivo*, following subcutaneous implantation in rats. These results demonstrated the superior performance of the PVBI/EO_{10} coating, compared to the PVB 50/50 coating described in **Chapter 3.2**. However, further investigation of implant stability was needed, particularly concerning the location of the implants, to ensure that it was maintained *in vivo* following the incorporation of 1080.

5.4 Experimental

5.4.1 Materials

The materials described in Chapter 5 are the same as **Chapter 2.6.1**, **Chapter 3.4.1**, and **Chapter 4.4.1**, unless stated below.

All reagents were used as received unless otherwise specified. Sulphuric acid (H_2SO_4, 98%), sodium hydrogen carbonate ($NaHCO_3$), magnesium sulphate ($MgSO_4$), laboratory-grade oleic acid (OA), HPLC-grade acetonitrile (ACN), and methanol (MeOH), were purchased from Chem-Supply (Gillman, Australia). Trifluoroacetic acid (TFA, ≥ 99%) was purchased from Sigma-Aldrich (St. Louis, United States).

5.4.2 Instrumentation

The instrumentation used in Chapter 5 is the same as **Chapter 2.6.2**, **Chapter 3.4.2**, and **Chapter 4.4.2**, unless otherwise stated below.

Mass Spectrometry

Electrospray ionisation-mass spectrometry (ESI-MS) was performed on a Sciex Triple-ToF 5600 mass spectrometer, with samples introduced *via* a Shimadzu Prominence liquid chromatography system. Samples were solubilised in 1:1 ACN:MeOH containing 0.1% TFA and filtered through a 0.45 µm nylon syringe filter prior to analysis. Data analysis was performed using the Analyst TF 1.7 and PeakView 2.2 software packages.

Modulated Differential Scanning Calorimetry

Modulated differential scanning calorimetry (MDSC) was performed as described in **Chapter 3.4.2**, with the following exceptions. Neat samples of EO were analysed using Tzero pin hole hermetic pans.

3D Printing.

The 3D printed flexural testing stage (**Figure A5.7c**) and probe tip (**Figure A5.7d**), were designed in Solidworks (2020 SP5.0) and printed from poly(lactic acid) (PLA) 3D printing filament, using a Prusa i3 MK3S+ 3D printer (Prusa Research, Prague, Czech Republic).

5.4.3 Procedures

The procedures in Chapter 5 were conducted as outlined in **Chapter 2.6.3**, **Chapter 3.4.3**, and **Chapter 4.4.3** unless stated below.

Synthesis of Ethyl Oleate

Under an inert atmosphere (Argon, Ar), OA (5.62 mL, 17.77 mmol) and H_2SO_4 (94.0 µL, 1.76 mmol) were dissolved in EtOH (5.20 mL, 89.08 mmol) in a round bottomed flask and heated at reflux with stirring, in the presence of dried molecular sieves (3 Å, 4 g). After 2 h, the reaction mixture was cooled to ambient temperature and diluted with dichloromethane (DCM) (100 mL). The organic phase was washed with saturated $NaHCO_3$ solution (100 mL × 3), dried ($MgSO_4$), filtered and concentrated in vacuo. The resulting residue was dried under high vacuum (23 °C, 0.01 mbar) to afford the product as a yellow oil (4.69 g, 85%). Proton nuclear magnetic resonance (^{1}H NMR) (600 MHz, $CDCl_3$) δ_H 5.35 (2H, s, 2CH), 4.12 (2H, q, CH_2), 2.28 (2H, t, CH_2), 2.0 (2H, q, CH_2), 1.62 (2H, quin. CH_2), 1.23-1.30 (23H, m, 10CH_2, CH_3), 0.87 (3H, t, CH_3) ppm (Appendix,

Figure A5.5a). ^{13}C NMR (150 MHz, $CDCl_3$) δ_C 174.0, 130.1, 129.9, 60.2, 34.5, 32.0, 29.9, 29.8, 29.6, 29.4, 29.3, 29.2, 29.2, 27.3, 27.3, 25.1, 22.8, 14.3, 14.2 ppm (Appendix,

Figure A5.5b). ESI-MS (m/z) calculated for $C_{20}H_{38}O_2$ $[M + H]^+$ 311.3; found 311.3 (Appendix, **Figure A5.6**).

Preparation of Coating Formulations

Implant Reverse Enteric Coating Formulation (PVBI/EO$_{10}$)

The pH-responsive polymer formulation was prepared by dissolving PVBI (9 g) and EO (1 g) in EtOH (100 mL) under stirring to afford a 10% w.v^{-1} solution. The fluidisation air flow was at ambient temperature (23 ± 1 °C) throughout the coating of the pH-responsive polymer formulation.

Implant Manufacture

Implant manufacture was undertaken as described in **Chapter 3.4.3** and **Chapter 4.4.3**, with the following exceptions. The ABS filament substrates prepared as previously described were measured to be 0.63 ± 0.06 mm diameter and 7.38 ± 0.08 mm length (n = 1000).

Mechanical Testing

The flexural strength and modulus of each implant were determined *via* a three-point flexural test, using an EZ-Test EZ-LX (Shimadzu Corporation, Kyoto, Japan) universal tester. Testing was conducted using a custom 3D printed testing apparatus, with a 6 mm support span and a 1.08 mm 3D printed probe tip width (Appendix, **Figure A5.7**). Schematic drawings of the 3D printed stage (Appendix, **Figure A5.8**) and the probe tip (Appendix,

Figure A5.9) are provided in the SI. The flexural strengths (σ_F) and moduli (E_f) were calculated as previously reported for samples of a single composition and bearing a circular cross section,[15, 16] using the measured dimensions of the apparatus and Appendix **Equation A5.1** in the SI. While typically, the diameter of the sample would also be considered as a variable, there is a paucity of the literature and modelling on more complex composite materials in three-point flexural testing. Therefore, the implant diameter was fixed equal to that of the core of the implants (1.14 mm, which remains constant across all implants) to assess the contribution of the polymer coating to the mechanical properties. Implants were tested at a stroke rate of 0.1 mm.min^{-1} until failure, at ambient temperature (23 °C).

In Vitro Release Experiments

In vitro release experiments were conducted as described in **Chapter 3.4.3**. However, an additional qualitative interrogation of polymer dissolution and core release was also undertaken, wherein the dissolution of an implant in a glass Petri dish containing pH 1.5 release medium was conducted, and a video footage was recorded using an Olympus SZ61TR stereomicroscope fitted with a Gryphax Arktur (Jenoptik) camera module and the included software (Appendix, **Figure A5.2c**).

In Vivo Stability Experiments

Animal work was conducted under approval S-2015-176 from the University of Adelaide Animal Ethics Committee.

Non-toxic NaOAc implants were prepared as described in **Chapter 3.2.8**. Male Sprague-Dawley rats (10–11 weeks of age, n = 6) were each subcutaneously implanted with a mini microchip for identification (superficial to the right scapula) and three implants (superficial to the left scapula and two locations caudally, approximately 1 cm to the left of the spine) (as described in **Chapter 3.4.3**, **Figure 3.8).** Sterilised implants and microchips were administered under general anaesthesia *via* syringe implanters (**Chapter 3.4.3,**

Figure A3.6). Anaesthesia was induced as described in **Chapter 3.4.3**. Implants intended for different durations *in situ* (i.e., 12, 9, and 6 weeks or 4, 2, and 1 week(s)) were implanted in a reverse time order. Rat monitoring and recovery of the explants were conducted as previously described in **Chapter 3.4.3**.

Computed Tomography

CT scans were used to determine implant integrity and measure the implant diameter *in vivo*. Scans were reconstructed using the bone 0.5 volume settings (resolution 0.172 × 0.172 × 0.5 mm). To determine the diameter of each implant, an average diameter was calculated from measurements made at three points along the length of the implant. For visual demonstration purposes, the CT images were adjusted (*via* exposure, offset, and gamma correction parameters) in Adobe Photoshop (v22.4.1), to provide the best contrast for the implant.

Statistical Analyses

All results are expressed as the mean ± std. dev. The mean values of the flexural strength, flexural modulus, fibrous capsule thickness and type 1 collagen content were compared between two groups using unpaired two-tailed Student's t-tests. Only p-values < 0.05 were considered significant. All statistical tests were performed using the Minitab 17 (v17.1.0) software package. Exact p-values, t-values, and degrees of freedom (DF) are summarized in Appendix, **Table A5.3**).

5.5 Appendix

Table A5.1: Solubility ($mg.mL^{-1}$) of PVBI with and without plasticisation at pH 1.0, 1.5 and 2.0 (37 °C).

Copolymer	Solubility ($mg.mL^{-1}$)					
	pH 1.0		pH 1.5		pH 2.0	
	Avg. (n=3)	Std. Dev.	Avg. (n=3)	Std. Dev.	Avg. (n=3)	Std. Dev.
PVBI	10.5	0.3	3.7	0.4	-	-
PVBI/EO_5	9.3	0.1	3.3	0.3	-	-
PVBI/EO_{10}	10.1	0.2	2.5	0.1	-	-

Table A5.2: Water absorption (% w.w^{-1}) determined for the copolymer series (pH 7.4, 37 °C).

Copolymer	Days (d)															
	1	**2**	**3**	**6**	**8**	**10**	**15**	**27**	**38**	**59**						
PVBI[a]	1.31 ± 0.11	1.17 ± 0.12	1.20 ± 0.14	1.01 ± 0.16	0.90 ± 0.19	0.85 ± 0.22	0.86 ± 0.18	0.65 ± 0.22	0.55 ± 0.22	0.42 ± 0.25						
	1	**2**	**3**	**4**	**5**	**6**	**7**	**9**	**11**	**13**	**15**	**18**	**22**	**26**	**34**	**50**
PVBI/EO$_5$[b]	1.13 ± 0.14	1.03 ± 0.16	0.98 ± 0.33	1.08 ± 0.35	1.07 ± 0.34	1.09 ± 0.36	1.06 ± 0.34	1.06 ± 0.33	0.86 ± 0.51	1.00± 0.37	0.79 ± 0.33	0.700 ± 0.33	0.57 ± 0.25	0.58 ± 0.24	0.52 ± 0.24	0.43 ± 0.28
PVBI/EO$_{10}$[b]	1.48 ± 0.08	1.13 ±0.25	1.08 ± 0.29	1.05 ± 0.30	1.04 ± 0.31	1.01 ± 0.29	1.01 ± 0.32	0.96 ± 0.28	0.97 ± 0.30	0.93 ± 0.28	0.91 ± 0.30	0.87 ± 0.28	0.87 ± 0.28	0.85 ± 0.29	0.78 ± 0.30	0.73 ± 0.28
	1	**2**	**3**	**5**	**7**	**9**	**11**	**14**	**22**	**26**	**34**	**50**				
PVBI/EO$_{15}$[c]	1.65 ± 0.56	1.28 ± 0.25	1.27 ± 0.24	1.23 ± 0.19	1.20 ± 0.21	1.20 ± 0.17	1.18 ± 0.19	1.20 ± 0.21	1.11 ± 0.19	1.10 ± 0.22	1.09 ± 0.20	1.01 ± 0.18				

Determined from [a] n = 8, [b] n = 5, and [c] n = 4 samples

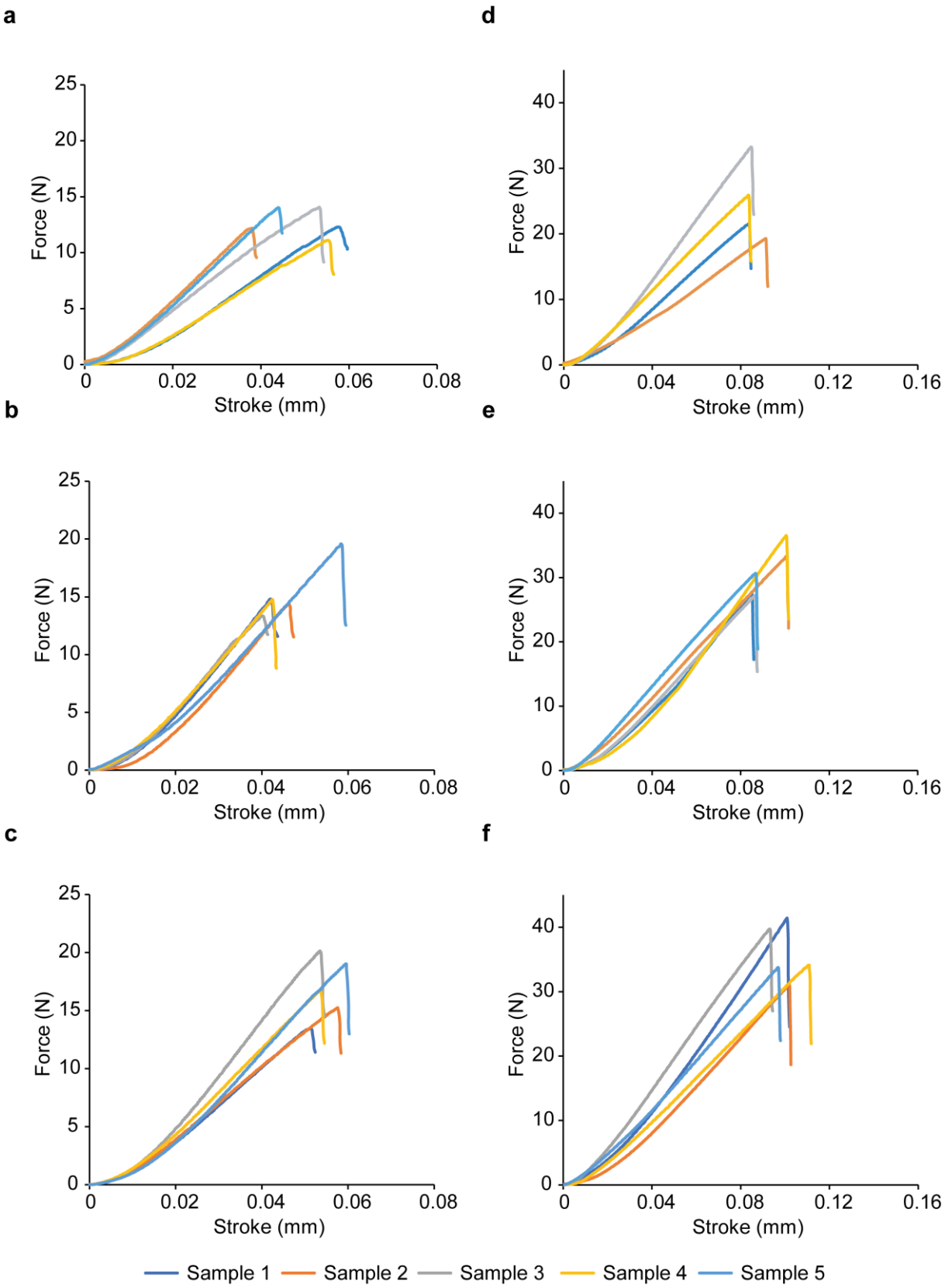


Figure A5.1: Force versus stroke graphs obtained *via* three-point flexural testing of implants coated with a) 100, b) 200 and c) 300 µm PVBI, and d) 100, e) 200 and f) 300 µm PVBI/EO_{10} (n = 5 for all samples).

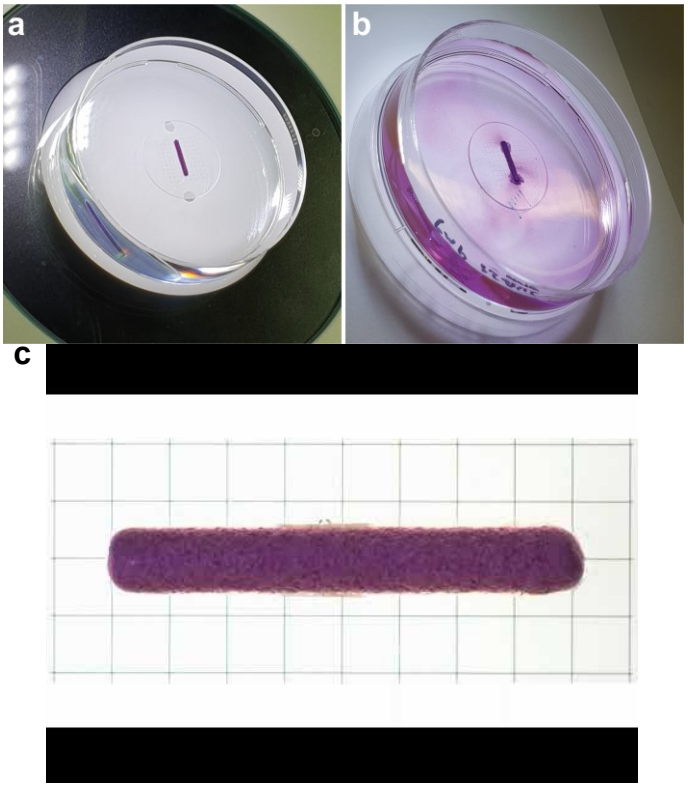


Figure A5.2: a) An implant coated with a 300 µm PVBI/EO_{10} coating submerged in a pH 1.5 release solution prior to release, b) during release, and c) an embedded time-lapse video footage of the release (×500 speed, 20 s duration).

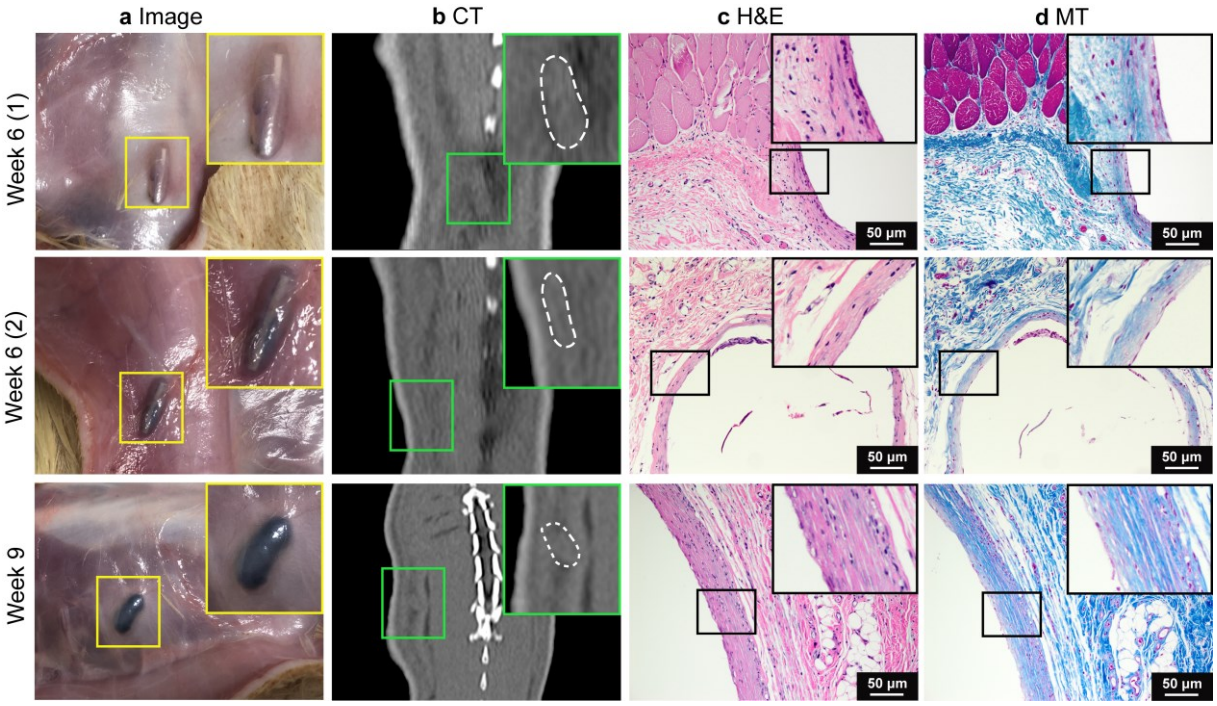


Figure A5.3: Representative results of the PVBI/EO_{10} implant stability *in vivo.* a) Macroscopic images (post-mortem) of implants *in situ*, captured prior to explantation — note the loss of the core material for both 6-week samples (1) and (2). b) CT scans of intact implants captured immediately prior to euthanasia, with implants circled in white. c) H&E and d) MT-stained samples of the explanted tissue, for implants following 6 and 9 weeks *in situ*.

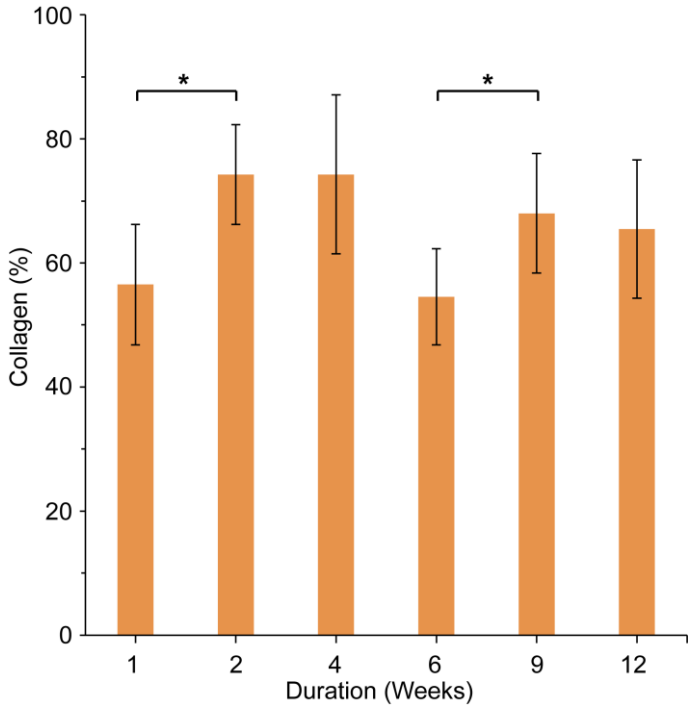


Figure A5.4: Histological analysis results of type I collagen content as measured from tissue explants using colour thresholding in ImageJ, *p < 0.05 × t-test of difference = 0 (vs <).

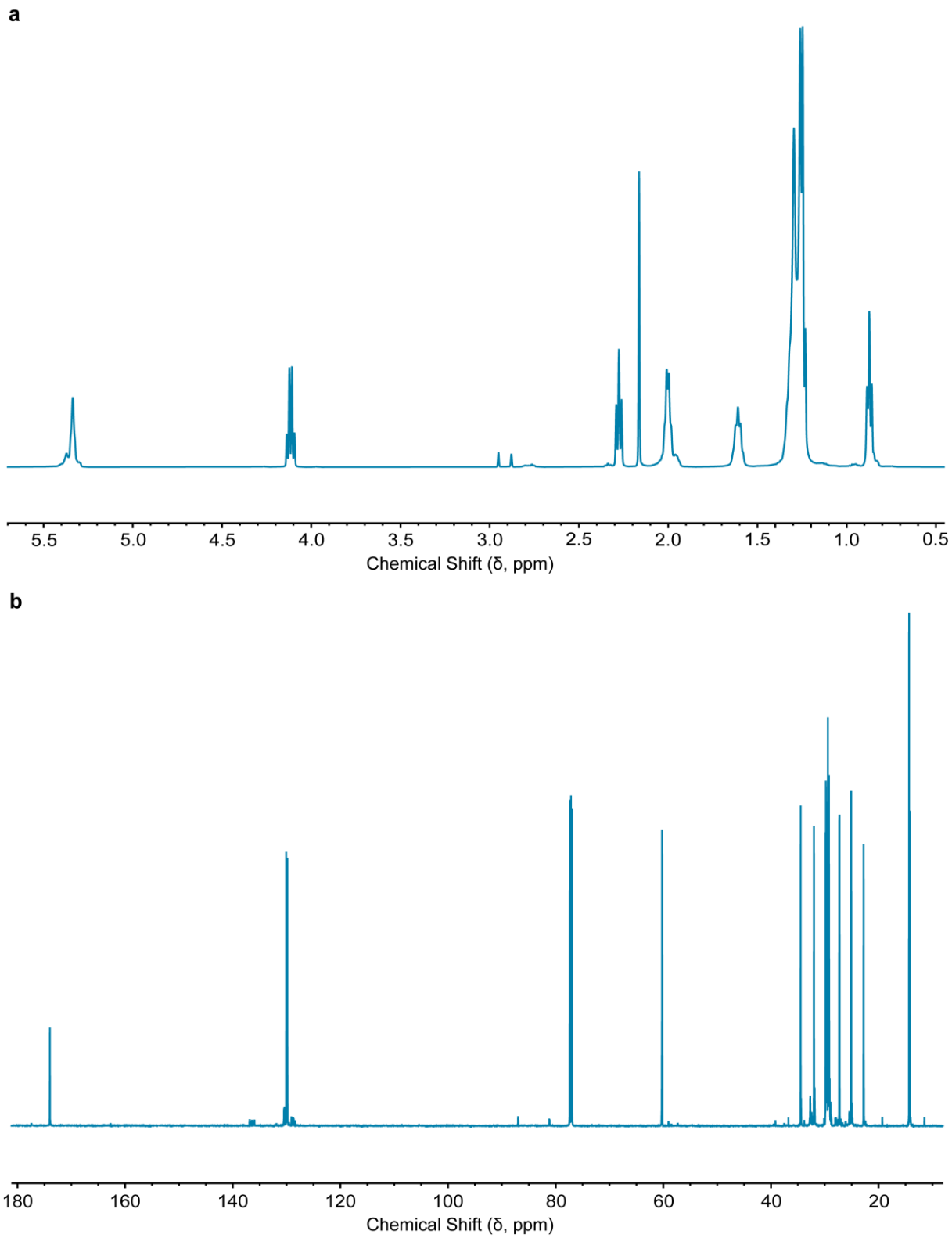


Figure A5.5: a) ^{1}H NMR (500 MHz, $CDCl_3$, 21 °C) and b) ^{13}C NMR (150 MHz, $CDCl_3$, 21 °C) spectra of ethyl oleate.

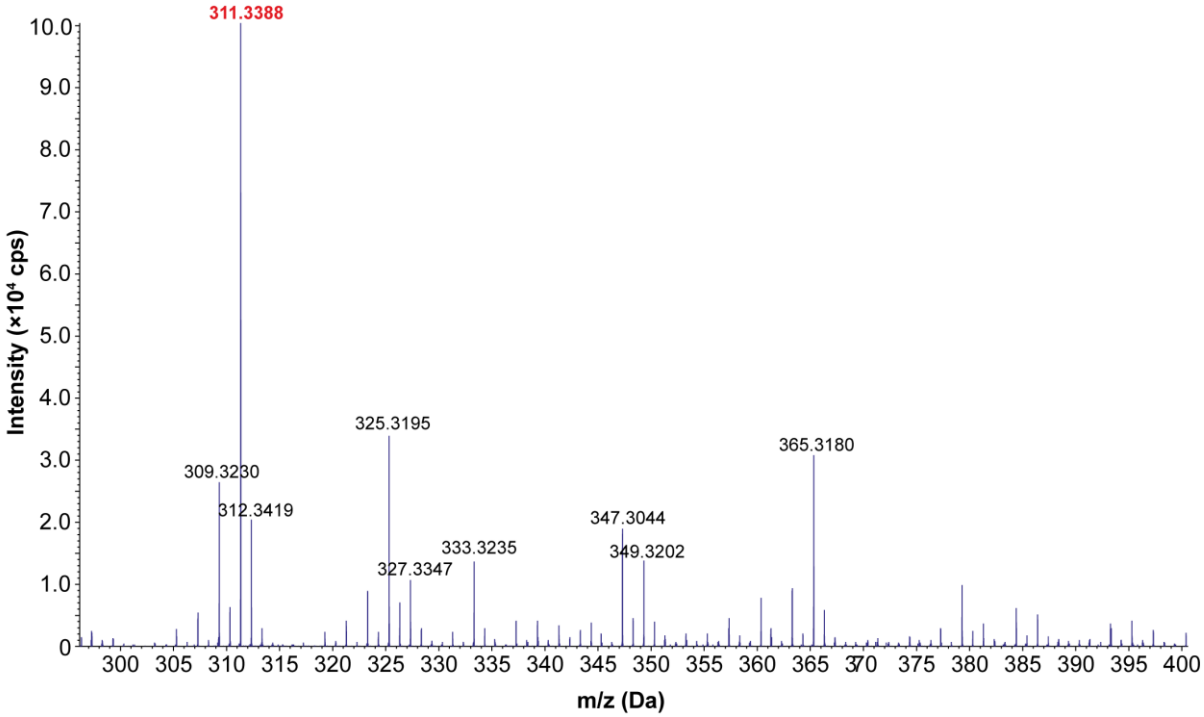


Figure A5.6: ESI-MS spectrum of ethyl oleate.

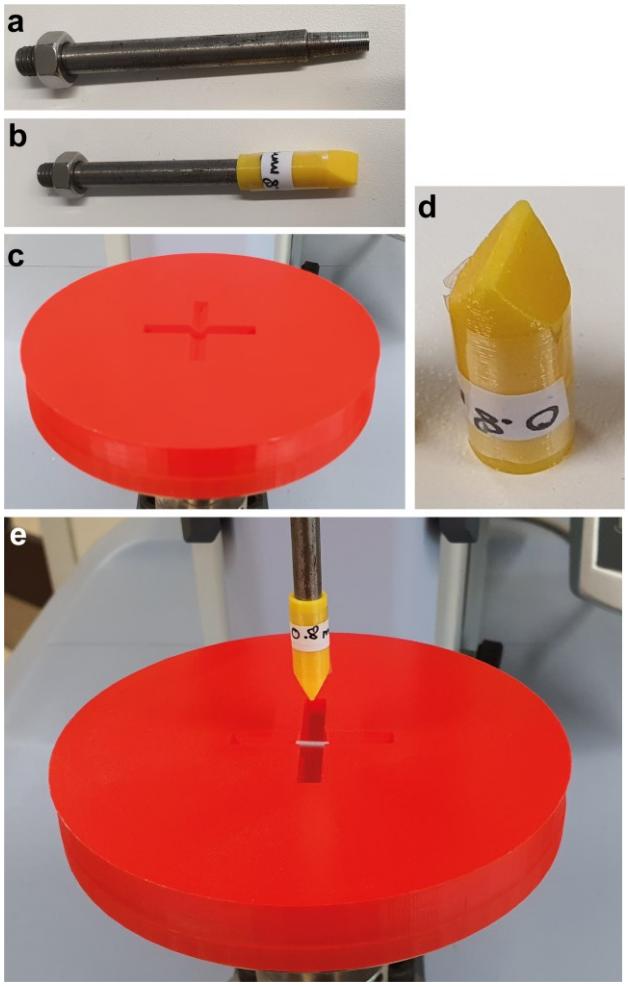


Figure A5.7: Images of the a) stainless steel Shimadzu EZ-Test EZ-LX mechanical tester probe, b) mechanical tester probe fitted with the 3D-printed probe tip, c) 3D-printed flexural testing stage, d) 3D-printed probe tip and e) three-point flexural testing apparatus, prior to an implant being tested.

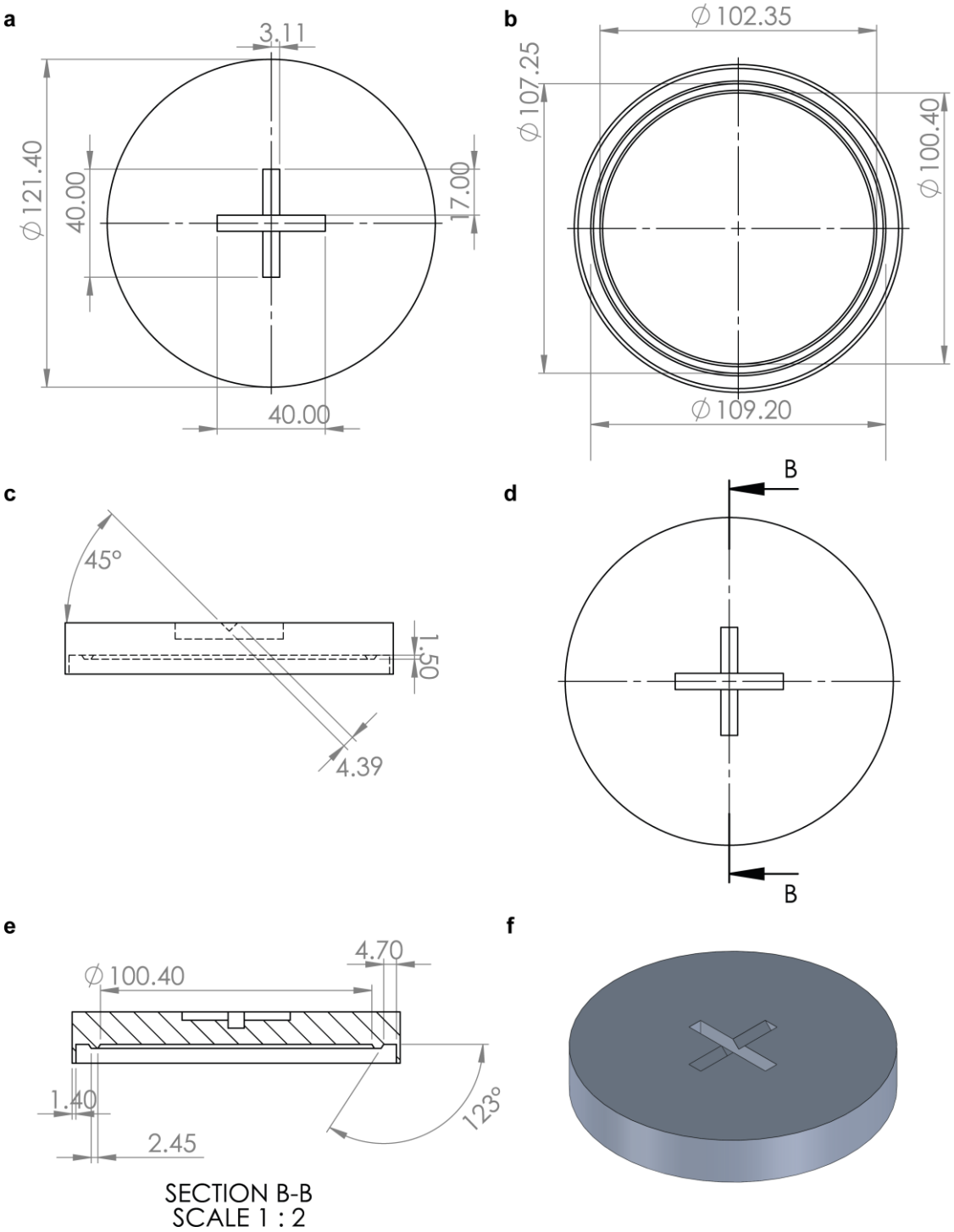


Figure A5.8: 3D-printed three-point flexural testing stage schematic drawings generated in Solidworks showing the a) top, b) bottom, c) left, d) demarcation of B-B cross-section, e) Left B-B cross-section and f) isometric views.

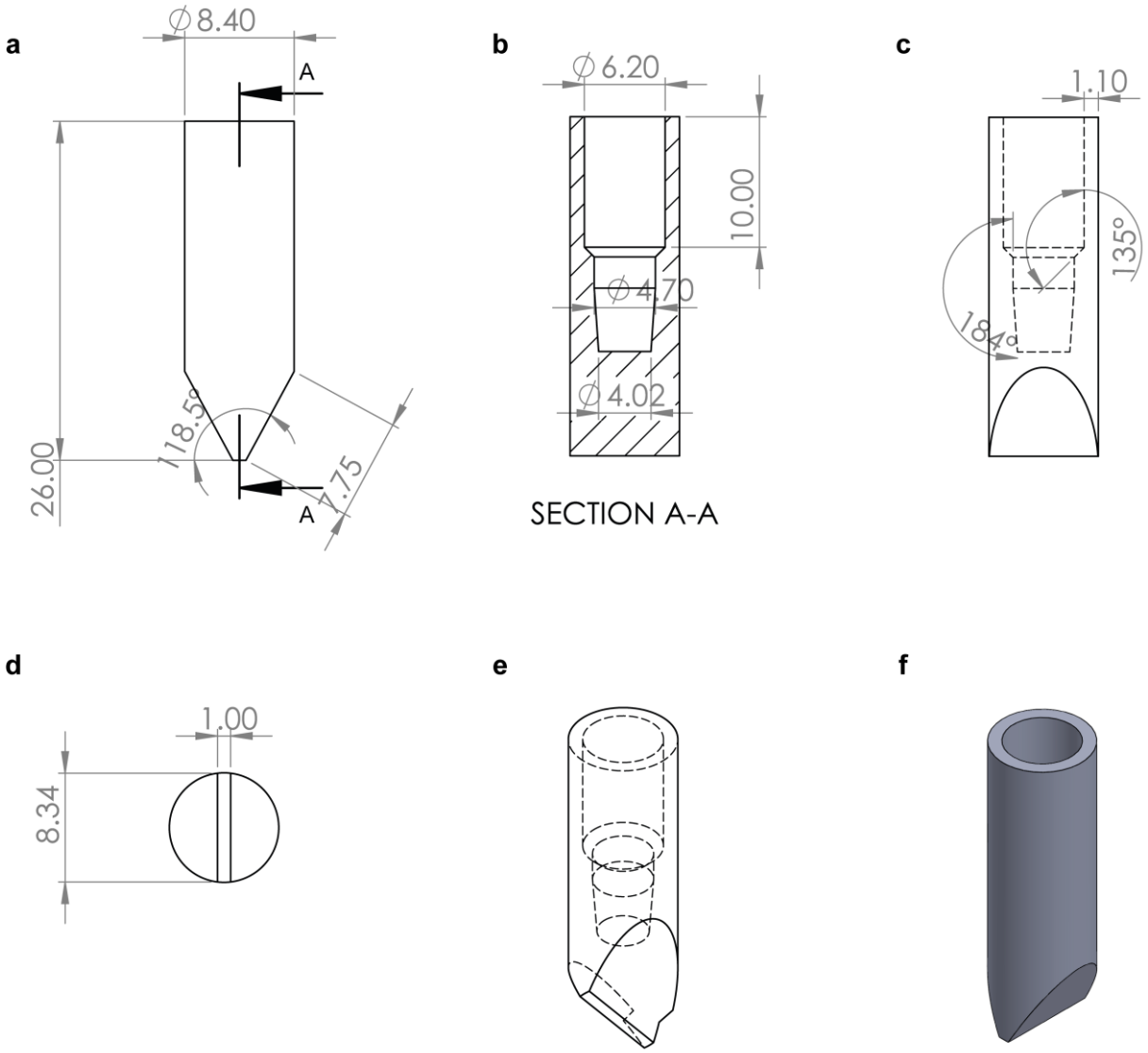


Figure A5.9: 3D-printed probe tip schematic drawings generated in Solidworks showing the a) demarcation of A-A cross-section, b) front A-A cross-section, c) front, d) bottom, e) hidden line visible and f) isometric views.

The flexural strengths (σ_F) and moduli (E_f) were calculated using **Equation A5.1** below:

Equation A5.1:

$$\sigma_F = \frac{8F_{max}l}{\pi d^3}$$

$$E_f = \frac{4F_{max}l^3}{D3\pi d^4}$$

The σ_F and E_f values are calculated where *D* is the deflection at *F* (in mm) within the linear portion of the force versus stroke curve, *d* is the diameter of the implant (in mm), *F* is the maximum force exerted on the implant prior to failure (in N), *l* is the support span (in mm) of the three-point flexural testing apparatus.

Table A5.3: Summary of two-tailed Student's t-test results.

Test of Mean	t-value	DF	p-value
σ_F of PVBI vs. PVBI/EO_{10} (100 µm) implants	-4.93	4	0.008[a]
σ_F of PVBI vs. PVBI/EO_{10} (200 µm) implants	-7.57	6	<0.001[a]
σ_F of PVBI vs. PVBI/EO_{10} (300 µm) implants	-8.31	6	<0.001[a]
E_f of PVBI vs. PVBI/EO_{10} (100 µm) implants	-0.69	7	0.514[a]
E_f of PVBI vs. PVBI/EO_{10} (200 µm) implants	-0.11	7	0.916[a]
E_f of PVBI vs. PVBI/EO_{10} (300 µm) implants	-1.61	7	0.151[a]
FTC thickness of Week 0 vs. Week 2 samples	-5.05	17	<0.001[b]
Type 1 collagen content of Week 1 vs. Week 2 samples	-5.96	32	<0.001[b]
Type 1 collagen content of Week 6 vs. Week 9 samples	-3.77	21	0.001[b]

Tests performed utilising a [a] t-test of difference = 0 (vs. ≠) and [b] t-test of difference = 0 (vs <).

5.6 References

1. A. Dashevskiy, V. Mohylyuk, A. R. Ahmed, K. Kolter, F. Guth and R. Bodmeier, *Drug Dev Ind Pharm*, 2017, **43**, 1548–1556.

2. S. Thakral, N. K. Thakral and D. K. Majumdar, *Expert Opin Drug Deliv*, 2013, **10**, 131–149.

3. G. Kocak, C. Tuncer and V. Bütün, *Polymer Chemistry*, 2017, **8**, 144–176.

4. G. Wypych, *Handbook of plasticizers*, ChemTec Publishing, 4th edn., 2023.

5. J. R. Rumble, D. R. Lide and T. J. Bruno, *CRC handbook of chemistry and physics: a ready-reference book of chemical and physical data*, CRC Press, 97th edn., 2018.

6. A. N. Zaid, *Drug Des Devel Ther*, 2020, **14**, 4613–4623.

7. N. Shinji, Y. Hiroyuki, H. Yoshiyuki and N. Kazuo, *Int J Pharm*, 1994, **104**, 95–106.

8. V. Shah, *Handbook of Plastics Testing and Failure Analysis*, Wiley, New Jersey, 2020.

9. C. A. Wyse, J. McLellan, A. M. Dickie, D. G. M. Sutton, T. Preston and P. S. Yam, *J Vet Intern Med*, 2003, **17**, 609–621.

10. R. F. Reinoso, B. A. Telfer and M. Rowland, *J Pharmacol Toxicol Methods*, 1997, **38**, 87–92.

11. N. Nakagawa, M. Matsumoto and S. Sakai, *Skin Res Technol*, 2010, **16**, 137–141.

12. S. Joshi and H. U. Petereit, *Int J Pharm*, 2013, **457**, 395–406.

13. A. Jonquières, R. Clément and P. Lochon, *Prog Polym Sci*, 2002, **27**, 1803–1877.

14. R. Klopfleisch and F. Jung, *J Biomed Mater Res A*, 2017, **105**, 927–940.

15. R. Brown, *Handbook of Polymer Testing: Short-term Mechanical Tests*, Rapra Technology, Shropshire, 2002.

16. D. A. Stewardson, A. C. Shortall, P. M. Marquis and P. J. Lumley, *Dent Mater*, 2010, **26**, 730–736.

Chapter 6: Incorporation of Sodium Fluoroacetate and the Effects on Implant Performance

6.1 Overview

In Chapter 6, the non-toxic sodium acetate (NaOAc) core formulation of the PVBI/EO_{10} implants described in **Chapter 4.2.11**, is replaced with a toxic sodium fluoroacetate (1080) core formulation. Implants bearing the 1080 core formulation and the same PVBI/EO_{10} coating formulation used in **Chapter 5.2.1** are then subjected to the same testing conditions described in **Chapter 5.2**, to evaluate their performance. N.B., to highlight the change in core composition — but identical PVBI/EO_{10} coating — of the implants described in Chapter 5 and presented in Chapter 6, they will hereafter be referred to as NaOAc implants and 1080 implants, respectively. The 1080 implants were found to exhibit uniform coatings with low intrabatch variation. However, the *in vitro* release experiments were complexified by the presence of metachromasy, ostensibly due to interactions between 1080 and methylene blue (MB) in the 1080 core. The 1080 implants exhibited favourable release and stability properties *in vitro*, like the NaOAc implants in **Chapter 5.2**. However, limited stability was observed *in vivo*, with failures observed almost monthly from 39 d post implantation, and only a single 1080 implant was found to be stable at 230 d — the conclusion of the *in vivo* stability study. The poor stability was due to the acrylonitrile butadiene styrene (ABS) filament substrate used to enable fluidised-bed spray coating, which punctured the copolymer coating of the swollen implants *in vivo* and was likely exacerbated by the metachromatic interactions caused by 1080. These results demonstrated that implant design — rather than implant location — was a significant cause of failure and highlighted the need to re-engineer the population protecting implant (PPI) core design, to remove the ABS filament substrate, and prevent the premature failure of the 1080 implants *in vivo*.

The mechanical testing apparatus described in this chapter was designed and printed by Jarrod Kohlhagen, while Kyle Brewer conducted all mechanical testing experiments, and interpreted all the resulting data. The in vivo stability experiment

was conducted by Dr. Todd McWhorter, with technical assistance from Dr. Anthony Nicholson, and Julie Olson. Kyle Brewer assisted in the interpretation of the raw data and conducted all data reporting and visualisation. Dr. Nobuyuki Kawashima provided technical assistance with the scanning electron microscopy experiments described in this chapter, while Kyle Brewer acquired all micrographs, performed all interpretation of the results and conducted all data reporting and visualisation.

6.2 Results and Discussion

6.2.1 Manufacture and Evaluation of the 1080 Implants

1080 implants were manufactured *via* sequential fluidised-bed spray coating as previously reported for the NaOAc implants (**Chapter 3.4**). Initially, a 1080 core formulation containing 1080 (instead of NaOAc), poly(ethylene glycol) (PEG, binder) and MB (dye) (in a mass ratio of 1:1:0.026) was spray coated onto ABS filament substrates (n ≈ 1000). Of the resultant 1080 cores, ≈ 500 were then spray coated with the pH-responsive PVBI/EO_{10} copolymer formulation as previously described in **Chapter 5.2.2**. The physical dimensions of the implants at various stages of manufacture were measured using digital callipers and point-to-point measurements of epoxy-embedded, microtomed implants (**Table 6.1**). The 1080 implants exhibited low intrabatch variation (≤ 8%) for all digital calliper measurements of diameter and length, consistent with that observed for the NaOAc implants.

The mass of the 1080 core coating was determined from the average increase in mass of the ABS filament pieces, following core coating. A statistically relevant number of samples (n = 100, ~ 10% of the total batch size) were weighed to obtain this value. From the known composition of the spray coating formulation (i.e., 49.3% 1080), the average mass of 1080 contained in the core coating could be inferred. The core coated implants were determined to contain 3.12 ± 0.04 mg of 1080, equivalent to a lethal (> LD_{90}) dose for feral cats. Importantly, the mass of the 1080 core coating was found to exhibit a low percentage relative standard deviation (%RSD = 8.0%), which demonstrated that such a lethal dose could be

achieved with a high level of accuracy and consistency, despite the large batch size (n ≈ 1000).

Calliper measurements of the PVBI/EO_{10} coating thicknesses made at the ends of the implants showed slightly greater variability (%RSD ≈ 6.0–9.9%) compared to the middle of the implants (%RSD ≈ 2.4–5.6%). This difference likely resulted from a combination of the variation in length of the ABS filament substrates (1.1%) inherent to the manual cutting of the filament, and the difficulty of manually measuring the centre of each curved end. However, the low variation in coating thicknesses overall (< 10%), demonstrated excellent consistency between the middle (i.e., side midpoint) and ends. In comparison, the point-to-point measurements obtained from epoxy-embedded and microtomed implants were generally consistent with the calliper measurements, with a maximum percentage difference of ≈ 19%.

Scanning electron microscopy (SEM) analysis of the implants following coating with the 1080 core formulation revealed less pitting and an absence of cracking compared to the NaOAc implants (**Figure 6.1a** and **Chapter 5.2.2**,

Figure 5.2). Though the exact mechanism is unclear, this effect was attributed to the complexation of PEG with free sodium ions (Na^+). In solution, Na^+ are known to cause a concentration-dependent reduction in solution viscosity, due to the

complexation of Na^+ with PEG chains.[1] In the presence of NaOAc, the rapid evaporation of ethanol (EtOH) would lead to the deposition of viscous, mostly aqueous droplets on the substrate surface, which could trap air bubbles with continued evaporation, that eventually collapse and form pits. However, facilitated by the greater dissociation — and, therefore, increased free Na^+ concentration in solution — of 1080 (cf., NaOAc), the reduction in solution viscosity likely prevented the trapping of air bubbles in the deposited droplets, thereby reducing pitting. In addition, light dusting was observed on the 1080 cores, which was believed to be platelet-like 1080 crystals deposited upon the surface. Despite this, the 1080 cores exhibited a qualitatively superior coating.

SEM micrographs of the 1080 implants also revealed flared ends (**Figure 6.1a**) in contrast to the comparatively rounded NaOAc implants (**Chapter 5.2.2**, **Figure 5.2**). This change in end morphology occurred during coating of the 1080 core formulation and was attributed to a build-up of electrostatic charge on the implant surface during coating. The triboelectric generation of electrostatic charge due to collisions between implants, and implants with the walls of the coating chamber, could have caused an accumulation of charge on the surface of the implants.[2] In contrast with commonly coated substrates, such as pharmaceutical tablets or capsules, which generally have rounded/smooth morphologies, the ABS

filament used in this work was cylindrical and exhibited sharp edges at each end. It is likely that the morphology of the implants caused the localisation of charge at the ends of the implants, resulting in the electrostatic attraction of the coating formulation to the implant ends, and over several coating cycles, caused the disproportionate coating of the 1080 core formulation at the edges. It is likely that this effect was due to the incorporation of 1080, as it was not observed when coating was performed with the NaOAc core formulation and may be related to the differences in dissociation of the two compounds. Despite this, uniform, cohesive coatings were observed (**Figure 6.1b**), with only minor dusting occurring upon the implant surface. In addition, optical microscopy (OM), and SEM analysis of epoxy-embedded and microtomed implants (**Figure 6.1c**) showed that the thickness and uniformity of the 1080 core coating were unaffected by the flaring. The PVBI/EO_{10} coated 1080 implants exhibited slightly wider ends due to the coating of PVBI/EO_{10} over the flared ends of the 1080 cores.

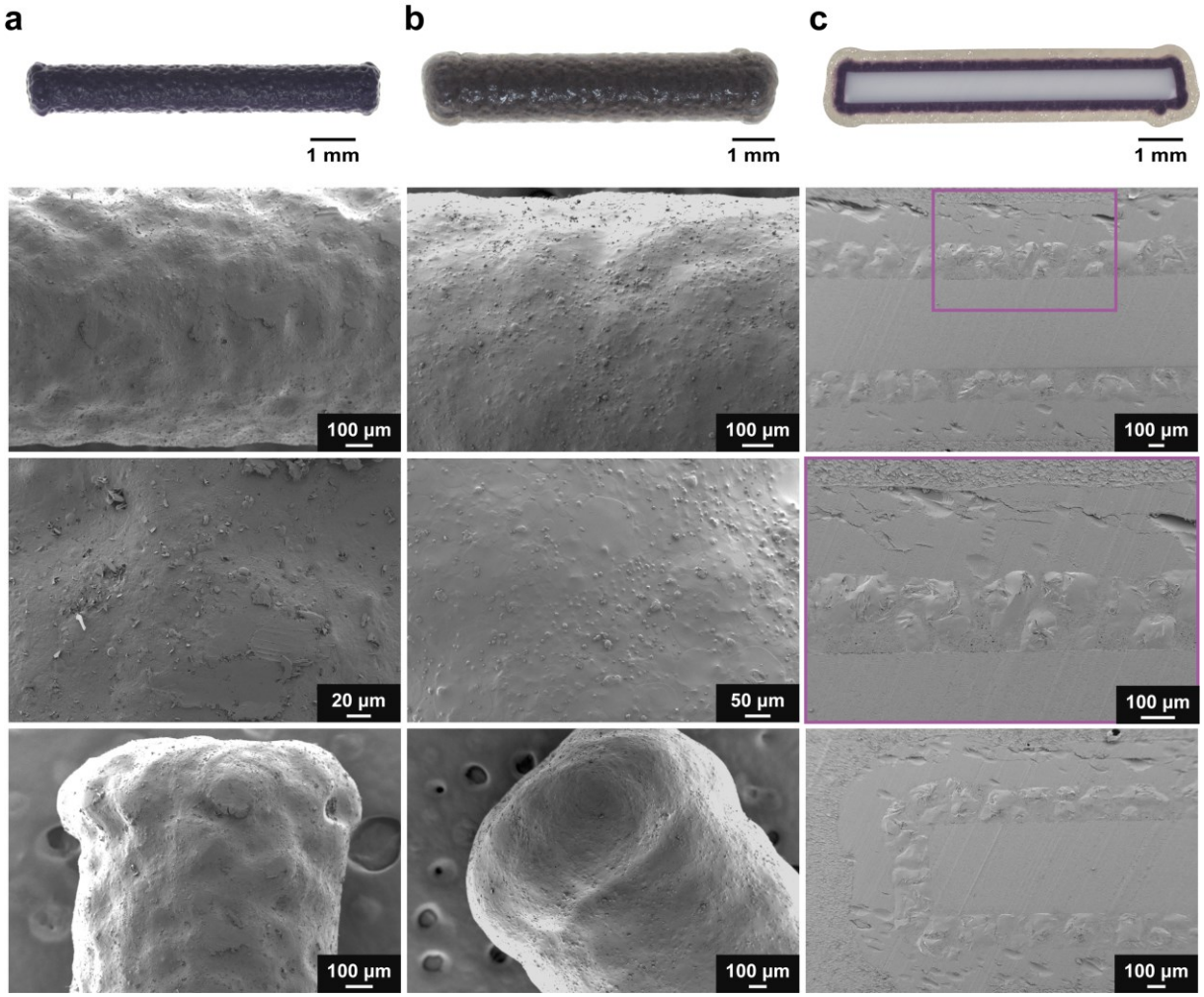


Figure 6.1: Representative digital images and scanning electron micrographs of a) a 1080 core, b) a 1080 core with a 300 µm PVBI/EO_{10} coating, and c) an epoxy-

embedded and microtomed 1080 core with a 300 μm PVBI/EO_{10} coating; note the ‘flared’ ends of the core and copolymer coated 1080 implants.

Table 6.1: Summary of implant dimensions at various stages during manufacture.

Coating Thickness (μm)	Diameter (mm) [a]	Length (mm) [a]	Mass (mg) [a]	Coating Thickness (Calliper) (μm) [a]		Coating Thickness (Microtomed) (um) [b]			
				Side Midpoint	End	Overall [c]	Ends [d]	Sides [e]	Side Midpoint [f]
1080 Core	1.04 ± 0.05 (4.8)	7.79 ± 0.09 (1.2)	9.30 ± 0.74 (8.0)	204 ± 8 (3.9)	200 ± 12 (6.0)	235 ± 31 (13.2)	238 ± 41 (17.2)	234 ± 20 (8.5)	235 ± 16 (6.8)
100	1.29 ± 0.04 (3.1)	8.07 ± 0.08 (1.0)	12.08 ± 0.74 (6.1)	125 ± 7 (5.6)	141 ± 15 (9.9)	132 ± 13 (9.8)	138 ± 13 (9.8)	127 ± 9 (7.1)	129 ± 6 (4.7)
200	1.43 ± 0.03 (2.1)	8.15 ± 0.11 (1.3)	14.76 ± 0.68 (4.6)	195 ± 7 (3.6)	181 ± 18 (9.9)	186 ± 12 (6.5)	186 ± 14 (7.5)	185 ± 10 (5.4)	183 ± 11 (6.0)
300	1.63 ± 0.04 (2.5)	8.34 ± 0.11 (1.3)	19.41 ± 0.79 (4.1)	295 ± 7 (2.4)	276 ± 18 (6.5)	246 ± 15 (6.1)	245 ± 18 (7.3)	247 ± 13 (5.3)	241 ± 12 (5.0)

All results are reported as the mean ± std. dev.; %RSD values are reported in parentheses. [a] Determined from n ≥ 50 digital calliper measurements; [b] Determined from n = 3 (1080 core, 100, and 200 μm) and n = 6 (300 μm) epoxy-embedded and microtomed implants; [c] Determined from 22 point-to-point measurements; [d] Determined from 10 point-to-point measurements; [e] Determined from 12 point-to-point measurements; [f] Determined from 2 point-to-point measurements.

6.2.2 Investigation of the Mechanical Properties of the 1080 Implants

The mechanical properties of the 1080 implants were measured to investigate the effects of the incorporation of 1080 in the core formulation. Flexural testing was conducted on 1080 implants, and the flexural strength (σ_F) and modulus (E_f) were determined as previously described in **Chapter 5.4.3**, The flexural testing results of the 1080 implants were compared to that of the NaOAc implants reported in **Chapter 5.2.3**. Though a moderate increase in σ_F was observed as the PVBI/EO_{10} coating thickness increased from 100–300 μm, no significant difference was observed between the 1080 or NaOAc implants at each PVBI/EO_{10} coating thickness (**Figure 6.2a**). The similar σ_F of the 1080 and NaOAc implants supported the assertion made in **Chapter 5.2.3** that the major contributor to implant σ_F was the PVBI/EO_{10} coating and its thickness, and not the composition of the core.

Similarly, no significant difference in E_f of the 1080 implants (cf., the NaOAc implants) was observed (**Figure 6.2b**), nor was an increase in E_f observed with respect to the PVBI/EO_{10} coating thickness, which suggested that the incorporation of 1080 afforded no change in the mechanical properties of the implant core. This was also consistent with our assertion that the core composition was the dominant contributor to the E_f of the implants. The similar E_f of the 1080 and NaOAc implants was likely due to the comparable bulk properties of both solid materials, resulting in similar mechanical properties once incorporated into the implant core.

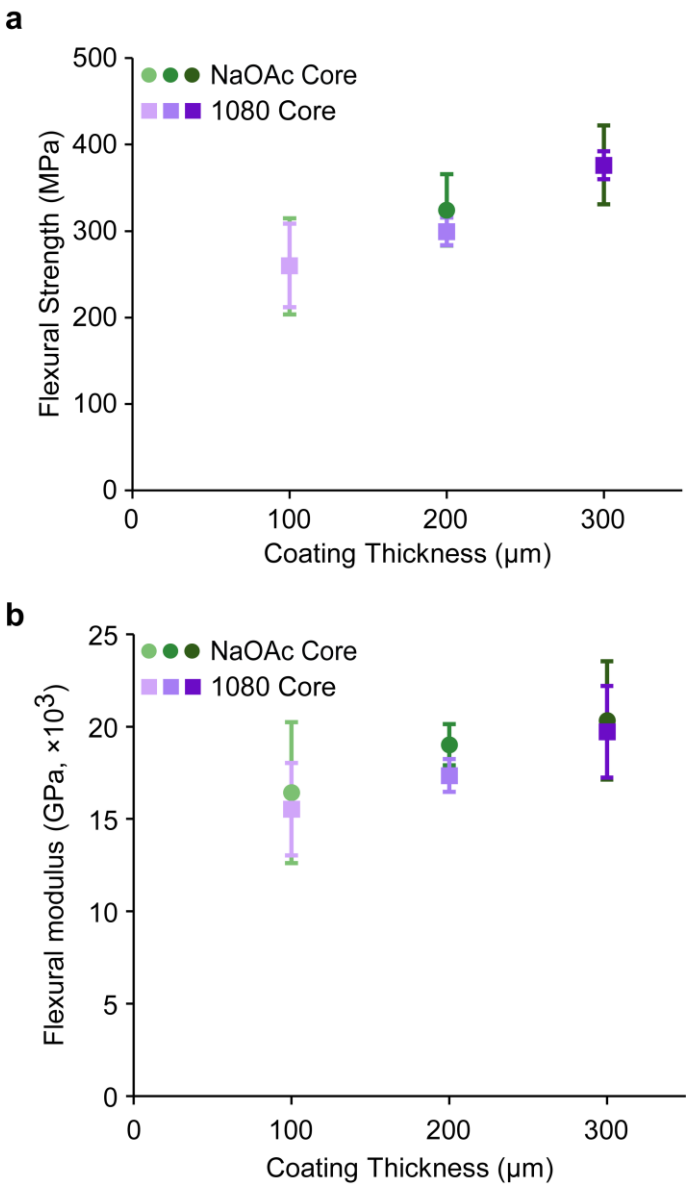


Figure 6.2: a) Flexural strength (σ_F) and b) flexural modulus (E_f) measurements of the NaOAc and 1080 implants at different PVBI/EO_{10} coating thicknesses, determined *via* three-point flexural testing (Appendix, **Figure A6.1**). All tests were performed at 23 ± 1 °C, and all values are reported as the mean ± std. dev. (n = 5), $p < 0.05$ × 2-sample t-test of difference = 0 (vs ≠ 0) (Appendix, **Table A6.1)**.

6.2.3 *In Vitro* Release Properties of the 1080 Implants

The dissolution characteristics of the 1080 implants under simulated gastric conditions were investigated *in vitro* at pH 1.0 and 1.5 by monitoring MB release from the core *via* ultraviolet-visible (UV-vis) spectrophotometry, as described in **Chapter 5.2.4**. However, preliminary testing revealed a marked change in the release profiles of tested implants, with a protracted and inconsistent release observed (**Figure 6.3a**). In addition, receiving solutions obtained following release

appeared purple, in contrast to the blue receiving solutions obtained from NaOAc implants. These observations suggested a change in the photophysical properties of MB in the receiving solution, when solubilised from the NaOAc and 1080 core formulations at low pH. UV-vis spectrophotometry revealed a hypsochromic shift (also called a blueshift) in the absorbance maximum of MB from 669 nm in a neat solution, to 647 nm in the NaOAc core solution, and 592 nm in the 1080 core solution (**Figure 6.3b**). Furthermore, there were also significant changes in other absorption bands of the spectra.

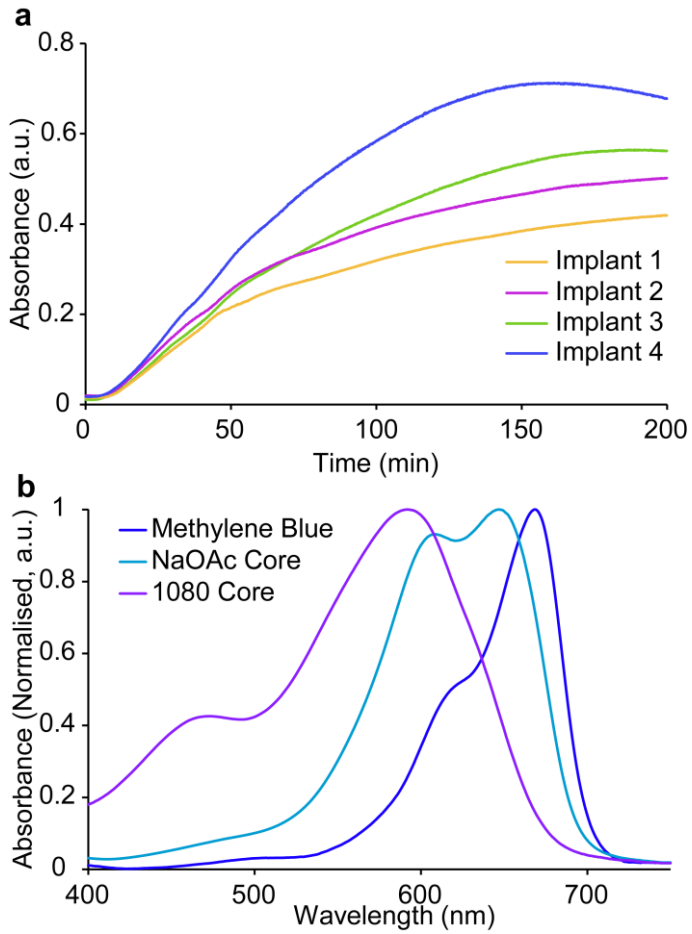


Figure 6.3: a) Release profiles for 1080 implants with a 300 µm PVBI/EO_{10} coating, at pH 1.5, 37 °C (n = 4). b) Comparison of normalised absorbance spectra of NaOAc and 1080 implants, and MB solubilised in a pH 1.5 solution.

This phenomenon is known as metachromasy, a hypsochromic shift caused by the aggregation of charged dye monomers — in this case MB cations — in solution.[3, 4] The aggregation of dye molecules can be induced under a variety of conditions, including increased dye concentration, solution pH, dye adsorption to polyelectrolytes, addition of salts, and changes in the dielectric constant of the solvent.[3–9] In aqueous solutions, monomeric MB cations exhibit an absorbance

maximum at 665 nm (n–π*). In contrast, dimers and trimers have been reported to exhibit respective absorbance maxima of 610 and 572 nm due to the formation of H-type aggregates, and the resulting hypsochromic shift of the n–π* transition.[9, 10] Recently, the formation of tetramers has also been proposed.[11]

The observed metachromasy of MB in release solutions from the NaOAc and 1080 core solutions was attributed to the presence of their respective anions in solution. When present in the core solution, NaOAc caused the formation of some dimers (608 nm) whereas 1080 almost exclusively caused the formation of trimers (592 nm). Compared to the NaOAc or 1080 core samples, no differences in the absorbance maxima were observed for PVBI/EO_{10} coated NaOAc or 1080 implants, when analysed under the same conditions. The absence of a demonstrable effect on the absorbance maxima, suggested that neither the presence of PVBI nor ethyl oleate (EO) affected the aggregation of MB, and provided further indication that NaOAc and 1080 caused the observed metachromasy. The significant aggregation of MB in the presence of 1080 implied that there was a complex association between the two that is absent for NaOAc. The specific mechanism underlying the metachromasy observed in these experiments was outside of the scope of this work and further investigation was not undertaken. Instead, it was hypothesised that monitoring release of the 1080 core implants *via* the absorbance at 592 nm would ameliorate this issue.

The release of MB at pH 1.0 and 1.5 (**Figure 6.4** and **Table 6.2**) displayed the same overall trends as previously reported for the NaOAc implants (**Chapter 5.2.4**, **Figure 5.3**).[12] The initial and complete release times for the 1080 implants were proportional to both the PVBI/EO_{10} coating thickness, and pH of the receiving solution. Considering that the 1080 implants were manufactured with the same PVBI/EO_{10} coating (cf., NaOAc implants), similar release characteristics were expected. However, whilst the initial release times (**Table 6.2**) were consistent with those of the NaOAc implants (**Chapter 5.2.4**, **Table 5.2**), complete release times for the 1080 implants at pH 1.0 and 1.5 were ~ 2 to 3 times greater. This was observed as a protracted release profile in both receiving solutions and for all coating thicknesses, and the measured absorbance appeared to gradually increase at later timepoints despite the implant being completely solubilised.

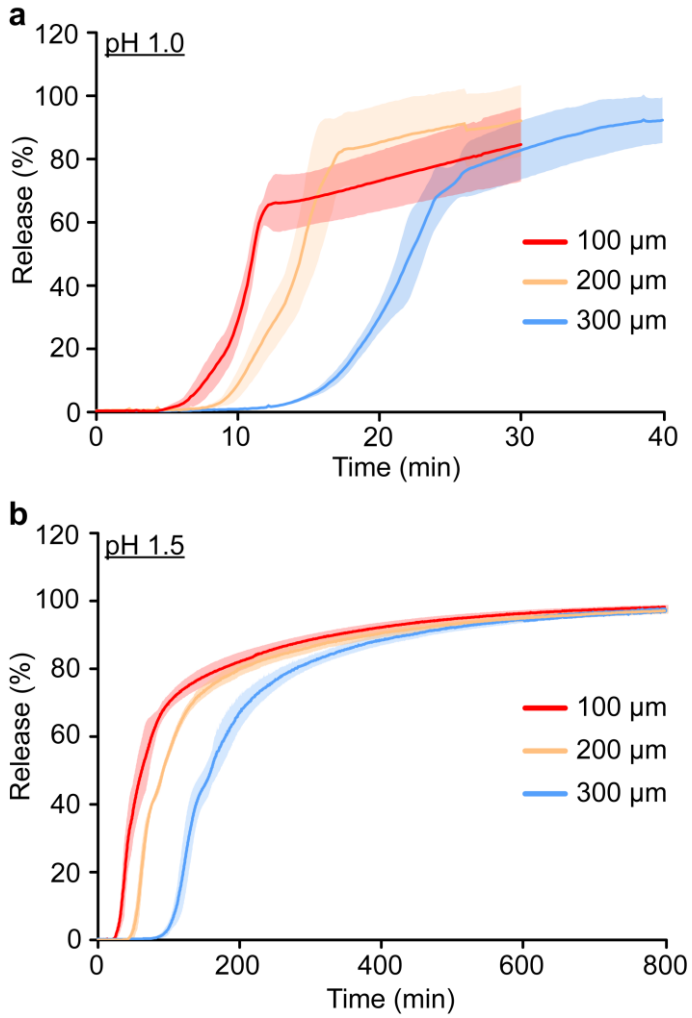


Figure 6.4: Release monitoring profiles of MB from 1080 implants with PVBI/EO_{10} coatings of 100, 200, or 300 µm thickness, at 37 °C, in a) pH 1.0 and b) pH 1.5 release media (3.5 mL). Traces are reported as the mean (solid line) ± std. dev. (shaded area) (n = 5).

The protracted release profiles were attributed to metachromasy and suggested that there was a temporal characteristic to the interactions that made monitoring more complex than first thought. Attempts to reproduce the effect by combining the core components (i.e., NaOAc or 1080, PEG 10 kDa, and MB), and solubilising them under the same conditions (i.e., concentration, temperature, and pH) were unsuccessful. Interestingly, this suggests that an additional structural or temporal factor — perhaps introduced during spray coating, or solubilisation of the core coated implant — was playing a key role. It was hypothesised that the aggregation of MB was caused by the ethanolic spray coating solution, as similar solvatochromic effects have been reported.[13] These aggregates could be released into the low pH solution without dissociating and potentially undergo further

aggregation thereafter. The difficulty in reproducing the observed metachromasy appeared to support this postulation.

The use of an alternative dye with similar solubility in the core formulation and no reported metachromasy, was hypothesised to mitigate these issues. Therefore, the 1080 core formulation was revised and MB was replaced with tartrazine (λ_{max} = 435 nm), a water and EtOH-soluble dye. A new batch of implants was prepared with tartrazine and the release characteristics investigated *in vitro* (**Table 6.2** and Appendix**, Figure A6.2**). Implants containing a 1080 core formulation and tartrazine exhibited similar release characteristics and release profiles to the NaOAc implants (Appendix, **Figure A6.3**), which confirmed that metachromasy between MB and 1080 was the cause of the protracted release profiles. However, a greater build-up of electrostatic charge was observed during the manufacture of the 1080 implants containing tartrazine in the core, leading to end-defects which precluded their further investigation (Appendix, **Figure A6.2**).

Table 6.2: Summary of 1080-implant *in vitro* release results when the core contained MB or tartrazine.

Coating Thickness (µm) [a]	pH 1.0				pH 1.5			
	Initial Release (min) [b]		Complete Release (min) [c]		Initial Release (min) [b]		Complete Release (min) [c]	
	Methylene Blue	Tartrazine	Methylene Blue	Tartrazine	Methylene Blue	Tartrazine	Methylene Blue	Tartrazine
100	7.0 ± 0.7	8.2 ± 0.4	37.8 ± 12.5	41.9 ± 5.4	15.5 ± 2.2	21.6 ± 0.9	155.0 ± 22.0	38.5 ± 2.5
200	9.6 ± 0.5	7.9 ± 0.6	24.6 ± 10.6	32.6 ± 5.5	26.4 ± 1.6	37.1 ± 6.0	184.8 ± 18.0	65.7 ± 3.6
300	15.0 ± 0.5	11.3 ± 0.3	37.4 ± 9.8	33.1 ± 2.1	52.2 ± 2.6	45.4 ± 5.4	213.8 ± 18.1	118.4 ± 9.2

All values are reported as the mean ± std. dev. (n = 5). [a] 1080-implants coated with the PVBI/EO_{10} formulation; [b] Initial release was defined as 5% of the total release of dye (MB or tartrazine) from the implant core; [c] Complete release was defined as 90% of the total release of dye (MB or tartrazine) from the implant core.

6.2.4 *In Vitro* Stability Properties of the 1080 Implants

The stability of the 1080 implants in a simulated subcutaneous environment was investigated *in vitro* by embedding the implants in a hydrogel that simulated the subcutaneous environment (i.e., as described in **Chapter 3.4.3**). 1080 implants bearing a 100 or 200 µm PVBI/EO_{10} coating displayed poor stability, with all the implants failing by 35 and 97 d *in vitro*, respectively (**Figure 6.5a**). In contrast, 1080 implants with a 300 µm PVBI/EO_{10} coating were stable for the duration of the study (529 d), like the NaOAc implants with the same coating thickness (**Chapter 5.2.5**). The same swelling behaviour was observed for the 1080 implants (*cf.* NaOAc implants) (**Figure 6.5b,c**), which was anticipated given the similar physicochemical properties of 1080 and NaOAc and the use of the same semi-permeable PVBI/EO_{10} coating. However, it is likely that the failures observed for the 100 and 200 µm implants were due to the flared ends, as seen during the OM and SEM imaging of whole and microtomed implants (**Figure 6.1**). While the coatings appeared uniform in thickness, the asymmetric shapes of the implant ends appeared to undergo a non-uniform swelling, which may have resulted in greater local mechanical stresses that caused the polymer coating to rupture and the implants to fail.

At thicker PVBI/EO_{10} coatings, the 1080 implants exhibited a more uniform morphology, which likely afforded more uniform swelling and a reduced chance of failure, as evidenced by the proportional relationship between coating thickness and implant stability. It was unclear what caused the flaring of the implant ends, but further investigation is warranted considering that flaring was also observed when coating the 1080 implants containing tartrazine in the core formulation. The observed flaring for the 1080 core implants containing either MB or tartrazine indicated that this phenomenon was related to the physicochemical properties of 1080. Regardless, like their NaOAc counterparts, the 1080 implants possessing a 300 µm PVBI/EO_{10} coating exhibited promising stability and were considered suitable for further testing.

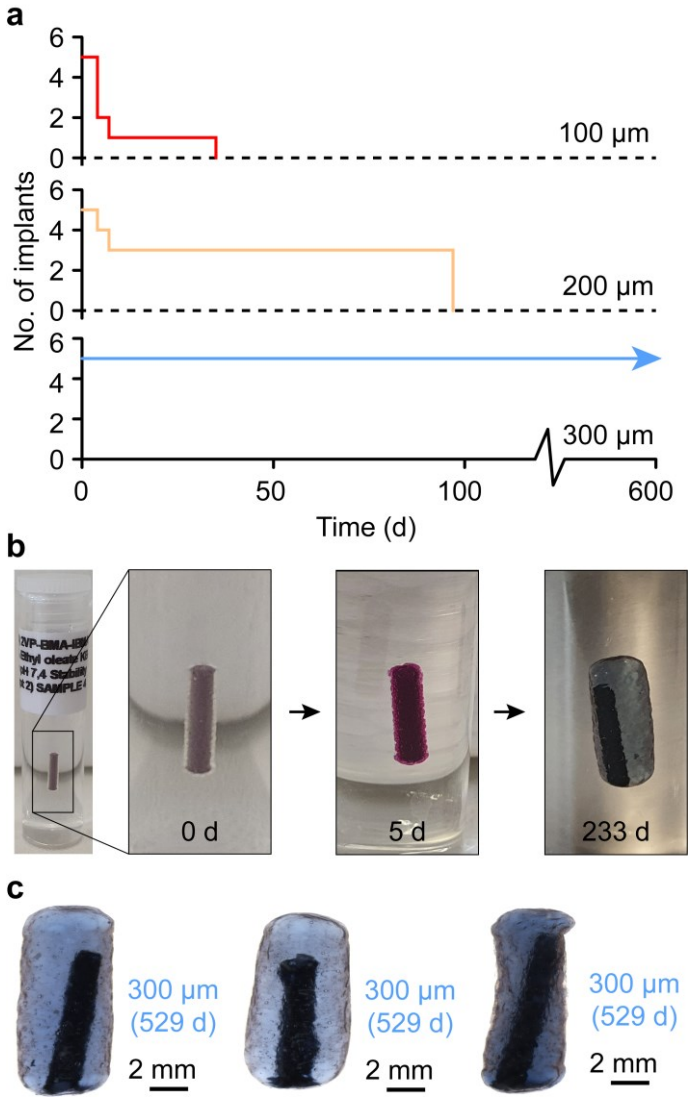


Figure 6.5: a) Stability results of 1080 implants with 100, 200, or 300 µm PVBI/EO_{10} coatings in Pluronics F127 (25% $w.w^{-1}$, in 10 mM phosphate-buffered saline (PBS)) at pH 7.4 and 37 °C (n = 6), over 529 d. Images showing b) the swelling of a 1080 implant with a 300 µm PVBI/EO_{10} coating over 233 d, and c) representative implants that were stable at 529 d.

6.2.5 Assessment of 1080 Diffusion from 1080 Implants *In Vitro*

The *in vitro* stability of the 1080 implants was determined *via* the observed containment of MB within the core during testing, which served as a proxy for all core materials. It was considered that at physiological pH, it was highly unlikely that the anionic 1080, or comparatively high molecular weight PEG 10 kDa, would diffuse across the semi-permeable PVBI/EO_{10} coating. However, the effective containment of 1080 within the implant core *in vivo* was crucial to ensure a lethal dose of 1080 would be present if the implant was consumed by a feral cat. In

addition, the diffusion of 1080 from an implant *in vivo* could result in the toxification of the native mammal bearing it — though only if the species was particularly sensitive to 1080 — and should be avoided. As a result, an accelerated *in vitro* stability study was conducted to determine whether 1080 would diffuse following swelling.

1080 implants were submerged in phosphate-buffered saline (PBS) (pH 7.4) and stored at 37 °C for 296 d. The receiving solutions were analysed periodically *via* high-performance liquid chromatography (HPLC) for the presence of 1080 (λ = 220 nm) and quantified, where detected (Appendix, **Figure A6.4**). 1080 implants at each coating thickness (100, 200, and 300 μm) (n = 3) were tested. However, all the 100 μm, and two 200 μm PVBI/EO_{10} coated 1080 implants failed within 4 d, as indicated by the release of MB into the receiving solution (Appendix, **Figure A6.5**). The failures occurred before the implants had swelled significantly, which precluded their analysis. The remaining 200 μm and all the 300 μm PVBI/EO_{10} coated implants appeared intact for the duration of the experiment, with no observed release of MB (Appendix, **Figure A6.6**). A single 1080 implant (300 μm of PVBI/EO_{10}) was found to release 1080 into the receiving solution. Cumulatively, 3.08 mg of 1080 was released into the receiving solution, which was equivalent to 98.7% of the total theoretical loading (Appendix,

Figure A6.7). In contrast, no 1080 was detected from the remaining implants. If the diffusion of 1080 through the PVBI/EO_{10} coating had occurred, it was expected that it would be detected in all samples once in a swollen state, independent of coating thickness. However, since 1080 was only detected for a single sample, and at every time point, it was likely a result of the failure of the PVBI/EO_{10} coating shortly after swelling, and not diffusion. These results demonstrated that for both *in vitro* and *in vivo* stability experiments, 1080 was effectively contained within the intact PVBI/EO_{10} coatings of the 1080 implants.

6.2.6 *In Vivo* Stability Properties of 1080 Implants

The *in vivo* stability of the 1080 implants with a 300 µm PVBI/EO_{10} coating was assessed following subcutaneous injection in rats, as described in **Chapter 5.4.3**, except stability was monitored over a longer period (230 d). Male Sprague-Dawley rats (n = 7) were each implanted with one 1080 implant, and one radiofrequency identification (RFID) microchip (control), superficial to the left and right scapula, respectively (

Figure 6.6a, top). Body weight measurements were recorded weekly to monitor rat wellbeing (Appendix**, Figure A6.8**), and implant integrity was qualitatively monitored *via* computed tomography (CT) immediately following implantation (

Figure 6.6b and Appendix,

Figure A6.10) and every 6 weeks thereafter. CT images recorded of the implants (12- and 18-weeks post-implantation) revealed that considerable swelling had occurred for all implants following implantation (Appendix,

Figure A6.10). Following implantation, at 39 d Rat #1 was found deceased. Post-mortem examination of the 1080 implant revealed it had failed *in situ* with the core material observed leaking from the fibrous tissue capsule (FTC) that had formed. Similarly, 56 and 61 d after implantation Rats #2 and #3 had lost body mass and were exhibiting signs of 1080 poisoning (e.g., ataxia, tremors, hunched posture, and hypothermia), and were euthanised. 1080 toxicosis was confirmed through analysis of liver tissues from Rats #1 and #2, where 1080 was detected in concentrations of 2.0 and 0.87 $mg.kg^{-1}$, respectively. This trend continued, with two more deaths after 83 and 96 d (Rats #4 and #5), and another rat (#6) euthanised 127 d following implantation due to 1080 toxicosis (

Figure 6.6a, bottom). The surviving rat (#7) exhibited no signs of 1080 toxicosis and was euthanised 230 d after implantation to conclude the study.

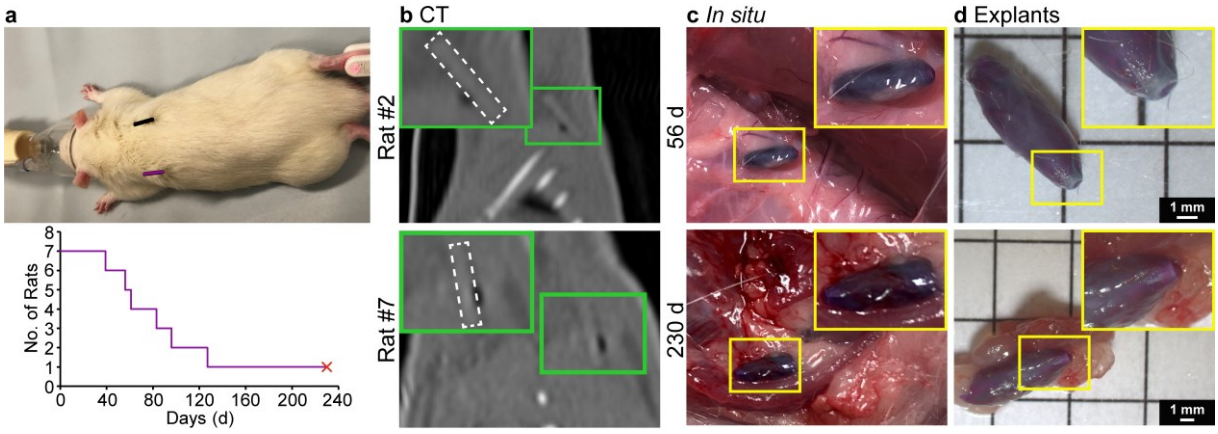


Figure 6.6: a) 1080 implant (purple) and microchip (black) locations (top), and number of surviving rats over time (bottom); the body masses of the rats were monitored throughout the study (Appendix, **Figure A6.8**). b) CT images captured immediately following implantation (i.e., day 0), with implants outlined in white. c) Representative macroscopic images (post-mortem) of implants *in situ* captured prior to explantation, after 56 d (failed) (top) and 230 d (stable) (bottom). d) Representative OM images of explants after 56 (failed) (top) and 230 d (stable) (bottom) taken on a 5 × 5 mm grid; note the protrusion of the ABS filament

substrate through the polymer coating in both samples. Additional images of the remaining explants are available in the Appendix (**Figure A6.9c,d**).

These results clearly demonstrated that the 1080 implants exhibited poor stability *in vivo*, despite the favourable *in vitro* stability results, and in contrast to the favourable *in vitro/in vivo* stability of the NaOAc implants (**Chapter 5.2**). No marked inflammation was observed during post-mortem examination/explantation at any time point, and a FTC formed around all implants (

Figure 6.6c and Appendix, **Figure A6.9c**). The NaOAc implants exhibited increased FTC thicknesses from week 1 to 2 and were constant thereafter, commensurate with the expected changes in cell populations (i.e., the formation and maturation of granulation tissue into a fibrous capsule).[12, 14] These changes indicated that the NaOAc implants exhibited comparable biocompatibility to RFID microchips, which served as a control. Considering the 1080 implants bear the same PVBI/EO_{10} coating and the tissue reaction was indistinguishable at a gross level, the 1080 implants appeared to also exhibit favourable biocompatibility. Importantly, histological examination of the implants was not conducted, as suitable biocompatibility had already been established (**Chapter 5.2.6**). Instead, post-mortem examinations of the implants (**Figure A6.9c**) and OM of the explants (**Figure A6.9d**) were undertaken to interrogate the mechanism of 1080 implant failure. While the implants appeared intact *in situ*, inspection of the explants showed that the ABS filament substrate had pierced the polymer coating following

swelling, causing the premature release of 1080 and the toxification of the rats. It is likely that once in a swollen state, the ABS filament was able to float freely within the solubilised 1080 core and pierced the polymer coating when movement of the implanted animal caused sufficient pressure at the implant location. However, this occurred inconsistently as the final implant remained intact, with the 1080 effectively contained, at the conclusion of the experiment (230 d). Interestingly, when removed from the fibrous tissue capsule and broken, the PVBI/EO_{10} coatings of the implants were discoloured and appeared similar in colour to the solutions of the *in vitro* release experiments (Appendix. **Figure A6.9d**). It appeared that in the presence of 1080, MB (likely in an aggregated state, as suggested by the observed metachromasy) had interacted with and stained the PVBI/EO_{10} coating. The extent of this interaction and the mechanism through which it occurred was not immediately apparent. However, it was hypothesised that it could have led to a change in the physical properties of the coating, possibly making it more brittle and prone to fracture, as this effect was not observed in the NaOAc implants.[12]

It was previously thought that implant location contributed to the failure of the NaOAc implants *in vivo* (**Chapter 5.2.6** and the PVB implants in **Chapter 3.2.8**). However, the data reported herein suggested that the failures were likely primarily due to the ABS filament substrate and its rupturing of the PVBI/EO_{10} coating. In addition, the integrity of the PVBI/EO_{10} coating may have been reduced by the aggregates of MB in the swollen 1080 core and contributed to the observed failures.

6.3 Conclusions

PPIs with toxic 1080-loaded cores (containing a lethal dose of 1080 for feral cats, ≈ 3.12 mg) and pH-responsive PVBI/EO_{10} coatings were manufactured *via* fluidised-bed spray coating with low intrabatch variation. The implants had cohesive and uniform coatings as demonstrated by OM and SEM analysis. The *in vitro* stability of the 1080 implants bearing a 300 µm polymer coating was found to be favourable in a hydrogel model of the subcutaneous environment, despite water permeation and swelling of the core. Diffusion of 1080 through the polymer coating of the swollen implants was not detected and confirmed that 1080 was

contained effectively within the swollen core. However, *in vitro* release experiments conducted under simulated gastric conditions, were complicated by the metachromasy exhibited by MB. Aggregation of MB cations during release from the core, was likely caused by the presence of — and possible interactions with — 1080. Regardless, release experiments conducted on implants containing the non-metachromatic dye tartrazine in the core, demonstrated that the complete release of 1080 from the core was likely to occur within the gastric emptying time of a feral cat.

The *in vivo* stability of the 1080 implants was limited, primarily due to the presence of the ABS filament substrate in the core, and possibly affected by a reduction in mechanical integrity of the PVBI/EO_{10} coating, caused by an interaction between the coating and MB aggregates. Previous *in vivo* experiments involving NaOAc implants exhibited greater stability but were only monitored over a short period and may have been facilitated by comparatively minor interactions between NaOAc and MB, and reduced effects on the integrity of the polymer coating.

The ABS filament substrate was found to have punctured the polymer coatings of almost all the tested implants, causing inconsistent implant stability and rat survival, which ranged from ~ 39–230 d. To improve the performance of future implants, a water-soluble coating substrate containing a non-metachromatic dye could be used. Replacing MB with a non-metachromatic dye would eliminate any potential reduction in mechanical integrity of the coating caused by metachromasy. However, removal of the ABS filament substrate would also be necessary to prevent the puncturing of the polymer coating *in vivo*. A water-soluble core would solubilise during swelling, which the PVBI/EO_{10} coating appears able to accommodate when sufficiently thick (i.e., at 300 µm). The coating may then remain intact and stable for a sufficient period and reduce the likelihood of failure *in vivo*.

6.4 Experimental

6.4.1 Materials

The materials described in Chapter 6 are the same as **Chapter 3.4.1**, **Chapter 4.4.1**, and **Chapter 5.4.1**, unless stated below.

All reagents were used as received unless otherwise specified. Analytical grade orthophosphoric acid (H_3PO_4) was purchased from Chem-Supply (Gillman, Australia). Tartrazine (80%) was purchased from Sigma-Aldrich (St. Louis, United States). Sodium fluoroacetate (1080, 93%) was purchased from Animal Control Technologies Australia (ACTA, Somerton, Australia).

6.4.2 Instrumentation

The instrumentation used in Chapter 5 is the same as **Chapter 3.4.2**, **Chapter 4.4.2**, and **Chapter 5.4.2**, unless otherwise stated below.

High-performance Liquid Chromatography

HPLC was conducted using a Shimadzu Prominence LC system (Shimadzu Corporation, Kyoto, Japan) fitted with a Shimadzu pump (LC-20AD), autosampler (SIL-20AHT) and photodiode array detector (SPD-M20A), and fitted with an Inertsustain Cyano column (3 µm, 4.6 × 250 mm) (GL Sciences, Tokyo, Japan). The HPLC was operated using an isocratic mobile phase consisting of 0.1% $v.v^{-1}$ orthophosphoric acid (H_3PO_4) in 1:1 $v.v^{-1}$ water:MeOH. Elution was conducted at a flow rate of 0.4 $mL.min^{-1}$ over 18 min. All analyses were performed at ambient temperature (23 ± 1 °C), with an injection volume of 10 µL. The presence of 1080 was determined *via* its absorbance (λ = 220 nm, retention time (R_t) = 8.4 min).

6.4.3 Procedures

All procedures were conducted as previously described in **Chapter 3.4.3**, **Chapter 4.4.3**, and **Chapter 5.4.3**, unless otherwise stated below.

Preparation of 1080 Core Coating Formulations

The 1080 core formulation was prepared by dissolving PEG 10 kDa (15.0 g), 1080 (15.0 g) and MB or tartrazine (400 mg) in 64/36% $v.v^{-1}$ EtOH/water, under stirring. The temperature-controlled fluidisation air flow was set to 40 °C during coating.

Implant Manufacture

Manufacture of the 1080 implants was conducted as previously described in **Chapter 3.4.3** and **Chapter 5.4.3**, with the following exceptions. ABS filament substrates (0.63 ± 0.06 mm diameter and 7.39 ± 0.08 mm length, n = 1000), were coated with the 1080 core formulation. ABS filament substrates were coated in 45 min cycles, until ~ 6 mg of the core formulation had been deposited (i.e., equivalent to a 1080 dose of ~ 3 mg per implant). A curing step was employed following coating, where implants were dried in vacuo (16 h, 0.1 mbar, 23 ± 1 °C) and then stored in a desiccator prior to use. Core coated implants were coated with the PVBI/EO_{10} coating using the same approach as described in **Chapter 5.4.3**.

In Vitro Release Experiments

In vitro release experiments were performed as previously described in **Chapter 3.4.3** and **Chapter 5.4.3**, with the following exceptions. Implant release in pH 1.0 and 1.5 solutions was monitored inline using UV-vis spectrophotometry, *via* the presence of MB (λ = 664 or 600 nm) or tartrazine (λ_{max} = 435 nm) in the release solution.

In Vitro 1080 Diffusion Experiments

1080 implants at each PVBI/EO_{10} coating thickness (100, 200, and 300 μm, n = 3) were submerged in PBS (pH 7.4, 3.5 mL) and stored at 37 °C. An aliquot (1 mL) of the PBS receiving solution was removed weekly for HPLC analysis, and at each sampling interval, the removed aliquot was replaced with fresh PBS solution (1 mL). Receiving solution aliquots were analysed without further preparation *via* HPLC. The amount of 1080 was quantified *via* a peak area comparison between the sample and a five-point calibration curve prepared from the analysis of standard solutions of 1080 (28–448 ppm) prepared in PBS (pH 7.4).

In Vivo Stability Experiments

Animal work was conducted under approval S-2015-176 from the University of Adelaide Animal Ethics Committee.

1080 implants were prepared as previously described in **Chapter 3.4.3** and **Chapter 5.4.3**. Male Sprague-Dawley rats (10–11 weeks of age, n = 7) were each subcutaneously implanted with a mini microchip for identification (superficial to the right scapula) and a single 1080 implant (superficial to the left scapula, n = 7 implants total). Sterilised implants and microchips were administered *via* syringe implanters. General anaesthesia induced as described in **Chapter 3.4.3** and **Chapter 5.4.3**. All 1080 implants and microchips were implanted at day 0, with rats checked visually daily and weighed weekly. Rats were scanned *via* CT at implantation, every 6 weeks thereafter, and at the conclusion of the experiment. Rats were monitored daily, and if exhibiting symptoms consistent with 1080 poisoning (e.g., ataxia, tremors, hunched posture, and hypothermia), were immediately euthanised. Rats were euthanised using carbon dioxide (CO_2) and a post-mortem examination was conducted where implants were exposed and photographed prior to explantation then imaged thereafter *via* OM.

1080 Residue Testing

Rats #1 and #2 exhibited symptoms consistent with 1080 poisoning and were euthanised. Liver samples from rats #1 and #2 were analysed for 1080 residue by the Chemical Residue Laboratory at the Department of Agriculture and Fisheries (Queensland Government), using their in-house 1080 analysis method.

Statistical Analyses

All the results are expressed as mean ± std. dev. Unpaired, two-tailed Student's t-tests were used to compare the flexural strength and flexural modulus results for NaOAc and 1080 implants. p-values < 0.05 were considered significant. Minitab 17 (v17.1.0) was used for all statistical analyses. Exact p-values, t-values, and degrees of freedom (DF) are summarised in Appendix, **Table A6.1.**

6.5 Appendix

6.5.1 Supplementary Figures

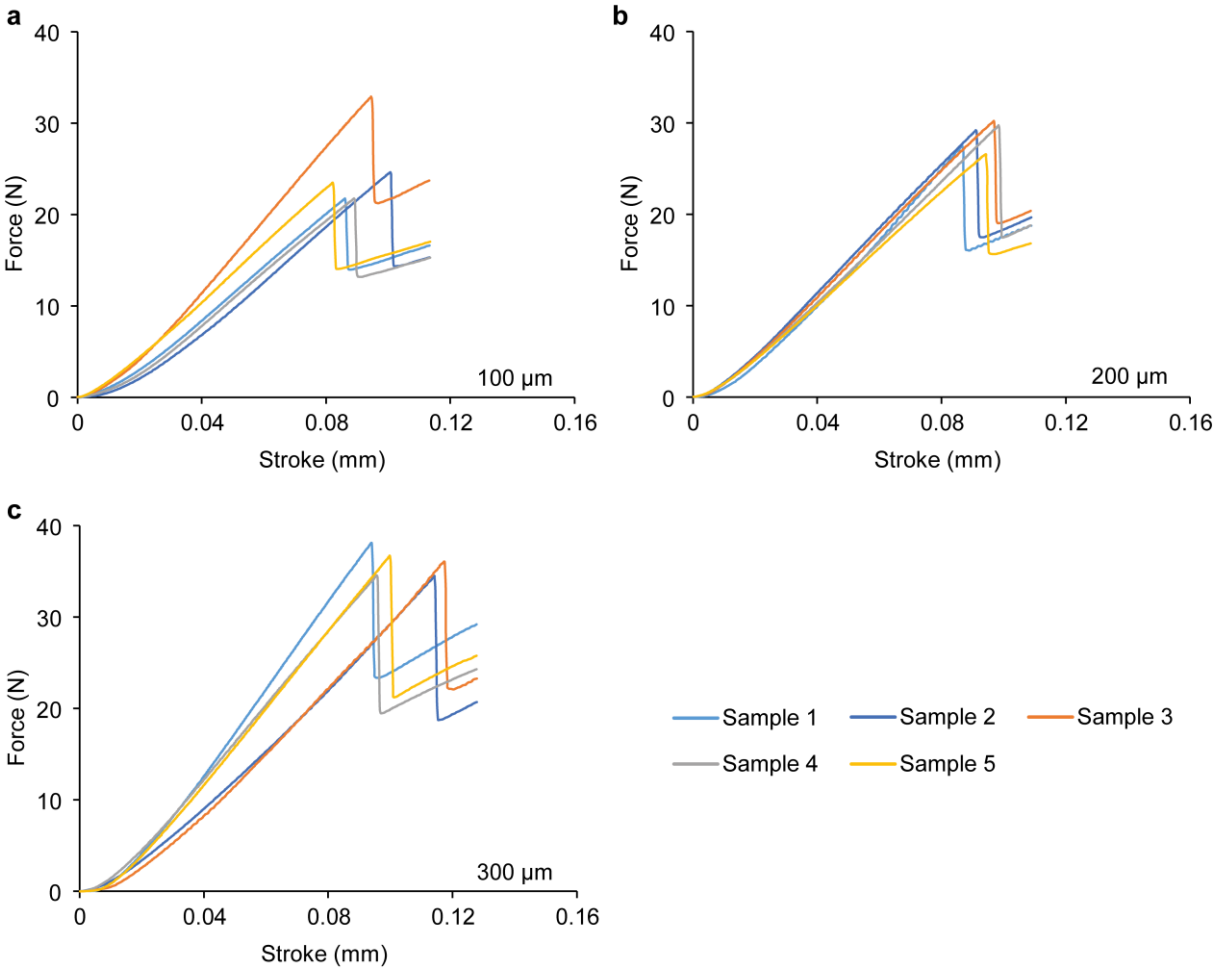


Figure A6.1: Force versus stroke graphs obtained *via* three-point flexural testing of 1080 implants with a) 100, b) 200 and c) 300 µm PVBI/EO_{10} coatings (n = 5 for all samples).

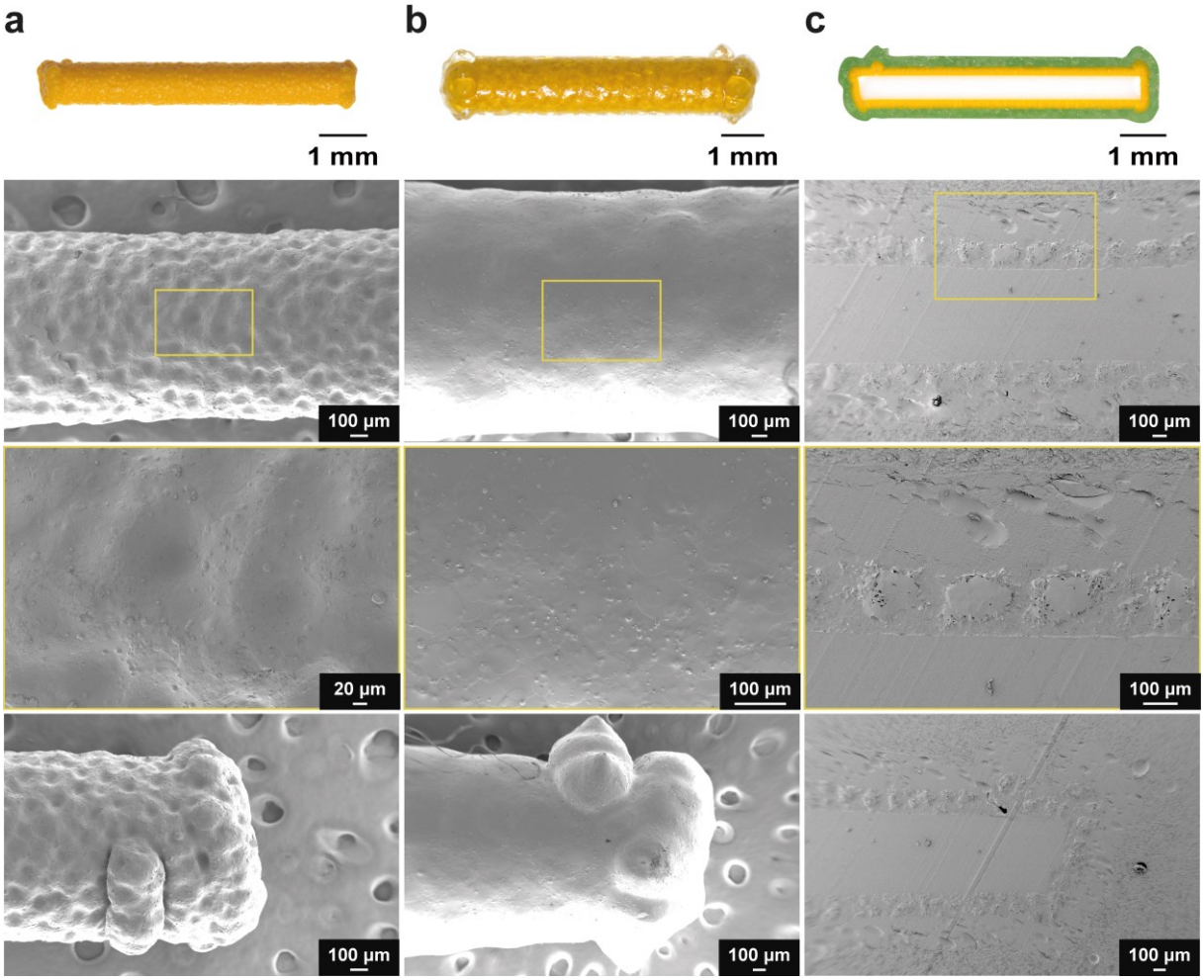


Figure A6.2: Representative digital images and scanning electron micrographs of a) a 1080/tartrazine implant (i.e., containing tartrazine in the core instead of MB), b) a 1080/tartrazine implant with a 300 µm PVBI/EO_{10} coating, and c) an epoxy-embedded and microtomed 1080/tartrazine implant with a 300 µm PVBI/EO_{10} coating.

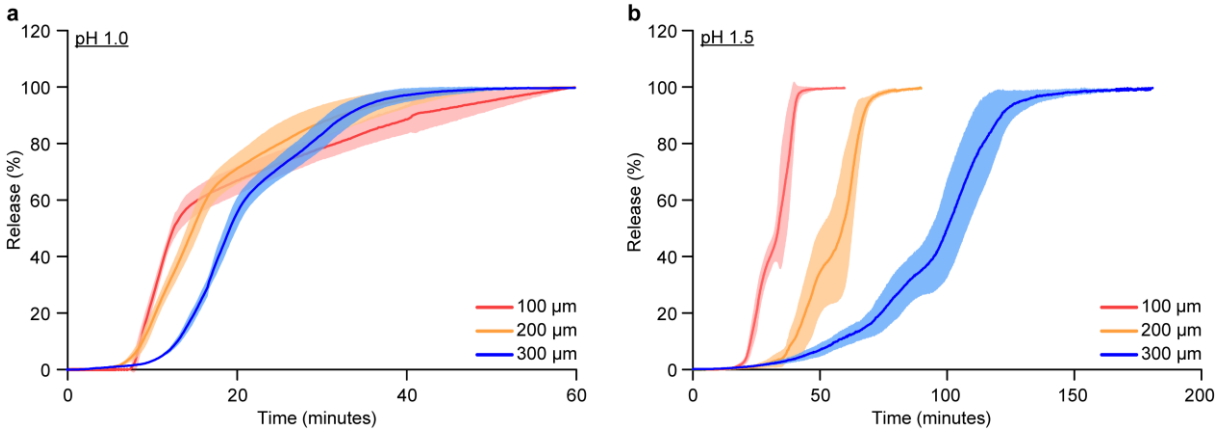


Figure A6.3: Release monitoring profiles of tartrazine from 1080/tartrazine implants at each PVBI/EO_{10} coating thickness (100, 200 or 300 µm) at 37 ± 1 °C, in pH 1.0 or pH 1.5 (3.5 mL) release media. Traces are reported as the mean (solid line) ± std. dev. (shaded area) (n = 5).

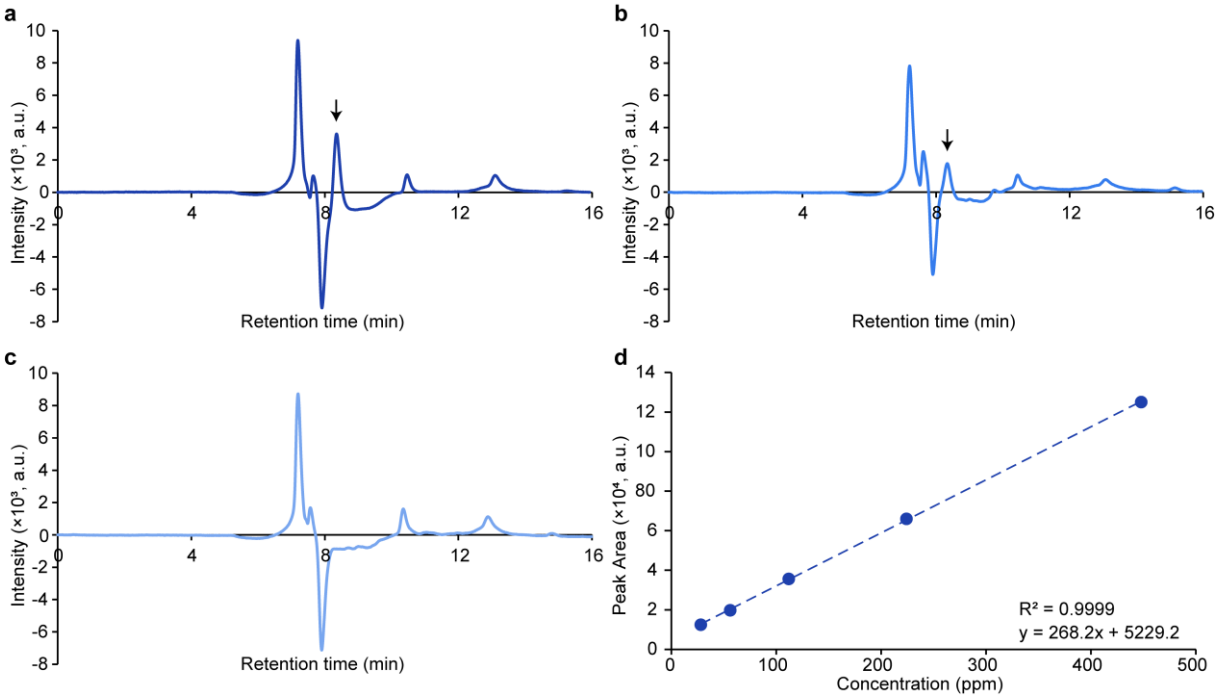


Figure A6.4: Representative HPLC chromatograms of a) a 224 ppm 1080 standard solution prepared in PBS (pH 7.4) used in the generation of a standard curve, b) the presence and c) absence of 1080, determined in the receiving solution (PBS, pH 7.4) of respective 1080 implants (300 µm PVBI/EO_{10} coating) at 173 d. The peaks attributed to 1080 are indicated — where present — with arrows.

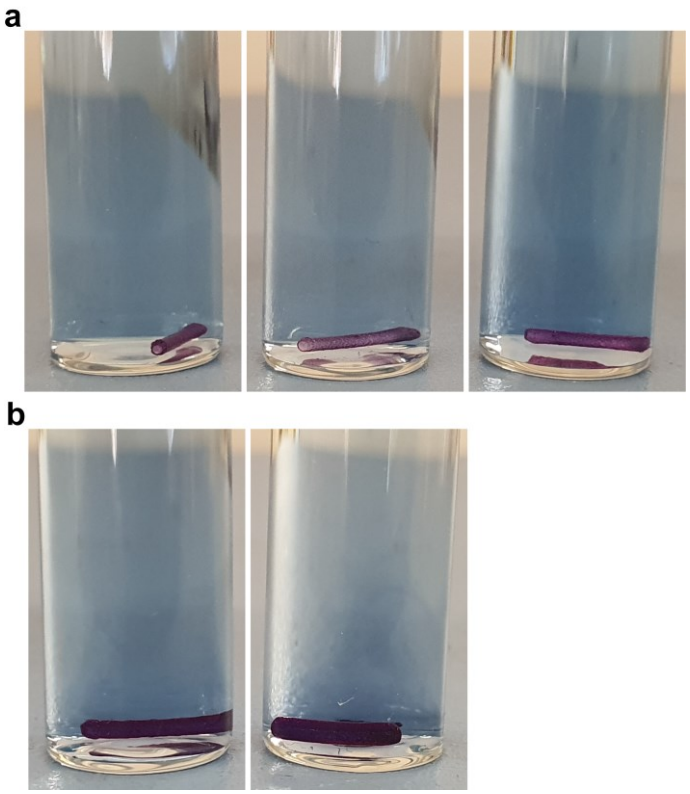


Figure A6.5: Digital images of the 1080 implants with a) 100 µm and b) 200 µm PVBI/EO_{10} coatings that failed under accelerated swelling conditions (PBS, PH 7.4, 37 °C).



Figure A6.6: Representative digital images of a 1080 implant (300 µm PVBI/EO_{10} coating) captured under accelerated swelling conditions (PBS, pH 7.4, 37 °C).

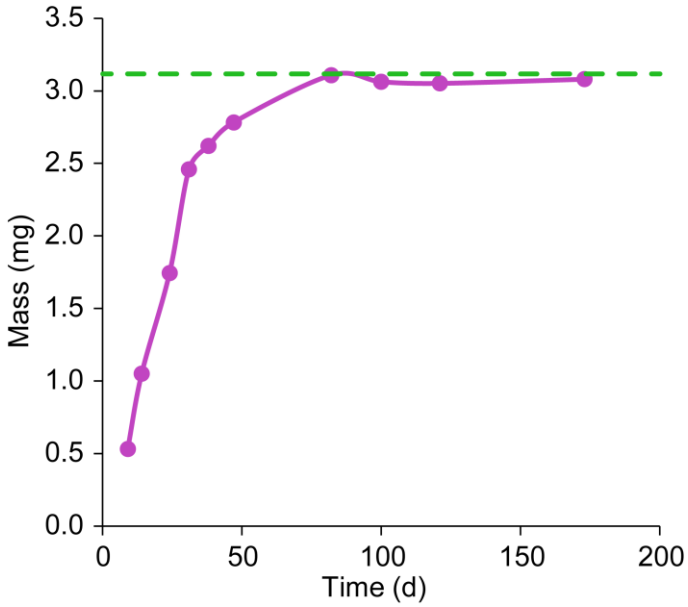


Figure A6.7: Cumulative release profile of 1080 from a failed 1080 implant (300 µm PVBI/EO_{10} coating) under accelerated swelling conditions (PBS, pH 7.4, 37 °C). The presence of 1080 was determined *via* HPLC (λ = 220 nm). Note the dashed line indicates the average calculated loading (3.12 mg) of 1080.

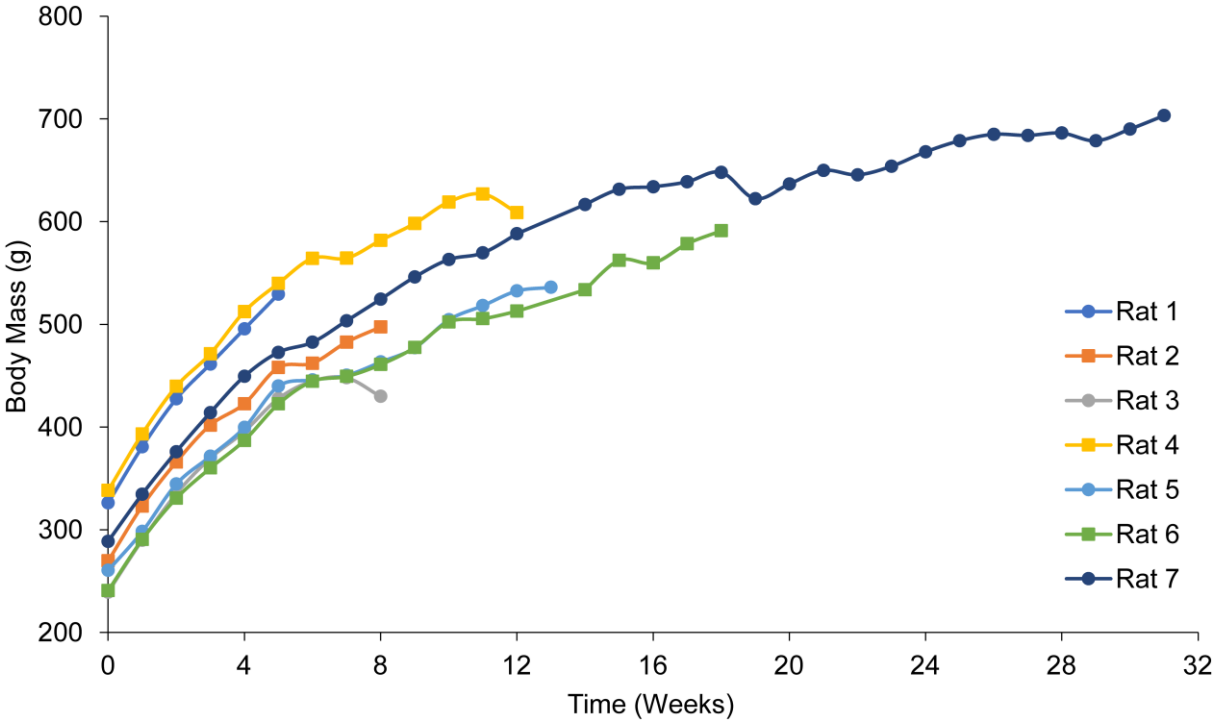


Figure A6.8: Rat body masses (n = 7), recorded during the *in vivo* stability experiment of the 1080 implants bearing a 300 µm PVBI/EO_{10} coating.

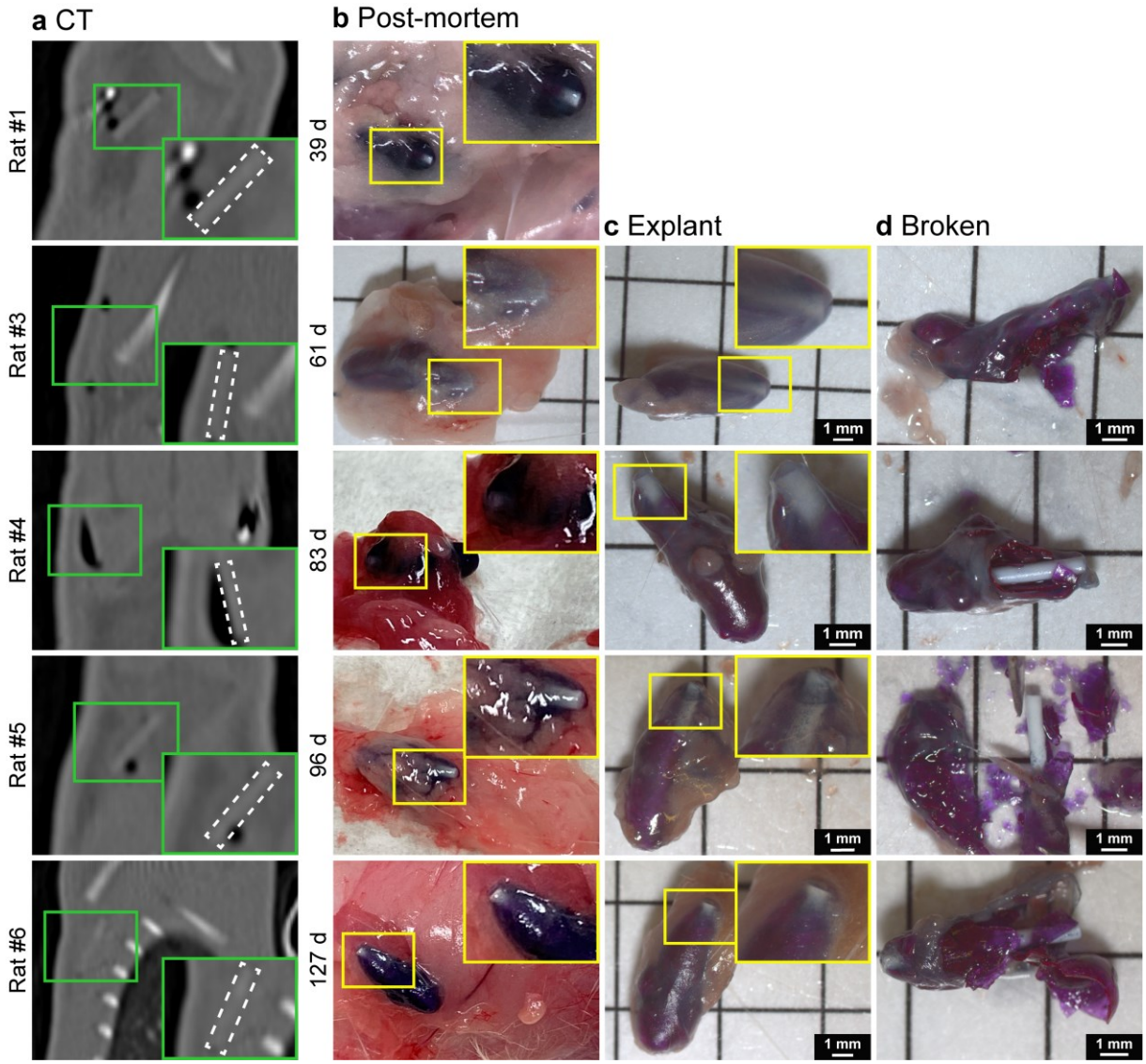


Figure A6.9: A summary of images captured during the *in vivo* stability study of the 1080 implants bearing a 300 µm PVBI/EO_{10} coating. a) CT images captured immediately following implantation (i.e., day 0), note the implants outlined in white. Photographs captured b) during post-mortem examination *in* or *ex situ*, c) following explantation and the removal of most of the surrounding subcutaneous tissues, and d) following dissection of the fibrous tissue capsule and breakage of the explant. Note, the 5 × 5 mm grid used in the images of b) and c).

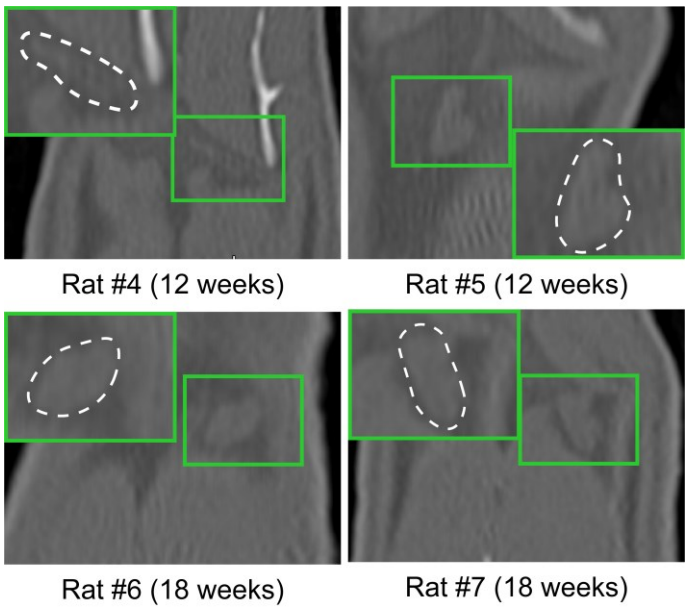


Figure A6.10: CT scans of 1080 implants (300 μm PVBI/EO_{10} coatings) recorded at the latest time point available prior to failure *in vivo*, with implants outlined in white.

Table A6.1: Summary of two-tailed Student's t-test results (t-test of difference = 0 (vs. ≠).

Test of Mean	t-value	DF	p-value
Flexural strength of NaOAc *vs.* 1080 implants (100 μm PVBI/EO_{10})	-0.03	7	0.973
Flexural strength of NaOAc *vs.* 1080 implants (200 μm PVBI/EO_{10})	1.26	5	0.265
Flexural strength of NaOAc *vs.* 1080 implants (300 μm PVBI/EO_{10})	0.02	4	0.988
Flexural modulus of NaOAc *vs.* 1080 implants (100 μm PVBI/EO_{10})	0.44	6	0.679
Flexural modulus of NaOAc *vs.* 1080 implants (200 μm PVBI/EO_{10})	2.62	7	0.035
Flexural modulus of NaOAc *vs.* 1080 implants (300 μm PVBI/EO_{10})	0.34	7	0.743

6.6 References

1. C.-E. Brunchi and L. Ghimici, *Rev Roum Chim*, 2013, **58**, 183–188.
2. M. Marucci, A. Holmgren, H. Carlsson, A. Jarke, M. O. Johansson and C. v. Corswant, *Chem Biochem Eng Q*, 2012, **26**, 379–384.
3. E. Rabinowitch and L. F. Epstein, *J Am Chem Soc*, 1941, **63**, 69–78.
4. J. A. Bergeron and M. Singer, *J Biophys Biochem Cytol*, 1958, **4**, 433–457.
5. G. S. Singhal and E. Rabinowitch, *J Phys Chem*, 1967, **71**, 3347–3349.
6. E. Touitou and P. Fisher, *J. Pharm. Sci.*, 1986, **75**, 384–386.
7. S. Jockusch, N. J. Turro and D. A. Tomalia, *Macromolecules*, 1995, **28**, 7416–7418.
8. J. S. Kellner-Rogers, J. K. Taylor, A. M. Masud, N. Aich and A. H. Pinto, *Energy Ecol Environ*, 2019, **4**, 85–102.
9. D. Heger, J. Jirkovský and P. Klán, *J Phys Chem A*, 2005, **109**, 6702–6709.
10. B. Heyne, *Photochem Photobiol Sci*, 2016, **15**, 1103–1114.
11. A. Fernández-Pérez and G. Marbán, *ACS Omega*, 2020, **5**, 29801–29815.
12. K. Brewer, T. J. McWhorter, C. Sloper, K. Moseby, J. L. Read, D. Peacock and A. Blencowe, *ACS Appl Polym Mater*, 2022, **4**, 6687–6699.
13. A. G. Gilani, M. Salmanpour and T. Ghorbanpour, *J Mol Liq*, 2013, **179**, 118–123.
14. R. Klopfleisch and F. Jung, *J Biomed Mater Res A*, 2017, **105**, 927–940.

Chapter 7: Implant Cores Prepared *via* Hot-melt Extrusion and the Effects on Implant Performance

7.1 Overview

This chapter describes the preparation and evaluation of population protecting implants (PPIs) with a revised core design — a completely water-soluble, sodium acetate (NaOAc)-containing core, prepared *via* hot-melt extrusion (HME). The HME core was designed to be used in combination with fluidised-bed spray coating of the PVBI/EO_{10} formulation, as developed in **Chapter 5.2.1**, to produce complete implants. The formulation of the hot-melt-extruded core is described, and its effects on implant performance are discussed. The revised design of the implants containing a hot-melt-extruded core is compared to those described in **Chapters 5.2** and **Chapter 6.2**, that contain an acrylonitrile butadiene styrene (ABS) filament substrate, through investigation of their manufacturing quality and *in vitro* stability and release results. N.B., to highlight the change in core design of the implants described in Chapters 5 and 6, and those presented in Chapter 7, they will hereafter be referred to as ABS implants and HME implants, respectively. A poly(ethylene glycol) (PEG)-based HME formulation was developed based on a formulation first reported by Isreb et al.[1], and a novel gel permeation chromatography (GPC) analytical approach was successfully used to determine the homogeneity and loading accuracy of the resultant HME cores. Manufactured HME cores were found to exhibit low intrabatch variation, and excellent loading accuracy of the formulation components. Following fluidised-bed spray coating, HME implants exhibited uniform and cohesive PVBI/EO_{10} coatings. The incorporation of a HME core was found to reduce the flexural modulus of the implants (cf., ABS implants), which may increase their resistance to damage caused by mechanical stressors *in vivo*. Under simulated gastric conditions, HME implants were found to release their core material within the gastric half-emptying time (GET) of a feral cat (≤ 2.5 h), despite a moderate increase in release time caused by the formation of an interfacial gel layer during dissolution. The *in vitro* stability of the HME implants was moderately reduced (cf., ABS implants), ostensibly due to an increase in the rapidity and magnitude of swelling afforded by

the entirely water-soluble HME core. However, an increased coating thickness may afford HME implants that are able to withstand the changes in osmotic pressure caused by the HME core. Ultimately, the *in vitro* and *in vivo* evaluation of HME implants with thicker PVBI/EO_{10} coatings is required to determine whether a significant increase in implant stability is observed compared to the ABS implants.

The gel permeation chromatography experiments described in this chapter were conducted by Wei Ge. Kyle Brewer processed and interpreted all the raw data generated by these experiments and performed all data reporting and visualisation.

7.2 Results and Discussion

7.2.1 Hot-Melt Extrusion Optimisation of a Poly(ethylene glycol)-based Formulation

The poor *in vivo* stability of the 1080 implants was primarily attributed to the presence of the ABS filament substrate within the core, which appeared to puncture the PVBI/EO_{10} coating of swollen implants *in situ*. It was hypothesised that an entirely water-soluble core could replace the combination of ABS filament substrate and NaOAc core used in the ABS implants. Additionally, by using a water-soluble core, it would be possible to determine whether removal of the ABS filament substrate was sufficient to extend the stability of the implants *in vivo*.

To prepare a water-soluble core without the use of an ABS filament substrate, an alternative manufacturing approach (cf., fluidised-bed spray coating) was required. However, to enable the application of the PVBI/EO_{10} coating, the water-soluble cores would need to be prepared accurately, within the same size and shape constraints of the previous NaOAc cores that contained a filament substrate. HME was considered the most ideal approach in this regard, as the bulk materials could be homogenised during extrusion, and could be extruded and cut to a specified diameter and length, respectively.

We investigated the development of PPIs containing a PEG HME core containing NaOAc (again as an analogous compound to sodium fluoroacetate, 1080), based on the blended PEG HME formulation reported by Isreb et al.,[1] and briefly

described in **Chapter 1.6.2**. The thermal stabilities of 1080 (up to 200 °C)[2] and NaOAc (up to ~ 300 °C),[3] and the relatively low extrusion temperature of the PEG HME core, made it a suitable choice for this work. A HME formulation based on poly(vinyl alcohol) (PVA) was also investigated, as it has been reported to exhibit similarly favourable properties.[4, 5] However, the PVA formulation could not be extruded as a homogenous extrudate, and further investigation was not conducted. A brief description of the work is provided in **Appendix 7.6.2**.

The diameter of a single HME core (once cut) was set at 1.20 mm, to enable application of the PVBI/EO_{10} coating using the method described in **Chapter 3.4.3** and **Chapter 5.4.3**. As a HME core with a 300 µm coating would retain the ability to fit a conventional syringe implanter (i.e., 2 mm internal diameter). The density of the core material was estimated to be 1.21 mg.mm^{-3} — i.e., PEG with a volume-average molecular weight (M_V) of 600 kDa[6, 7] (PEG 600 kDa) — as PEG 600 kDa was the primary component in the PEG-based formulation. (N.B., the same calculations were used for the PVA formulation given that PVA 4-88 exhibits a similar density of 1.19 mg.mm^{-3}).[8] The mass of a single HME core was set at 10.64 mg, to enable loading of a 3.00 mg dose of NaOAc, as the active pharmaceutical ingredient (API) content of the formulation was 28.7% w.w^{-1} (equivalent to a 3:7 w.w^{-1} of NaOAc:PEG). From these values, the volume and length of a single HME core were calculated as 8.79 mm^3 and 7.78 mm, respectively. Importantly, the calculated diameter of a HME core from these values suggested that a HME core with the above dimensions would be suitable for spray coating and produce implants within the desired size constraints.

Therefore, based on a 10.64 mg HME core, a formulation consisting of NaOAc, polymer, and dye, at a mass ratio (% w.w^{-1}) of 30.0/69.3/0.7 — was postulated. Notably, the required loading of NaOAc (~ 30%) to ensure an analogously lethal dose of 1080, restricted the amount of polymeric material that could be incorporated. The mass ratio (%) of dye was reduced from 1.32% (used in the methylene blue (MB)-only NaOAc core described in **Chapter 4.4.3**), to 0.66%, as the dissolution of a single HME core would result in a higher concentration of solutes during the ultraviolet-visible (UV-vis) spectrophotometry release experiments, (cf. a filament-containing NaOAc core), due to the absence of the ABS filament substrate. This mass ratio of tartrazine would result in a sufficiently

concentrated solution following the dissolution of a single HME core, to enable the inline monitoring of core dissolution as previously described in **Chapter 3.4.3.**

The PEG-based HME formulation was first prepared using the same ratio of different molecular weight (MW) PEGs as previously reported by Isreb et al.[1] (PEG-A, **Table 7.1**), with NaOAc, PEG 600 kDa, PEG 6 kDa (i.e., PEG with a number-average molecular weight (M_n) of 6 kDa) and tartrazine at a target mass ratio (% w.w^{-1}) of 29.4/35/35/0.6. Successful extrusion was achieved at 91 °C, and the PEG-A extrudate appeared homogenous immediately following extrusion.

Table 7.1: Summary of the feed ratios of the tested PEG-based HME formulations.

HME Formulation	Mass Ratio (% w.w^{-1})			
	NaOAc	PEG 600 kDa	PEG 6 kDa	Tartrazine
PEG-A	28.7	35	35.7	0.66
PEG-B	28.9	45.1	25.6	0.66

However, upon cooling, NaOAc was observed on the surface of the extrudate, which suggested it was heterogeneously dispersed throughout the extrudate (Appendix, **Figure A7.1**). Re-extrusion of the extrudate failed to improve its homogeneity. The heterogeneity was attributed to insufficient mixing by the single-screw extruder, which may have been exacerbated by the relatively high crystallinity of PEG 6 kDa (~ 196 J.g^{-1} cf., PEG 600 kDa 137 J.g^{-1}) (**Figure A7.2a,b**). The physical state of NaOAc within the extrudate may have contributed to the heterogeneity of the extrudate. However, like previous reports by Cantin et al.,[9] the melting point endotherms of both PEGs (~ 57 and ~ 61 °C for PEG 6 kDa and 600 kDa, respectively) coincided with the melting point endotherm of NaOAc — as the trihydrate — at ~ 57 °C. The overlapping endotherms of both PEGs and NaOAc, precluded determination of the physical state of NaOAc. To increase the plasticity of the extrudate, a second formulation (PEG-B) was prepared, with the PEG 600 kDa content increased from 35 to 45% at the expense of the PEG 6 kDa.

The PEG-B formulation required a greater extrusion temperature (102 °C) to achieve consistent extrusion, due to the increased PEG 600 kDa content and its

high complex viscosity.[1] In addition, to afford the target diameter of 1.20 mm, a small weight was affixed to the end of the extrudate during extrusion (

Figure A7.3). After a single extrusion, once cooled the PEG-B extrudate was again heterogenous (**Figure 7.1a**). However, repeated extrusions appeared to increase the homogeneity of the extrudate, and so the PEG-B extrudate was re-extruded a total of three times. The increased ratio of high to low MW PEG (i.e., PEG 600 kDa:PEG 6 kDa) within the melt facilitated the incorporation of NaOAc and appeared to produce a qualitatively homogenous extrudate (**Figure 7.1b**). It is likely that the less crystalline PEG 600 kDa (Appendix, **Figure A7.2b**) reduced the crystallinity of the PEG-B extrudate (**Figure A7.2d,e**), and effectively plasticised the PEG 6 kDa to afford improved physical mixing of the NaOAc. Approximately one metre lengths of the homogenous PEG-B extrudate were produced for further evaluation.

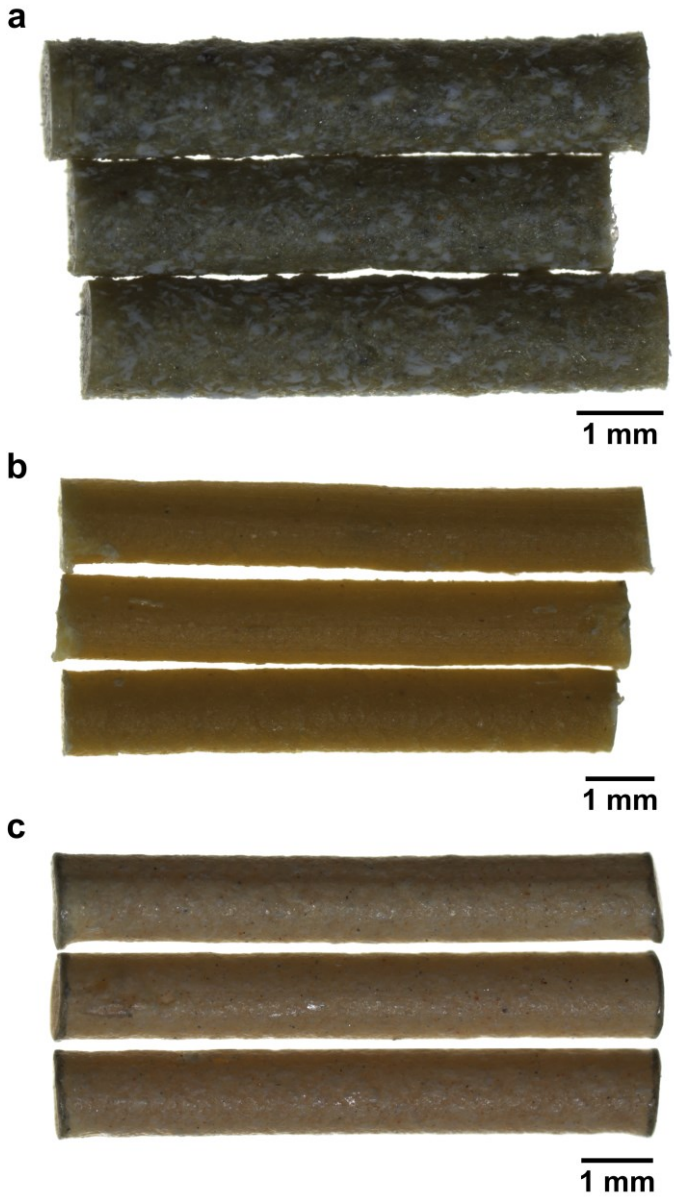


Figure 7.1: Images of PEG-B extrudate samples after a) a single extrusion, b) a total of three extrusions, and c) images of PEG-B cores following rotary tumbling. Note the homogenous appearance of the samples following three extrusions in b), and the smooth edges afforded by rotary tumbling in c).

7.2.2 Critical Evaluation of the Loading Accuracy of PEG-B Extrudates

The accuracy of the NaOAc loading in each implant, which relates to the dose of poison, is key to its field performance. A lethal dose of 1080 will eliminate a problem individual and protect a reintroduced or remnant population. In contrast, a sublethal dose risks the persistence of a problem individual within the target area, and the development of aversive behaviours. However, as NaOAc is non-

chromophoric, its loading could not be accurately determined *via* conventional methods (e.g., UV–vis spectrophotometry or high-performance liquid chromatography). To interrogate the loading and distribution of NaOAc (analogous to 1080) within the PEG-B extrudate, the composition of PEG-B extrudate samples was instead quantified *via* GPC (Appendix,

Figure A7.4) — a previously unreported approach to determining the composition of HME formulations. The concentrations of PEG 6 and 600 kDa, and tartrazine (and hence, their mass fraction, % $w.w^{-1}$) were determined from a peak area comparison of the samples and standard curves. The mass fraction of each component was determined and compared to their target loadings (**Table 7.1**). The mass fraction of NaOAc was then inferred from these data.

Table 7.2: Feed and calculated mass ratios and loading accuracy of the components in the PEG-B extrudate.

Material	PEG 6 kDa	PEG 600 kDa	Tartrazine	NaOAc
Feed (% w.w^{-1}) [a]	25.6	45.1	0.52	28.8
Extrudate (% w.w^{-1}) [b]	27.0 ± 1.0 (3.7)	42.7 ± 1.5 (3.5)	0.45 ± 0.01 (2.2)	29.9 ± 2.1 (7.0)
Loading Accuracy (%) [c]	106 ± 4	95 ± 3	87 ± 2	104 ± 7

[a] Values obtained from the masses of each component in the bulk PEG-B feed material. [b] Values reported as mean ± std. dev. (percentage relative standard deviation, %RSD) from n = 10 extrudate samples. [c] Calculated from the feed and extrudate mass fraction values.

The percentage relative standard deviation (%RSD) of the mass fractions of PEG 6 and 600 kDa, and tartrazine were extremely low (%RSD < 4%), which demonstrated that the extrudate had excellent homogeneity over a considerable length of extrusion. In addition, the inferred loading accuracy of NaOAc was excellent (104%) and equivalent to a mass of approximately 2.95–3.39 mg per implant — based on an implant mass of 10.64 mg as proposed in **Chapter 7.2.1**. If the PEG-B formulation was prepared with 1080, this would have been equivalent to a lethal dose (> LD_{90}) for a feral cat.[10] PEG 6 and 600 kDa exhibited similarly favourable loading accuracies (106 and 95%, respectively), indicating their effective and homogeneous incorporation into the extrudate. In contrast, tartrazine showed a moderately lower loading accuracy (87%). Considering the loading accuracy of the remaining components, this reduction was likely not caused by an extrusion-related issue (e.g., insufficient mixing or thermal degradation). It was postulated to be due to the photolytic degradation of tartrazine in the GPC mobile phase during dissolution and storage, as the discolouration of PEG-B samples following prolonged exposure to light — when solubilised in mobile phase, or acidic solutions — was observed. This postulation was supported by previous reports of the photolytic degradation of tartrazine.[11, 12] The photolytic degradation of tartrazine would have resulted in an apparent reduction in the mass fraction of tartrazine, and therefore a reduction in the loading accuracy. However, as tartrazine was incorporated to enable the inline monitoring of the release of the implant core, and only comprises < 1% of the mass of the core, the absolute loading was not crucial. Ultimately, the PEG-B extrudate was found to exhibit exceptional homogeneity and loading accuracy, making it suitable for implant manufacture.

7.2.3 Manufacture and Evaluation of the HME Implants

The PEG-B extrudate (as ~ 1 m length filaments) was manually cut to size, using a custom 3D printed filament cutting tool (Appendix, **Figure A7.5**). The first and last 5–10 cm of extrudate were discarded, as thinning occurred at these locations due to the proximity of the extrudate to the nozzle and weight, respectively. Exclusion of this material ensured that the extrudate samples were afforded with uniform diameters. The remaining material was cut into ~ 8 mm long pieces (hereafter referred to as PEG-B cores). ~ 10 m of extrudate was processed, resulting in the preparation of n ≈ 1400 PEG-B cores. The PEG-B cores were found to exhibit some residual material at the cut edges (**Figure 7.1b**), likely due to the malleability of the PEG-based formulation. These artefacts were considered likely to interfere with the spray coating process, and therefore, the PEG-B cores were rotary tumbled to obtain a smooth finish at each end, prior to coating (**Figure 7.1c**).

The dimensions of the PEG-B cores were close to the target values (**Table 7.3**) and exhibited low intrabatch variation (%RSD < ~ 1%). The average mass of a single PEG-B core was greater than estimated (12.05 mg cf., 10 mg) due to a combination of a higher than estimated core density, and longer PEG-B cores (cf. to the target length of 7.78 mm) following cutting. The larger PEG-B cores resulted in a NaOAc dose of ~ 3.60 mg per core. However, in future batches this could easily be rectified by reducing the core length or diameter. Importantly, the PEG-B cores showed extremely low intrabatch variation dimensionally (%RSD = 3.5%), which, combined with the excellent loading accuracies, demonstrated the effectiveness of the approach, and so the PEG-B cores were used in subsequent implant manufacture.

PEG-B cores (n = 600) were spray coated with the pH-responsive PVBI/EO_{10} formulation as previously reported (**Chapter 5.2.2**), at thicknesses of 100 (n = 150), 200 (n = 150), and 300 μm (n = 300). The dimensions and masses of the PVBI/EO_{10} coated PEG-B cores (hereafter referred to as HME implants) showed little intrabatch variation (%RSD < 2.5%) and were compatible with conventional syringe implanters at all coating thicknesses (**Table 7.3**). Calliper measurements of the PVBI/EO_{10} coating thicknesses were consistent with the point-to-point measurements of microtomed samples, though generally ~ 10% larger. There was < 10% difference between measurements obtained *via* each

measurement method, and all coating thickness measurements showed relatively low variation (%RSD < 20%).

The PEG-B cores and HME implants were analysed *via* optical microscopy (OM) and scanning electron microscopy (SEM) (**Figure 7.2**). SEM analysis of the PEG-B cores revealed a uniform, homogenous extrudate, with the cut ends visibly abraded due to the rotary tumbling process (**Figure 7.2a**). There were no signs of defects observed in the cores, which appeared to be of comparable quality to the previously reported ABS implant cores (**Chapter 5.2.2** and **Chapter 6.2.1**). HME implants with a 300 μm PVBI/EO_{10} coating exhibited cohesive coatings when imaged using OM (**Figure 7.2b**).

Table 7.3: Summary of HME implant dimensions at various stages during manufacture.

Coating Thickness (µm)	Diameter (mm) [a]	Length (mm) [a]	Mass (mg)[a]	Coating Thickness (Calliper) (µm) [a]		Coating Thickness (Microtomed) (µm) [b]			
				Side Midpoint	End	Overall [c]	Ends [d]	Sides [e]	Side Midpoint [f]
PEG-B Core	1.20 ± 0.013 (1.1)	8.37 ± 0.09 (1.1)	12.05 ± 0.42 (3.5)						
100	1.41 ± 0.016 (1.1)	8.57 ± 0.13 (1.5)	15.82 ± 0.38 (2.4)	109 ± 3 (2.8)	102 ± 20 (19.6)	115 ± 15 (13.0)	113 ± 14 (12.4)	117 ± 16 (13.7)	129 ± 20 (15.5)
200	1.57 ± 0.018 (1.1)	8.74 ± 0.09 (1.0)	19.55 ± 0.45 (2.3)	186 ± 3 (1.6)	184 ± 15 (8.2)	170 ± 18 (10.6)	174 ± 21 (12.1)	166 ± 15 (9.0)	165 ± 16 (9.7)
300	1.78 ± 0.018 (1.0)	8.96 ± 0.08 (0.9)	25.51 ± 0.46 (1.8)	293 ± 3 (1.0)	296 ± 15 (5.1)	275 ± 21 (7.6)	274 ± 25 (9.1)	275 ± 16 (5.8)	277 ± 10 (3.6)

All results are reported as the mean ± std. dev. (%RSD). [a] Determined from n ≥ 50 digital calliper measurements; [b] Determined from n = 6 epoxy-embedded and microtomed implants; [c] Determined from 22 point-to-point measurements; [d] Determined from 10 point-to-point measurements; [e] Determined form 12 point-to-point measurements; [f] Determined from 2 point-to-point measurements.

Slight defects in the PVBI/EO_{10} coating were observed once the HME implants were microtomed and imaged *via* SEM (**Figure 7.2c**). However, these defects were due to the microtoming process, where the PVBI/EO_{10} coating was damaged, or the PEG-B core material was 'smeared' in the cutting direction (due to its malleability) during microtoming. Overall, the PVBI/EO_{10} coatings were uniform and cohesive. In conjunction with the dimensional analysis, these data demonstrated that the HME implants had uniform PVBI/EO_{10} coatings, with no observable coating defects.

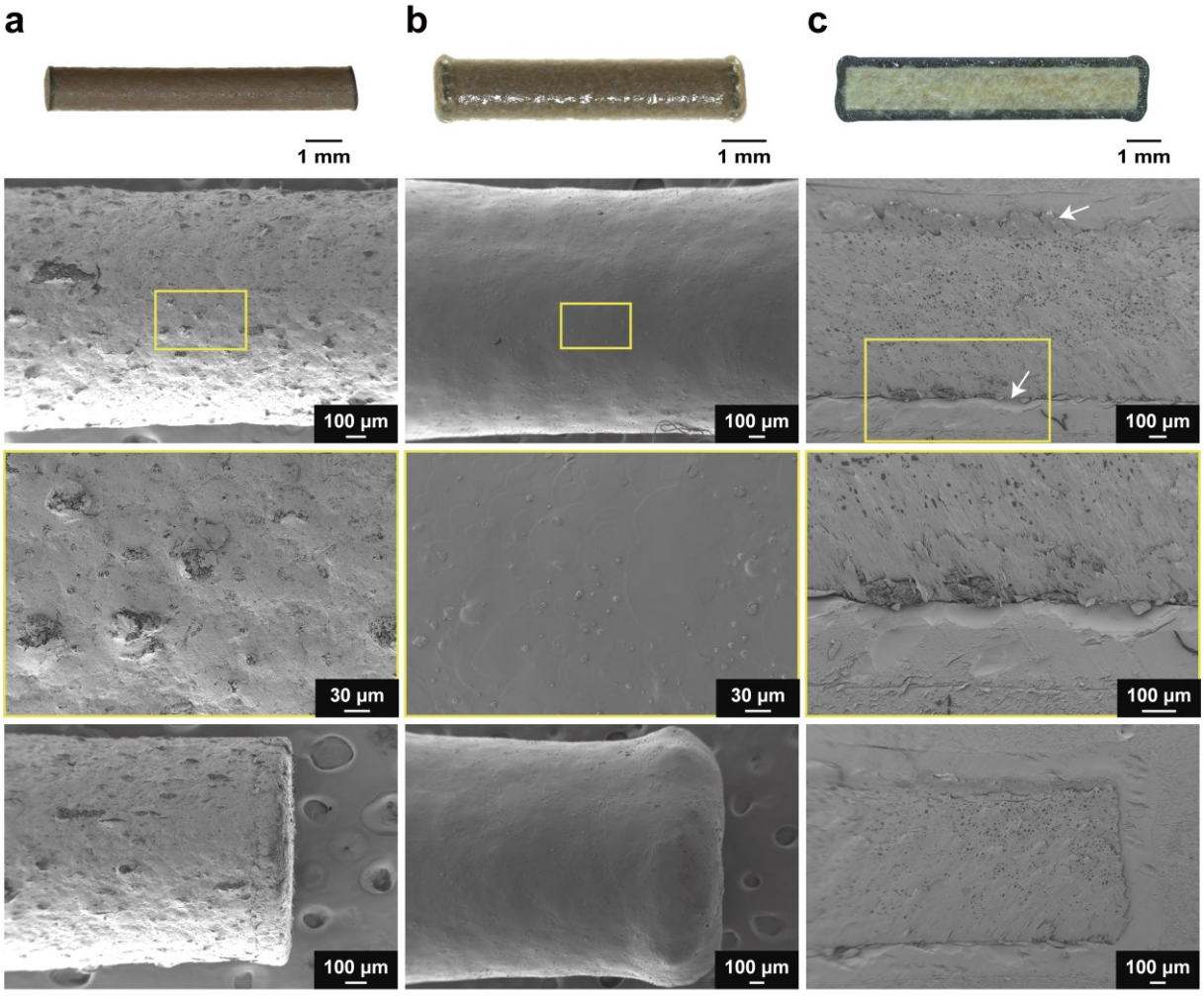


Figure 7.2: Representative digital images and scanning electron micrographs of a) a PEG-B core, b) a HME implant with a 300 µm PVBI/EO_{10} coating, and c) an epoxy-embedded and microtomed HME implant with a 300 µm PVBI/EO_{10} coating; note the slight defects caused by the microtoming process (white arrows).

7.3 Implant Performance

7.3.1 Investigation of the Mechanical Properties of the 1080 Implants

The flexural strengths (σ_F) and moduli (E_f) of the HME implants were investigated *via* three-point flexural testing (**Figure 7.3** and Appendix **Figure A7.6**) and compared to the ABS implants (**Chapter 6.2.2**). When the ABS implant core was replaced with the PEG-B core, the σ_F of the resultant HME implants was moderately reduced and increased commensurately with the thickness of the PVBI/EO_{10} coating (**Figure 7.3a**). The similar trend in σ_F results for both implant types demonstrated the dependence of σ_F upon the PVBI/EO_{10} coating and thickness, regardless of the core composition. In contrast, the E_f of the HME implants was significantly lower than the ABS implants (**Figure 7.3b**). The lower E_f of the HME implants was likely due to the softer and more malleable PEG-B core formulation compared to the stiffer combination of the NaOAc or 1080 core formulation and ABS filament. Together, the E_f results for the HME implants and ABS implants suggested that the E_f was primarily dependent on the composition of the implant core. However, the thickness of the PVBI/EO_{10} coating likely also had a minor contribution to the E_f, as observed in the small increase in E_f commensurate with the increase in PVBI/EO_{10} coating thickness. Implants with moderate flexibility would likely withstand the mechanical stressors experienced in the subcutaneous environment of a native animal. As such, the decrease in E_f — meaning the HME implants had a greater flexibility than the ABS implants — was considered an improvement.

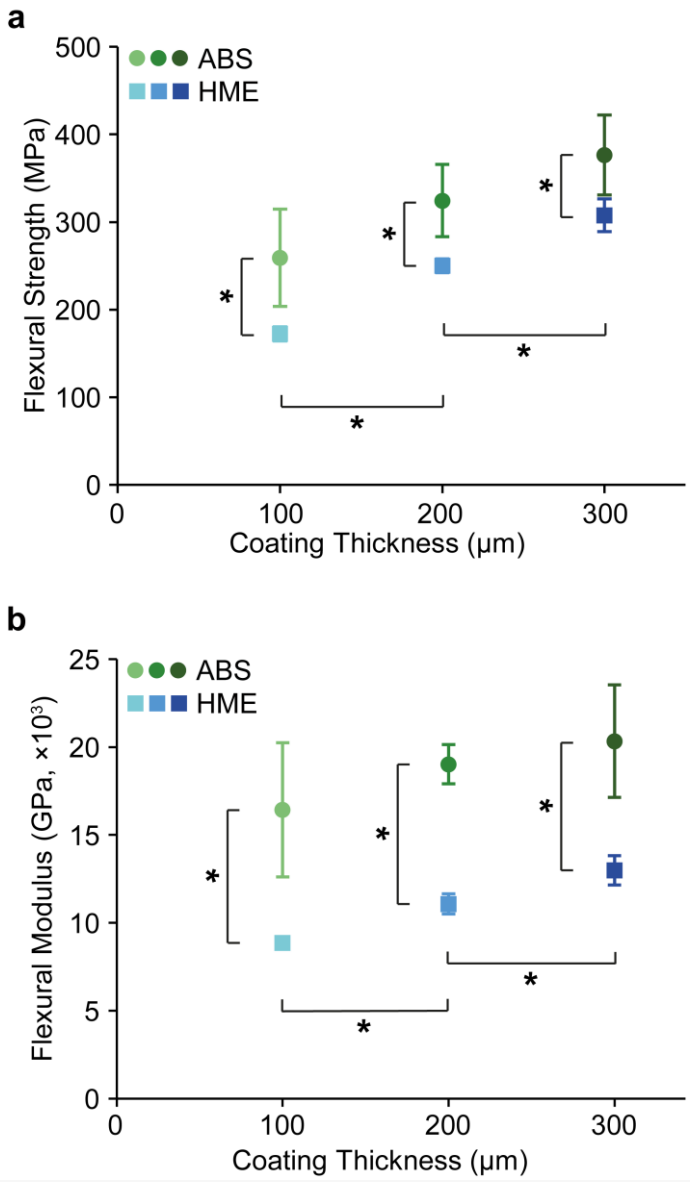


Figure 7.3: a) Flexural strength (σ_F) and b) flexural modulus (E_f) measurements of ABS implants and HME implants (n = 5), determined from force *versus* stroke curves generated through three-point flexural testing (Appendix, **Figure A7.6**). All tests were conducted at ambient temperature (23 °C) and all values are reported as the mean ± std. dev. (n = 5), *p < 0.05 × 2-sample t-test of difference = 0 (vs ≠ 0) (**Table A7.1**).

7.3.2 *In Vitro* Release Properties of the HME Implants

The dissolution characteristics of the HME implants were investigated *in vitro* at pH 1.0 and 1.5 (**Figure 7.4**) as described in **Chapter 5.2.4**, to mimic the pH of the gastric environment of a feral cat (pH ~ 1.6)[13, 14] and determine the pH-dependent release properties of the implants. At both pH 1.0 (**Figure 7.4a**) and 1.5 (**Figure 7.4b**), the initial release time for the HME implants increased with an increase in

PVBI/EO_{10} coating thickness from 100 to 300 µm (**Table 7.4**). Considering the same PVBI/EO_{10} coating was used for both ABS and HME implants, similar initial release times were expected, and observed (**Chapter 5.2.4**). However, the complete release times of the HME implants exceeded those of the ABS implants at all coating thicknesses and pH values. These protracted release profiles were attributed to the high molecular weight PEG (600 kDa) in the PEG-B core. As previously reported, during dissolution in an aqueous medium, high molecular weight PEG exhibits a swelling behaviour, and forms an interfacial gel layer prior to dissolution.[9] Invariably, the formation of a gel layer impedes erosion of the PEG, resulting in a slower, partially diffusion-mediated release of any entrapped materials. For the ABS implants, dissolution of the core was likely due to the erosion and dissolution of the lower molecular weight PEG (10 kDa), resulting in the rapid release of the dye (methylene blue (MB)) contained in the NaOAc or 1080 cores (**Chapter 5.2.4** and **Chapter 6.2.3,** respectively). Whereas the HME implants likely exhibited slower release due to the swelling of PEG 600 kDa, and the partially diffusion-limited release of tartrazine. Regardless, the complete release times of the HME implants at pH 1.0 and 1.5 (**Table 7.4**), were still within the GET of a feral cat (≤ 2.5 h cf., ~ 2.5–4 h).[15]

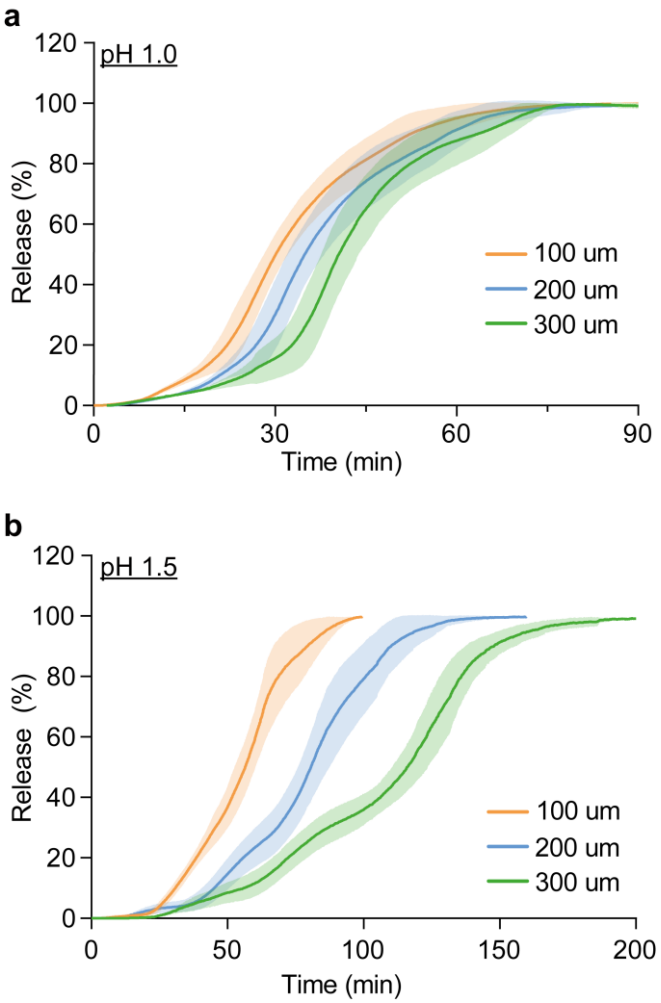


Figure 7.4: Release monitoring profiles of tartrazine from HME implants with PVBI/EO_{10} coatings of 100, 200 or 300 µm, at 37 °C, in a) pH 1.0 or b) pH 1.5 release media (3.5 mL). Traces are reported as the mean (solid line) ± std. Dev. (shaded area) (n = 5).

Table 7.4: Summary of HME implant *in vitro* release results.

Coating Thickness (µm) [a]	pH 1.0		pH 1.5	
	Initial Release (min) [b]	Complete Release (min) [c]	Initial Release (min) [b]	Complete Release (min) [c]
100	11.5 ± 0.8	53.2 ± 7.0	26.3 ± 1.8	76.6 ± 8.9
200	16.3 ± 1.2	58.2 ± 7.9	36.6 ± 6.6	109.2 ± 10.9
300	17.8 ± 0.9	61.9 ± 8.9	41.5 ± 9.5	146.6 ± 9.0

[a] HME core-implants coated with the PVBI/EO_{10} formulation; [b] Initial release was defined as 5% of the total release of tartrazine from the implant core; [c] Complete release was defined as 90% of the total release of tartrazine from the implant core. All values are reported as the mean ± std. dev. (n = 5).

7.3.3 *In Vitro* Stability Properties of the HME Implants

The *in vitro* stability of the HME implants was assessed as described in **Chapter 5.2.6** (**Figure 7.5**), where failure was determined by the observed release of tartrazine (i.e., yellow dye) into the Pluronics hydrogel medium. HME implants coated with 100 or 200 μm of the PVBI/EO_{10} coating failed rapidly under the testing conditions, with all samples (n = 5) failing in less than 20 and 40 d, respectively (**Figure 7.5a**). In contrast, HME implants bearing a 300 μm PVBI/EO_{10} coating were stable for at least 280 d (n = 3) but experienced two failures at 64 d and 200 d. Compared to the ABS implants, the HME implants coated with 100 or 200 μm of the PVBI/EO_{10} coating were considerably less stable. The observed decrease in stability appeared to be due to the swelling of the PEG-B core (e.g., **Figure 7.5b**) and the increased osmotic pressure caused by a greater concentration of solubilised components in the PEG-B core (cf., the NaOAc or 1080 cores). This combination of factors likely led to an increase in the rapidity and magnitude of the swelling, which caused the rupture of the thinner 100 and 200 μm PVBI/EO_{10} coatings of the HME implants. In contrast, the 300 μm PVBI/EO_{10} coatings were generally able to withstand the osmotic pressure (see swollen implants after 114 d, **Figure 7.5c**) and accommodate the swelling of the PEG-B core. Overall, 60% of the tested HME implants with a 300 μm PVBI/EO_{10} coating were stable for at least 280 d. The greater force required to stretch the thicker PVBI/EO_{10} coatings likely prevented their rupture. It is possible that the gel layer produced during the dissolution of the PEG-B core could also provide some mechanical support to the HME implants *in vivo*, which was not present for the ABS implants and may afford greater stability as a result, although further testing of the implants in their swollen state at 37 °C would be required.

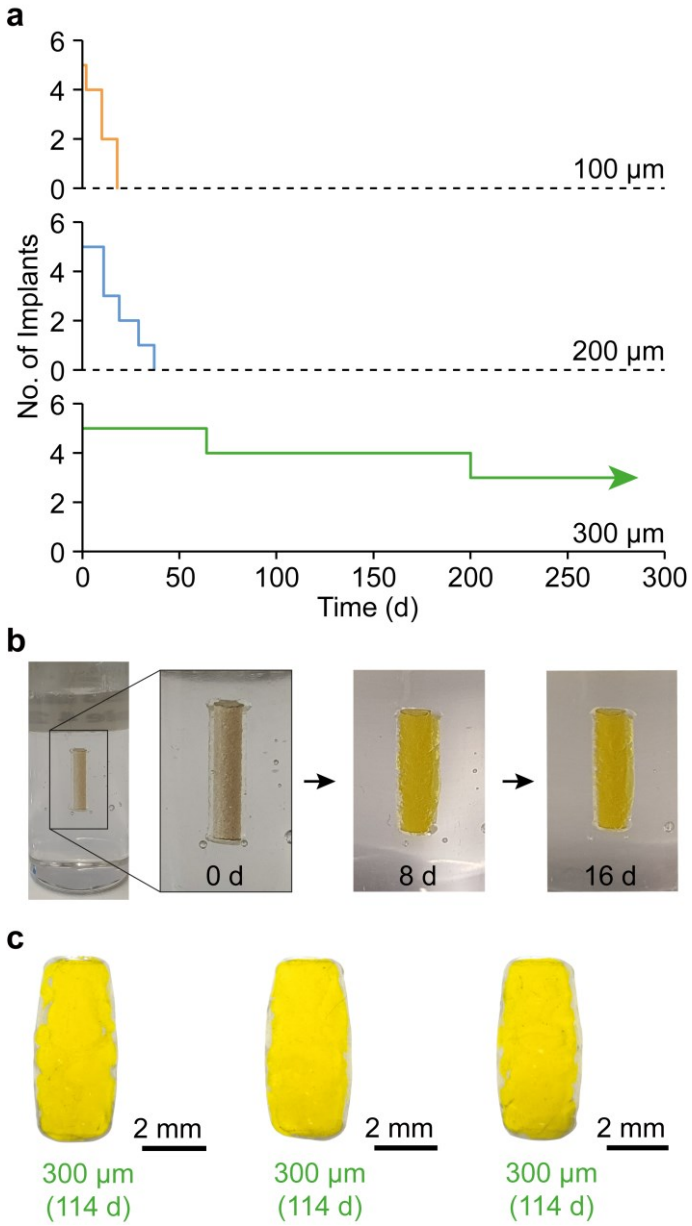


Figure 7.5: a) Stability results of HME implants with 100, 200, or 300 µm PVBI/EO_{10} coatings, in Pluronics F127 (25% $w.w^{-1}$, in phosphate-buffered saline (PBS)) at pH 7.4 and 37 °C (n = 6), over 280 d. b) Images showing the swelling of a HME implant (300 µm PVBI/EO_{10}) over 16 d, and c) representative implants that were stable at 114 d.

7.4 Conclusions

The PEG-B core, a water-soluble HME formulation, was investigated to enable the elimination of the ABS filament substrate used in the spray-coated cores of the ABS implants and to improve the stability of the resultant HME implants. Based on a reported formulation, the PEG HME formulation required an increase in the proportion of PEG 600 kDa, to enable the incorporation of NaOAc. The resultant

PEG-B formulation exhibited excellent homogeneity and accuracy of the loaded compounds (± ~ 5%) when extruded. The loading accuracy was determined *via* GPC, using an analytical approach that had not been previously reported, and provided a facile alternative for formulations containing a non-chromophoric API. The resultant PEG-B cores were prepared with low intrabatch variation (%RSD < 2.5%), and following coating with PVBI/EO_{10}, exhibited uniform and cohesive coatings at each thickness (100, 200, and 300 µm). The mechanical properties of the HME implants were like the ABS implants, showing a similar σ_F, supporting the dependence of σ_F upon the PVBI/EO_{10} coating and its thickness. Contrastingly, the E_f of the HME implants was significantly lower than the ABS implants due to the greater malleability of the PEG-B core, which provided further evidence that the E_f of the implants was predominantly dependent on the composition of the core. The PEG-B core was found to swell during stability testing, which caused the premature failure of implants bearing a 100 or 200 µm PVBI/EO_{10} coating. However, HME implants bearing a 300 µm PVBI/EO_{10} coating exhibited favourable stability. All implants released their core contents within the GET of a feral cat (≤ 2.5 h). In the future, PEG-B implants with a reduced core size could be facilely manufactured to contain a lower — but still lethal dose — of 1080. In addition, a thicker PVBI/EO_{10} coating could be used, that would likely better withstand the osmotic pressure during swelling and improve the stability of the implants. Overall, the HME implants exhibited favourable properties, and demonstrate that HME is a viable method for manufacturing implant cores without an ABS filament substrate. However, *in vivo* stability studies are required to determine whether removal of the ABS filament substrate from the implant core, affords an increase in implant stability.

7.5 Experimental

7.5.1 Materials

The materials described in Chapter 7 are the same as those in **Chapter 3.4.1**, **Chapter 4.4.1**, **Chapter 5.4.1**, and **Chapter 6.4.1**, unless stated below.

All reagents were used as received unless otherwise specified. Analytical grade sodium chloride (NaCl) was purchased from Chem-Supply (Gillman, Australia).

Glycerol (≥ 99.5%), D-sorbitol (≥ 98%), PVA (Mowiol® 4-88), and PEG (M_n = 6 and M_v = 600 kDa) were purchased from Sigma-Aldrich (St. Louis, United States).

7.5.2 Instrumentation

Instrument details are as outlined in **Chapter 3.4.2**, **Chapter 4.4.2**, **Chapter 5.4.2**, and **Chapter 6.4.2**, unless stated below.

Differential Scanning Calorimetry

Samples (~ 5–10 mg) were prepared in Standard Aluminium Pans (DSC Consumables Inc, Minnesota, United States). Under nitrogen flow (cell purge rate, 50 mL.min^{-1}), analyses were conducted using a temperature program of 25 °C to 150 °C (first heating), 150 °C to −80 °C (first cooling), and −80 °C to 150 °C (second heating). A ramp rate of 10 °C.min^{-1} was used throughout the temperature program. Enthalpies of fusion and solidification were calculated for the samples *via* the linear integration of their respective thermal transitions, using the Universal Analysis software package (v4.5A) (TA Instruments, New Castle, United States). The first heating cycle was used to determine the enthalpy of fusion for extrudate samples, to determine the effects of the processing conditions.

Hot-melt Extrusion

All hot-melt extrusion was performed using a custom-manufactured DCycle Extruder (DC Engineering, South Australia, Australia), fitted with a 1.2 mm diameter brass die. Images and simplified schematic drawings describing the extruder are provided in the Appendix (**Figure A7.7** and **Figure A7.8**, respectively).

Gel Permeation Chromatography

All analyses were conducted using a Shimadzu Corporation (Tokyo, Japan) Prominence liquid chromatography system (LC) fitted with two Agilent (Santa Clara, United States) columns in series (PL aquagel-OH Mixed-M (8 µm) and PL aquagel-OH 20 (5 µm)). The LC system was also fitted with Shimadzu (Tokyo, Japan) differential refractive index (DRI, RID-20A) and ultraviolet–visible light (UV,

SPD-10A) detectors. The mobile phase consisted of 0.05 M NaCl in 1:4 $v.v^{-1}$ methanol (MeOH):water, and the instrument was operated at a column temperature of 50 °C and a flow rate of 0.8 $mL.min^{-1}$.

7.5.3 Procedures

All procedures were conducted as described in **Chapter 3.4.3**, **Chapter 4.4.3**, **Chapter 5.4.3**, and **Chapter 6.4.3**, unless stated below.

Preparation of Hot-Melt Extrusion Formulations

Poly(ethylene glycol)

Two PEG formulations (A and B) were investigated for HME: PEG-A contained NaOAc (28.7 g), PEG 600 kDa (35.0 g), PEG 6 kDa (35.7 g) and tartrazine (0.66 g); PEG-B contained NaOAc (28.9 g), PEG 600 kDa (45.1 g), PEG 6 kDa (25.6 g) and tartrazine (0.66 g). For both PEG formulations, the components were combined in a 650 W commercial blender (Sunbeam, PB7650, Boca Raton, Florida) and blended into a homogenous powder. Care was taken to blend intermittently (15 s on, 60 s off) to avoid heating and melting the material. The components were blended for approximately ~ 5–10 min, until a qualitatively homogenous powder was obtained.

Hot-melt Extrusion

Poly(ethylene glycol)

For both PEG-A and PEG-B formulations, the powdered material (~ 15 g) was introduced to the hopper of the DCycle extruder. Operating at 80 °C, the extruder temperature was increased (in ~ 2 °C increments) and the extrusion rate varied from 4 to 8 rpm until successful extrusion was achieved. All the material was extruded, then cut into 5–10 mm pieces, and returned to the hopper for re-extrusion. The material was extruded at least three times to ensure its homogeneity, prior to further investigation or processing.

For the PEG-B formulation only, the end of the extrudate was bent, and a small weight (3.75 g) affixed, to stretch the extrudate and achieve the target diameter of 1.2 mm (Appendix,

Figure A7.3). The diameter of the extrudate was monitored during extrusion using a digital calliper. During the final (i.e., fourth) extrusion, the first and last 5–10 cm of extrudate was discarded.

The homogenous PEG-B extrudate was cut into ~ 8 mm lengths using a 3D printed filament cutting apparatus (Appendix, **Figure A7.5**) and a razor blade, to afford a batch of PEG-B cores (n ≈ 1400). The PEG-B cores were then rotary tumbled (Chicago Electric Power Tools, Single Drum Rotary Rock Tumbler, Carol Stream, United States) for 16 h in a container lined with 600 grit abrasive paper, in the presence of three small ceramic weights, prior to fluidised-bed spray coating (Appendix, **Figure A7.9**).

Investigation of Hot-Melt Extrusion Formulation Homogeneity

Standard solutions of PEG 6 and 600 kDa and tartrazine were accurately prepared at concentrations of 5.05, 5.09, and 0.62 $mg.mL^{-1}$, respectively, in the GPC mobile phase. Calibration curves of PEG 6 and 600 kDa, and tartrazine were prepared by injecting the standard solutions at a range of injection volumes (5–15, 5–20, and 0.5–20 µL, respectively). The known mass of each PEG or tartrazine sample for each injection volume was then correlated to the peak area obtained from the respective DRI and UV detectors.

PEG-B extrudate samples (~ 12 mg, n = 10) were obtained from random locations along ~ 10 m of extrudate and dried *in vacuo* for 24 h (23 °C, 0.02 mbar). Dried PEG-B samples were then solubilised in GPC mobile phase (4 mL). All PEG-B extrudate samples were analysed using the same conditions as the standards. The calibration curves and the obtained peak area of each analyte in the extrudate sample were then used to determine their mass in the extrudate sample. The mass of the remaining component, NaOAc, was then inferred from these data.

In Vitro Release Experiments

The *in vitro* release experiments were conducted as outlined in **Chapter 3.4.3**. An image of the stopper and polyester mesh used to suspend the implants in the cuvette during UV-vis spectrophotometric analysis is provided in the Appendix (

Figure A7.10).

Statistical *Analyses*

All results are expressed as the mean ± std. dev. The mean values of the σ_F and E_f were compared between two groups using unpaired two-tailed Student's t-tests. p-values < 0.05 were considered significant. All statistical tests were performed using the Minitab 17 (v17.1.0) software package. Exact p-values, t-values, and degrees of freedom (DF) are summarized in the Appendix (**Table A7.1**).

7.6 Appendix

7.6.1 Supplementary Figures



Figure A7.1: Image of a PEG-A extrudate sample, showing a heterogenous dispersion of NaOAc.

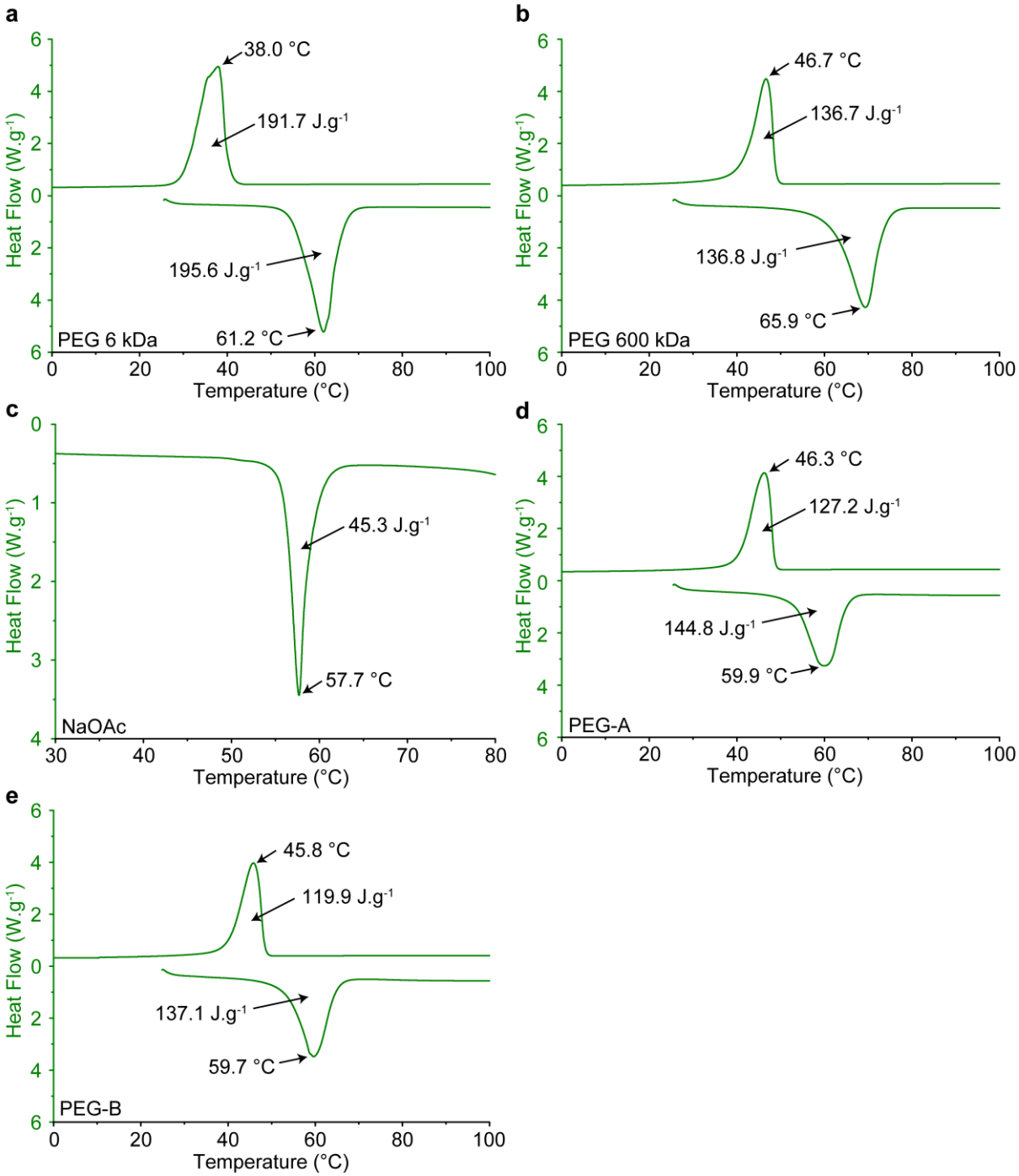


Figure A7.2: Heat flow ($W.g^{-1}$) curves (exo up) obtained *via* DSC analysis of neat a) PEG 6 kDa, b) PEG 600 kDa, c) NaOAc, and extruded d) PEG-A, and e) PEG-B formulations.

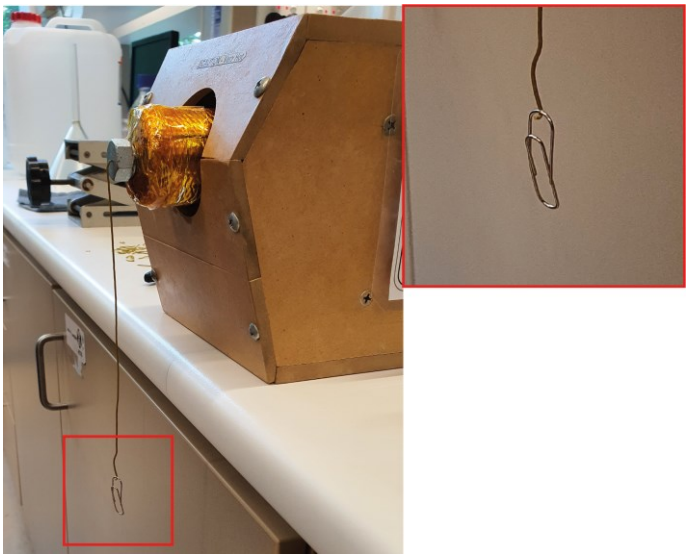


Figure A7.3: Digital images of the DCycle Extruder during extrusion, showing a small weight (i.e., paperclip, m = 3.75 g) affixed to the end of the extrudate, to achieve the target diameter (i.e., 1.2 mm).

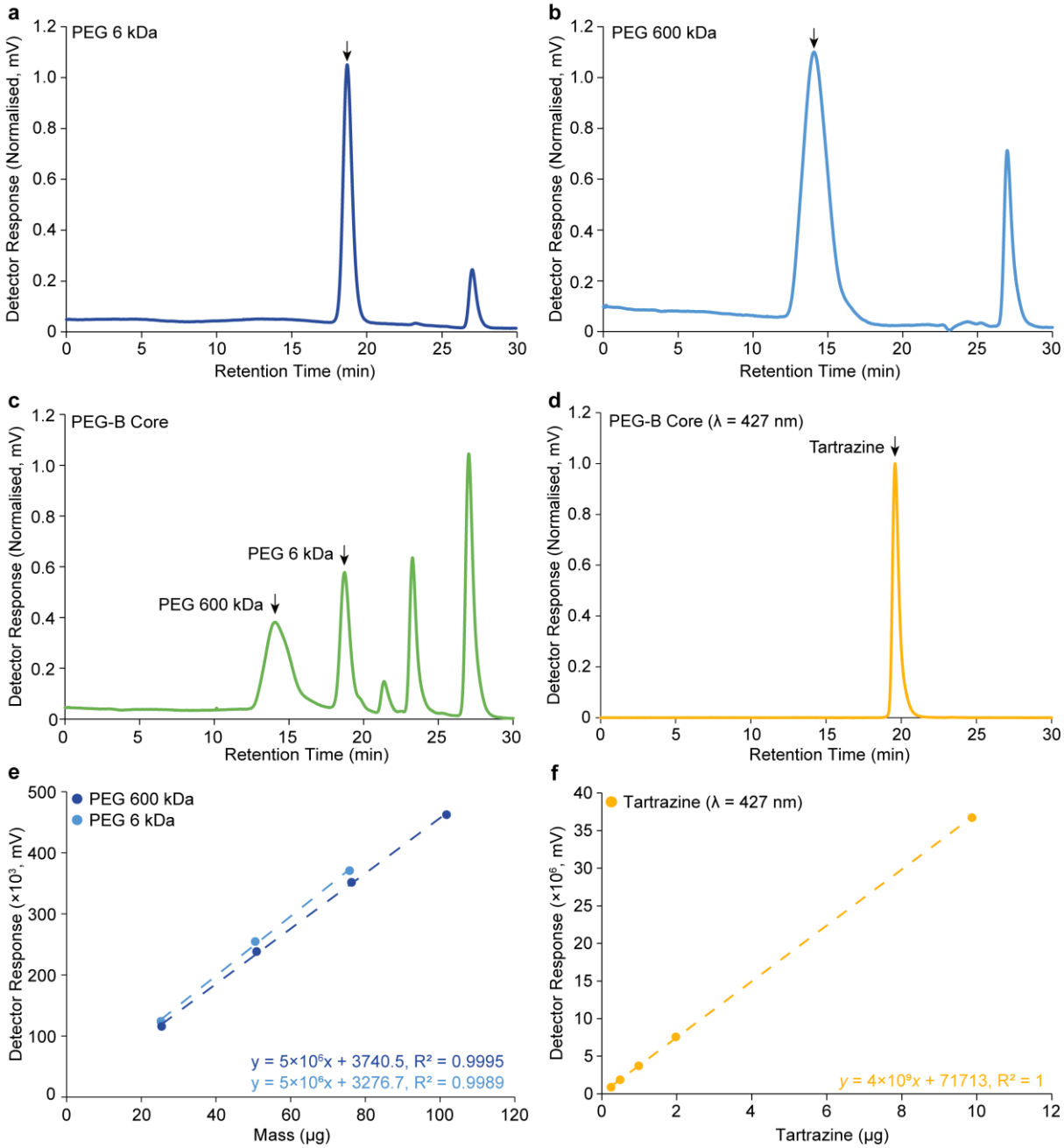


Figure A7.4: Representative GPC DRI chromatograms of PEG a) 6 and b) 600 kDa standards, and c) a PEG-B core sample. d) GPC UV chromatogram a PEG-B core sample. Standard curves prepared for e) PEG 6 and 600 kDa using the DRI detector, and f) tartrazine using the UV detector.

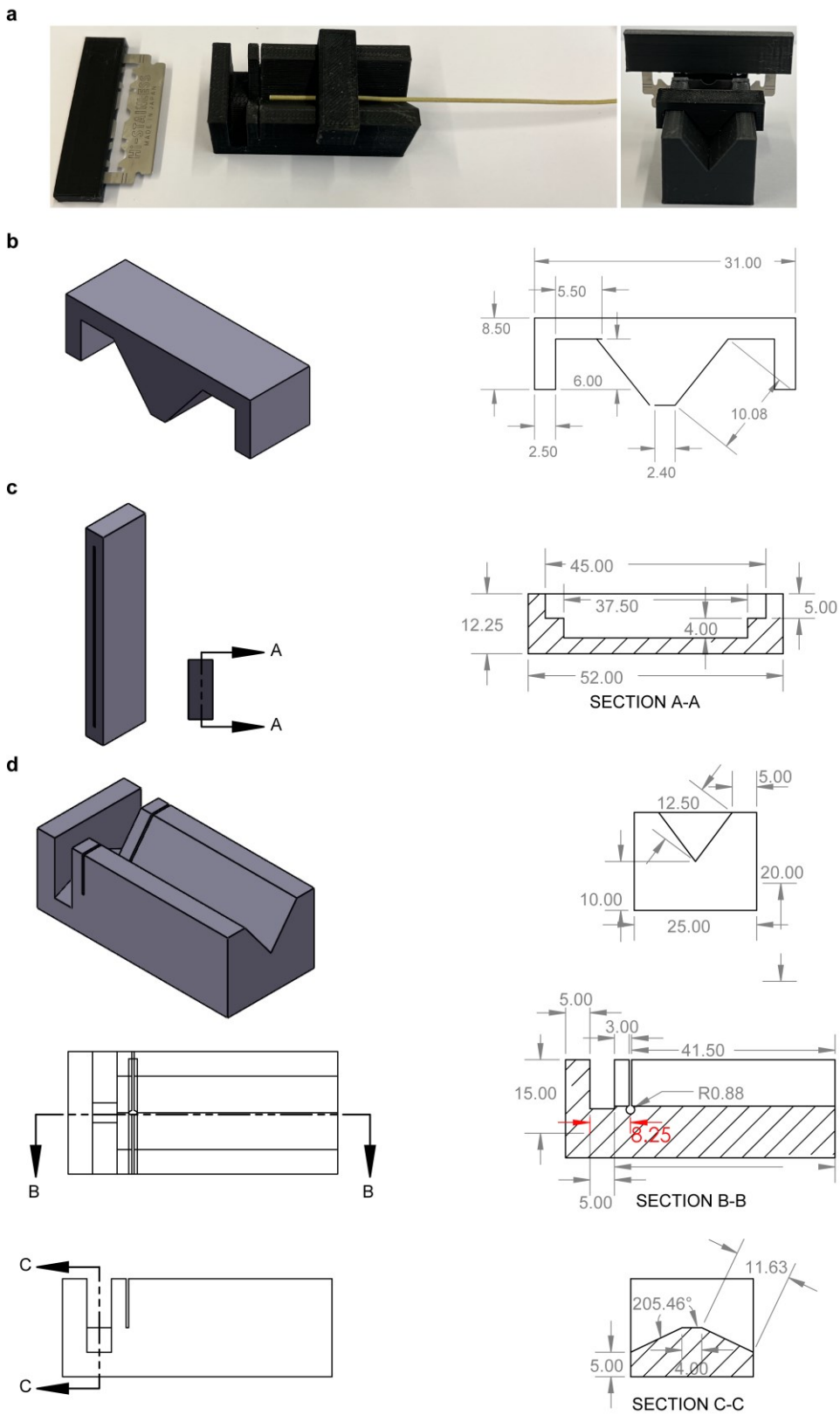


Figure A7.5: a) Images of the filament cutting apparatus, and schematic drawings of the filament cutting apparatus generated in Solidworks, showing the b) tamp used to secure filament during cutting, c) a double-edged razor blade holder used to cut the filament, and d) the cutting jig used to cut the PEG-B filament. Note the measurement labelled in red, which corresponds to the modelled distance between the cutting blade and the end stop for the filament.

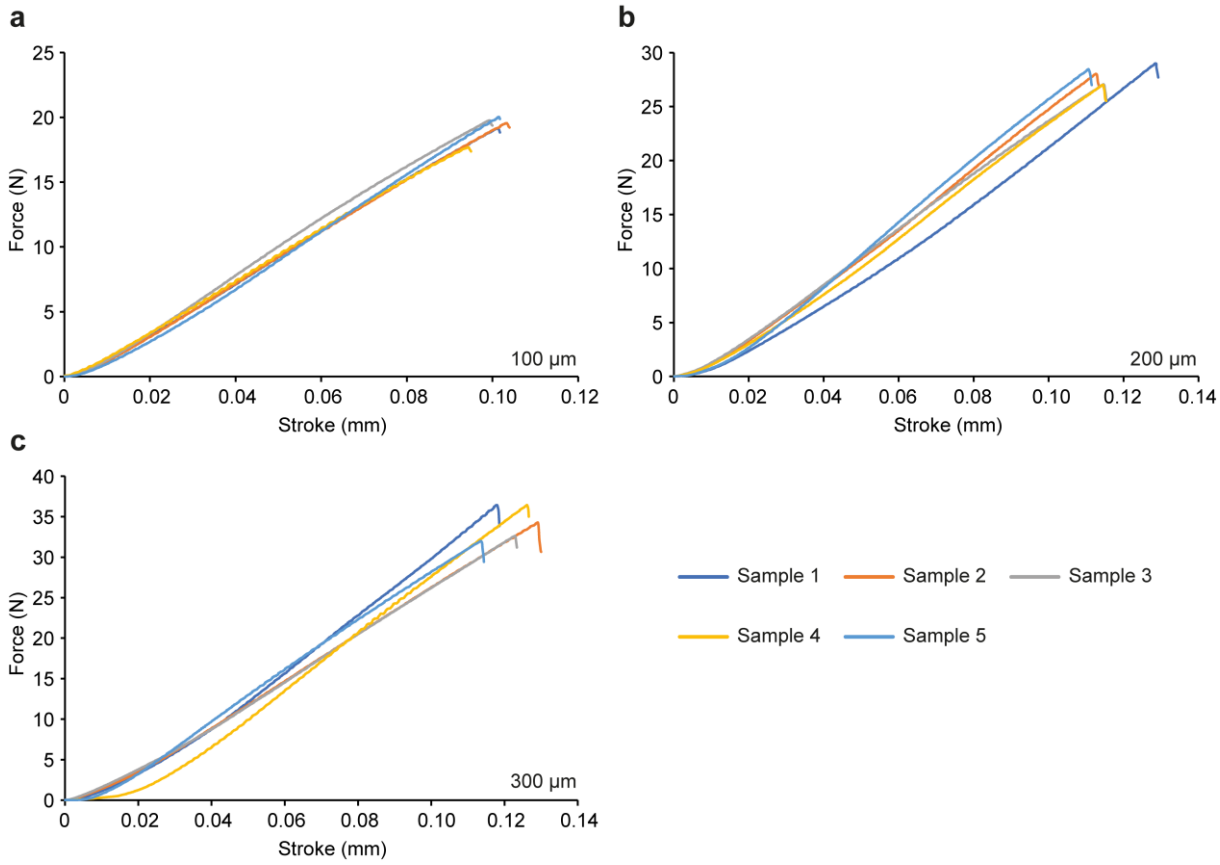


Figure A7.6: Force *versus* stroke graphs obtained *via* three-point flexural testing of HME implants coated with a) 100, b) 200, and c) 300 µm PVBI/EO$_{10}$ (n = 5 for all samples).



Figure A7.7: Images of the custom DCycle Extruder used to extrude the PEG-A and PEG-B hot-melt extrusion formulations.

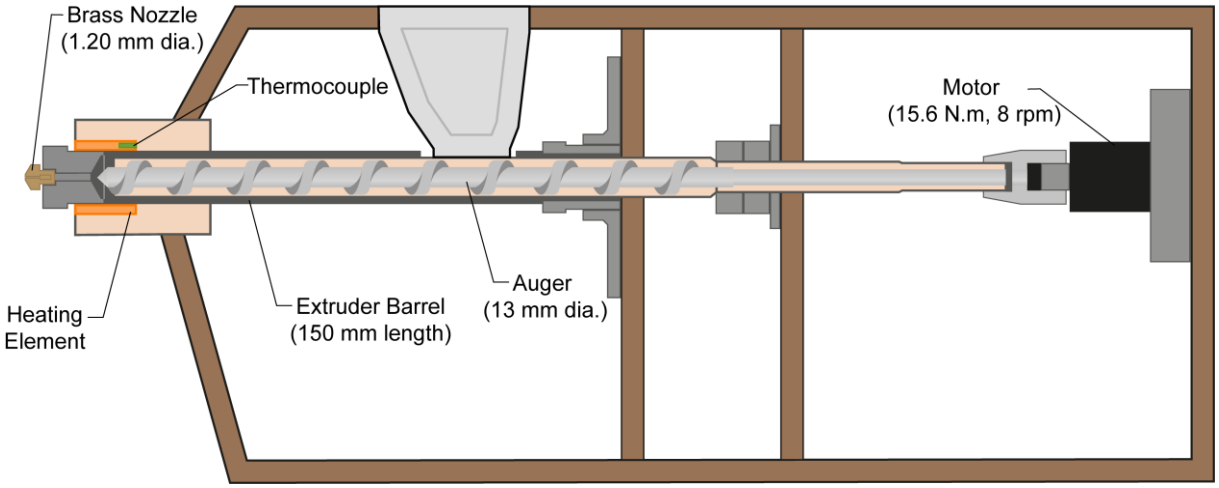


Figure A7.8: Simplified schematic drawing of DCycle Extruder design, showing relevant dimensions of the internal components.

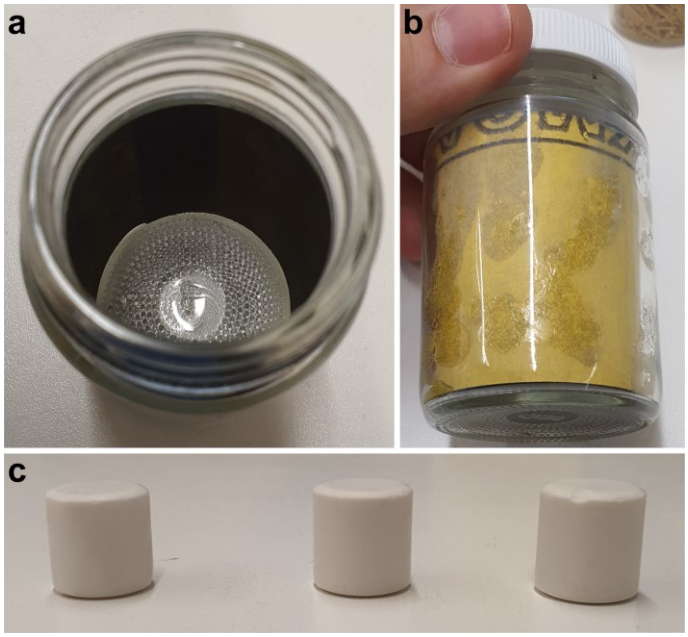


Figure A7.9: Images showing a) the abrasive paper (600 grit) lining b) the tumbling container, and c) the ceramic weights, all used to smooth the edges of the PEG-B cores.

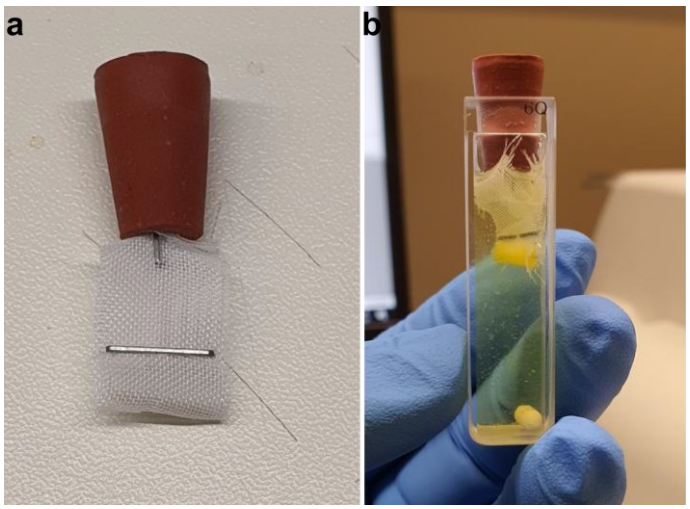


Figure A7.10: Images of the *in vitro* release experimental apparatus, showing a) the stopper and polyester mesh and b) an implant suspended in the release solution during dissolution.

Table A7.1: Summary of two-tailed Student's t-test results (t-test of difference = 0 (vs. ≠).

Test of Mean	t-value	DF	p-value
σ_F of (NaOAc) ABS *vs.* HME implants (100 µm)	3.45	4	0.026
σ_F of (NaOAc) ABS *vs.* HME implants (200 µm)	3.97	4	0.017
σ_F of (NaOAc) ABS *vs.* HME implants (300 µm)	3.12	5	0.026
σ_F of (NaOAc) ABS *vs.* HME implants (100 µm vs. 200 µm)	-15.29	7	< 0.001
σ_F of (NaOAc) ABS *vs.* HME implants (200 µm vs. 300 µm)	-6.41	5	< 0.001
E_f of (NaOAc) ABS *vs.* HME implants (100 µm)	4.42	4	0.012
E_f of (NaOAc) ABS *vs.* HME implants (200 µm)	14.18	5	< 0.001
E_f of (NaOAc) ABS *vs.* HME implants (300 µm)	4.97	4	0.008
E_f of (NaOAc) ABS *vs.* HME implants (100 µm vs. 200 µm)	-8.01	5	< 0.001
E_f of (NaOAc) ABS *vs.* HME implants (200 µm vs. 300 µm)	-4.23	7	0.004

7.6.2 Hot-melt extrusion of poly(vinyl alcohol)

Preparation of Poly(vinyl alcohol) and Sorbitol/Glycerol Hot-melt Extrusion Formulations

For all PVA formulations, the components were combined in ultrapure water and solubilised with stirring (85–90 °C) (**Table A7.2**). The resultant solutions were cooled to room temperature (23 ± 1 °C), then frozen whilst rotating (~ 300 rpm) on a rotary evaporator (Buchi Rotavapor R-200, Flawil, Switzerland) at atmospheric pressure, using an acetone/dry ice bath (~ −78 °C). Frozen samples were immediately freeze-dried (Martin Christ, Alpha 1-2 LDplus, Osterode, Germany) for 48 h (−56 °C, 0.54 mbar), and received as moderately flexible films.

Hot-melt Extrusion of Poly(vinyl alcohol) and Sorbitol/Glycerol

For all PVA HME formulations, samples were cut into irregularly shaped, ~ 5 mm pieces (~ 15 g total) and fed into the hopper of the DCycle extruder, which was fitted with a 1.2 mm diameter brass die. Initially operating at 150 °C, the extruder temperature was increased to 190 °C (in ~ 5°C increments), and the extrusion rate was varied from 4–8 rpm, to facilitate extrusion.

Results and Discussion

Like PEG, PVA was reported as compatible with relatively low extrusion temperatures (~ 140–180 °C), which were considered appropriate for the incorporation of either NaOAc or 1080. Jaeghere et al.[5] were able to tune the glass transition temperature (T_g) of extrudates containing PVA 4-88 (whereby, “4” is the viscosity (mPa.s) of a 4% aqueous solution at 20 °C, and “88” is the degree of hydrolysis of polyvinyl acetate (mol%)), *via* plasticisation with sorbitol. Incorporation of sorbitol from 0 to 40% w.w^{-1} reduced the T_g value of PVA 4-88 from 67.0 to 13.1 °C and enabled the solubilisation of the nonsteroidal anti-inflammatory drug celecoxib (15% w.w^{-1}) in a 40% w.w^{-1} sorbitol/PVA 4-88 formulation. Like the PEG formulation described by Isreb et al.,[1] the sorbitol/PVA formulation achieved relatively high drug loading and was considered a promising candidate formulation for the preparation of a NaOAc core.

The use of a PVA-based formulation was investigated using PVA 4-88 (i.e., Mowiol® 4-88). As previously reported,[4, 5] sorbitol and glycerol are effective plasticisers of PVA and so two formulations containing PVA 4-88/glycerol (PVA/G) and PVA 4-88/sorbitol (PVA/S) were investigated, with plasticiser concentrations of 3.5, 7.1 and 10.5% w.w^{-1} and 7.0% w.w^{-1}, respectively (**Table A7.2**). Initially, the glycerol-containing formulations (PVA/$G_{3.5}$, PVA/$G_{7.1}$, and PVA/$G_{10.5}$) were prepared from aqueous solutions *via* solvent casting. However, heterogenous samples were obtained, wherein the NaOAc precipitated during drying (80 °C), likely due to the high loading of NaOAc (~ 30%). To avoid precipitation, the glycerol- and sorbitol-containing (PVA/$S_{7.0}$) formulations were instead prepared from aqueous solutions *via* freeze-drying. Qualitatively, the PVA/G formulation afforded a homogenous, flexible film, whereas the PVA/S formulation afforded comparatively inflexible, solid material.

Table A7.2: Summary of the feed ratios of the tested PVA-based HME formulations.

HME Formulation	Mass Ratio (% w.w^{-1})				
	PVA 4-88	NaOAc	Glycerol	Sorbitol	Dye[a]
PVA/$G_{3.5}$	65.7	30.1	3.5	–	0.67
PVA/$G_{7.1}$	62.2	30.1	7.1	–	0.66
PVA/$G_{10.5}$	58.8	30.0	10.5	–	0.66
PVA/$S_{7.0}$	62.3	30.0	–	7.0	0.66

[a]PVA formulations containing glycerol used methylene blue, whereas PVA formulations containing sorbitol used tartrazine, due to the metachromasy previously observed with MB in the presence of NaOAc (**Chapter 6.2.3**).

To investigate the effects of the plasticisation agent and NaOAc loading on the T_g value of PVA 4-88, PVA/G films were analysed *via* modulated scanning differential calorimetry (MDSC). However, the glass transition of neat PVA 4-88 (57.8 °C) was found to overlap with a broad endotherm caused by the melting point transition of NaOAc trihydrate (58 °C),[16] observed between ~ 49–56 °C (Appendix, **Figure** A7.11).

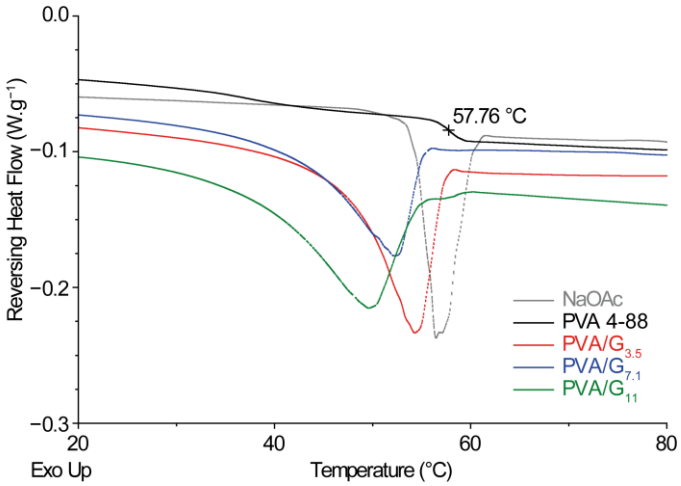


Figure A7.11: Overlay of the reversing heat flow curves ($W.g^{-1}$) from MDSC analyses of NaOAc, PVA 4-88, PVA/G3.5, PVA/$G_{7.1}$, and PVA/G_{11}, showing their respective glass transitions and T_g values, and melting point endotherms.

The presence of the NaOAc trihydrate endotherm precluded the determination of the T_g value of the PVA/G and PVA/S films, though if NaOAc was replaced with 1080 as intended, such an issue would not occur. Despite this, the HME of the PVA/$G_{7.1}$ and PVA/$S_{7.0}$ formulations was explored to determine whether an appropriate extrudate could be produced. Extrusion of the PVA/$G_{7.1}$ and PVA/$S_{7.0}$ formulations was attempted from 150 to 190 °C. Higher extrusion temperatures were not explored due to the expected thermal decomposition of glycerol[17] in the PVA/G samples and 1080 in future preparations. In all cases, a homogenous extrudate was not achieved at any extrusion temperature (Appendix,

Figure A7.12).

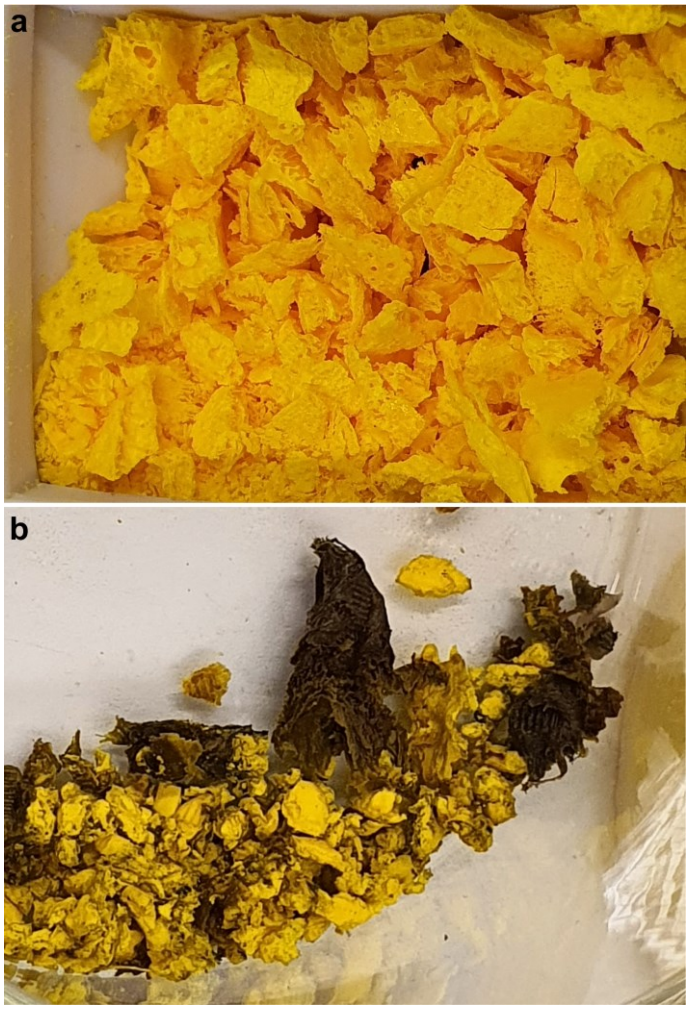


Figure A7.12: Example images of a failed extrusion, showing a) PVA/$S_{7.0}$ material prior to extrusion, and b) PVA/$S_{7.0}$ material following attempted extrusion.

It is likely that the high NaOAc loading and low PVA 4-88 content prevented the formation of a homogenous melt during extrusion. As a result, further development was conducted using the PEG-based formulation.

7.7 References

1. A. Isreb, K. Baj, M. Wojsz, M. Isreb, M. Peak and M. A. Alhnan, *Int J Pharm*, 2019, **564**, 98–105.

2. L. S. Karaffa, *The Merck Index: An Encyclopedia of Chemicals, Drugs, and Biologicals*, RSC Publishing, 2013.

3. M. D. Judd, B. A. Plunkett and M. I. Pope, *J Therm Anal*, 1974, **6**, 555–563.

4. L. Y. Lim and L. S. C. Wan, *Drug Dev Ind Pharm*, 1994, **20**, 1007–1020.

5. W. De Jaeghere, T. De Beer, J. Van Bocxlaer, J. P. Remon and C. Vervaet, *Int J Pharm*, 2015, **492**, 1–9.

6. L. Seidl, R. Grissa, L. Zhang, S. Trabesinger and C. Battaglia, *Adv Mater Interfaces*, 2022, **9**, 2100704.

7. A. Eckert, M. Abbasi, T. Mang, K. Saalwächter and A. Walther, *Macromolecules*, 2020, **53**, 1716–1725.

8. M. L. Hallensleben, in *Ullmann's Encyclopedia of Industrial Chemistry*, John Wiley & Sons, 2000, pp. 605–621.

9. O. Cantin, F. Siepmann, F. Danede, J. F. Willart, Y. Karrout and J. Siepmann, *J Drug Deliv Sci Technol*, 2016, **36**, 130–140.

10. C. T. Eason and C. M. Frampton, *Wildl Res*, 1991, **18**, 445–449.

11. T. C. dos Santos, G. J. Zocolo, D. A. Morales, G. d. A. Umbuzeiro and M. V. B. Zanoni, *Food Chem Toxicol*, 2014, **68**, 307–315.

12. N. Chekir, D. Tassalit, O. Benhabiles, N. Kasbadji Merzouk, M. Ghenna, A. Abdessemed and R. Issaadi, *Int. J. Hydrogen Energy*, 2017, **42**, 8948–8954.

13. P. Ryan, A. Odunayo, J. Price, S. Hecht, S. Hillsman, G. Galyon, J. Steiner and M. K. Tolbert, *J Vet Intern Med*, 2020, **34**, 1879–1885.

14. M. K. Tolbert, S. Olin, S. MacLane, E. Gould, J. M. Steiner, S. Vaden and J. Price, *J Vet Intern Med*, 2017, **31**, 1414–1419.

15. C. A. Wyse, J. McLellan, A. M. Dickie, D. G. M. Sutton, T. Preston and P. S. Yam, *J Vet Intern Med*, 2003, **17**, 609–621.

16. T. R. Kyriakides, H.-J. Kim, C. Zheng, L. Harkins, W. Tao and E. Deschenes, *Biomed Mater*, 2022, **17**, 022007.

17. M. Castelló, J. Dweck and D. Aranda, *J Therm Anal Calorim*, 2009, **97**, 627–630.

Chapter 8: Conclusions and Future Work

8.1 Conclusions

Populations of reintroduced mammals are uniquely at risk of depredation by control-averse or incursive feral cats, commonly known as ‘problem individuals’. Often, a single problem individual is responsible for the complete depredation of a reintroduced population, a phenomenon known as ‘catastrophic predation’. This work investigated the development of the population protecting implant (PPI) — a toxic, subcutaneous implant, that was intended to target problem individuals by exploiting the pH-differential between the subcutaneous and gastric environments of a native mammal and feral cat, respectively. In short, the PPI imbues implanted animals with an artificial toxicity, that is only activated during a successful predation event. By removing a problem individual following a single predation event, the remaining population of reintroduced mammals is protected from further predation, and catastrophic predation is avoided. Invariably, reducing predation in this way will increase the likelihood of a successful reintroduction program, which is crucial to the ongoing survival of threatened mammal species in Australia.

Both the design and function of the PPI were predicated upon its pH-responsiveness, which was required to mediate the spatiotemporal release of an encapsulated poison — in this case sodium fluoroacetate (1080). The PPI design was modelled after conventional film coated pharmaceutical formulations, due to their demonstrated ability to encapsulate and control the release of active pharmaceutical ingredients (APIs). Accordingly, a PPI design was proposed that incorporated a poison-loaded ‘core’, coated with a reverse enteric polymer coating.

At the time of writing, only a single technology with similar function to the proposed PPI was available — the hard-shell delivery vehicle (HSDV) developed by Scientec Research Pty Ltd. The HSDV is a poison-loaded capsule manufactured *via* hot-melt extrusion, for insertion into dried meat baits and use during poison baiting programs that target foxes and feral cats. Prior to the initial development of the PPI, the suitability of the HSDV platform was investigated in collaboration with Scientec Research Pty Ltd. Several HSDV designs were evaluated, including the original HSDV and a cylindrical implant-shaped HSDV, both bearing the same

Eudragit® E 100 coating, and three cylindrical HSDVs bearing polyester-based coatings. In all cases, the HSDVs were found to exhibit high intrabatch variability in terms of their physical dimensions and performed poorly during *in vitro* stability and release experiments. Importantly, the poor release performance of the Eudragit®-coated HSDVs *in vitro*, was attributed to the hydrophilicity of the coating, which promoted swelling due to osmotic water absorption. In addition, the end-sealing process used in their manufacture was found to be insufficient, as failures were observed at the sealed ends of the Eudragit®-coated HSDVs, when swollen. Overall, both Eudragit® E 100, and the proprietary hot-melt extrusion process employed by Scientec, were deemed inappropriate for use in developing the PPI, and alternatives were needed.

Few reverse enteric polymers were commercially available at the time of writing, and none exhibited the required physicochemical properties of a coating for long-term *in vivo* stability. In addition, fluidised-bed spray coating was identified as a suitable method to manufacture implants, as it would remove the need for a complex end-sealing process (i.e., as one would require during hot-melt extrusion), and simply require a substrate upon which to coat the core and polymer coatings. Accordingly, Objective 1 was to synthesise a library of pH-responsive copolymers and explore the tuneability of their physicochemical properties to afford reduced hydrophilicity (*cf.*, Eudragit® E 100) and compatibility with fluidised-bed spray coating. From a series of copolymers of 2-vinylpyridine (VP) and butyl methacrylate (BMA), a candidate copolymer (i.e., PVB 50/50) was identified as having favourable physicochemical properties and was evaluated further. Using a batch-type sequential fluidised-bed spray coating process, PPIs were successfully prepared bearing a PVB 50/50 coating, by coating an acrylonitrile butadiene styrene (ABS) filament substrate with a non-toxic sodium acetate (NaOAc) core, followed by an ethanolic PVB 50/50 solution. The resultant PVB implants exhibited favourable release properties and stability *in vitro*. However, a combination of swelling and mechanical stress was thought to have caused poor stability *in vivo*, when implanted in male Sprague-Dawley rats. The need for further optimisation of the pH-responsive copolymer's physicochemical properties was highlighted in these experiments.

Using the PVB copolymer as a platform for further optimisation, a library of copolymers additionally bearing either methyl methacrylate (i.e., PVBM) or

isobornyl methacrylate (i.e., PVBI) monomers, were then synthesised. The physicochemical properties of the resultant PVBM and PVBI copolymers could be tuned and therefore optimised, by varying the mol% fraction of the constitutive monomers. A new lead polymer — PVBI 50/30/20 — was identified through these experiments, due to its favourable solubility, and low water absorption, thereby achieving Objective 1. However, implants manufactured with the PVBI 50/30/20 coating were dusted, and fractured during handling and storage, likely due to the high glass transition temperature (T_g) of the copolymer, and optimisation of the fluidised-bed spray coating approach was required (Objective 2). To maintain the optimised physicochemical properties of the copolymer but reduce its T_g value, PVBI 50/30/20 was plasticised with varying ratios of ethyl oleate (EO) — a common hydrophobic plasticiser. It was found that a 10% $w.w^{-1}$ concentration of EO in the coating formulation (i.e., PVBI/EO_{10}), reduced the T_g value of the copolymer sufficiently to enable the formation of uniform and cohesive coatings on coated implants, which achieved Objective 2. Objective 3 was to investigate the manufacture of the implants using fluidised-bed spray coating. Implants bearing the PVBI/EO_{10} coating exhibited excellent (i.e., low) intrabatch variability, which required no further optimisation. The *in vitro* performance of the PVBI/EO_{10} implants needed to be evaluated to ensure adequate stability, release and mechanical strength had been afforded (Objective 4). The PVBI/EO_{10} implants exhibited excellent *in vitro* performance. At gastric pH, the implants were found to release their encapsulated NaOAc core within the gastric emptying time (GET) of a feral cat, and effectively contain it at physiological pH, for more than 12 months, thereby satisfying Objective 4. The stability of the implants was also investigated *in vivo* (Objective 5), and revealed favourable stability up to 12 weeks, following implantation in male Sprague-dawley rats. In addition, the PVBI/EO_{10} coating was found to exhibit comparable biocompatibility with conventional radiofrequency identification microchips. However, two failures were observed *in vivo*, which conflicted with the excellent *in vitro* stability results. Whilst swelling was still observed, it was posited that the implant failures were due to their location, as — like the PVB implants — the PVBI/EO_{10} implants that failed during stability testing were all implanted in the same caudal location. In both experiments, implants with the longest stability were located superficial to the left scapula, as a result it was thought necessary to constrain implantation to this location to maximise stability. Notably, when implanted for 1 week at the same high-stress (i.e., most caudal)

location, the PVBI/EO_{10} implants were more stable than the PVB implants, which suggested the PVBI/EO_{10} coating exhibited an increased ability to withstand swelling *in vivo*. While these results satisfied Objective 5, the tested implants contained a non-toxic NaOAc core, and so it was prudent to determine — with implants located superficial to the left scapula — whether these properties were conserved once a toxic 1080 core was used.

The same approach to achieving Objectives 3–5 was employed with the toxic version of the PPI. A core formulation containing 1080 (instead of NaOAc) was coated, followed by the lead pH-responsive PVBI/EO_{10} coating. Like the NaOAc implants, the 1080 implants exhibited excellent (i.e., low) intrabatch variation, stability results *in vitro* (> 18 months), and rapid release properties *in vitro*. However, three key challenges were faced with the 1080 implants. Following coating, the 1080 cores exhibited ‘flaring’ at each end, ostensibly due to electrostatic effects caused by 1080 during coating. Like the NaOAc core formulation, methylene blue (MB) was incorporated into the 1080 core, to enable monitoring of core release at low pH. However, in the presence of 1080, significant metachromasy was observed, which precluded the effective monitoring of release. During the *in vivo* interrogation of stability, the 1080 implants showed a significant reduction in performance. Implant failures — and the resultant toxification of implanted rats — occurred approximately every 30 d, until a single implant remained at the conclusion of the experiment (230 d). From the postmortem explantation and inspection of the 1080 implants it appeared that the PVBI/EO_{10} coating had been stained. Ostensibly, the staining was due to interactions with MB and/or 1080, which could have affected the integrity of the PVBI/EO_{10} coating — though the mechanism through which this would occur is unclear. Finally, following swelling *in vivo*, the ABS filament substrate — which was then able to move freely within the aqueous implant interior — was found to have punctured the PVBI/EO_{10} coating, causing its rupture and the premature release of 1080. It was not possible to completely decouple the three issues in this work i.e., the flaring, metachromasy caused by MB, and damage caused by the ABS filament substrate. While metachromasy was mitigated by replacing MB with tartrazine, flaring was still present, which precluded determining whether it alone contributed significantly to implant failure. From the available data, it is likely that the ABS filament substrate was the primary cause of the 1080 implant failures *in vivo*, as NaOAc implant

failures (both with PVB and PVBI/EO_{10} coatings) were also observed *in vivo*. Considering the increase in the number of failures exhibited by the 1080 implants, it is likely that the metachromasy and flaring exacerbated this effect, by reducing the integrity of the coating and causing non-uniform swelling, respectively. Importantly, the *in vivo* results highlighted that these shortcomings of the PPI design needed to be addressed in a modified version of the PPI design, to satisfy Objectives 3–5.

It was hypothesised that a water-soluble core — that did not contain an ABS filament substrate — would solubilise during swelling, thereby preventing puncturing of the PVBI/EO_{10} coating and potentially increase implant stability. To that end, implant cores were prepared with a poly(ethylene glycol) (PEG)-based non-toxic NaOAc core *via* hot-melt extrusion (HME). Importantly the PEG cores did not require the use of an ABS filament substrate, and contained tartrazine, a non-metachromatic dye. The resultant PEG cores exhibited excellent intrabatch variability, with accurate loading of NaOAc. Which demonstrated the effectiveness of the use of HME to accurately prepare implant cores. However, the manual cutting of the PEG cores during their preparation introduced end defects, due to the inherent malleability of the core material. The end defects were ameliorated by rotary tumbling, which appeared to prevent significant flaring following coating with the PVBI/EO_{10} formulation, though it would be prudent to utilise an inline cutting process in the future, to avoid introducing end defects and maximise throughput during implant manufacture. In addition, for the first time, gel permeation chromatography (GPC) was used to determine the composition of an extrudate and loading of an API (i.e., NaOAc). The reported GPC method can provide an accurate means of evaluating extrudate homogeneity in the absence of a chromophoric API. Fluidised-bed spray coating of the PEG cores produced HME implants with uniform and cohesive PVBI/EO_{10} coatings and was the first reported combination of HME and fluidised-bed spray coating, for the manufacture of a subcutaneous implant.

The flexural testing of the HME implants, combined with testing of the NaOAc and 1080 implants, demonstrated that the flexural modulus of the implants was dependent on the core composition, whereas the flexural strength was dependent on the PVBI/EO_{10} coating and its thickness. These results suggested that the relative mechanical properties of composite flexural testing samples (compared to

those of a singular composition) could be interrogated without significant changes to conventional flexural testing methodologies, which to the author's knowledge has not been previously reported.

The *in vitro* performance of the HME implants revealed similar release properties to the NaOAc and 1080 implants, with complete release being achieved within the GET of a feral cat. Interestingly, a small decrease in stability was observed *in vitro* (60%, 280 d), which occurred despite having resolved the issues associated with the ABS filament substrate, metachromasy, and core flaring. Instead, these failures were attributed to an increase in the rapidity and magnitude of swelling due to the greater concentration of solubilised components in the core. While the HME implants may be less likely to fail *in vivo*, due to the absence of the ABS filament substrate, these results suggested that the PVBI/EO_{10} coating may not withstand the increased osmotic pressure caused by the PEG core. It is possible that this effect could be mitigated by increasing the PVBI/EO_{10} coating thickness.

8.2 Future Work

8.2.1 Targeted Control of Problem Individuals

The primary focus of future experimentation should be to increase the coating thickness of the HME implants, to determine whether the observed failures can be eliminated when testing stability *in vitro*. It would likely require a reduction in the core diameter, and an increase in length, to ensure the HME implants remain compatible with conventional 2.12 mm diameter syringe implanters. However, as this work has demonstrated, these changes can be implemented easily. If the *in vitro* failures can be mitigated, then the HME implants could be further tested to determine whether the improvements in stability are translated *in vivo.* A minimum *in vivo* stability of 6–12 months would warrant continued investigation of the HME implants in the field. Implants that are stable for this period would be an effective means of protecting populations of vulnerable — but 1080 resistant — mammals from predation during the first 6–12 months of a reintroduction program. It is within this period that catastrophic predation often occurs,[1] and reintroduced populations are completely depredated. Implants failures following the first 6–12 months would administer a non-lethal dose to the implanted animals, the effects of which would

be negligible for 1080 resistant mammals. It may be possible to repeat implantation after this period, to provide protection for a further 12 months. In addition, it would be prudent to determine whether EO — the plasticiser used in the PVBI/EO_{10} coating — leaches from the coating under physiological conditions, as it was not investigated in this work. Though it may be possible to consider plasticiser leaching negligible over short periods, ultimately it is intended for the implants to be stable over several years. While this would afford protection for the natural life of the implanted animals, sufficient leaching of the plasticiser during this time could disrupt the integrity of the coating and cause implant failure. If EO does leach from the coating, re-engineering of the pH-responsive polymer composition would likely be required. The incorporation of other hydrophobic, low-T_g value monomers instead of methyl methacrylate or isobornyl methacrylate, may afford similar hydrophobicity to the PVBI 50/30/20 copolymer described herein, whilst reducing its T_g value and removing the need for plasticisation. As demonstrated in this work, the physicochemical and thermal properties of copolymers of VP can be tuned significantly, which supports this assertion.

Given the swelling exhibited by the implants described in this work, a preliminary investigation into the use of additive manufacturing — specifically 3D printing — to produce PPIs was also conducted in this work. It was hypothesised that an inert, biocompatible capsule — essentially an open-ended cylinder — could be 3D printed, filled with a core material, and sealed using the PVBI/EO_{10} formulation. Importantly, this design may impede swelling, by reducing the surface area of both the PVBI/EO_{10} copolymer and the PEG core, and thereby increase the stability of the implants. By localising the PVBI/EO_{10} coating at a single location at one end of the implant, this design would also prevent damage to, and failure of the implant, due to flexure or crushing forces. Common photopolymer resins used in 3D printing would invariably exhibit higher flexural strength and modulus values than the implants described in this work and could likely withstand any mechanical stresses experienced *in vivo*. While more details are provided in **Appendix 8.3.1**, notably, the 3D printed implants could be manually filled with a PEG core and sealed by tamping powdered PVBI/EO_{10} in the end of the capsule, and temporarily heating it above its T_g value. However, during preliminary testing it was difficult to form an effective seal, and failures were observed immediately during *in vitro* stability testing. Optimisation of this approach is required before a direct

comparison can be drawn with the ABS or HME implants. However, these preliminary results demonstrated that it is possible to produce 3D printed implants, and further investigation is warranted.

A final consideration would be to alter the shape of the implant. As briefly discussed in **Chapter 1.6**, spherical shaped implants could be produced using a combination of extrusion-spheronisation and fluidised-bed spray coating. It is likely that multiple implants would be required to afford a lethal dose of 1080 and maintain a suitable implant size. If multiple spherical implants were required, it may be necessary to temporarily constrain them to the implantation site until a fibrous tissue capsule has formed. This would prevent the migration of the implants away from the implantation site, and ensure they are all consumed by a problem individual. However, as noted earlier, it is not currently known whether the location of an implant will significantly affect consumption. The use of a spherical implant would likely enable the use of a thinner copolymer coating, given that the spheres would be isotropic and would lack any sharp vertices, unlike the cylindrical shaped ABS and HME implants. An isotropic shape would also distribute the stretching forces incurred during swelling evenly across its surface area, as the osmotic pressure would be equal in all directions. This would afford a reduction in regions of higher localised stress, thereby reducing the likelihood of the rupture of the coating and increasing the stability of the implants *in vivo*. Together, these properties might make spherical shaped implants more effective than their cylindrical counterparts, which warrants their further investigation.

8.2.2 Next-generation Poison Baits

In their current form, the implants require further development before they are appropriate for use in reintroduction programs. However, the current implant design, and the pH-responsive copolymers described in this work, may have applications elsewhere. For instance, as described in **Chapter 2.2**, Curiosity® and Hisstory® poison baits are buffered to pH 7.5 *via* the addition of sodium bicarbonate,[2] ostensibly to minimise the swelling and dissolution of the Eudragit® E 100 coating (soluble pH < 5) of the HSDV. However, there are multiple reports of HSDVs leaking following insertion into baits and in many cases, short-term exposure (< 8 d) to the weather conditions at the trial locations.[3–7] Premature

release of sodium fluoroacetate (1080, Hisstory baits) or para-aminopropiophenone (PAPP, Curiosity baits) from the HSDVs could result in sub-lethal dosing of the poison baits, as both 1080 and PAPP degrade rapidly in the environment. Sub-lethal dosing would render the poison baits both inhumane and ineffective at controlling feral cats and could potentially induce aversive behaviours in animals that consume them. The 1080 implants described in this work could be a suitable alternative to the HSDV, with potentially better performance. Compared to the HSDVs used in Curiosity® baits, the 1080 implants would likely have greater stability. The poor solubility of the PVBI/EO_{10} coating at pH values greater than 2, would likely negate the need to buffer the baits. While the uniform PVBI/EO_{10} coatings afforded by fluidised-bed spray coating would be less likely to fail following swelling, compared to the poorly end-sealed extrudates of the HSDVs. Importantly, the minimum 1080 implant stability demonstrated *in vivo* (~ 40 d) is likely longer than the lifetime of a poison bait, due to the decomposition of the bait medium and/or the degradation of 1080 as observed with conventional fox baits.[8, 9] The stability testing conditions reported in **Chapter 3.2.7**, could even be considered accelerated test conditions, given that dried meat baits are likely have reduced (and finite) moisture content, compared to the subcutaneous environment.

An important consideration for this application, however, is the storage, transport and preparation of these baits prior to deployment.[3] Curiosity® baits are often transported frozen, thawed to enable the insertion of a HSDV, then 'sweated' immediately before deployment — a process wherein baits are heated (generally *via* direct exposure to sunlight), to cause the exudation of fats and oils onto the bait surface, which is thought to increase bait attractiveness. In some cases, the HSDV is inserted into the meat bait, which is then frozen, transported to the trial site, and sweated prior to deployment.[2] In any case, exposure to temperature extremes during these processes could be detrimental to the 1080 implant, and the HSDV. The PVBI/EO_{10} (implant) and Eudragit® E 100 (HSDV) coatings exhibit T_g values of 35 and 48 °C, respectively. Freezing and sweating could lead to respective HSDV/implant temperatures of −20 and 42 °C.[5] At temperatures far below their T_g values (i.e., −20 °C), the coatings of both the HSDV and the 1080 implant would be brittle, and may be more likely to break during storage and handling. Similarly, at 42 °C, a temperature close to (Eudragit® E 100) or

exceeding (PVBI/EO_{10}) their T_g values, the coatings would be rubbery and prone to deformation. It is possible that the reported failures of HSDVs in Curiosity® baits could be due to a combination swelling and end-seal failure, and the freezing and sweating processes. It is not known if this has been previously investigated, however testing of implant stability following these processes would be necessary. Otherwise, where practicable, 1080 implants could be inserted into baits following sweating, and immediately prior to deployment.

8.2.3 Reverse Enteric Pharmaceutical Formulations

As highlighted in **Chapter 1.4**, there remains a need within the pharmaceutical sector for reverse enteric polymer coatings (i.e., those soluble at low pH, and insoluble at high pH) that effectively contain bitter APIs — a process called taste-masking. The pH-responsive copolymer series investigated in this work, exhibited potential as reverse enteric coatings for taste-masking applications. Selected copolymers were preliminarily evaluated for taste-masking in **Chapters 3.5.3 and 4.5.2**, and PVBM 40/50/10 was found to exhibit the most favourable taste-masking properties. Suglets® fluidised-bed spray coated with the PVBM 40/50/10 formulation, effectively contained a model drug formulation for 72 h in a simulated salivary solution (pH 6.8, 37 °C), and released it within 9 min in a simulated gastric environment (pH 1.5, 37 °C). Given the short residence time of most oral formulations in the oral environment (< 5 min), and the need for rapid release within the gastric environment, the PVBM 40/50/10 coated Suglets® showed excellent taste-masking performance. Importantly, taste-masking was achieved with a coating mass gain of 6.5% $w.w^{-1}$, which is comparatively lower than similar commercially available formulations such as Kollicoat® Smartseal 30D (40% $w.w^{-1}$), as described in **Chapter 1.4**. In addition, while selected copolymers were evaluated using fluidised-bed spray coating, it is possible that other common processing methods will be applicable to these copolymers. For example, all the copolymers synthesised in this work may be compatible with hot-melt extrusion processes, as they were thermally stable up to ~ 270 °C. The tuneability of the physicochemical properties of the copolymers that was demonstrated in **Chapter 3.2** and **Chapter 4.2**, also suggests that copolymers with specific T_g values could be synthesised. This could enable processing at a desired temperature, perhaps to obtain an extrudable copolymer at a temperature lower than the degradation

temperature of an API. Though preliminary, these results demonstrate the potential application of PVBM 40/50/10 — and the investigated polymer series in general — in taste-masking pharmaceutical formulations and warrants their further investigation.

8.3 Appendix

8.3.1 Implants Prepared *via* Additive Manufacturing

A 3D implant ‘capsule’, designed to accommodate a PEG-B core (**Chapter 7.2.3**), was modelled with dimensions that minimised its overall size (2.30 mm diameter, 9.40 mm length,

Figure A8.1a), while remaining suitable for printing. Implant capsules were printed in Vero PureWhite resin (Stratasys, Rehovot, Israel), using a Stratasys J735^{TM} PolyJet resin printer. As shown in

Figure A8.1b, a slightly wider cavity was incorporated into the open end of the implant capsule, intended to retain a PVBI/EO_{10} polymer ‘plug’ to seal the implant and confer its pH-responsiveness.

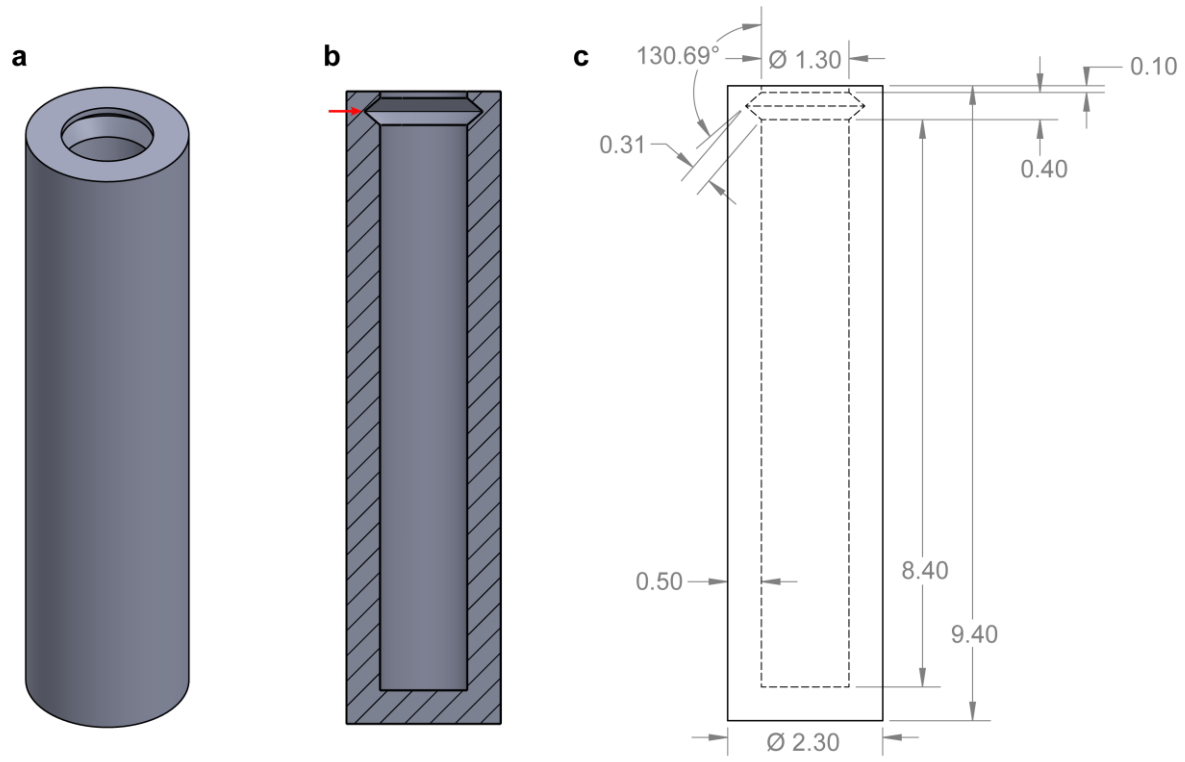


Figure A8.1: Schematic drawings generated in Solidworks showing a) a 3D isometric view of the 3D printed capsule, b) a 3D cross-sectional view of the 3D printed capsule, and c) a schematic drawing of the 3D printed capsule with annotated measurements (in mm). Note the red arrow in b) indicating the location of the polymer seal.

PEG cores were inserted into the capsules, and the end of the implant (including the cavity) was manually filled and tamped with powdered PVBI/EO_{10} until full. The filled implant capsules were then placed in a sample oven at 55 °C (16 h). Heating the implant capsules at a temperature ~ 20 °C above the T_g of PVBI/EO_{10}, caused the copolymer to 'flow' and form a densified plug, which solidified once the capsule was cooled to ambient temperature (23 °C), thus sealing the implant (**Figure A8.2a**). As shown in **Figure A8.2b,c**, the PEG cores filled the implant capsules below the cavity, as intended. However, the dimensions of the modelled cavity were poorly resolved, likely due to their diminutive size. Deformation of the PEG cores was also observed (**Figure A8.2c**), likely caused by the tamping process. Together, these results suggested the ends were not sealed effectively, which was confirmed during preliminary stability testing in Pluronics F127 (conducted as previously described in **Chapter 3.4.3**) (data not shown).

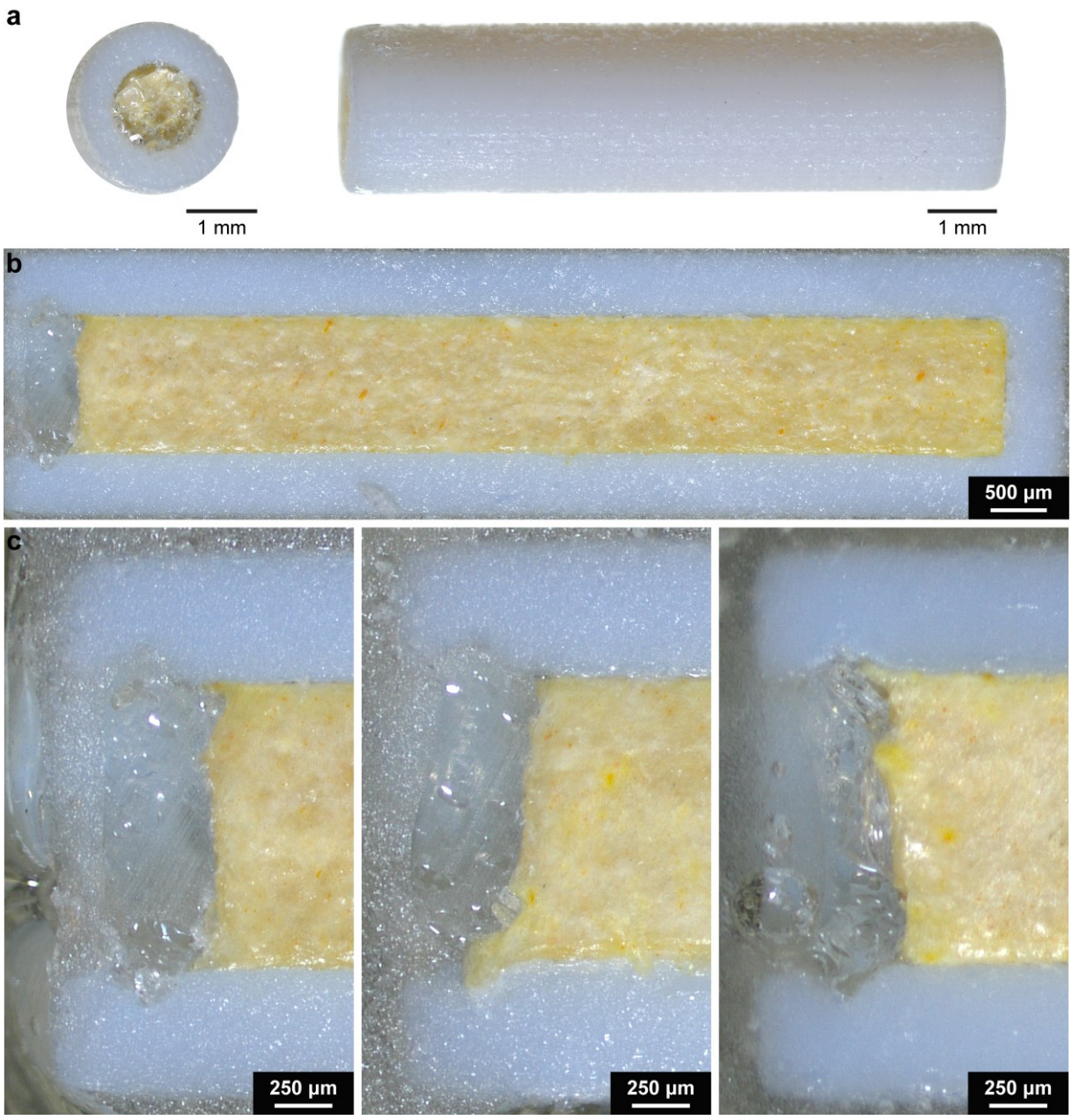


Figure A8.2: Digital images of a) the end and b) side of a representative 3D printed implant containing a PEG core and a PVBI/EO_{10} polymer seal, and c) a series of 3D printed implant cross-sections, obtained following epoxy embedment and microtoming.

8.4 References

1. K. Moseby, D. Peacock and J. Read, *Biol Conserv*, 2015, **191**, 331–340.

2. M. Johnston, *Field assessment of the Curiosity® bait for the management of feral cats after fire at Wilsons Promontory National Park*, Department of Sustainability and Environment, Heidelberg, Victoria, 2012.

3. M. Johnston, L. Bould, M. O'Donoghue, M. Holdsworth, P. Marmion, R. Bilney, A. Reside, D. Caldwell, R. Gaborov and T. Gentles, *Field efficacy of the Curiosity® bait for management of a feral cat population at Roxby Downs, South Australia*, Department of Environment and Primary Industries, Heidelberg, Victoria, 2014.

4. M. J. Johnston, F. Gigliotti, M. O'Donoghue, M. Holdsworth, S. Robinson, A. Herrod and K. Eklom, *Field assessment of the Curiosity® bait for management of feral cats in the semi-arid zone (Flinders Ranges National Park)*, Department of Sustainability and Environment, Heidelberg, Victoria, 2012.

5. M. Johnston, M. O'Donoghue, M. Holdsworth, S. Robinson, A. Herrod, K. Eklom, F. Gigliotti, L. Bould and N. Little, *Field assessment of the Curiosity® bait for managing feral cats in the Pilbara*, Department of Sustainability and Environment, Heidelberg, Victoria, 2013.

6. P. J. de Tores, D. R. Sutherland, J. R. Clarke, R. F. Hill, S. W. Garretson, L. Bloomfield, L. Strümpher, A. S. Glen and J. Cruz, *Wildl Res*, 2011, **38**, 39–50.

7. M. J. Johnston, D. Algar, N. Hamilton and M. J. Lindeman, *A bait efficacy trial for the management of feral cats on Christmas Island*, Department of Sustainability and Environment, Heidelberg, Victoria, 2010.

8. S. E. Allsop, S. J. Dundas, P. J. Adams, T. L. Kreplins, P. W. Bateman and P. A. Fleming, *Pac Conserv Biol*, 2017, **23**, 240–257.

9. G. Saunders and L. McLeod, *Improving fox management strategies in Australia*, Bureau of Rural Sciences, Canberra, 2007.

Chapter 9: Research Outputs

9.1 Publication Status of Thesis Research

K. Brewer, T. J. McWhorter, C. Sloper, K. Moseby, J. L. Read, D. Peacock and A. Blencowe, Toward Targeted Invasive Predator Control: Developing pH-Responsive Subcutaneous Implants for Native Mammals, *ACS Applied Polymer Materials*, 2022, **4**, 6687–6699. **Published 28th August 2022**

K. Brewer and A. Blencowe, Composition-Property Relationships of pH-Responsive Poly[(2-vinylpyridine)-*co*-(butyl methacrylate)] Copolymers for Reverse Enteric Coatings, *Pharmaceutics*, 2023, **15**. **Published 30th January 2023**

K. Brewer, T. J. McWhorter, K. Moseby, J. L. Read, D. Peacock and A. Blencowe, pH-Responsive Polymer Implants for the Protection of Native Mammals: Assessment of Material Properties and Poison Incorporation on Performance, *Polymers*, 2023, **15**, 878. **Published 10th February 2023**

K. Brewer, T. J. McWhorter, K. Moseby, J. L. Read, D. Peacock and A. Blencowe, pH-responsive Subcutaneous Implants Prepared *via* Hot-melt Extrusion and Fluidised-bed Spray Coating for Targeted Invasive Predator Control, *Journal of Drug Delivery Science and Technology*, 2023, 104277. **Published 22nd February 2023**

9.2 Other Published Works During Candidature

M. Arafat, Y. Song, **K. Brewer**, P. Fouladian, A. Parikh, H. Albrecht, A. Blencowe and S. Garg, Pharmaceutical Development of 5-Fluorouracil-Eluting Stents for the Potential Treatment of Gastrointestinal Cancers and Related Obstructions, *Drug Design, Development, and Therapy*, 2021, **15**, 1495–1507. **Published 9th April 2021**

A. D. Manning, T. A. Andrewartha, A. Blencowe, **K. Brewer**, I. J. Gordon and M. J. Evans, Bettering the devil you know: Can we drive predator adaptation to restore native fauna?, *Conservation Science and Practice*, 2021, **3**, e447. **Published 18th April 2021**

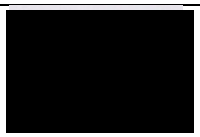
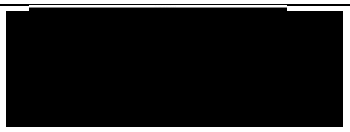
K. Brewer, F. Bai and A. Blencowe, pH-Responsive Poly(ethylene glycol)-*b*-poly(2-vinylpyridine) Micelles for the Triggered Release of Therapeutics, *Pharmaceutics*, 2023, **15**, 977. **Published 18th March 2023**

T. Andrewartha, M. Evans, A. Blencowe, **K. Brewer**, I. J. Gordon and A. D. Manning, Landscapes of Nausea: Successful Conditioned Taste Aversion in a Wild Red Fox Population, *Conservation Science and Practice*, 2023, **5**, e12984. **Published 10th July 2023**

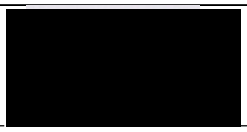
9.3 Statement of Authorship

Title of Paper	**Composition-Property Relationships of pH-Responsive Poly[(2-vinylpyridine)-*co*-(butyl methacrylate)] Copolymers for Reverse Enteric Coatings**	
Publication Status	**Published**	
Publication Details Relevant reference details	K. Brewer and A. Blencowe, Pharmaceutics, 2023, 15. The published article is available online at: https://doi.org/10.3390/pharmaceutics15020454	
PRINCIPAL AUTHOR		
Name of Principal Author (Candidate)	**Kyle Brewer**	
Contribution to the Paper Brief description of your work in this publication	Conceptualisation, methodology, formal analysis, investigation, writing (original draft), writing (review and editing) and visualisation.	
Overall Percentage (%)	85%	
Certification	I hereby certify this statement of contribution is correct and I give permission for the inclusion of the paper in the Thesis.	
Signature	[redacted]	Date: 24/02/2023
CO-AUTHOR CONTRIBUTIONS		
By signing the Statement of Authorship, each author certifies that: I. the candidate's stated contribution to the publication is accurate (as detailed above); II. permission is granted for the candidate in include the publication in the thesis; and III. the sum of all co-author contribution is equal to 100% less the candidate's stated contribution.		
Name of Co-Author 1	**Anton Blencowe**	
% Contribution to the Paper	15%	
Signature	[redacted]	Date: 24/02/2023

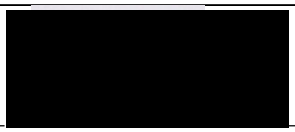
Title of Paper	**Toward Targeted Invasive Predator Control: Developing pH- Responsive Subcutaneous Implants for Native Mammals**	
Publication Status	**Published**	
Publication Details Relevant reference details	K. Brewer, T. J. McWhorter, C. Sloper, K. Moseby, J. L. Read, D. Peacock and A. Blencowe, ACS Appl. Polym. Mater., 2022, 4, 6687-6699. The published article is available online at: https://doi.org/10.1021/acsapm.2c01041	
PRINCIPAL AUTHOR		
Name of Principal Author (Candidate)	**Kyle Brewer**	
Contribution to the Paper Brief description of your work in this publication	Conceptualisation, methodology, investigation, formal analysis (excluding *in vivo* studies), writing (original draft), and visualisation	
Overall Percentage (%)	70%	
Certification	I hereby certify this statement of contribution is correct and I give permission for the inclusion of the paper in the Thesis.	
Signature	[redacted]	Date: 24/02/2023
CO-AUTHOR CONTRIBUTIONS		
By signing the Statement of Authorship, each author certifies that: IV. the candidate's stated contribution to the publication is accurate (as detailed above); V. permission is granted for the candidate in include the publication in the thesis; and VI. the sum of all co-author contribution is equal to 100% less the candidate's stated contribution.		
Name of Co-Author 1	**Todd J. McWhorter**	
% Contribution to the Paper	10%	
Signature	[redacted]	Date: 24/02/2023
Name of Co-Author 2	**Catherine Sloper**	
% Contribution to the Paper	4%	
Signature	[redacted]	Date: 24/02/2023
Name of Co-Author 3	**Katherine Moseby**	
% Contribution to the Paper	2%	

Signature		Date: 27/02/2023
Name of Co-Author 4	**John L. Read**	
% Contribution to the Paper	2%	
Signature		Date:25/02/2023
Name of Co-Author 5	**David Peacock**	
% Contribution to the Paper	2%	
Signature		Date: 25/02/2023
Corresponding Author	**Anton Blencowe**	
% Contribution to the Paper	10%	
Signature		Date: 24/02/2023

Title of Paper	**pH-Responsive Polymer Implants for the Protection of Native Mammals: Assessment of Material Properties and Poison Incorporation on Performance**	
Publication Status	**Published**	
Publication Details Relevant reference details	K. Brewer, T. J. McWhorter, K. Moseby, J. L. Read, D. Peacock and A. Blencowe, Polymers, 2023, 15, 878. The published article is available online at: https://doi.org/10.3390/polym15040878	
PRINCIPAL AUTHOR		
Name of Principal Author (Candidate)	**Kyle Brewer**	
Contribution to the Paper Brief description of your work in this publication	Conceptualisation, methodology (*in vitro* studies), investigation, formal analysis, writing (original draft, reviewing/editing), visualisation.	
Overall Percentage (%)	70%	
Certification	I hereby certify this statement of contribution is correct and I give permission for the inclusion of the paper in the Thesis.	
Signature	[redacted]	Date: 24/02/2023
CO-AUTHOR CONTRIBUTIONS		
By signing the Statement of Authorship, each author certifies that: VII. the candidate's stated contribution to the publication is accurate (as detailed above); VIII. permission is granted for the candidate in include the publication in the thesis; and IX. the sum of all co-author contribution is equal to 100% less the candidate's stated contribution.		
Name of Co-Author 1	**Todd J. McWhorter**	
% Contribution to the Paper	10%	
Signature	[redacted]	Date: 24/02/2023
Name of Co-Author 2	**Katherine Moseby**	
% Contribution to the Paper	2.5%	
Signature	[redacted]	Date: 27/02/2023
Name of Co-Author 3	**John L. Read**	
% Contribution to the Paper	2.5%	

Signature		Date:25/02/2023
Name of Co-Author 4	**David Peacock**	
% Contribution to the Paper	2.5%	
Signature		Date: 25/02/2023
Corresponding Author	**Anton Blencowe**	
% Contribution to the Paper	12.5%	
Signature		Date: 24/02/2023

Title of Paper	**pH-responsive subcutaneous implants prepared *via* hot-melt extrusion and fluidised-bed spray coating for targeted invasive predator control**	
Publication Status	**Published**	
Publication Details Relevant reference details	K. Brewer, T. J. McWhorter, K. Moseby, J. L. Read, D. Peacock and A. Blencowe, J Drug Deliv Sci Technol, 2023, 104277. The published article is available online at: https://doi.org/10.1016/jJddst.2023.104277	
PRINCIPAL AUTHOR		
Name of Principal Author (Candidate)	**Kyle Brewer**	
Contribution to the Paper Brief description of your work in this publication	Conceptualisation, methodology, investigation, formal analysis, writing (draft and reviewing/editing), visualisation.	
Overall Percentage (%)	75%	
Certification	I hereby certify this statement of contribution is correct and I give permission for the inclusion of the paper in the Thesis.	
Signature	[redacted]	Date: 24/02/2023
CO-AUTHOR CONTRIBUTIONS		
By signing the Statement of Authorship, each author certifies that: I. the candidate's stated contribution to the publication is accurate (as detailed above); II. permission is granted for the candidate in include the publication in the thesis; and III. the sum of all co-author contribution is equal to 100% less the candidate's stated contribution.		
Name of Co-Author 1	**Todd J. McWhorter**	
% Contribution to the Paper	2.5%	
Signature	[redacted]	Date: 24/02/2023
Name of Co-Author 2	**Katherine Moseby**	
% Contribution to the Paper	2.5%	
Signature	[redacted]	Date: 27/02/2023
Name of Co-Author 3	**John L. Read**	
% Contribution to the Paper	2.5%	

Signature		Date:25/02/2023
Name of Co-Author 4	**David Peacock**	
% Contribution to the Paper	2.5%	
Signature		Date: 25/02/2023
Corresponding Author	**Anton Blencowe**	
% Contribution to the Paper	15%	
Signature		Date: 24/02/2023